PREDICTING PETROPHYSICAL PROPERTIES BY SIMULTANEOUS INVERSION OF SEISMIC AND RESERVOIR ENGINEERING DATA

A DISSERTATION
SUBMITTED TO THE DEPARTMENT OF GEOPHYSICS
AND THE COMMITTEE ON GRADUATE STUDIES
OF STANFORD UNIVERSITY
IN PARTIAL FULFILLMENT OF THE REQUIREMENTS
FOR THE DEGREE OF DOCTOR OF PHILOSOPHY

Andrés Eduardo Mantilla
November 2002

I certify that I have read this dissertation and that, in my opinion, it is fully adequate, in scope and quality as a dissertation for the degree of Doctor of Philosophy.

_____

Amos M. Nur (Principal Adviser)

I certify that I have read this dissertation and that, in my opinion, it is fully adequate, in scope and quality as a dissertation for the degree of Doctor of Philosophy.

_____

Roland Horne

I certify that I have read this dissertation and that, in my opinion, it is fully adequate, in scope and quality as a dissertation for the degree of Doctor of Philosophy.

_____

Biondo Biondi

I certify that I have read this dissertation and that, in my opinion, it is fully adequate, in scope and quality as a dissertation for the degree of Doctor of Philosophy.

_____

Jack Dvorkin

Approved for the University Committee on Graduate Studies:

_____

This page intentionally left blank

Abstract

Porosity and permeability are the most difficult properties to determine in subsurface reservoir characterization, yet usually they have the largest impact on reserves and production forecasts, and consequently on the economy of a project. The difficulty of estimating them comes from the fact that porosity and permeability may vary significantly over the reservoir volume, but can only be sampled at well locations, often using different technologies at different scales of observation. An accurate estimation of the spatial distribution of porosity and permeability is of key importance, though, because it translates into higher success rates in infill drilling, and fewer wells required for draining the reservoir.

The purpose of this thesis is to enhance the characterization of subsurface reservoirs by improving the prediction of petrophysical properties through the combination of reservoir geophysics and reservoir engineering observations and models. This goal is fulfilled by formulating, implementing, and demonstrating the applicability of the joint inversion of seismic- and production-related observations, and the use of *a-priori* information about the relationship —not necessarily linear— between porosity and permeability.

From a fluid flow model based on the diffusivity equation, and a seismic model that is founded on principles of elasticity and rock physics, I determine the sensitivity of production and seismic measurements to variations in petrophysical properties. I use these models and sensitivities in the framework of a gradient-based optimization algorithm that yields spatial estimates of porosity and permeability. Being constrained by physical models and observations, the resulting estimates are appropriate for making reservoir management decisions.

Solution to the aforementioned problem requires the integration of rock physics, petrophysics, flow modeling, well testing, and optimization theory, as well as the study of upscaling and griding issues in order to guarantee the consistency of the analysis and the coherency of results. Elastic properties - and therefore seismic data - are mostly affected by porosity and lithology. In some cases, they may also be affected by fluid

replacement, which is controlled by permeability. Production data are mainly affected by the distribution of permeability in the reservoir, and boundary conditions, although there is some influence of porosity in storage terms of the mass balance equations the model is based on.

The integrated inversion of production and seismic data guarantees a solution that is consistent with both types of measurements, while if they are used separately there will be two answers that are likely to be inconsistent because they are not constrained to all available data.

To demonstrate the applicability of the methods, I provide in this thesis a rock physics and seismic characterization of reservoir heterogeneities in the Cretaceous fluvial sandstones of the K2 Unit of the Apiay-Guatiquía Oil Field. I first determine the magnitude and orientation of principal stresses in the area, which is important to determine the level of effective stress that is relevant for rock physics analyses. Then I study the petrophysical properties of the K2 Unit reservoir at the pore, well log, and field scales. Finally, I apply the joint inversion methodology I propose to the estimation of petrophysical properties in the drainage area of one of the wells in this field.

Acknowledgements

I would like to thank professor Amos Nur for his invaluable advise and continued support during my time at Stanford. Professor Nur had the patience that my research project required, and trusted me when I faced difficult times. I feel honored to have had such a great adviser.

I want to thank the members of my committee, professors Roland Horne, Steve Graham, Biondo Biondi, and Jack Dvorkin, for their useful comments and feedback. I received from Jack my first rock physics lessons: I had the opportunity of collaborating with him in several projects, which became some of the most rewarding experiences I had at Stanford. Thanks Jack for your support and the many lessons you taught me. The help of professor Louis Durlofsky, who was part of my oral examination committee, is also greatly appreciated.

ECOPETROL provided both economic support and data for this work, which was crucial to its success. I also received fellowships from the Geophysics Department, the Stanford Rock Physics Lab, and grants from the U.S. Department of Energy, which I greatly appreciate. Special thanks to Vinh Phan and professor Roland Horne for kindly letting me use their programs as a starting point for my research. I also thank professor Mark Zoback for his useful comments, and for letting me use his license of the SFIB software; and Lourdes Colmenares for her help with some of the stress plots.

I feel lucky to be part of a great research group, the Stanford Rock Physics Project. I enjoyed most of the courses I took at Stanford, but those of professor Gary Mavko were simply the best lectures I have ever attended. I could not have had a better Rock Physics instructor. I thank him for all the hard work he puts together to deliver an excellent class every time. This work benefited from extensive discussions with Tapan Mukerji and Manika Prasad, who excel in their respective areas. I cannot thank them enough for all the support they gave me over the past few years. Margaret Muir is simply the best. Her silent, hard work is what makes the group run smoothly.

I have been fortunate to share my time at Stanford with a number of great people. Sandra Vega, Per Avseth, Wendy Wempe, Youngseuk Keehm, and Ran Bacharah the

best officemates I could have possibly had. I also enjoyed and learned from many discussions with Mario Gutiérrez. I thank him for being my mentor, and for offering me a place to stay when I first came to Stanford. His wife Elizabeth Díaz is one of the nicest persons I have ever met: not only is she witty, but also a very caring woman. I also appreciated the friendship of Juan Mauricio Flórez, Gabriel Alvarez, Alejandro Valenciano, Laura Chiaramonte, Tiziana Vanorio, Lars Gommessen, Darcy Karakelian, Isao Takahashi, Klaus Leurer, Diana Sava, Haibin Xu, and Mike Zimmer.

My stay at Stanford would not have been so great without my friends. Among them the nicest words should go to Xyoli Pérez-Campos, who has been my accomplice in adventures and enterprises, my partner at parties, my confident and supporter during many rough times. She gave me her hand and walked me out of storms, and made me realize how bright a day could be if you stay away from troubled people. Oscar Moreno was not only an excellent roommate, but has been a great friend since always. It has been a great luck to have the opportunity to share some time with him again at Stanford.

A number of Venezuelans are part of my list of good friends, even though they would not recognize that *arepas* and the Gulf of Coquivacoa are both Colombian. Among them the most memorable are Manuel Díaz, Alexander Medina and his wife Ninoska, Bolivia Vega, Ezequiel González and Pili, Carlos Cobos and Ofelia. Thanks to all other friends from the Latinoamerican crowd, or simply, from the world: Cirlia Albornoz, Roberto Dugnani, Irina Fernández, Loly Díaz, David Gutiérrez, Melissa Luzardo, Martín Cocco, Rita Saloma, Liliana Quintanar and Nasser Qureshi, Rolando Lozano, Edgar Rangel, Kristina Prince, Victor Calo and Natacha, Rafael Aldaz, Leo Grimaldi, and Jane Korach.

Infinite thanks to my parents Abelardo and Elsa, my brother Juan Carlos, my sister Silvia Juliana, and the rest of my family for their continued trust and support. Finally, I want to thank my friends in Colombia, who always cheered me up while in this enterprise: Juan Carlos Ruiz, Mauricio Corredor, Ivonne Walteros, Lina Chaparro, Martha Martínez, Adriana Franco, Cristina Forero, Rocío Molina, Néstor Meza, Néstor Rivera, Jorge Nieto, Victoria Peña, Claudia Sánchez, and Martha López.

Oh ! … and many thanks to the people in Housing Assignment Services, who managed to gave me 4½ years of housing in a place for great parties—and quite a nice opportunity to meet some folks in the Stanford Police Department. If EV 118F does not make it to Stanford history books, I am pretty sure it will stay in our memories for good.

Contents

List of Tables

This page intentionally left blank

List of Figures

This page intentionally left blank

Chapter 1

Introduction

1.1 Purpose of this Dissertation

The purpose of this thesis is to enhance the characterization of subsurface reservoirs by combining reservoir geophysics and reservoir engineering observations and models to improve the prediction of petrophysical properties. This goal is fulfilled by formulating, implementing, and demonstrating the applicability of an emerging technology, the integration of seismic and production-related observations with *a-priori* information, through the application of a very old, yet very powerful approach: the inverse problem. The joint inversion approach I propose leads to better and less uncertain results because of the larger amount of data and constraints available to inform the predictions. The formulation I present can be easily adapted to include additional information, and has the potential for reducing the time required for completing reservoir characterization studies.

1.2 The Quest for Inter-Well Petrophysical Properties

Porosity and permeability are the most difficult properties to determine in reservoir characterization, yet usually they have the largest impact on reserves and production forecasts, and consequently on the economy of a project. An accurate estimation of the spatial distribution of porosity and permeability translates into higher success rates in infill drilling, and fewer wells required for draining the reservoir. The difficulty of estimating them comes from the fact that porosity and permeability may vary significantly over the reservoir volume, but can only be sampled at well locations, often using different technologies at different scales of observation. All other reservoir properties can be quantified more easily. For example, we can measure fluid properties over the expected range of reservoir thermodynamic conditions through relatively simple laboratory tests. Likewise, the external geometry of a reservoir can generally be

determined using surface seismic and well-established interpretation techniques. Porosity data, on the other hand, can only be measured in core samples, or inferred from density, sonic, and/or neutron logs along well paths. Permeability is even harder to predict: lab measurements provide information about its absolute value at the core scale, but the only way to obtain permeability estimates at a larger scale is through transient pressure tests, which may yield an average of permeability over the drainage area of a well. The internal distribution of lithology and facies in a reservoir —and the intrinsic variation in petrophysical properties it represents— remains beyond the resolution of most geophysical methods. Such lithology variations can be determined only in cases where conditions favor the application of advanced seismic interpretation techniques, which must be supported by a sound rock physics analysis of the reservoir being evaluated (e.g., *Avseth*, [2000], *Takahashi*, [2000]; *Dolberg et al.*, [2000]). Even in those cases the predictions have a limited degree of certainty, which has been the driving force behind the recent academic and industrial interest on probabilistic approaches to estimate petrophysical properties from seismic data (e.g., *Mavko and Mukerji,* [1998], *Mukerji et al.*, [2001a, 2001b]).

1.3 Static vs. Dynamic Data, and the Value of Data Integration

The variables in a reservoir data set can be classified as *dynamic* or *static*, depending on whether they are affected by changes in fluid saturation, temperature and pressure. Most of the success in data integration for reservoir characterization purposes has been obtained with static data, through the application of geostatistical techniques. Static data, such as core measurements and most well logs, do not vary substantially upon changes in the reservoir system. Dynamic data may change with time as a result of the movement of fluids through the reservoir. Examples of dynamic data are production performance curves, transient pressure tests, permanent down-hole pressure gauge data (e.g., *Athichanagorn*, [1999], *Khong*, [2001]), and repeat well logging of producing intervals with saturation-sensitive tools (e.g., *Moos and Dvorkin* [1996], *Gutierrez et al.* [2001]). Seismic data may or may not be dynamic depending on how changes in temperature, pressure, and fluid saturation affect elastic properties; and on whether they are acquired at different times during the production life of the reservoir.

The petroleum industry recognized long ago that in reservoir characterization the value of each piece of data does not lie in its isolated use, but rather in the value it adds to the analysis when integrated with other sources of information. Recognition of this axiom gave birth to the big wave of integrated reservoir characterization studies that started during the 1980s and continues today. Even so, disciplines in the earth sciences remain notoriously separated. Earth scientists from different fields have endeavored several efforts to predict the spatial distribution of petrophysical properties from the standpoints of their respective disciplines, only to find that the isolated pieces of knowledge they possess cannot lead to a quantitative answer by themselves.

In the case of surface seismic, for example, the lack of vertical resolution, imperfect data, and the interaction of different factors that affect the elastic properties of rocks — such as lithology, porosity, fluid type, and pore pressure—contribute to the uncertainty of porosity and permeability estimates derived from the sole interpretation of seismic data. The counterbalancing effects of these factors on the elastic behavior of reservoir rocks could easily lead to multiple defensible and sometimes inconclusive solutions if seismic information alone is used in the interpretation. Clearly, a quantitative interpretation requires the incorporation of other variables, and the analysis of the reservoir system as a whole.

In this research I use a joint inversion scheme for estimating petrophysical properties from the integration of seismic and production-related observations with *a-priori* information. By simultaneously inverting production and seismic measurements —a powerful combination of dynamic and static information— one can obtain data-driven estimates of petrophysical properties. The incorporation of *a-priori* information further reduces the spectrum of feasible solutions.

1.4 The Advantages of an Inversion Framework

The appeal of inversion methods is that they integrate field observations with models of physical processes relevant to those observations, in a framework that, when properly constrained, delivers a well-informed, defensible solution. Inversion methods have proven very useful in the earth sciences, in particular for characterizing subsurface targets with usually scarce data. In fact, the theory of inverse problems for data

interpretation originated in the field of seismology, where scientists deal with the difficult problem of estimating the structure of the Earth's interior from only surface data.

Inverting surface seismic and production data to estimate the petrophysical properties of a subsurface reservoir is by no means easier than the problems that seismologists face. The physical processes that govern fluid flow and acoustic wave propagation through porous media require complex forward models, should the system be accurately represented. Thus, the inversion of production and seismic observations is a non-linear and multi-dimensional problem.

The inverse formulation I use in this work takes advantage of a powerful data integration scheme that involves dynamic and static information, and delivers estimates that (1) guarantee the match of production- and seismic-related measurements; (2) benefit from models supported by the physics of fluid flow and acoustic wave propagation in porous media; and (3) comply with the restrictions given by *a-priori* experimental observations about the relationship between porosity and permeability.

1.5 A Brief Overview of Developments in Inverse Theory

Inverse theory originated during the times of Laplace and Gauss, who worked on for overdetermined problems using the least absolute values (l_1 norm), and the least-squares (l_2 norm) criteria. The concept of an *ill-posed problem*, in many cases associated with underdetermined conditions, was introduced by Hadamard in the early 1900s. As mentioned before, seismologists developed the theory of inverse problems for data interpretation. Geiger posed in 1910 the estimation of the hypocenter location of an earthquake as an inverse problem [*Mosegaard and Tarantola*, 2002]. His method became practical with the advent of digital computers, which also gave rise to important developments in inverse theory.

In the late seventies, *Rietsch* [1977] introduced the concept of *non-informative* prior distribution that describes the reference state of information, and *Jackson* [1979] incorporated *a-priori* information in linear inverse problem formulations, later generalized for non-linear inverse problems by *Tarantola and Valette* [1982a, 1982b], in two influential papers that also introduced the notion of *conjunction* of states of

information, and a Gaussian approach for solving non-linear parameter estimation problems.

The works of *Tarantola* [1987], and *Menke* [1989] are important monographs in the field of inverse theory for data interpretation. Even though both of them are written from a geophysical point of view, the concepts exposed in those books are general in character, and can be applied in other fields. *Menke*'s [1989] book covers discrete linear and non-linear inverse problems, while *Tarantola*'s [1987] monograph focuses on the description a least-squares probabilistic formulation for non-linear parameter estimation.

Non-linear inversion methods can be classified into *gradient* and *non-gradient*, depending on whether they take advantage of the information contained in the gradient of the objective function. Examples of gradient techniques are the *steepest descent*, *Gauss-Newton*, *singular-value decomposition*, *quasi-Newton*, and *conjugate gradient* algorithms [e.g., *Gill et al.*, 1993], while the non-gradient group includes methods based on *simulated annealing*, *genetic algorithms, neural networks*, and *polytope*, among others. The former are generally faster, but require the computation of *sensitivity coefficients*, i.e., the first derivatives of matching variables with respect to parameters.

1.6 A Literature Review on Applications of Inverse Theory and Data Integration to the Petroleum Industry

1.6.1 Inversion of seismic amplitude data

Reservoir geophysicists commonly use inversion to obtain acoustic velocity and/or impedance from seismic amplitude data. Seismic amplitude is appropriate for structural interpretation because it reflects the presence of an interface between two layers of different elastic properties. Impedance and velocity, being physical properties of the layer, are more suitable for characterizing features within the reservoir.

During the past two decades the algorithms and software for inverting seismic data for impedance and/or velocity improved considerably, turning impedance interpretation into a common place in reservoir characterization. Most algorithms rely on the acoustic approximation of the elastic wave equation, which allows us to model seismic amplitudes with the *convolutional* model (*Tarantola* [1984], *Russell*, [1988]).

1.6.2 Inversion of production data

Even though several works have demonstrated the feasibility of using optimization algorithms to invert production data for petrophysical property estimation, the industry's conventional approach to production history-matching still relies on the experience, criteria, and ability of reservoir engineers to manipulate the parameters of a simulation model, in such a way that field observations are reproduced. In such an approach, reservoir parameters are updated manually, often in two steps: the *pressure* match, and the *saturation* match [*Mattax and Dalton*, 1991; *Saleri and Toronyi*, 1988]. Since commonly the number of parameters to update is large, reservoir engineers often use zonation techniques to simplify the process. This time-consuming, trial-and-error updating process is repeated until the predictions of a reservoir simulator yield a reasonable fit of the production history.

The nineties were a very prolific decade for the application of inverse theory to reservoir parameter estimation from production data. *Oliver* [1994] used a least-squares formulation and the generalized pulse-spectrum technique (GPST) —a method that did not require the computation of sensitivity coefficients [*Tang and Chen*, 1985, 1989]— to obtain porosity and permeability estimates from pressure data and geostatistical information. This was the first attempt to integrate dynamic and static information. A modification of the GPST method that approximated the sensitivity coefficients appealed to a number of researchers (e.g., *Chu et al.* [1995a, 1995b], *Chu et al.* [1996]), because it was suitable for multiphase flow problems, and allowed a Gauss-Newton implementation. However, *He et al.* [1996] found that the modified GPST method caused inaccurate sensitivity coefficients for porosity.

Landa et al. [1996], and *Landa* [1997] introduced a method —yet another modification of the GPST approach— for efficiently computing the full matrix of sensitivity coefficients. *Landa et al.* [1996] presented an application of the substitution method in which they assumed a linear relationship between porosity and the log of permeability, and inverted well test data to find the spatial distribution of permeability in an Indonesian field.

1.6.3 Alternatives for Reducing the Computational Cost in Production Data Inversion

Since the finite-differences reservoir simulator is expensive to evaluate, a number of researchers have looked for inversion schemes that take advantage of (1) alternative, less expensive fluid-flow forward models; and/or (2) *reparameterization techniques* that reduce the number of parameters required to fully describe the reservoir.

Streamline simulators, which propagate saturations, phases, and concentrations along streamlines, are a natural alternative to finite-difference models, and some works on production data inversion use them (e.g., *Datta-Gupta et al.* [1995], *Wen et al.* [1998]). However, they are based on a number of assumptions that may lead to oversimplification in some scenarios (i.e., gravity-dominated flow, frequently changing flow conditions, and/or compressible systems). A fast, brute force alternative is to use *neural networks* (e.g., *Ounes et al.* [1994]), but they are by no means a physical representation of the reservoir, require intensive training, and their application to reservoir parameter estimation is not yet very clear. Not being supported by the physics of fluid flow, the use of neural networks as a replacement for the finite-difference reservoir simulator may be quite a gamble.

Reparameterization techniques come at the price of smoother results, and potential errors in uncertainty quantification [*Omre et al.*, 1999]. The simplest reparameterization approach is *zonation* (e.g., *Bissell et al.* [1994]), which consists of assuming that reservoir properties are constant over a zone of the reservoir model that is larger than a grid block. This approach leads to marked discontinuities and piecewise smoothness in the solution. *Landa*'s [1997] *object modeling* approach, also used by *Phan* [1998] can be seen as an adaptation of the zonation technique. More complex reparameterization techniques include the use of gesotatistical methods, and decomposition techniques based on wavelets [*Lu*, 2001], and singular values.

Geostatistical reparameterization methods —e.g., the *pilot point* [*La Venue et al.*, 1995], and the *sequential self-calibration* [*Gómez-Hernández et al.*, 1998] methods— incorporate *a-priori* information about the spatial correlation of parameters, and take advantage of different forms of kriging to limit the unknowns to a number of master-points. In such approaches the reservoir parameter estimation problem is posed as one of

finding the petrophysical properties of master points. Most of these techniques rely on the variogram as a measure of spatial correlation. If the variogram is known, the properties at all other locations can be estimated via kriging. However, the variogram is a two-point measurement of spatial correlation —hence the term *linear* geostatistics— and often fails to capture the complexity of a reservoir's underlying depositional environment, leading to artifacts in the results.

Strebelle [2000] developed a technique, called *multiple-point* geostatistics, that is capable of capturing the spatial correlation of non-linear features from a training image of the reservoir. The technique yields a better representation of subsurface systems by sampling from an *a-priori* cumulative distribution function that is conditioned to the features found in the training image. [*Caers,* 2002] reported the sole case of history matching with this technique: an application to a rather simple representation of the reservoir, consisting of two facies, each one with constant permeability. An objective evaluation of the applicability and benefits of using non-linear geostatistics in production history matching cannot be done at this point.

The assumption of a unique relationship between porosity and permeability deserves some special attention. Such an approach reduces the number of parameters by a factor of two. However, only very few reservoir systems could be properly represented by such a relationship. Core measurements show that often for a given porosity reservoir rocks exhibit permeability values that might be different by one or more orders of magnitude. Furthermore, there might be different porosity-permeability trends for different facies, e.g., as a result of a depositional system that favors rapid transitions between high- and low-energy sedimentation, and/or changes in sediment provenance. Although correcting for the scale difference between cores and simulation grid blocks would reduce the dispersion in porosity permeability trends, accounting for *undersampling* —the volume of available cores is orders of magnitude smaller than the reservoir volume— and *biased sampling* —wells tend to be drilled in good quality areas, and core recovery is better in sands than in shales— is likely to restore, or even increase such dispersion. Thus, assuming a unique porosity-permeability relationship may lead to significant oversimplification.

1.6.4 Inversion of production data and seismic-derived attributes

The advent of four-dimensional seismic technology represented an additional challenge to industry and academia, in terms of simultaneous modeling of seismic- and production–related processes. In most cases scientists have taken a forward modeling approach when trying to reproduce production and time-lapse seismic data (e.g., *Jenkins et al.* [1997], *Talley et al.* [1998], *Fanchi* [1999], *Doyen et al.* [2000], *Sengupta* [2000]).

Landa [1997], and *Landa and Horne*, [1997] presented the first attempts to estimate petrophysical properties from the joint inversion of production data and seismic-derived attributes, and are major contributions in this field. Those works described the inverse problem formulation in detail, and used synthetic data to demonstrate its capabilities, under both *pixel* and *object* modeling approaches. The advantage of working with synthetic data is that the true solution to the problem is known, and thus the effectiveness of the formulation can be tested —i.e., whether the algorithm converges to the global minimum, or at least to a solution close to it.

In the *pixel modeling* approach, each grid block receives a value of porosity and permeability. This approach results in a total number of parameters that is twice the number of grid blocks in the problem. Object modeling consists of describing the reservoir as a set of geometrical objects with constant permeability and porosity, which results in a significant reduction in the number of parameters. *Phan* [1998] extended the application of *Landa*'s [1997] work to three-dimensional reservoir models.

A number of recent works report the use of inverse theory to estimate petrophysical properties from time-lapse seismic and production data. *He et al.* [1998] and *Huang et al.* [1997, 1998] assumed unique relationships between porosity and permeability, and performed a joint inversion of seismic and production data for porosity. The inverse problem formulations (parameters being inverted, matching variables, forward models, objective functions, optimization algorithms, sensitivity coefficients, etc.) used in those works are not thoroughly described, neither the authors provide details about the performance of those implementations in synthetic data. Consequently, the appropriateness and effectiveness of those implementations cannot be independently evaluated.

Guerin et al. [2000] used porosity- and clay fraction-dependent relationships for permeability, with the spatial distribution of porosity and clay volume coming from the integration of static data via linear geostatistics. They use a two-step approach which involves (1) inversion of production data to estimate both the direction of water influx (lateral or underneath) from the aquifer and the exponent of a parametric model for the relative permeability to gas; and (2) inversion of seismic data to estimate parameters of the elastic forward model, such as mineral moduli, and fluid properties, given the pore pressure and saturation values obtained upon the match of production performance. Such an approach results in strong uncoupling between the fluid flow and seismic components of the model, and yields estimates that strongly depend on the validity of the initial estimates of porosity and clay volume, which are entirely obtained from static data.

Van Ditzhuijzen et al. [2001] reported the use of time-lapse seismic and production data to invert for the position, size and throw of faults and slumps in the East Flank of the Statfjord field, in an approach similar to the object modeling of *Landa* [1997].

1.7 Overview of this Work

Clearly, the problem of jointly inverting seismic-derived attributes and production data for the simultaneous estimation of porosity and permeability is a complex, computationally intensive one. I attacked this challenge with a mindset for the times to come. Recent advances in the microprocessor design and construction have delivered at least a 20-fold increase in speed between *Landa*'s [1997] workstation (a DEC alpha running at 125 MHz), and conventional present-day computers, not to mention RAM and cache memory, or the speed of high performance machines. *Keehm* [2002] reported a 30-fold gain in speed between his linear code for pore scale, two-phase flow simulation, and a far-from-optimal parallel version of the same model. On the other hand, the trend in industry and academia is take advantage of other types of data and incorporate them into the reservoir parameter estimation problem, to provide additional constraints and make the problem less ill-posed. For instance, *Wang* [1999] worked on the integration of resistivity data to the inversion for petrophysical properties.

Thus, rather than working with reparameterization techniques or alternative simulation models that reduce the computational overhead, I chose the more accurate

pixel modeling approach and the finite-differences simulator, and I focused on finding better constrained formulations of the inverse problem. I made these decisions with the goal of gaining on effectiveness and robustness, while reducing the number of iterations required for convergence. The formulations I present here do not prevent the use of reparameterization, though.

The avenues I took in this work build on the approaches proposed by *Landa* [1997], and *Phan* [1998] for inverting measurements of bottom-hole pressure (*Pwf*), and water cut (*wcut*) in wells, and seismic-derived estimates of change in water saturation (ΔSw). The approach I take to improve the resolution power of their formulation includes (1) the selection of a seismic attribute that is less uncertain than the seismic-derived change in water saturation, (2) a rigorous modeling of the elastic properties of rocks, and (3) the incorporation of a-priori information about the non-unique relationship between porosity and permeability.

The objective function used by *Landa* [1997], and *Phan* [1998] has the following form:

$$E = \sum_{i=1}^{t_{Pwf}} \sum_{j=1}^{n_{wells}} W_{Pwf} \left(Pwf_{obs}^{t_i, well_j} - Pwf_{calc}^{t_i, well_j} \right)^2 + \sum_{i=1}^{t_{wcut}} \sum_{j=1}^{n_{wells}} W_{wcut} \left(wcut_{obs}^{t_i, well_j} - wcut_{calc}^{t_i, well_j} \right)^2 + \sum_{i=1}^{t_{Ip}} \sum_{j=1}^{n_{blocks}} W_{seis} \left(\Delta Sw_{obs}^{t_i, block_j} - \Delta Sw_{calc}^{t_i, block_j} \right)^2 \quad . \quad (1.1)$$

Time-lapse seismic monitoring is based on the differences from data sets recorded at different times, with variations in acquisition geometry, waveform, bandwidth and coherent noise [*Biondi et al.*, 1998]. Such differences may translate into lack of repeatability, which in some cases impairs the isolation of the seismic signature that is related to changes in fluid, temperature, and pore pressure (e.g., *Hughes* [2000]). Although four-dimensional seismic acquisition, processing, and interpretation methods improved significantly during the last decade, under the state of the art of 4D seismic technology it is not possible to predict the change in water saturation to the level of certainty required for practical purposes, especially without integrating time-lapse data with a reservoir simulation model. Should a reservoir simulator be involved in the

estimation of ΔSw, the results would be biased by the underlying models of porosity and permeability used in the simulator, even in a scenario of perfect repeatability of seismic surveys. If this happens, the values of ΔSw are no longer independent of porosity and permeability, and consequently, are inappropriate for petrophysical property estimation [*Tarantola*, 1987].

To overcome this problem I modify equation 1.1 by replacing the term that accounts for the misfit in seismic-derived change in water saturation with one that depends on the misfit in acoustic impedance. Acoustic impedance depends strongly on porosity, and has the spatial coverage of seismic data, which makes it an appealing attribute for porosity mapping. Furthermore, impedance can be estimated via inversion of seismic amplitude —a process that does not involve any flow modeling— and can be derived from a single 3D seismic survey. This broadens the applicability of the formulation I propose, because 3D seismic data is much more widely available than 4D seismic data.

I expand the objective function to include additional terms that account for *a-priori* information about the relationship between porosity and permeability. The first approach I propose limits the region of feasible permeability estimates for a given porosity. If one can find mathematical relationships that bound the trend of observed data in a porosity-permeability scatter plot, then it is possible to design an error surface that penalizes the offset from such bounds, and reduces the variance of permeability estimates. On top of this, I incorporate prior information in the form of conditional probability density functions of permeability given porosity, which can be estimated from core data, and modified to account for scale differences and unavoidable sampling problems.

I implement this formulation in a computer model that automatically updates the porosity and permeability fields, until the data is matched within a certain tolerance. I use the computer model to test the feasibility, and demonstrate both the advantages of simultaneously inverting seismic and production data, and the importance of incorporating *a-priori* information to the parameter estimation problem. Finally, I use the model for a practical application: the prediction of petrophysical properties in the K2 Unit reservoir of the Apiay-Guatiquía Field, which is located in the Llanos Basin of Colombia.

1.8 Description of Chapters

Chapter 2 contains the mathematical basis of the proposed integrated inversion approach. I use a model based on conservation of mass, Darcy's law [*Darcy*, 1856], and equations of state to simulate the flow of fluids through the reservoir, and from it I address the influence of petrophysical properties on production data. I use rock physics models to predict the elastic properties of reservoir rocks, and *Gassmann*'s [1951] fluid substitution equations to model the influence of saturation changes on their seismic response. Then I address the sensitivity of seismic to variations in storage and transport properties by computing the derivatives of the seismic model with respect to porosity and permeability. Having described the models and derived the equations for computing the sensitivities, I discuss their integration to the inversion approach that makes concurrent use of them. Then I present the methodology I use to incorporate *a-priori* information. Finally, I address implementation details of the simultaneous inversion methodology I propose.

In Chapter 3 I describe the application of the model to a synthetic data set, with the purpose of testing the integrity of the computer implementation and evaluating the benefits of using the formulation I propose. Using statistics that are relevant to the performance of the proposed algorithm, I compare it to other conventional approaches. Although the use of more data slows convergence and makes the method computationally intensive, a single run generates results that are consistent with all data considered. This can still be more efficient than a trial and error approach that requires several runs of a less computationally demanding process. To emphasize the importance of feeding the model with accurate input data, I show how results and convergence depend on the initial model.

In the first part of Chapter 4 I introduce the Apiay-Guatiquía field data set, and discuss the geology of the area, with emphasis on the regional tectonics and sedimentology characteristics that are relevant to the purposes of this dissertation. In the second part of Chapter 4 I describe a method that predicts the distribution of stresses around an inclined borehole drilled under an arbitrarily oriented stress field. I use this method in a forward-modeling approach to determine the magnitude and orientation of

principal stresses, and the failure regime in the K2 Unit reservoir of the Apiay-Guatiquía field, based on least stress estimates from leak-off tests, and well-log data and images.

Chapter 5 describes a rock-physics-based feasibility study of predicting petrophysical properties from seismic data. I use the magnitude of principal stresses I estimated in Chapter 4 to compute the mean effective pressure for the K2 Unit reservoir. From core measurements and well log data I derive relationships between petrophysical properties and seismic at the effective pressure conditions of the reservoir. Finally, I study the effects of porosity, fluid replacement, pore pressure, and scale-dependent heterogeneities on velocity and acoustic impedance, which can ultimately be obtained from seismic via impedance inversion. From this analysis I conclude that, given the conditions of this reservoir, the parameter that most influences seismic response is porosity, which makes seismic reservoir characterization very feasible and appealing in this case.

In Chapter 6 I discuss the application of the inverse problem formulation I propose for predicting the spatial variation of petrophysical properties in the K2 Unit reservoir of the Apiay-Guatiquía field. I use a computer implementation of the model to simultaneously invert production and seismic data, and determine in this way the best distribution (in the least-squares sense) of petrophysical properties in the reservoir.

1.9 References

Avseth, P., 2000, *Combining Rock Physics and Sedimentology for Seismic Reservoir Characterization of North Sea Turbidite Systems*, Ph.D. dissertation, Stanford University.

Athichanagorn, S., 1999, *Development of an Interpretation Methodology for Long-Term Pressure Data from Permanent Downhole Gauges*, Ph.D. dissertation, Stanford University.

Biondi, B., G. Mavko, T. Mukerji, D. Lumley, C. Deutsch, R. Gundensø, and M. Thiele, 1998, Reservoir monitoring: a multidisciplinary feasibility study: *The Leading Edge*, **17**, 1404-1414.

Bissell, R., Y. Sharma, and J. E. Killough, 1994, History matching using the method of gradients: two case studies: Paper SPE 28590.

Caers, J., 2002, Geostatistical history matching under training-image based geological model constraints: Paper SPE 77429.

Chu, L., A. C. Reynolds, and D. S. Oliver, 1995a, Computation of sensitivity coefficients for conditioning the permeability field to well-test pressure data: *In Situ*, **19**,179-223.

Chu, L., A. C. Reynolds and D. S. Oliver, 1995b, Reservoir description from static and well test data using efficient gradient methods. Paper SPE 29999.

Chu, L., M. Komara, and R. A. Schatzinger, 1996, An efficient technique for inversion of reservoir properties using iteration method. Paper SPE 36512.

Datta-Gupta, A., L. W. Lake, and G. A. Pope, 1995, Characterizing heterogeneous permeable media with spatial statistics and tracer data using sequential simulated annealing: *Mathematical Geology*, **27**, 763-787.

Dolberg, D., J. Helgesen, T. Håkon-Hanssen, I. Magnus, G. Saigal, and B. K. Pedersen, 2000, Porosity prediction from seismic inversion, Lavreans Field, Haten Terrace, Norway: *The Leading Edge*, **19**, 392-399.

Doyen, P. M., D. E. Psalia, D. Astratti, L. B. Kvamme, and N. F. Al-Najjar, 2000, Saturation mapping from 4D seismic data in the Statfjord field: *Transactions of the 2000 Offshore Technology Conference*, paper OTC 12100.

Fanchi, J. R., 1999, Predicting 4D seismic performance using an integrated flow model: Paper SPE 56517.

Gassmann, F., 1951, Über die elastizität poröser medien: *Vier. der Natur*, Gesellschaft, **96**, 1–23.

Gill, P. E., W. Murray and M. Wright, 1993, *Practical Optimization*, Academic Press, San Diego, 401 pp.

Gómez-Hernández, J. J., A. Sahuquillo, and J. E. Capilla, 1998, Stochastic simulation of transmissivity fields conditional to both transmissivity and piezometric data: 1.The Theory: *Journal of Hydrology*, **203**,162-174.

Guerin, G., W. He, R. Anderson, and L. Xu, 2000, Optimization of reservoir simulation and petrophysical characterization in 4D seismic: *Transactions of the 2000 Offshore Technology Conference*, paper OTC 12100.

Gutierrez, M. A., J. Dvorkin, and A. Nur, 2001, Theoretical rock physics for bypassed oil detection behind the casing: La Cira-Infantas oil field, *The Leading Edge*, **20**, 192-197.

He, N., A. C. Reynolds, and D. S. Oliver, 1996, Three-dimensional reservoir description from multiwell pressure data and prior information: Paper SPE 36509.

He, W., G. Guerin, R. N. Anderson, and U. T. Mello, 1998, Time-dependent reservoir characterization of the LF sand in the South Eugene Island 330 Field, Gulf of Mexico: *The Leading Edge*, **17**, 1434-1438.

Huang, X., L. Meister, and R. Workman, 1997, Reservoir characterization by integrating time-lapse seismic and production data: Paper SPE 38695.

Huang, X., L. Meister, and R. Workman, 1998, Improving production history matching using time-lapse seismic data: *The Leading Edge*, **17**, 1430-1433.

Hughes, J. K., 2000, Examination of Seismic Repeatability as a Key Element of Time-Lapse Seismic Monitoring: Paper SPE 68246.

Jackson, D.D., 1979, The use of a priori data to resolve non-uniqueness in linear inversion, *Geophysics Journal of the R. Astron. Soc.*, **57**, 137–157.

Jenkins, S. D., M. W., Waite, and M. F. Bee, 1997, Time-lapse monitoring of the Duri steamflood: a pilot and case study: *The Leading Edge*, **16**, 1267-1273.

Keehm, Y., T. Mukerji, and A. Nur, 2002, Efficient Parallel Implementation of Two-phase Lattice-Boltzmann Flow Simulation, *SEG Annual Meeting Expanded Technical Program Abstracts*, Paper RP 1.4.

Khong, K. C., 2001, *Permanent Downhole Gauge Data Interpretation*, M.S. dissertation, Stanford University.

Landa, J. L., M. M. Kamal, C. D. Jenkins, and R. N. Horne, 1996, Reservoir characterization constrained to well test data: a field example. Paper SPE 36511.

Landa, J. L., 1997, *Reservoir Parameter Estimation Constrained to Pressure Transients, Performance History and Distributed Saturation Data*, Ph.D. dissertation, Stanford University.

Landa, J. L., and R. N. Horne, 1997, A procedure to integrate well test data, reservoir performance history and 4-D seismic information into a reservoir description: Paper SPE 38653.

La Venue,A. M., B. S. RamaRao, G. de Marsily, and M. G. Marietta, 1995, Pilot point methodology for automated calibration of an ensemble of conditionally simulated transmissivity fields, #2 Application: *Water Resources Research*, **31**, 495-516.

Lu, P., 2001, *Reservoir Parameter Estimation Using Wavelet Analysis*, Ph.D. dissertation, Stanford University.

Mattax, C. C. and R. L. Dalton, 1991, *Reservoir Simulation*, SPE Monograph Vol. 13, Society of Petroleum Engineers.

Mavko, G. and T. Mukerji, 1998, A rock physics strategy for quantifying uncertainty in common hydrocarbon indicators: *Geophysics*, **63**, 1997-.

Menke, W., 1989, *Geophysical Data Analysis: Discrete Inverse Theory*: revised edition, Academic Press, London, 289 pp.

Moos, D., and J. Dvorkin, 1996, Sonic logging through casing for porosity and fluid characterization in the Wilmington Field, CA: *SEG Annual Meeting Expanded Technical Program Abstracts*, **66**, 134-137.

Mosegaard K., and A. Tarantola, 2002, Probabilistic approach to inverse problems, in *International Handbook of Earthquake and Engineering Seismology*, Academic Press, [in press].

Mukerji, T., A. Jørstad, P. Avseth, G. Mavko, and J. R. Granli, 2001a, Mapping lithofacies and pore-fluid probabilities in a North Sea reservoir: seismic inversions and statistical rock physics: *Geophysics*, **66**, 988-1001.

Mukerji, T., P. Avseth, G. Mavko, I. Takahashi, and E. F. González, 2001b, Statistical rock physics: Combining rock physics, information theory, and geostatistics to reduce uncertainty in seismic reservoir characterization: *The Leading Edge*, **20**, 313-319.

Oliver, D. S., 1994, Incorporation of transient pressure data into reservoir characterization: *In Situ*, **18**, 243-275.

Omre, H., H. Tjelmeland, and H. T. Wist, 1999, Uncertainty in history matching − Model specification and sampling algorithms: *Technical Report Statistics* No.6/1999, Department of Mathematical Sciences, Norwegian University of Science & Technology - Trondheim.

Ounes, A., R. S. Doddi, Y. Lin, G. Cunningham, and N. Saad, 1994, A new approach combining neural networks and simulated annealing for solving petroleum inverse problems: *4th European conference on the mathematics of oil recovery*.

Phan, V., 1998, *Inferring Depth-Dependent Reservoir Properties from Integrated Analysis Using Dynamic Data*, M.S. dissertation, Stanford University.

Russell, B.H., 1988, *Introduction to Seismic Inversion Methods*, Society of Exploration Geophysicists, 90 pp.

Rietsch, E., 1977, The maximum entropy approach to inverse problems: *Geophysics*, **42**, 489–506.

Saleri, N.G., and R. M. Toronyi, 1988, Engineering control in reservoir simulation, Part I: Paper SPE 18305.

Sengupta, M., 2000, *Integrating Rock Physics and Flow Simulation to Reduce Uncertainties in Seismic Reservoir Monitoring*, Ph.D. dissertation, Stanford University.

Strebelle, S., 2000, Sequential Simulation Drawing Structures from Training Images: Ph.D. dissertation, Stanford University.

Takahashi, I., 2000, *Quantifying Information and Uncertainty of Rock Property Estimation from Seismic Data*, Ph.D. dissertation, Stanford University.

Talley, D. J., T. L. Davies, R. D. Benson, and S. L. Roche, 1998, Dynamic reservoir characterization of Vacuum Field, *The Leading Edge*, **17**, 1396-1402.

Tang Y. N., and Y. M. Chen, 1985, Application of GPST algorithm to history matching of single-phase simulator models: Paper SPE 13410.

Tang Y. N., and Y. M. Chen, 1989, Generalized pulse-spectrum technique for two-dimensional and two-phase history matching: *Applied Numerical Mathematics*, **5**, 529-539.

Tarantola, A., and B. Valette, 1982a, Generalized nonlinear inverse problems solved using the least squares criterion: *Reviews of Geophysics and Space Physics*, **20**, 219-232.

Tarantola, A., and B. Valette, 1982b, Inverse problems = Quest for information: *Geophysics,* **50**, p 159-170.

Tarantola, A., 1984, Inversion of seismic reflection data in the acoustic approximation: *Geophysics,* **49**, 1259-1266.

Tarantola, A., 1987, *Inverse Problem Theory: Methods for Data Fitting and Model Parameter Estimation*, Amsterdam, Elsevier Science Publishing Company.

van Ditzhuijzen, R., T. Oldenziel, and C. P. J. W. van Kruijsdijk, 2001, Geological parameterization of a reservoir model for history matching incorporating time-lapse seismic based on a case study of the Statfjord Field: Paper SPE 71318.

Wang, P., 1999, *Integrating Resistivity Data Into Parameter Estimation Problems*, M.S. dissertation, Stanford University.

Wen, X. H., C. Deutsch, C., and A. S. Cullick, 1998, Integrating pressure and fractional flow data in reservoir modeling with fast streamline based inverse methods: Paper SPE 48971.

This page intentionally left blank

Chapter 2

The Mathematical Basis

It has been long recognized that in the characterization of petroleum and other subsurface reservoirs, the importance of each piece of information lies not in its isolated use, but in the value it adds to the integrated analysis of the complete data set. Some data that may seem inconclusive by themselves become useful and enhance the value of the data set as a whole when they are integrated with other pieces of information. For instance, it is very unlikely that an interpretation of production observations alone can yield porosity and permeability fields that have the accuracy required for reservoir characterization purposes. Production data can only be collected at wells, and although they are to some extent influenced by the entire distribution of petrophysical properties, the sensitivity of production data to porosity and permeability at locations far from wells is quite small. Clearly, integrating additional data with better coverage would help to constrain the solution. Among all data available for reservoir characterization, three-dimensional seismic surveys provide the best volume coverage [*Nur*, 1989, *Biondi et al.*, 1998], which makes seismic data a very valuable source of information about the properties of subsurface rocks.

This research work is based on the application of inverse theory to integrating seismic and reservoir engineering data, towards the prediction of porosity and permeability —the petrophysical properties that control the storage capacity and flow of fluids, and that strongly influence the propagation of seismic waves through subsurface reservoirs. To solve the inverse problem, we take advantage of forward models that are solidly founded on both elasticity and the physics of fluid flow in porous media. Using a discrete representation of the reservoir, we compute with a reservoir simulator the production measurements we want to match, and the pore pressure and fluid saturation at each grid block for the time of seismic acquisition. We take the latter results and use rock physics to predict the seismic properties of the reservoir rock under the given scenario of porosity, pore pressure, and fluid saturation. We also incorporate *a-priori* information

into the process, in the form of bivariate probability density functions that can be estimated from core measurements.

In this chapter I describe the forward models and the parameter estimation theory behind our approach. I invert observed data and *a-priori* information by minimizing the least squares misfit between observations and simulated results, using a Gauss-Newton formulation. Our implementation of the problem can simultaneously estimate porosity and permeability, either enforcing a certain regression between the two, or using a variety of uncorrelated approaches that I describe here.

2.1 Inverse vs. Forward Problems

Scientists in many fields develop mathematical models, based on fundamental physical laws and characterized by certain parameters, to reproduce the behavior of actual physical systems. Such models —known in the literature as *forward models*, or *transfer functions*, and denoted g in this work— are useful for solving engineering problems under two fundamental schemes: the *forward* approach and the *inverse* approach. The *forward problem* amounts to computing the response $\tilde{d}_{cal}$ of the mathematical model g to a set of parameters $\tilde{\alpha}$ that characterize the system, i.e.,

$$\tilde{d}_{cal} = g(\tilde{\alpha}) \tag{2.1}$$

The *inverse problem*, on the other hand, consists of finding the set of parameters $\tilde{\alpha}$ that would cause a response $\tilde{d}_{cal}$ of the mathematical model g, that best fit the observed behavior $\tilde{d}_{obs}$ of the system.

An example of these techniques is depicted in Figure 2.1, in which we illustrate the application of forward and inverse formulations to seismic modeling, with the convolutional method as the transfer function.

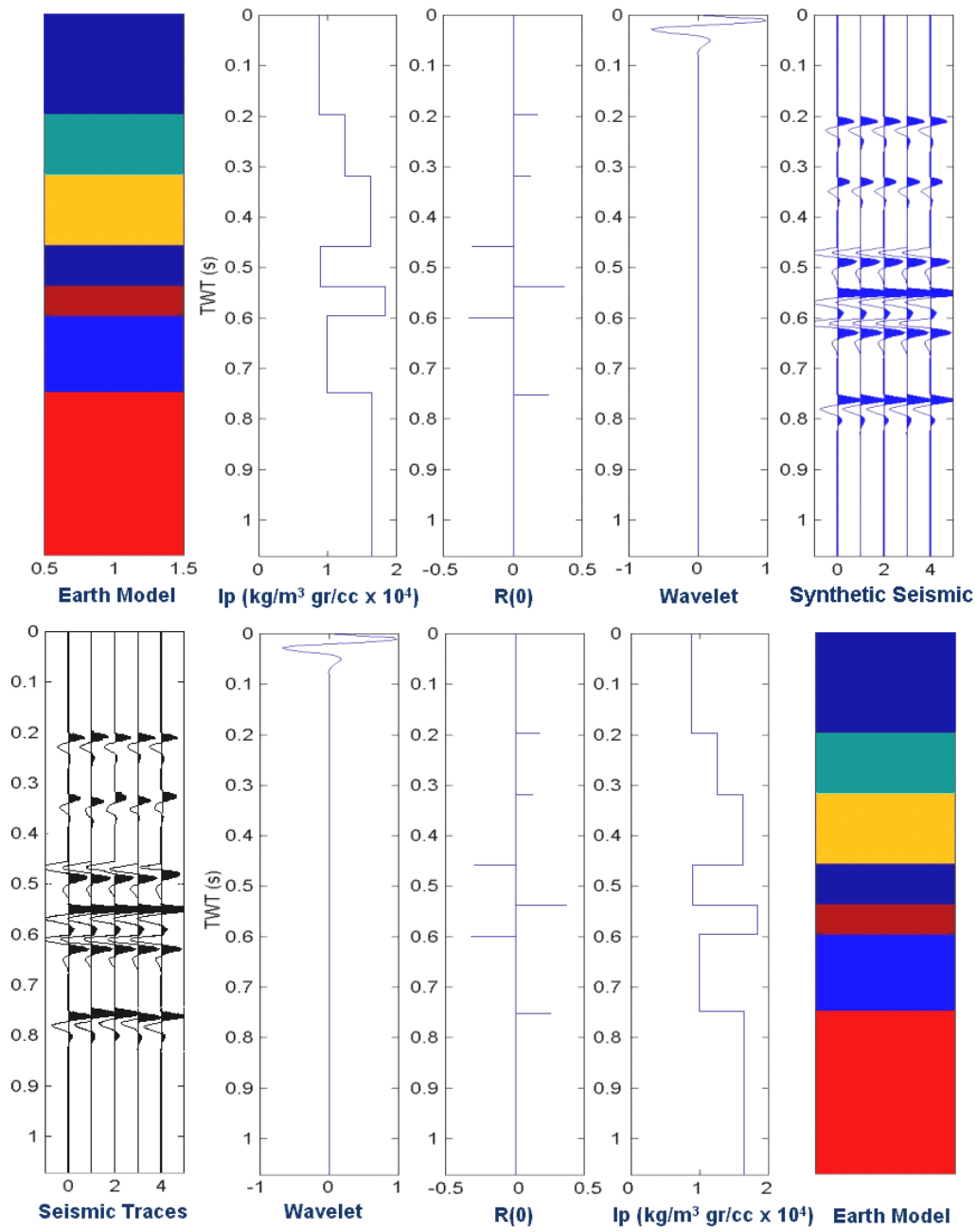

Figure 2.1: A schematic plot that depicts the application of forward and inverse problems to seismic modeling.

At the top of the figure, each layer in the Earth model is characterized by its acoustic impedance, which can be computed from logs of p-wave velocity and bulk density. The normal-incidence reflectivity $R(0)$ of a layer interface is a function of the impedance contrast between the layers on each side. Forward modeling combines —via convolution— the sequence of reflectivity coefficients with a seismic pulse —

represented by the wavelet— to generate synthetic traces. The problem is that we often do not have a good model of either the Earth or the seismic source. We may have surface seismic data, though, and want to use them to infer each layer's thickness and impedance. The inverse approach, illustrated in the bottom panels, extracts the signature of the pulse from seismic traces to deliver the inverted normal-incidence reflectivity series $R(0)$, from which the acoustic impedances of each layer can be computed. Convolution of the inverted $R(0)$ with the appropriate wavelet results in synthetic traces that can be optimized to fit the real traces.

In many fields of science, using a forward model is enough to solve most engineering problems, because the parameters needed for the model to mimic the system behavior can be measured directly. This is not the case for the majority of applications in the earth sciences, where scientists often deal with systems that are not easily accessible (e.g., subsurface reservoirs). Although the performance of such systems can often be measured (e.g., in terms of rates of fluid flow from wells, pore pressure, water cut, water salinity, etc.), their properties can only be indirectly inferred through remote sensing (e.g., well logs, 3D, and 4D seismic). In such scenarios inversion has proven very useful for determining the parameters that characterize the response of the system.

2.2 Inversion Approach

Systems that are relatively simple can often be described with linear mathematical models. In such cases one can invert the observed data directly by analytically determining the inverse of the transfer function. Multidimensional, non-linear problems are more complex and require iterative inversion schemes. The problem of simultaneously inverting reservoir engineering and seismic data to estimate porosity and permeability involves modeling complex processes —those of fluid flow through porous media, and acoustic wave propagation— and cannot be solved by linear inversion methods. Thus, we rely on iterative algorithms to find solutions to the problem.

The inverse formulation we use in this work consists of three fundamental components: (1) a forward model based on the physics of the problem, capable of reproducing the system performance, (2) an objective or error function —a measure of the misfit between the observed system performance and the behavior predicted by the

model—, and (3) an optimization algorithm capable of finding the model parameters that result in a minimum value of the objective function. The inversion algorithm involves the following steps:

1. Estimate a reasonable initial set of parameters —the so-called *initial guess*.
2. Run the forward model to calculate the response of the system.
3. Compute the value of the objective function. If the objective function is less than a certain pre-established tolerance, no further calculations are required and the set of parameters is accepted as a solution to the problem.
4. Apply the minimization algorithm to determine a *perturbation* to the set of parameters that would result in a smaller misfit. If the change to the set of parameters is smaller than a pre-established tolerance, stop the calculations (otherwise the model would produce about the same results, and the algorithm would fall in an infinite loop).
5. Apply the perturbation to update the parameters and return to step 2.

2.3 Forward Model

The problem we are dealing with requires a forward model with two components: (1) a reservoir simulator to model the flow of fluids through porous media, and (2) a model to compute the acoustic properties of reservoir rocks. In this section I discuss the theoretical foundation of those models in a fairly general way, yet with sufficiently detail for describing how they are used in the algorithm. I also discuss important assumptions of the models, and their practical implications. More detailed descriptions of the reservoir simulation model are given in *Aziz and Settari* [1986], and *Mattax and Dalton*, [1991]. Rock physics models are extensively discussed in the literature —e.g., *Wang and Nur* [1989, 1992, 2000], and *Mavko et al.* [1998]. Because of the many factors that influence the velocity of rocks, the reader is advised of the importance of validating rock physics models with site-specific experimental data at the core and field scales, before using them for practical applications in a specific area.

2.3.1 Fluid Flow Model

We used a two-phase (oil-water), three-dimensional formulation of the so-called black-oil simulator to forward-model fluid flow through the reservoir. The black-oil model assumes that the number of components in the system is equal to the number of phases, and that oil and water are immiscible fluids. The model is based on conservation of mass, Darcy's law [*Darcy*, 1856] for fluid flow through porous media, equations of state that predict the thermodynamic behavior of rock and fluid properties, and capillary pressure and relative permeability relationships.

2.3.1.1 Differential Form of the Fluid Flow Equation

Assuming that flow occurs only by convection, and combining the aforementioned fundamental laws, yields a system of differential equations that for multiphase, multidimensional, isothermal flow in a consistent set of units is as follows:

$$\sum_p \nabla \cdot \left(\rho_p \frac{K k_{rp}}{\mu_p} \left(\nabla p_p - \gamma_p \nabla D \right) \right) - \tilde{q}_p = \sum_p \frac{\partial}{\partial t} \left(\phi \rho_p S_p \right), \tag{2.2}$$

where ρ_p, μ_p, p_p, S_p, and k_{rp} are the density, viscosity, pressure, saturation and relative permeability to phase p, respectively; $\tilde{q}_p$ is a source term that represents production from, and injection into the reservoir; ϕ and K are porosity and absolute permeability; t and D are time and depth; and γ_p is given by:

$$\gamma_p = \frac{1}{144} \rho_p g \,, \tag{2.3}$$

where g is the acceleration due to gravity.

We use the following the following exponential forms to model relative permeability to water and oil:

$$k_{rw} = k_{rwro}\left(\frac{S_w - S_{wc}}{1 - S_{wc} - S_{orw}}\right)^{nw}, \text{ and} \tag{2.4}$$

$$k_{ro} = k_{rocw}\left(\frac{1 - S_w - S_{orw}}{1 - S_{wc} - S_{orw}}\right)^{now}, \tag{2.5}$$

where the term in parenthesis is a function of S_w that varies between 0 and 1, the exponents *nw* and *now* are calibration factors, k_{rwro} is the relative permeability to water at residual oil saturation (S_{orw}) and k_{rocw} is the relative permeability to oil at connate water saturation (S_{wc}).

Capillary pressure provides the link between the pressures of the oil and water phases. In our approach we assumed that the oil-water capillary pressure p_{cow} is negligible —which is reasonable for most oil-water reservoirs. That is,

$$p_{cow} = (p_o - p_w) = 0. \tag{2.6}$$

By using equation 2.6 and recalling that the saturation of oil and water phases must add up to one, we can rewrite equation 2.2 as a function of oil pressure and water saturation.

2.3.1.2 Discrete Fluid Flow Model

The system of differential equations given by expression 2.2 can only be solved explicitly in a few cases (e.g., for some well testing applications), under very limiting assumptions. The behavior of multiphase, multidimensional flow conflicts with those assumptions and makes it imperative to discretize the problem to get a numerical solution. In such a case, the finite-difference discrete form of equation 2.2 can be described by:

$$\sum_p \sum_l T_{p_{l,1}} \left[\left(p_{p_l} - p_{p_{i,j}} \right) - \gamma_p \left(D_l - D_i \right) \right] - \tilde{q}_p^w = \frac{1}{\Delta t} \frac{V}{5.615} \left[\left(\frac{\phi S_p}{B_p} \right)_{i,j}^{n+1} - \left(\frac{\phi S_p}{B_p} \right)_{i,j}^{n} \right], \quad (2.7)$$

where V is the bulk volume of block i, l is the number of adjacent blocks connected to block i (6 for a central block in a 3D problem); B_p is the formation volume factor of phase p; and the transmissibility of phase p through the face that separates blocks i and l is given by:

$$T_{p_{l,i}} = \alpha \frac{\overline{K}_{l,i} A k_{rp}}{\overline{\Delta x}_{l,i} \mu_p B_p}. \quad (2.8)$$

In equation 2.8, α is a unit conversion constant, $\overline{K}_{l,i}$ is the harmonic average of permeability in the two grid blocks involved in the calculation, and $\overline{\Delta x}_{l,i}$ is the distance between block centers.

In our model the grid block bulk volume V is constant, but porosity varies with pressure according to a known equation of state, which is a function of the isothermal rock compressibility. In practical terms this implies that the model is applicable only to reservoirs that do not undergo thickness changes associated with production/injection — those made of strong, well-consolidated rocks that do not deform significantly with pore pressure depletion and restoration— or to those with strong pressure support and efficient fluid replacement from an active aquifer.

2.3.1.3 Treatment of Wells in the Fluid Flow Model

The source term in equations 2.2 and 2.7 represents well production and injection, and can be modeled as follows:

$$\tilde{q}_p^w = \left[\frac{2\pi K h}{\ln(r_o / r_w) + S} \right] \left(\frac{k_{rp}}{\mu_p B_p} \right) \left(p_p - p_{wf} \right) = WI \left(\frac{k_{rp}}{\mu_p B_p} \right) \left(p_p - p_{wf} \right), \quad (2.9)$$

where h is the thickness of the block, p_{wf} is the well-flowing pressure, S is the skin factor, *WI* is known as the *well index*, r_w is the well radius and r_0 is given by *Peaceman*'s [1983] equations, depending on the well trajectory in the model, as follows:

$$r_o = \begin{cases} 0.14\sqrt{(\Delta x)^2 + (\Delta y)^2} & \text{vertical well} \\ 0.14\sqrt{(\Delta y)^2 + (\Delta z)^2} & \text{horizontal well along the } x \text{ direction} \\ 0.14\sqrt{(\Delta x)^2 + (\Delta z)^2} & \text{horizontal well along the } y \text{ direction} \end{cases}, \qquad (2.10)$$

where Δx, Δy, and Δz represent the grid block dimensions along the x, y, and z directions, respectively.

By rearranging the pressure-dependent and saturation-dependent terms, equation 2.7 can be written in a residual, matrix form as:

$$\mathbf{R} = \mathbf{T}\mathbf{y}^{n+1} - \mathbf{Q} - \mathbf{D}\left(\mathbf{y}^{n+1} - \mathbf{y}^{n}\right), \qquad (2.11)$$

where **D** and **Q** are diagonal matrices of storage and source terms, respectively, **T** is the matrix of tranmissibility terms, **R** is the vector of residuals, and $\mathbf{y}^n$ and $\mathbf{y}^{n+1}$ are the vectors of oil pressure and water saturation at each grid block, at time steps n and n+1, respectively. In the fully implicit formulation we use, pressure- and saturation-dependent terms are evaluated at the pressure and saturation of time step $n+1$, so equation 2.11 is non-linear, and has to be solved by iterative methods. It is customary to use a Newton-Raphson optimization scheme to find the solution vector $\mathbf{y}^{n+1}$ for each time step. Our implementation uses a sparse-matrix direct algorithm to solve the resulting system of equations:

$$\mathbf{J}\tilde{\delta} = -\mathbf{R}, \qquad (2.12)$$

where $\mathbf{J}$ is the Jacobian of $\mathbf{R}$, and $\tilde{\delta}$ is the vector of updates to the solution vector **y** between time steps n and n+1.

2.3.2 Rock Physics Model

Rock physics plays a key role in understanding the factors that influence acoustic measurements, providing the required framework for linking petrophysical properties and geophysical measurements [*Mavko and Nur*, 1996]. In this work we deal with the elastic behavior of porous rocks, which controls the propagation of seismic waves through the reservoir. The shear and bulk moduli of an elastic material (symbolized by μ and K, respectively, and not to be confused with viscosity and absolute permeability) are the inverse of its shear and bulk compressibilities. The moduli can be computed from density, and P- and S-wave velocities as follows:

$$\mu = \rho V_s^2, \text{ and} \tag{2.13}$$

$$K = \rho V_p^2 - \frac{4}{3}\mu. \tag{2.14}$$

Our elastic earth model is characterized by porosity, saturation, and effective pressure. Pore pressure P_p relates to effective pressure P_{eff} through the following expression:

$$P_{eff} = P_{conf} - \alpha P_p, \tag{2.15}$$

where P_{conf} is the confining pressure, and α is the effective pressure coefficient, which is generally close to 1, but for low porosity rocks can be significantly smaller [*Wang and Nur*, 1992]. We assume an initial distribution of porosity that is updated at each iteration of the inversion algorithm, retrieve from the flow model the pore pressure and saturation for all grid blocks at the time of seismic acquisition, and input them to a rock physics forward-model that delivers the acoustic properties of saturated rock, namely velocity and impedance.

We use depth-converted acoustic impedance —derived from seismic via impedance inversion— as the seismic variable to match in our objective function. However, there is

nothing that prevents the use of seismic amplitude in the inversion process. If the problem involves matching seismic amplitudes, the seismic component of the forward model should be capable of generating synthetic amplitude data. Although our implementation includes such capability, we have used it only for seismic forward modeling problems that are not the subject of this thesis. An overview of the theoretical foundation of our seismic model is included here only for the sake of completeness.

2.3.2.1 Fluid Properties

Batzle and Wang [1992] proposed empirical relations to compute the density and velocity —and by extension the bulk and shear moduli— of common fluids in petroleum reservoir systems.

The effective bulk modulus of a fluid mixture is a saturation-weighted average of the bulk modulus of the individual components [*Mavko and Nolen-Hoeksema*, 1994; *Marion et al.*, 1994]. The type of average that should be used —arithmetic or harmonic— depends on whether the fluids form patches or mix uniformly in the porous space, which can be determined from the diffusion length scale that characterizes the problem [*Cadoret*, 1993; *Mavko and Mukerji*, 1998]. However, *Sengupta* [2000] found that for most oil-water systems, the difference in effective bulk modulus between the patchy and uniform saturation models is small. This is because the compressibility of most low- to intermediate-specific gravity oils is similar to that of water. Moreover, the influence of irreducible water and residual oil saturation further reduces the already small separation between the harmonic and arithmetic averages of the components' bulk moduli. In such a scenario, we select the Reuss harmonic average for computing the effective bulk modulus of an oil-water mixture. Consequently, in our model the effective bulk modulus K_{fl} of the oil-water fluid mixture is given by:

$$\frac{1}{K_{fl}} = \frac{(1 - S_w)}{K_o} + \frac{(S_w)}{K_w}. \tag{2.16}$$

$$\frac{1}{K_{fl}} = \frac{(1-S_w)}{K_o} + \frac{(S_w)}{K_w}. \tag{2.17}$$

where K_o and K_w are the bulk moduli of oil and water, respectively.

2.3.2.2 Rock Properties

The bulk density of a saturated rock ρ_b is equivalent to the volumetric average of the constituent densities:

$$\rho_b = \rho_{min} + (1-\phi)\rho_{fl}, \tag{2.18}$$

where ϕ is porosity, ρ_{min} and ρ_{fl} are the densities of the mineral phase and the saturating fluid mixture, respectively. Tables of density, P-wave velocity and S-wave velocity for common minerals are available in the literature (e.g., *Mavko et al*. [1998]).

P- and S-wave velocities are related to porosity and effective pressure through pressure-dependent velocity-porosity models that can be either theoretical, or experimentally determined from laboratory and field observations. The relationships determined by *Han* [1986] and *Castagna et al.* [1985] from laboratory measurements are examples of empirical velocity-porosity models for sedimentary rocks. Most theoretical models predict the effective moduli of the porous media based on the moduli of pure constituents, their volume fractions, and the geometric details that describe how they are arranged. Knowing the elastic moduli, one can derive the P- and S-wave velocities from equations 2.13, 2.14, and 2.18.

The velocity of acoustic waves in crustal rocks may also vary with mineral composition, texture, and cementation (e.g., *Vernik* [1994], *Avseth* [2000]), and may exhibit frequency- and scale-dependent dispersion (e.g., *Mukerji* [1995], *Rio et al.*, [1996]). Unless explicitly noted, we assume that over the range of effective pressures observed during the production history, the measured data follows velocity-porosity-effective pressure trends that can be approximated by a unique, smooth surface. It follows from this assumption that the first derivatives of the velocity model with respect

to porosity and pressure must exist, which is required when using a gradient-based technique to solve the inverse problem. The uniqueness condition implies in practical terms that the reservoir consists of the same rock type, and mineralogy and textural variations in the rock are second-order effects that do not call for the use of different trends for properly modeling velocity.

The physics of acoustic wave propagation imposes limits to the range of feasible elastic moduli of dry rocks —and by extension to their P- and S-wave velocities— for a given porosity. Those limits, known as the *Voigt* and *Reuss* bounds, must be observed for the velocity-porosity-effective pressure model to be valid. The Voigt bound is given by the arithmetic average of the constituents' moduli, and results from applying isostrain boundary conditions to the system. The Reuss bound represents a scenario of isostress boundary conditions, and is given by the harmonic average of the constituents' moduli [*Mavko et al.*, 1998].

Because of the nature of our fluid-flow forward model, we focus on the seismic response of non-compacting oil-water reservoirs, i.e., those composed of consolidated rocks, and/or those that have strong pore pressure maintenance. Figure 2.2 shows a velocity-porosity-effective pressure model fitted through the range of high effective pressures, from a set of measurements in core sandstone samples from a consolidated reservoir. If effective pressures over the reservoir volume are not expected to lie outside this range at any stage of production, one can use a model that is linear in both porosity and effective pressure. A general expression that describes such a model is:

$$V = a + b\phi + c(P_{eff} - P_{ref}), \tag{2.19}$$

where V can be either P- or S-wave velocity, ϕ is porosity, P_{eff} is effective pressure, and P_{ref} is the reference effective pressure at which coefficients a and b where determined. We assume that in the range of porosity and pressure variations relevant to our problem, the dependence of velocity on porosity and pressure is linear. Softer rocks may exhibit a non-linear velocity response to changes in effective pressure, though. In such cases, an exponential model of the following form can be used:

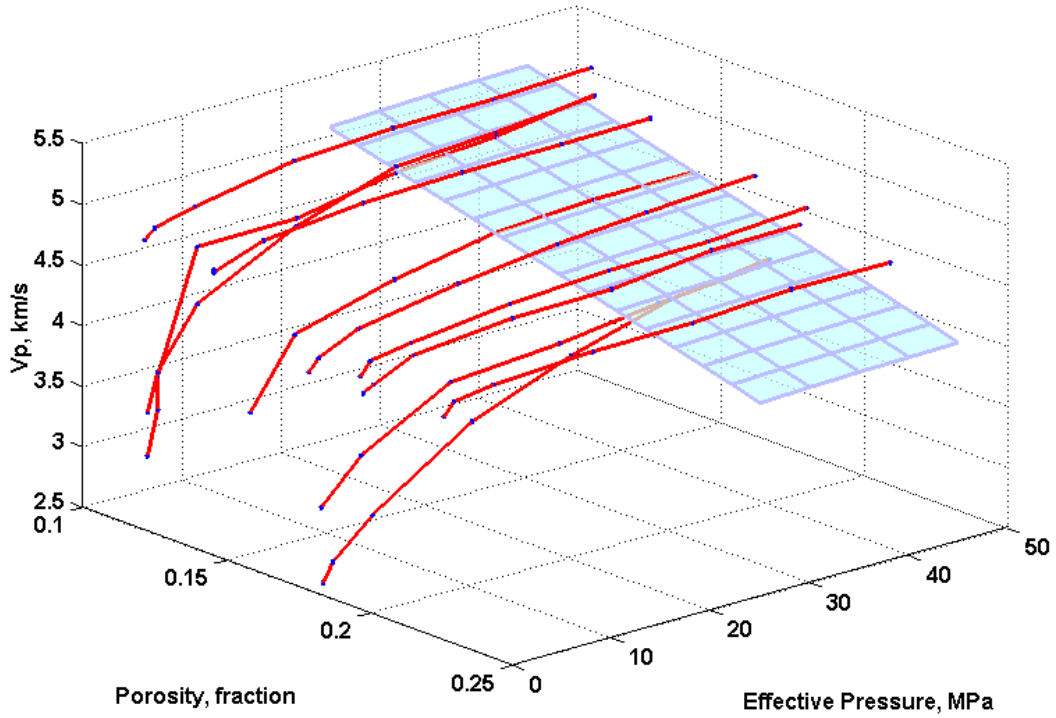

Figure 2.2: A plot of P-wave velocities measured in core sandstone samples from a consolidated reservoir. The mesh is a surface that describes the velocity-porosity-effective pressure model derived from the measurements, for the range of effective pressures expected during production in that particular scenario.

$$V = V_{\max}(\phi)\left[1 - c\,\mathrm{e}^{(-dP_{eff})}\right], \tag{2.20}$$

where $V_{\max}(\phi)$ are the asymptotes of velocity at high effective pressure, given by:

$$V_{\max}(\phi) = a + b\phi\,. \tag{2.21}$$

The coefficients a, b, c, and d in equations 2.19 to 2.21 must be determined experimentally.

As fluids move through the reservoir, changes in saturation induce variations in the elastic properties of rocks. At the low-frequency limit those changes can be modeled with *Gassmann*'s [1951] fluid substitution equations, which are given by:

$$\widetilde{K}_{sat} = \frac{\phi\widetilde{K}_{dry} - (1-\phi)\widetilde{K}_{fl}\cdot\widetilde{K}_{dry} + \widetilde{K}_{fl}}{(1-\phi)\widetilde{K}_{fl} + \phi - \widetilde{K}_{fl}\cdot\widetilde{K}_{dry}}, \text{ and} \tag{2.22}$$

$$\mu_{sat} = \mu_{dry}, \tag{2.23}$$

where:

$$\widetilde{K}_{sat} = \frac{K_{sat}}{K_m}; \quad \widetilde{K}_{dry} = \frac{K_{dry}}{K_m}; \quad \widetilde{K}_{fl} = \frac{K_{fl}}{K_m}, \tag{2.24}$$

In equations 2.22 to 2.24, ϕ represents porosity, K and μ are the elastic bulk and shear moduli, and the subscripts *fl*, *dry* and *m* stand for fluid, dry-rock, and mineral, respectively. By combining equations 2.14 through 2.24 it is possible to compute the P- and S-wave velocities of the rock, at the pressures and saturations predicted by the reservoir simulator at the time of seismic data acquisition.

2.3.2.3 Seismic Response

The propagation of waves trough an elastic medium is governed by the elastic wave equation. One simple, yet powerful and commonly used approach for computing the seismic response of a certain earth model is the so-called *convolutional model* [*Tarantola*, 1984; *Russell*, 1988; *Sheriff and Geldart,* 1995], which can be derived from an acoustic approximation of the elastic wave equation. In the convolutional model a seismic trace *s(t)* is the result of convolving a seismic wavelet $w(t)$ with a time series of reflectivity coefficients $r(t)$, with the addition of a noise component $n(t)$, as follows:

$$s(t) = w(t) * r(t) + n(t). \tag{2.25}$$

The normal incidence reflectivity coefficient is a function of acoustic impedance, i.e., the ability of an elastic medium to allow the passage of an acoustic wave. The acoustic

impedance of a rock is a function of two porosity-dependent rock properties: bulk density and velocity. For instance, the P-wave acoustic impedance is given by:

$$I_p = \rho_b V_p . \tag{2.26}$$

The reflectivity coefficient can be computed from:

$$r(t) = \frac{I_2 - I_1}{I_2 + I_1}, \tag{2.27}$$

where I represents the acoustic impedance and the subscripts 1 and 2 refer to two subsequent layers in the stratigraphic column.

The wavelet represents the signature of the seismic source. It is usually extracted from the seismic survey through deconvolution of traces around locations where the earth's reflectivity series can be computed from well log data.

There could be two types of noise in a seismic section: uncorrelated or random noise and coherent noise. The latter is predictable and in many cases removable by specific processing algorithms, such as predictive deconvolution, f-k filtering and inverse velocity stacking, among others. When coherent noise is very complex and cannot be removed, it must be taken into account in the convolutional model. The random character of uncorrelated noise makes it easier to remove by stacking of several traces corresponding to the same common mid-point.

2.4 Objective Function

In our approach we use a weighted least-squares objective function of the following form:

$$E = \sum_{i=1}^{nobs} w_i \left(d_i^{obs} - d_i^{calc} \right)^2 , \tag{2.28}$$

where d_i^{obs} represents the observed data; d_i^{calc}, the response of the system, as predicted by the forward model; *nobs,* the number of observations; and w_i are the weighting factors used to account for data quality and relevance, and for equalizing the magnitude of different types of data. E is the mathematical definition of the error surface that we want to minimize, so that the misfits between observed and calculated variables are reduced. Equation 2.28 can be expressed in a matrix form as:

$$E = \left(\tilde{d}_{obs} - \tilde{d}_{cal}\right)^{\mathrm{T}} \mathbf{W}\left(\tilde{d}_{obs} - \tilde{d}_{cal}\right), \tag{2.29}$$

where **W** is a diagonal matrix of weighting factors, $\tilde{d}_{obs}$ represents the set of measurements, and $\tilde{d}_{cal}$ the set of responses computed from the forward model.

2.5 Optimization Algorithms

As pointed out before, the problem of estimating petrophysical properties from seismic and reservoir engineering data is non-linear with respect to the set of parameters $\tilde{\alpha}$ that characterize the system (porosity and permeability in this case), and can be solved only using iterative approaches. In this thesis we use a gradient-based optimization scheme to solve the problem in hand. Our approach builds on a three-dimensional adaptation [*Phan,* 1998; *Phan and Horne,* 1999] of the formulation proposed by *Landa* [1997] for a similar data integration problem. We use the Gauss-Newton algorithm to find the direction of descent, along with modified Cholesky factorization for stabilization purposes. Then we perform a line search optimization to find a set of parameters along the direction of descent that results in a smaller value of the objective function. I describe in this section those algorithms, along with the methods we use to constrain the solution.

2.5.1 The Gauss-Newton Method

We focus on the multivariate problem of finding the optimal point $\tilde{\alpha}^*$, represented by the set of parameters $\tilde{\alpha}$ within the feasible region *D* that results in the smallest misfit *E* —in the least-squares sense— between measured and observed variables, i.e.,

$$E(\tilde{\alpha}^*) = \min_{\tilde{\alpha}} E(\tilde{\alpha}) \quad , \quad \tilde{\alpha} \in D \tag{2.30}$$

The necessary conditions that a set of parameters $\tilde{\alpha}^*$ must satisfy to be a minimum of the smooth multidimensional error surface *E* are the following:

1. The set of parameters $\tilde{\alpha}^*$ is a stationary point. A point is stationary if all components of the gradient ∇E of the multidimensional error surface—the vector of all derivatives of the error surface with respect to the inversion parameters $\tilde{\alpha}$ — are zero, i.e.,

$$\nabla E(\tilde{\alpha}^*) = \left.\frac{\partial E}{\partial \tilde{\alpha}}\right|_{\tilde{\alpha}^*} = 0 . \tag{2.31}$$

Let **G** be the matrix of *sensitivity coefficients* —the partial derivatives of matching variables as calculated by the forward model— given by:

$$\mathbf{G} = \frac{\partial \tilde{d}_{cal}}{\partial \tilde{\alpha}} . \tag{2.32}$$

Deriving the objective function with respect to the parameters $\tilde{\alpha}$ yields:

$$\nabla E = \frac{\partial E}{\partial \tilde{\alpha}} = -2 \frac{\partial \tilde{d}_{cal}}{\partial \tilde{\alpha}}^{\mathrm{T}} \mathbf{W}\left(\tilde{d}_{obs} - \tilde{d}_{cal}\right) = -2\mathbf{G}^T \mathbf{W}\left(\tilde{d}_{obs} - \tilde{d}_{cal}\right). \tag{2.33}$$

2. The matrix **H** of second derivatives of the error surface E with respect to the parameters $\tilde{\alpha}$ —the *Hessian matrix*—, evaluated at the solution $\tilde{\alpha}^*$, is semi-positive definite, i.e., all its eigenvalues are positive or zero. The Hessian matrix is symmetric, and its terms are given by:

$$\mathbf{H} = \frac{\partial^2 E}{\partial \tilde{\alpha}_i \partial \tilde{\alpha}_j} = \frac{\partial^2 E}{\partial \tilde{\alpha}_j \partial \tilde{\alpha}_i} = -2\left[\frac{\partial \mathbf{G}^T}{\partial \tilde{\alpha}_i}\mathbf{W}\left(\tilde{d}_{obs} - \tilde{d}_{cal}\right)\right] + 2\mathbf{G}^T\mathbf{W}\mathbf{G}\,. \tag{2.34}$$

Solving equation 2.31, which is non-linear with respect to $\tilde{\alpha}$, allows us to determine a stationary point. If the error function is smooth, we can linearize equation 2.31 by applying a Taylor series expansion to the gradient of the error surface ∇E in the vicinity of a certain point $\tilde{\alpha}_0$, and truncating the series after the first order term. This procedure results in the linear system of equations:

$$\mathbf{H}^0 \delta\tilde{\alpha} = -\nabla E\left(\tilde{\alpha}_0\right). \tag{2.35}$$

The solution of matrix equation 2.35 yields the *direction of descent* $\delta\tilde{\alpha}$, along which we can find a new set of parameters $\tilde{\alpha}$ that results in a smaller error and is closer to a stationary point. At each subsequent iteration of the inversion algorithm, we must complete the following steps:

1. Run the forward model and evaluate the error E.
2. Compute the vector of first derivatives of the error surface with respect to the parameters $\tilde{\alpha}$ —the gradient vector ∇E.
3. Either compute or approximate the Hessian matrix **H**.
4. Solve the linear system described by equation 2.35 to find the direction of descent vector $\delta\tilde{\alpha}$, and
5. Perform a line search along the direction of descent to find a new set of parameters $\tilde{\alpha}$.

When matrix **H** is computed exactly, the technique described is known as *Newton's method*. This method benefits from fast, quadratic convergence —in fact, it is often used

as the benchmark for comparing the performance of other algorithms— but in some cases it may result in a Hessian matrix that is not positive-definite. Under such conditions the vector $\delta\tilde{\alpha}$ is not guaranteed to be a direction of descent and could lead to a stationary point that is a maximum, or a saddle point, rather than a minimum. Furthermore —and perhaps more limiting— Newton's method requires the evaluation of second derivatives of the objective function. In many cases the analytical expressions for the second derivatives of the error surface are not available; the numerical approximation of such derivatives can be computationally prohibitive if the objective function is expensive to evaluate. Such is the case for a model that uses a finite-difference reservoir simulator.

The alternative is to modify the Hessian matrix so that it becomes positive definite, but stays close to the exact Newton's Hessian. In this way the desirable quadratic performance of the algorithm is not seriously compromised. One method that yields a matrix with such characteristics is the so-called *Gauss-Newton method*, which consists of approximating the Hessian matrix by taking only the second term in equation 2.34:

$$\mathbf{H}_{GN} = 2\mathbf{G}^T\mathbf{W}\mathbf{G}\,. \tag{2.36}$$

If the matrix of weights **W** is positive definite, it can be demonstrated that the Gauss-Newton matrix $\mathbf{H}_{GN}$ is at least semi-positive definite at the minimum. At some iterations of the inversion algorithm $\mathbf{H}_{GN}$ may not be positive-definite, but it can also be shown that, as long as $\mathbf{H}_{GN}$ does not become singular, the vector $\delta\tilde{\alpha}$ is still a direction of descent.

Landa [1997] found that the most efficient way to solve equation 2.35 is by using Cholesky factorization. The advantages of using this method are two-fold: (1) it is more stable and efficient, and (2) since Cholesky factors only exist if $\mathbf{H}_{GN}$ is positive-definite, Cholesky factorization is an intrinsic check for positive-definiteness. When the matrix $\mathbf{H}_{GN}$ is not positive-definite, we stabilize it via *modified* Cholesky factorization.

2.5.2 Modified Cholesky Factorization

As discussed before, failure of the Cholesky factorization method implies that the matrix being factored is not positive-definite, and for the practical purpose of inversion indicates the need of further stabilization. The modified Cholesky factorization method consists of adding a non-negative diagonal matrix **E** to the original matrix **H** to get a more stable, positive-definite matrix $\hat{\mathbf{H}}_{GN}$:

$$\hat{\mathbf{H}}_{GN} = \mathbf{H}_{GN} + \mathbf{E}. \tag{2.37}$$

2.5.3 Line Search

In practical terms, a properly designed line search implementation can be seen as a step-length control method that enhances the performance of the inversion algorithm when finding a direction of descent is more expensive than evaluating the objective function; this is the case of the problem in hand. We use line search to find a new set of parameters $\tilde{\alpha} + \rho\delta\tilde{\alpha}$ along the direction of descent $\delta\tilde{\alpha}$ that results in a smaller value of the objective function *E*. As noted before, the existence of such a point along $\delta\tilde{\alpha}$ is guaranteed by the Gauss-Newton formulation when the Gauss-Newton matrix $\mathbf{H}_{GN}$ is positive-definite. For any positive value of the step length ρ, $\tilde{\alpha} + \rho\delta\tilde{\alpha}$ is a point along the direction of descent $\delta\tilde{\alpha}$, and the value of the objective function along such direction is a function that depends solely on ρ, i.e.,

$$E(\rho) = E(\tilde{\alpha} + \rho\delta\tilde{\alpha}). \tag{2.38}$$

The line search approach used in this work (after *Bard* [1970]) finds the optimum step-length ρ^* along $\delta\tilde{\alpha}$ by minimizing a quadratic approximation to the objective function $E(\rho)$, given by:

$$E^*(\rho) = a + b\rho + c\rho^2 . \tag{2.39}$$

where coefficients *a*, *b,* and *c* are as follows:

$$a = E(0), \tag{2.40}$$

$$b = \delta\tilde{\alpha}\nabla E \text{, and} \tag{2.41}$$

$$c = \frac{E(\tilde{\alpha} + \rho_0\delta\tilde{\alpha}) - b\rho_0 - a}{{\rho_0}^2} . \tag{2.42}$$

The minimization of equation 2.39 yields the optimum step length, given by:

$$\rho^* = -\frac{b}{2c} . \tag{2.43}$$

Line search is a local minimization problem that involves only objective function evaluations, and consequently, is not as expensive as the computation of the direction of descent, which requires both objective function and gradient evaluations. Line search may fail, though, when parameters are close to the limits of the feasible region, and the objective function is concave towards the boundary. For this reason, it is important to use line search along with penalty functions, which make the objective function concave towards the feasible region.

2.6 Constraints

The need for constraints in the parameter estimation problem arises from the fact that porosity and permeability cannot take values that are negative or unreasonably large for the reservoir being modeled, i.e.,

$$\phi_{min} < \phi_i < \phi_{max}, \ \forall \ i \in [1, nblocks], \text{ and} \tag{2.44}$$

$$K_{min} < K_i < K_{max}, \ \forall \ i \in [1, nblocks], \tag{2.45}$$

where ϕ and K represent porosity and permeability, i denotes a particular block in the discrete model, and *min* and *max* subscripts represent the minimum and maximum values the respective parameter can take. The limits to the feasible region in our case can be determined from the physics of porous materials, and/or from core and well-log observations. For instance, the reservoir systems we consider in this work cannot have porosities larger than the critical porosity, which is the porosity value beyond which the arrangement of mineral particles that compose the rock cannot take any load and become a suspension [*Nur*, 1992; *Nur et al.*, 1995]. Core and well-log data can help to further reduce the feasible range of porosity. In the case of permeability, the limits can be estimated from core measurements and well tests.

Algorithms for constrained inverse problems are less robust and more difficult to implement, though. The alternative is to solve an unconstrained problem that is equivalent to the constrained one, but easier to solve. In this work this is achieved by means of the so-called *penalty functions*.

Constraints can also be interpreted in terms of the additional information content they provide about the parameters. A discussion of this alternative interpretation is relevant to this thesis, for the purpose of incorporating *a-priori* information in the objective function. Our approaches to integrating *a-priori* information to the inversion are not only very useful in terms of improving the quality of inversion estimates, but also let us expand the applicability of our technique to more heterogeneous systems —those where the presence of different lithologies, textural variations or differences in diagenesis result in separate velocity-porosity trends— through the application of classification methods. If the elastic properties of different facies are such that they can be classified from seismic data, then one can use different constraints for each of them.

2.6.1 Penalty Functions

One approach to limit the feasible region of porosity and permeability is to modify the objective function by using penalty functions. In this work the penalized objective function has the following form:

$$\hat{E} = E + \sum_{i=1}^{npar} \varepsilon \frac{E}{\left|\alpha_{min,max} - \alpha_i\right|} = E + P\,. \tag{2.46}$$

where *npar* is the number of parameters in the problem, α_{min} and α_{max} are the absolute minimum and maximum feasible values of each parameter, respectively —i.e., the absolute minimum and maximum porosity and permeability values— and ε is a small positive number, e.g., 10^{-3}. We use four penalty terms in our implementation, one for each of the limiting values of porosity and permeability. Each penalty term is a function of the overall misfit, so penalty terms are significant when the inversion parameters are away from the minimum $\tilde{\alpha}^*$, but vanish for any acceptable solution, where the misfit is smaller than a tolerance τ, and each parameter is far from the limits of the feasible region (α_{min} and α_{max}). On the other hand, if a certain parameter approaches one of the limits in a certain iteration of the inversion algorithm, the denominator of the corresponding penalty term becomes very small, which results in a high penalty for that particular parameter.

2.6.2 Interpretation of constraints in terms of information content

The most general way of describing the state of knowledge about the true value of a system's parameters is through a probability density function (PDF), or alternatively, through a cumulative probability density function (CDF) (*Tarantola* [1987]; *Menke*, [1989]). For instance, if we have complete certainty about the value of a certain parameter, e.g. $\phi = \phi_0$, we can describe its probability density by:

$$f(\phi) = \delta(\phi - \phi_0), \tag{2.47}$$

where δ is Dirac's delta function. This results in null probability for any porosity value different than ϕ_0, while the probability of $\phi = \phi_0$ is equal to 1. This state is known in the literature as the *state of perfect knowledge*. By opposite analogy, the *state of total ignorance*, also known as the *reference state of information*, represents the situation in which we have the lowest possible knowledge about the value of a parameter, and its associated probability density function is termed the *non-informative probability density*, and denoted $\mu(\mathbf{x})$.

Following this approach one can approximate the constraints described by equations 2.44 and 2.45 in terms of the following probability density functions:

$$f(\phi) = \begin{cases} \left(\dfrac{1}{\phi_{max} - \phi_{min}}\right) & \forall\ \phi \in [\phi_{min}, \phi_{max}] \\ 0 & \text{otherwise} \end{cases}, \text{ and} \tag{2.48}$$

$$f(K) = \begin{cases} \left(\dfrac{1}{K_{max} - K_{min}}\right) & \forall\ K \in [K_{\min}, K_{\max}] \\ 0 & \text{otherwise} \end{cases}. \tag{2.49}$$

This formulation gives equal probability to any pair of porosity and permeability values in the domain defined by $\phi \in [\phi_{min}\ ,\ \phi_{max}]$ and $K \in [K_{min}\ ,\ K_{max}]$, and null probability to any values outside.

By convention, we assume that the relative information content $I(f|\mu)$ of a normalized probability density function $f(\mathbf{x})$ is given by the so-called *Kullback distance* [*Kullback*, 1967], measured with respect to the non-informative probability density function $\mu(\mathbf{x})$ [*Tarantola*, 1987; *Mosegaard and Tarantola*, 2002], i.e.,

$$I(f|\mu) = \int f(\mathbf{x}) Log\left(\frac{f(\mathbf{x})}{\mu(\mathbf{x})}\right) d\mathbf{x}, \tag{2.50}$$

and, by definition:

$$I(\mu|\mu) = 0 . \tag{2.51}$$

Kullback distance is a generalization of Shannon's measure of information content in the context of normalized probability density functions. We assume for the purposes of this work that equations 2.48 and 2.49 represent the reference state of information for the parameter estimation problem in hand.

2.7 Use of *a-priori* Information

In parameter estimation theory, *a-priori*, or *prior* information is the information about the *model parameters* (porosity and permeability, in this case) obtained independently of the measurements that are considered 'data' in the objective function (often called in the literature *matching variables*, or *directly observable parameters*) [*Tarantola*, 1987]. Such *a-priori* information can refer directly to the model parameters, or can be relevant to other variables that provide indirect knowledge about the outcome of the parameter estimation problem. For instance, one may not know the value of permeability at a certain location, but may have information about its spatial correlation length, and may be able to use it in the parameter estimation problem.

In this section I describe two approaches to incorporate *a-priori* information that, rather than enforcing a single relationship between porosity and permeability, describe a *trend* characterized by a set of porosity-dependent permeability bounds in the first approach, and by a bivariate probability density function in the second. The discussion about optimization methods in section 2.5 is not affected by the modifications described here. I will show in Chapter 3 that the application of these two approaches significantly improves the inversion results and makes more physical sense than using only the absolute maximum and minimum limits for porosity and permeability. I also discuss in this section an alternative for estimating the bivariate PDF of porosity and permeability when core data is not available, but when there is *a-priori* information in the form of models of spatial correlation.

2.7.1 Porosity-dependent Permeability Bounds

Although penalty terms efficiently contained the solution within the porosity and permeability ranges given by [ϕ_{min} , ϕ_{max}] and [K_{min} , K_{max}], the formulation we described in section 2.6.1 proved inadequate for limiting the actual feasible region of porosity and permeability for a real reservoir, because it does not to provide a link between porosity and permeability. Notice that for such formulation one could express the conditional distribution of permeability given porosity as:

$$f(K|\phi) = \begin{cases} \left(\dfrac{1}{K_{max} - K_{min}}\right) & \forall\ K \in [K_{min}, K_{max}] \\ 0 & \text{otherwise} \end{cases}, \tag{2.52}$$

which is the same as equation 2.49, i.e., the marginal PDF of permeability is equal to the conditional PDF of permeability given porosity, meaning that porosity does not provide any information on permeability. This contradicts many results that demonstrate the existence of a relationship between the two. For instance, theoretical models based on the Kozeny-Carman equation suggest that permeability is proportional to porosity to the third power. Modeling the relationship between porosity and permeability with a single equation often results in oversimplification, though, and in most cases does not yield acceptable solutions to the parameter estimation problem in hand.

Our implementation further limits the feasible region, as initially defined by equations 2.44 and 2.45, through the application of porosity-dependent permeability bounds that can be estimated from core data. Most reservoirs exhibit clear trends in the porosity vs. log-of-permeability space (Figure 2.3) that can be limited by a set of upper and lower porosity-dependent permeability bounds as follows:

$$K_l(\phi_i) < K_i < K_u(\phi_i),\ \forall\ i \in [1, nblocks], \tag{2.53}$$

where K_l and K_u represent the lower and upper bounds of permeability for a given porosity ϕ_i, respectively. Such bounds can in practice be estimated from core data. Equation 2.53 provides a not necessarily linear link between porosity and permeability. This represents a state of information that can be described by the following set of uniform conditional probability density functions:

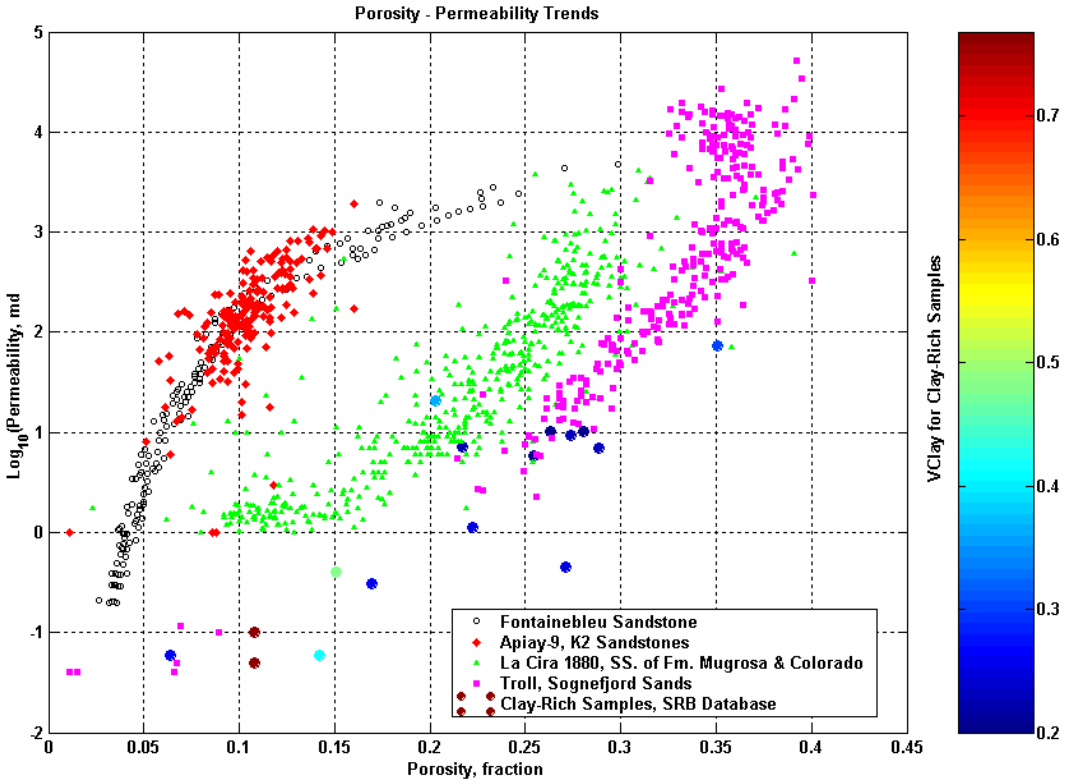

Figure 2.3: A plot of porosity and permeability for various data sets. The color bar on the right corresponds to the fraction of clay for a set of clay-rich sandstone samples.

$$f(K|\phi)=\begin{cases}\left(\dfrac{1}{K_u(\phi)-K_l(\phi)}\right) & \forall\ K\in[K_l(\phi),K_u(\phi)] \\ 0 & \text{otherwise}\end{cases}. \qquad (2.54)$$

We designed a penalty term that takes advantage of these observations, and applied the following modification to the objective function:

$$\hat{E} = E + P + \sum_{i=1}^{nblocks} w_i d_i^2 \ , \tag{2.55}$$

where w is the weight given to the *a-priori* information, and d is the offset distance from a given permeability point to the upper or lower bound, whichever is closer to the point. Let l be the distance between the bounds for a particular value of porosity, i.e.,

$$l(\phi_i) = K_u(\phi_i) - K_l(\phi_i). \tag{2.56}$$

Then, for a particular block i with porosity ϕ_i and permeability K_i, the offset distance d is given by:

$$d_i(K_i, \phi_i) = |K_i - K_l(\phi_i)| + |K_i - K_u(\phi_i)| - l(\phi_i). \tag{2.57}$$

Notice that the offset d is zero for any value of K within the bounds defined by K_l and K_u. Thus, solving the problem described by equation 2.55 is equivalent to solving the unconstrained problem. Figure 2.4 shows that in the log-of-permeability vs. porosity space this formulation creates mirror surfaces of hemiparabolic cross-section along planes of constant porosity, with vertices at the points of intersection with K_l and K_u, and separated by a horizontal plane of zero penalty. However, equation 2.57 does not enforce a uniform PDF between K_l and K_u. Such a probability density is appropriate to describe the state of information, but is not desirable because we know the true conditional PDF of permeability given porosity has at least one mode. Therefore, in this approach we enforce the bounds described by equation 2.43, but let the observations determine the shape of the resulting conditional PDF. In the following section I describe a method that enforces an *a-priori* bivariate PDF that is more representative of an actual reservoir.

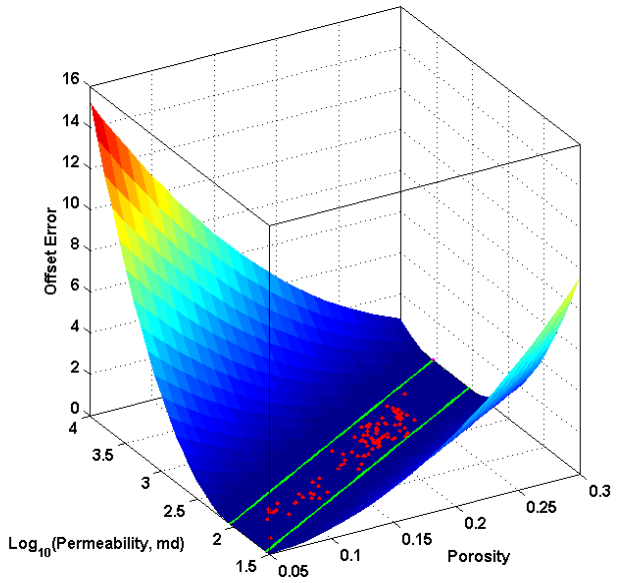

Figure 2.4: An error surface that bounds the reference porosity- permeability trend. The porosity-dependent bounds used to design the surface can be determined from core data, and need not be linear.

2.7.2 Incorporating a Set of *a-priori* Conditional CDFs of Permeability given Porosity

If the data set contains a collection of porosity and permeability measurements (e.g., from cores) that adequately represents the true petrophysical properties of the reservoir, then one can estimate a bivariate probability density function —or alternatively, a bivariate cumulative probability density function— that describes such state of *a-priori* information. The following equation describes a bivariate CDF of porosity and permeability:

$$CDF\left(k,\phi;K_i,\phi_i\right) = Prob\left\{K_i \le k\,,\phi_i \le \phi\right\}. \tag{2.58}$$

with k and ϕ some permeability and porosity quantiles. Instead of making strict use of equation 2.58, in this work we take a set of conditional cumulative distribution functions of permeability given porosity. This is appropriate when one of the parameters can be reasonably well resolved by the observations, and after proper upscaling of the observations from the core scale to the field scale. For a given bin m of the porosity

histogram with range $[\phi_m, \phi_{m+1})$, the conditional cumulative distribution function of permeability given that the porosity of block *i* (ϕ_i) belongs in bin *m* is given by:

$$CCDF^m(k; K_i | \phi_i) = Prob\{K_i \le k \mid \phi_i \in [\phi_m, \phi_{m+1})\}, \quad (2.59)$$

where *k* can be any permeability quantile.

The error function takes now the following form:

$$E = (\tilde{d}_{obs} - \tilde{d}_{cal})^T \mathbf{W}_d (\tilde{d}_{obs} - \tilde{d}_{cal}) + (\tilde{m}_{a-priori} - \tilde{m}_{cal})^T \mathbf{W}_m (\tilde{m}_{a-priori} - \tilde{m}_{cal}), \quad (2.60)$$

where $\tilde{d}$ represents the variables being matched; $\tilde{m}$, the *a-priori* information on the model parameters in the form of cumulative distribution functions; and $\mathbf{W}_d$ and $\mathbf{W}_m$, the weights given to data and a-priori information, respectively.

We compute $(\tilde{m}_{a-priori} - \tilde{m}_{cal})$ using an approach that resembles the *histogram identification* technique (*Deutsch and Journel* [1998]). Let $P^m_{a-priori}$ denote the target conditional CDF of permeability given porosity for porosity bin *m*, and P^m_{cal} denote the analogous CDF computed from the porosity and permeability values in a given inversion iteration. For the probability $P^m_{cal}(k|\phi)$ of a given quantile *k* —e.g., the permeability K_i of a block with porosity ϕ_i in $[\phi_m, \phi_{m+1})$— one can find (Figure 2.5) the corresponding quantile k_i^{target} from the distribution $P^m_{a-priori}(k|\phi)$. Then, $(m^i_{a-priori} - m^i_{cal})$ for the porosity and permeability of block *i* is the distance between the two quantiles, as follows:

$$(m^i_{a-priori} - m^i_{cal}) = |k_i^{target} - K_i|. \quad (2.61)$$

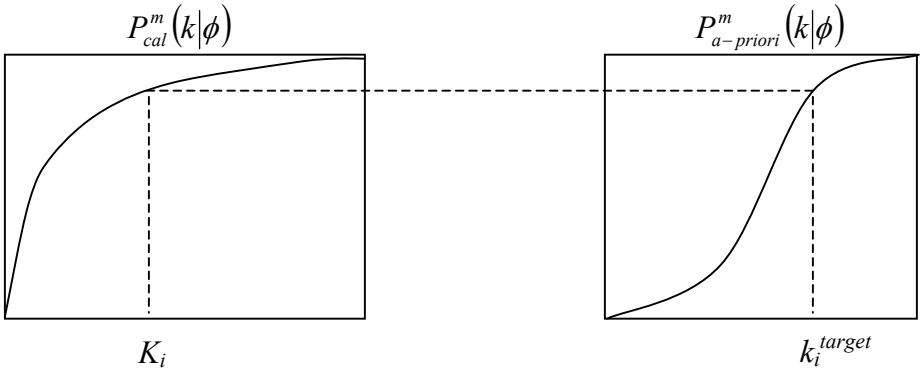

Figure 2.5: An error surface that bounds the reference porosity- permeability trend. The porosity-dependent bounds used to design the surface can be determined from core data, and need not be linear.

2.7.3 A Cokriging Alternative to Model the *a-priori* Bivariate CDF of Porosity and Permeability

There is no such thing as enough core samples. Cores contain by far the most representative information about the properties of subsurface rocks, and play a crucial role in reservoir characterization studies. However, coring is expensive and frequently entails drilling risks that make core acquisition hard to justify. Therefore, in many cases core measurements are insufficient, and quite often there is no core data available at all. In such scenarios it is not straightforward to estimate a bivariate PDF that provides *a-priori* information on the relationship between porosity and permeability.

One way to estimate the set of $P^m_{a-priori}(k|\phi)$ is to take advantage of the fact that well blocks are the best informed among all blocks in the model, because production data are collected at wells. Working with synthetic data we observed that after a few inversion iterations our algorithm delivers porosity and permeability estimates of good quality at well locations, under different configurations of the objective function. If reliable impedance data are available for all grid blocks, and impedance has good anticorrelation with porosity, the algorithm also produces reasonably good porosity estimates after a few iterations. Then it is viable to perform a collocated cokriging with the permeability values at well locations as hard data and the porosity estimates as soft data, which yields permeability estimates for all locations. Such permeability values can be used to estimate the mean of each $P^m_{a-priori}(k|\phi)$.

Our approach to approximating $P^m_{a-priori}(k|\phi)$ in the absence of representative core measurements can be described as follows:

1. Assume a parametric model for the conditional CDFs.
2. Estimate the means of each conditional PDF from the results of a collocated cokriging performed after a few inversion iterations; and
3. Assume a certain variance for each of the conditional CDFs $P^m_{a-priori}(k|\phi)$.
4. Assume all other parameters required to fully determine the shape of the parametric conditional CDFs.

Step 4 is not required if the assumed parametric model is Gaussian, because such a model is fully determined by two parameters: mean and variance. A more detailed description of how to estimate the means of each $P^m_{a-priori}(k|\phi)$ follows.

If *a-priori* information in the form of models of spatial correlation (i.e., variogram or covariance models) is available, then one can obtain a collocated cokriging estimate of permeability for each block, from the values of permeability at well locations and using porosity as secondary data. In such case the collocated simple cokriging estimator (*Goovaerts* [1997], *Deutsch and Journel* [1998]) is given by:

$$K^*(\mathbf{u}) = \lambda_\phi(\mathbf{u})[\phi(\mathbf{u}) - \phi_{mean}] + K_{mean} + \sum_{\alpha=1}^{\#wellblocks} \lambda_{K_\alpha}(\mathbf{u})[K(\mathbf{u}_\alpha) - K_{mean}]. \qquad (2.62)$$

In equation 2.62 $\mathbf{u}$ is the vector of coordinates for a given block, α denotes a well location, and $\lambda_K(\mathbf{u})$ and $\lambda_\phi(\mathbf{u})$ are the cokriging weights for porosity and permeability data at location $\mathbf{u}$; the only secondary datum considered is $\phi(\mathbf{u})$, i.e. the porosity at the location being estimated. The set of weights λ_K and λ_ϕ are obtained by solving the cokriging system:

$$\begin{cases} \sum_{\beta=1}^{\#wellblocks} \lambda_{K_\beta}(\mathbf{u}) C_{KK}(\mathbf{u}_\alpha - \mathbf{u}_\beta) + \lambda_\phi(\mathbf{u}) C_{K\phi}(\mathbf{u}_\alpha - \mathbf{u}) = \\ \qquad\qquad C_{KK}(\mathbf{u}_\alpha - \mathbf{u}), \forall \alpha \in [1, \#wellblocks] \\ \sum_{\beta=1}^{\#wellblocks} \lambda_{K_\beta}(\mathbf{u}) C_{\phi K}(\mathbf{u} - \mathbf{u}_\beta) + \lambda_\phi(\mathbf{u}) C_{\phi\phi}(0) = C_{\phi K}(0) \end{cases}, \tag{2.63}$$

where α and β are well locations, $C_{KK}(\mathbf{h})$ is the spatial auto-covariance between two permeability data separated a distance $|\mathbf{h}|$, $C_{\phi\phi}(\mathbf{h})$ is the analogous spatial auto-covariance for porosity, and $C_{\phi K}(\mathbf{h})$ is equal to $C_{K\phi}(\mathbf{h})$, the spatial cross-covariance between porosity and permeability. Notice that the spatial auto-covariance of porosity is only required at zero offset, i.e., for the collocated location.

The collocated cokriging estimator described by equation 2.62 represents the expected value of the PDF of permeability at location **u**, conditional to the permeability at well locations and the porosity at location **u**. Notice that this is different to the mean of $P^m_{a-priori}(k|\phi)$, which is the PDF of permeability given that the porosity of block *i* belongs in $[\phi_m, \phi_{m+1})$. We can estimate the mean of $P^m_{a-priori}(k|\phi)$ by taking the mean of the subset of cokriging estimates for all blocks with porosity in $[\phi_m, \phi_{m+1})$. Using the estimated means together with assumed variances for each $P^m_{a-priori}(k|\phi)$ one can estimate Gaussian conditional CDFs of permeability given porosity for each porosity bin.

2.8 References

Avseth, P., 2000, *Combining Rock Physics and Sedimentology for Seismic Reservoir Characterization of North Sea Turbidite Systems*, Ph.D. dissertation, Stanford University.

Aziz, K. and A. Settari, 1986, *Petroleum Reservoir Simulation*. Elsevier applied science publishers.

Bard, Y., 1970, *Nonlinear Parameter Estimatio*n, Academic Press, New York.

Batzle, M. and Z. Wang, 1992, Seismic properties of pore fluids: *Geophysics*, **57**, 1396-1408.

Biondi, B., G. Mavko, T. Mukerji, D. Lumley, C. Deutsch, R. Gundenso, and M. Thiele, 1998, Reservoir monitoring: a multidisciplinary feasibility study: *The Leading Edge*, **17**, 1404-1414.

Cadoret, T., 1993, *Effect de la Saturation Eau/Gaz sur les Proprétés Acoustiques des Roches*, Ph.D. thesis, University of Paris.

Castagna, J. P., M. L. Batzle and Eastwood, R. L., 1985, Relationships between compressional wave and shear wave velocities in clastic silicate rocks: *Geophysics*, **50**, 571-581.

Darcy, H., 1856, *Les Fontaines Publiques de la Ville de Dijon*: Dalmont, Paris.

Deutsch, C. V., and A. Journel, 1998, *GSLIB: Geostatistical Software Library and User's Guide*, Second edition, Oxford University Press, New York, 369 pp.

Gassmann, F., 1951, Über die elastizität poröser medien: *Vier. der Natur*, Gesellschaft, **96**, 1–23.

Gill, P. E., W. Murray and M. Wright, 1993, *Practical Optimization*, Academic Press, San Diego, 401 pp.

Goovaerts, P, 1997, *Geostatistics for Natural Resources Evaluation*, Oxford University Press, New York, 483 pp.

Han, D.-H., 1986, *Effects of Porosity and Clay Content on Acoustic Properties of Sandstones and Unconsolidated Sediments*, Ph. D. dissertation, Stanford University.

Kullback, S., 1967, The two concepts of information, *J. Amer. Statist. Assoc.*, **62**, 685–686.

Landa, J. L., 1997, *Reservoir Parameter Estimation Constrained to Pressure Transients, Performance History and Distributed Saturation Data*, Ph.D. dissertation, Stanford University.

Marion, D., T. Mukerji, and G. Mavko, 1994, Scale effects on velocity dispersion: From ray to effective medium theories in stratified media: *Geophysics*, **59**, 1613–1619.

Mavko, G., and R. Nolen-Hoeksema, 1994, Estimating seismic velocities in partially saturated rocks: *Geophysics*, **59**, 252–258.

Mavko, G., and A. Nur, 1996, Rock-Physics: the link between rock properties and seismic interpretation: *Abstracts of the NPF seminar: Geophysics for lithology prediction*, Kristiansand.

Mavko, G., and T. Mukerji, 1998, Bounds on low-frequency seismic velocities in partially saturated rocks: *Geophysics*, **63**, 918–924.

Mavko G., T. Mukerji, and J. Dvorkin, 1998, *The Rock Physics Handbook: Tools For Seismic Analysis In Porous Media*, Cambridge University Press, Cambridge, 329 pp.

Mattax, C. C. and R. L. Dalton, 1991, *Reservoir Simulation*, SPE Monograph Vol. 13, Society of Petroleum Engineers.

Menke, W., 1989, *Geophysical Data Analysis: Discrete Inverse Theory*: revised edition, Academic Press, London, 289 pp.

Mosegaard K., and A. Tarantola, 2002, Probabilistic approach to inverse problems, in *International Handbook of Earthquake and Engineering Seismology*, Academic Press, [in press].

Mukerji, T., 1995, *Waves and Scales in Heterogeneous Rocks*, Ph.D. dissertation, Stanford University.

Nur, A., 1989, Four-dimensional seismology and (true) direct detection of hydrocarbons: The petrophysical basis: *The Leading Edge*, **8**, 30-36.

Nur, A., 1992, Critical porosity and seismic velocities in rocks: *EOS*, Transactions American Geophysical Union, **73**, 43-66.

Nur, A., G. Mavko, J. Dvorkin, and D. Galmudi, 1995, Critical porosity: A key to relating physical properties to porosity in rocks: *The Leading Edge*, **17**, 357-363.

Peaceman, D. W., 1983, Interpretation of well-bock pressures in numerical reservoir simulation with nonsquare grid blocks and anisotropic permeability: *Society of Petroleum Engineers Journal*, 531-543; Transactions AIME, 275.

Phan, V, 1998, *Inferring Depth-Dependent Reservoir Properties from Integrated Analysis Using Dynamic Data*, M.S. dissertation, Stanford University.

Phan, V., and R. N. Horne, 1999, Determining depth-dependent reservoir properties using integrated data analysis. Paper SPE 56423.

Rio, P., T. Mukerji, G. Mavko, and D. Marion, 1996, Velocity dispersion in a laboratory simulated VSP: *Geophysics*, **61**, 584-593.

Russell, B.H., 1988, *Introduction to Seismic Inversion Methods*, Society of Exploration Geophysicists, 90 pp.

Sengupta, M., 2000, *Integrating Rock Physics and Flow Simulation to Reduce Uncertainties in Seismic Reservoir Monitoring*, Ph.D. dissertation, Stanford University.

Sheriff, R. E. and L. P. Geldart, 1995, *Exploration Seismology*, Cambridge University Press, New York, 592 pp.

Tarantola, A., 1984, Inversion of seismic reflection data in the acoustic approximation: *Geophysics,* **49**, 1259-1266.

Tarantola, A., 1987, *Inverse Problem Theory, Methods for Data Fitting and Model Parameter Estimation*, Elsevier Science Publishing Company, Amsterdam.

Vernik, L, 1994, Predicting lithology and transport properties from acoustic velocities based on petrophysical classification of siliciclastics: *Geophysics*, **59**, 420-427.

Wang, Z, and A. Nur, 1989, *Seismic and Acoustic Velocities in Reservoir Rocks, Volume 1: Experimental studies*: Society of Exploration Geophysicists, Tulsa, 420 pp.

Wang, Z, and A. Nur, 1992, *Seismic and Acoustic Velocities in Reservoir Rocks, Volume 2: Theoretical and Model Studies*: Society of Exploration Geophysicists, Tulsa, 450 pp.

Wang, Z, and A. Nur, 2000, *Seismic and Acoustic Velocities in Reservoir Rocks, Volume 3: Recent Developments*: Society of Exploration Geophysicists, Tulsa, 623 pp.

This page intentionally left blank

Chapter 3

Applications to a Synthetic Reservoir Model

The characterization of subsurface reservoirs requires the estimation of petrophysical properties that (1) correctly allocate of areas with different reservoir quality; (2) follow the trends observed in *a-priori* information; and, when used with appropriate mathematical models, (3) yield results that match observed data within certain acceptable tolerance. The first requirement is the basis for selecting locations for infill drilling, while the second imposes important limitations on petrophysical property estimates. As for the third condition, in this work we aim for values of porosity and permeability that result in both simulated production curves that match the observed production history of the reservoir, and synthetic seismic attributes that best fit the real seismic data. If production and seismic measurements can be reproduced, there is hope that production forecasts computed from the model are accurate, and appropriate for economic analysis and reservoir management.

In this chapter I present synthetic examples of petrophysical property estimation from the joint inversion of seismic and reservoir engineering data. The use of synthetic data allows us to test the integrity of our implementation under different scenarios. In contrast to a real case, synthetic data allows us to thoroughly check the four aforementioned requirements for proper reservoir characterization. Checking the first condition in a real case can only be done *a-posteriori*, i.e., after drilling wells and retrieving the pertinent information from them. Although this is one of the ultimate goals of most reservoir studies, this is clearly neither appropriate, nor affordable for testing an estimation technique.

In contrast with the approach taken by *Landa* [1997], and *Phan* [1998, 2002] our analyses focus on cases when time-lapse seismic is not available. We therefore use P-wave acoustic impedance instead of seismic-derived change in water saturation as the seismic attribute to match. When compared to the use of highly uncertain seismic-

derived estimates of water satration change, using impedance represents a reduction in permeability information, but also a much stronger data-driven constraint for porosity. We demonstrate that the integration of seismic and production data is still feasible in the absence of repeated surveys, and that it benefits from the good spatial coverage of acoustic impedance. I will also show the importance of integrating *a-priori* information about the relationship between petrophysical properties, to compensate for the smaller permeability resolution power of the data set. I also present a case in which I compute permeability from a linear relationship between porosity and log of permeability and invert for porosity only, and discuss the advantages and disadvantages of this approach.

The results we obtained provide useful insight into the advantages of this methodology, whose potential for data integration is rapidly transforming it into one of the important topics in reservoir characterization. I discuss here extensions of our technique that can be used for time-lapse seismic monitoring in softer, more fluid-sensitive rocks.

3.1 Variables Used in the Objective Function

Recall the general form of the objective function for weighted least-squares parameter estimation with data and *a-priori* information:

$$E = \left(\tilde{d}_{obs} - \tilde{d}_{cal}\right)^{\mathrm{T}} \mathbf{W}_d \left(\tilde{d}_{obs} - \tilde{d}_{cal}\right) + \left(\tilde{m}_{a-priori} - \tilde{m}_{cal}\right)^{\mathrm{T}} \mathbf{W}_m \left(\tilde{m}_{a-priori} - \tilde{m}_{cal}\right). \qquad (3.1)$$

Equation 3.1 can take different forms depending on the types of observations being inverted, and on whether *a-priori* information is used. Variables in the objective function may represent *dynamic* data, which depend on the flow of fluids through the reservoir, or *static* data, which do not change with fluid movement.

The production measurements we use in our simultaneous inversion approach are: botom-hole pressure (*Pwf*) measured at producing and injector wells, and the water cut (*wcut*) observed in producing wells.

Previous results have demonstrated the advantage of including the change in water saturation ΔSw —as derived from time-lapse seismic— in the reservoir parameter

estimation formulation [*Landa*, 1997; *Lu*, 2001; *Phan* 1998, 2002]. Since fluid replacement in the reservoir strongly depends on permeability, the seismic-derived change in water saturation between two instants in time provides information about the permeability field that, although indirect, has much better spatial coverage than any other production-related observation. The aforementioned studies assumed that all seismic modeling was done previous to the inversion, which makes the use of ΔSw appealing because it can be computed from the reservoir simulator, and no further models are required to solve the inverse problem.

Unfortunately, the state of the art of 4D seismic technology does not allow the quantification of water saturation change with the small level of uncertainty required for practical purposes. Moreover, using ΔSw limits the applicability of the method to only those cases where time-lapse seismic is available, which underestimates the potential of other seismic-derived attributes that are more reliable and easier to obtain, even from a single seismic survey. Consequently, we only include the change of water saturation in the objective function of a single scenario: the base case we use for comparison purposes.

Our approach to incorporating seismic information into the reservoir parameter estimation problem uses depth-converted P-wave acoustic impedance (Ip). Impedance can be obtained from the inversion of seismic amplitude data and well logs, and can be modeled using rock physics. Many authors have reported a high negative correlation — not to be confused with lack of correlation— between impedance and porosity for different reservoir rocks. In contrast to the inference of seismic-derived change in water saturation, the estimation of impedance does not require multiple seismic surveys. In fact, when working with time-lapse seismic it seems more appropriate to use impedance than water saturation change, because estimates of the latter are by far less reliable than estimates of the former.

In the examples I show in this chapter, we limit ourselves to cases in which only 3D seismic is available. In such cases the impedance information becomes static data, and represents scenarios in which:

1. Only one seismic survey is available, or
2. The elastic properties of reservoir rocks are not sensitive to fluid replacement, so acquiring time-lapse seismic does not add any value.

The latter happens when saturating fluids have similar compressibility, and/or when reservoir rocks are stiff —i.e., well compacted and/or cemented with stiff minerals—. The reservoir simulator we use in this work is more suitable for modeling these scenarios, because it assumes the two saturating fluids are immiscible and have low compressibility, and it is formulated for non-deformable grids —i.e., is not appropriate for modeling compacting, unconsolidated reservoirs. However, if the system is two-phase (oil + water), and compaction does not take place, the formulation we use yields pore pressure and water saturation estimates that are adequate for modeling the properties that control the time-lapse seismic response of the reservoir.

3.2 Reference and Initial Earth Models

Our main interests at this point are to test the integrity of our code implementation, and to evaluate the feasibility of carrying out a characterization project using the joint inversion technique we described in Chapter 2. Our testing scenario is a quarter five-spot pattern with a water injection well on the lower left corner and a producing well on the opposite corner. Before the advent of digital computers, engineers modeled reservoirs as 'layer-cakes', and drilled wells in regular patterns that —they thought— would result in radial or linear flow. Not many in those days would risk taking a stance too far from the assumption of homogeneous porosity and permeability. The quarter five-spot was a popular pattern for analyzing water-flooding problems, because there are analytical soultions for the flow of fluids between the injector well and the producer. Because of its simplicity, the quarter five-spot pattern survived the technological revolution that brought numerical reservoir simulation into play, and is still the model of choice for different types of analyses.

To facilitate the presentation of results we chose a two-dimensional (10x10x1) discrete representation of a square reservoir with 2100 ft. sides. The only parameters that will vary between two subsequent iterations are the heterogeneous fields of porosity and permeability. For all cases presented in this chapter, I assume permeability is isotropic in the horizontal plane. Figure 3.1 shows a plane view of the "true" porosity and permeability fields, as well as a scatter plot of permeability versus porosity in semi-

logarithmic scale. In this chapter I call the plots in Figure 3.1 the *reference plots*, and the corresponding values, the *reference solution*.

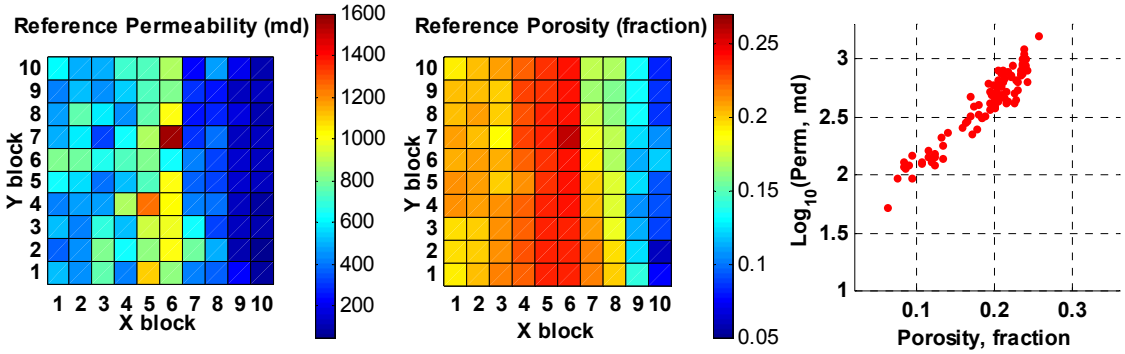

Figure 3.1: From left to right: Reference fields of permeability and porosity, and scatter plot of $\log_{10}$(permeability) versus porosity.

The data follow a trend whose mean can be approximated by:

$$\log(K) = a\phi + b\,, \tag{3.2}$$

If we let a be equal to 6.0, and b be equal to 1.5, the resulting trend is representative of core observations from clean, medium-to-coarse grain, well-consolidated sandstones — e.g., Fontainebleau sandstone, or sandstones of the Une Formation in the Apiay oilfield (Colombia). The volume support of seismic measurements and reservoir simulation models is significantly larger than that of cores, though. Upscaling a trend of porosity and permeability from the core scale to the reservoir model scale would reduce the dispersion of the trend, regardless of the average used to account for scale differences. Consequently, we populated the model with petrophysical properties such that for a given porosity the variation in permeability values is about half a log cycle. Porosity-permeability points are approximately normally distributed around the described regression, with standard deviation equal to 0.1, porosity in the range of [0.06,0.26], and permeability in the range of [50,1575] md. I summarize in Table 3.1 other important variables required to fully characterize the models.

Table 3.1: Variables used in the forward models

Fluid Flow Model	
Reservoir depth, ft	8000
Initial pore pressure, psi	3600 @ 8000 ft.
Oil isothermal compressibility, psi^{-1}	5.6×10^{-6} @ 14.7 psi
Oil density, lb/ft^3	49.1 @ 14.7 psi
Water isothermal compressibility, psi^{-1}	8.0×10^{-6} @ 14.7 psi
Water density, lb/ft^3	64.8 @ 14.7 psi
Connate water saturation S_{wc}	0.1
Residual oil saturation S_{or}	0.2
Oil relative permeability @ S_{wc}	1.0
Water relative permeability @ S_{or}	0.4
Relative permeability exponents (n_{ow}, n_{ow})	1.2
Rock Physics Model	
Mineral bulk modulus, GPa	36.6
Mineral density, kg/m^3	2650

We computed the response of the forward models to these reference fields of petrophysical properties and used the results as if they were measurements of production and seismic parameters. The synthetic data set consists of curves of bottom hole pressure and water-cut versus time for 2000 days of production/injection, and a map of acoustic impedance after 100 days of production. These synthetic observations are used in the same way as real measurements would have been in the objective function.

We purposely chose the initial guess of porosity and permeability to be far of the true values to determine (1) how much influence the initial guess has on final inversion results, and (2) how well-conditioned the problem is. This can be qualitatively evaluated by finding whether or not the initial guess leaves an artifact signature in the results; and by analyzing how well the estimates of porosity and permeability reproduce the reference fields, and the permeability vs. porosity scatter plot. We assume our data and models are noise-free and error-free, so one may hope that the inversion algorithm converges to a solution that, if not perfect, is at least close to the true values shown in Figure 3.1, regardless of the initial guess used.

The initial earth model, shown in Figure 3.2, consists of three horizontal bands, each of them with homogeneous porosity and permeability. The three blue dots in the scatter plot shown in the leftmost panel represent the porosity-permeability pairs for each band. The red dots represent the pairs of porosity and permeability from the reference fields. Notice that the initial earth model is considerably different than the target solution: the pairs of porosity and permeability values for the initial earth model are off the trend of reference data; the initial guess has a higher spatial correlation range than the reference fields; and the azimuth of maximum spatial correlation is perpendicular to that of the target porosity and permeability fields.

Since the model has a square shape and we assume that horizontal permeability is isotropic, the incorrect azimuth of maximum spatial correlation poses a particular challenge for reservoir parameter estimation with production data only, as we will demonstrate. Consider the transposed version of the fields shown in Figure 3.2, i.e., that obtained from a 180° rotation of the porosity and permeability fields along the diagonal that joins blocks (1,10) and (10,1). The simulator would predict the same bottom hole pressures and water cuts from the reference fields, and from the transposed version of them, this latter with the same azimuth of spatial correlation than the reference earth model.

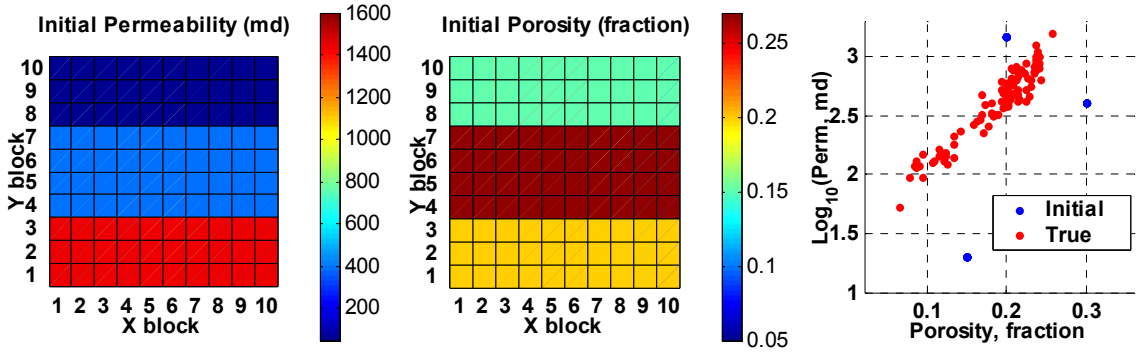

Figure 3.2: From left to right: Initial models of permeability and porosity, and scatter plot of $\log_{10}$(permeability) versus porosity. The red dots represent pairs of porosity and permeability from the reference fields. The blue points, the analogous pairs from the initial models.

We forward-modeled the response of the initial porosity and permeability fields, and compared it to that of the reference earth model. In Figure 3.3 we show production

curves for the initial guess (green) and the reference solution (blue), and the map of the predicted mismatch between the initial model impedance and the reference field impedance. The misfits shown in this plot contain information that can drive the inversion algorithm to better estimates of porosity and permeability.

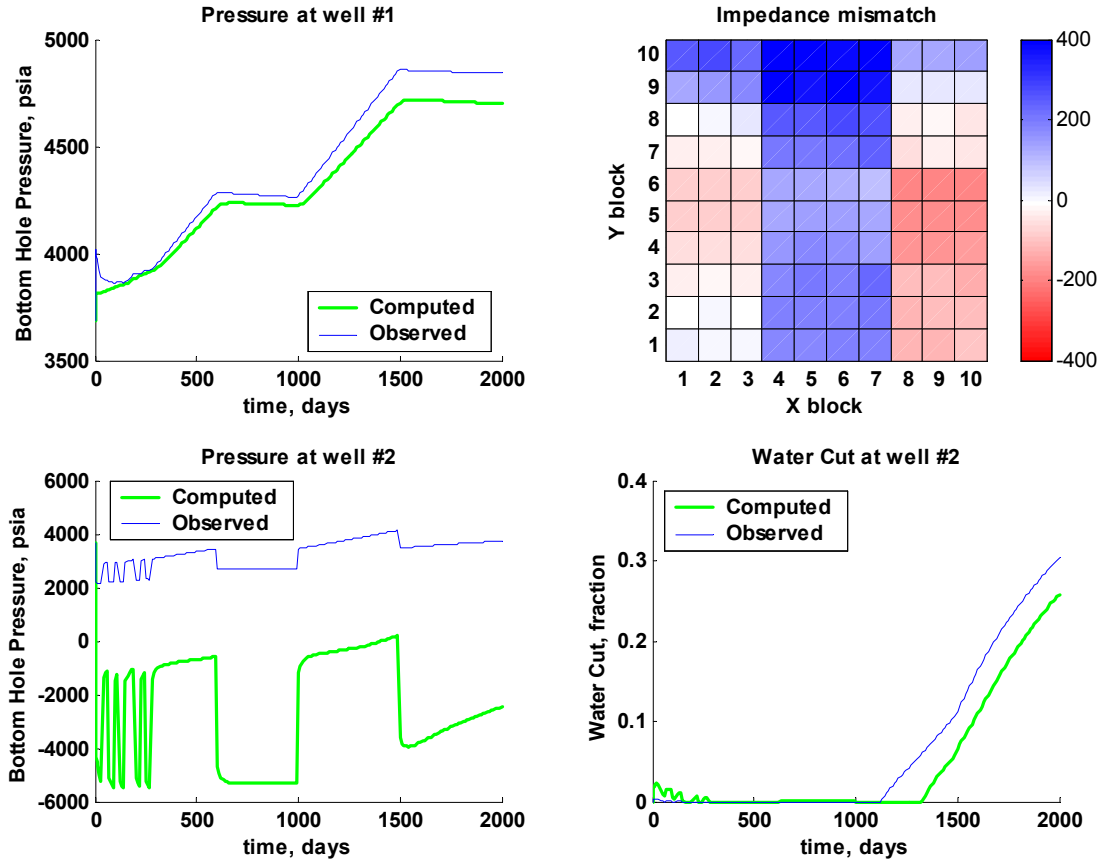

Figure 3.3: Production and seismic responses of the reference and initial models of permeability and porosity.

A word of caution about predicted bottom-hole pressures during the inversion is relevant at this point: When inverting production data one needs to ensure that flow rates are reproduced. This is achieved by fixing the flow rates observed at wells, and letting the simulator predict the history of bottom-hole pressures required to reproduce those flow rates, regardless of their value. Notice that permeability values around the producing well (upper-right corner) in the initial guess are so unrealistically low, that negative well flowing pressures would be required to reproduce most flow rates. This condition would be inadmissible for a final result, but can be tolerated at the start of the

inversion, even though it does not make physical sense. The careful earth scientist is expected to notice this condition and come up with a better initial model before running the inversion, though, because the farther the initial guess is from the solution, the more iterations are required to reach it. Since our interest is precisely on using an unrealistic initial guess to find how well-constrained the problem is, we accept the existence of negative well flowing pressures at the start.

3.3 Base Case: Former Attempts of Parameter Estimation using Data Integration

Our first case involves the inversion of bottom-hole pressure, water cut, and seismic-derived water saturation change to obtain estimates of permeability and porosity. In terms of matching variables, this represents the approach taken in some of the most influential works in reservoir parameter estimation in the recent past [*Landa*, 1997; *Lu*, 2001; *Phan* 1998, 2002]. However, we treat porosity and permeability independently, instead of enforcing a one-to-one relationship between them, as in most of the examples shown in those works. The objective function for this scenario takes the following form:

$$E = \sum_{i=1}^{t_{Pwf}} \sum_{j=1}^{n_{wells}} W_{Pwf} \left(Pwf_{obs}^{t_i,well_j} - Pwf_{calc}^{t_i,well_j} \right)^2 + \sum_{i=1}^{t_{wcut}} \sum_{j=1}^{n_{wells}} W_{wcut} \left(wcut_{obs}^{t_i,well_j} - wcut_{calc}^{t_i,well_j} \right)^2 + \sum_{i=1}^{t_{lp}} \sum_{j=1}^{n_{blocks}} W_{seis} \left(\Delta Sw_{obs}^{t_i,block_j} - \Delta Sw_{calc}^{t_i,block_j} \right)^2 , \quad (3.3)$$

where *Pwf* is the well flowing pressure, *wcut* is the water cut; ΔSw is the seismic-derived estimates of change in water saturation, the superscript *t* represents a given time-step, and the subscripts *obs* and *calc* denote whether the variable is observed or calculated, respectively.

We used the reservoir simulator to generate synthetic data of *Pwf* and *wcut* at all time steps, and ΔSw between 100 and 1800 days of production, as predicted from the reference models of porosity and permeability (Figure 3.1). As noted before, time-lapse seismic data provides valuable information about the patterns of fluid movement through the reservoir, but the state of the art of 4D seismic technology is such that it is not possible to

generate *independent* estimates of water saturation change that are accurate enough for practical parameter estimation purposes. Therefore, we present this case only for comparison purposes. Our initial model of porosity and permeability is the one shown in Figure 3.2. We constrained the feasible region of porosity and permeability using penalty functions, as described in section 2.6.1, with $\phi_{min} = 0.02$, $\phi_{max} = 0.36$, $K_{min} = 10$ md, and $K_{max} = 2000$ md.

The inversion results for this case are summarized in Figure 3.4. To make the comparison of results straightforward, the porosity and permeability color scales in all subsequent Figures are the same as in Figures 3.1 and 3.2. On the top row I present, from left to right, the reference fields of permeability and porosity, and the scatter plot of permeability vs. porosity for the results of inversion (blue dots) and the target solution (red dots). The bottom part shows, from left to right, the inversion estimates of permeability and porosity, and a plot of the logarithm of error versus iteration number. The red dots represent the error as given by equation 3.3. The blue dots represent the penalized error function, i.e., error plus penalty terms for maximum and minimum porosity and permeability.

The outcome represents a significant improvement from the initial model. However, the maps show that not all features are retrieved, and that permeability and porosity are not correctly allocated in some areas. The footprint of the initial earth model is quite significant, particularly in the permeability map. In this case, permeability is closer than porosity to the reference solution, because the data being inverted are more sensitive to permeability than to porosity [*Landa*, 1997; *Phan*, 1998].

An examination of the scatter plot of porosity and permeability reveals that (1) the trend that represents the inversion results is different to the trend of the reference solution, and (2) the variance of permeability estimates at nearly any given porosity is larger than that of the reference solution. The lower right plot shows how the error reduces as inversion progresses. Notice that early in the process there is some separation between the penalized and the penalty-free error curves. As the error reduces the separation progressively decreases, until it finally fades away. This demonstrates that penalty terms are not acting as a source of artificial error, and that incorporating them in the formulation is equivalent to solving the unconstrained problem. Once the curve flattens out, the estimates do not change significantly, so one can state that the algorithm

reached a minimum after 50 iterations. Errors in this plot are not normalized, so the absolute value is meaningless because it depends on the magnitude of weighting factors.

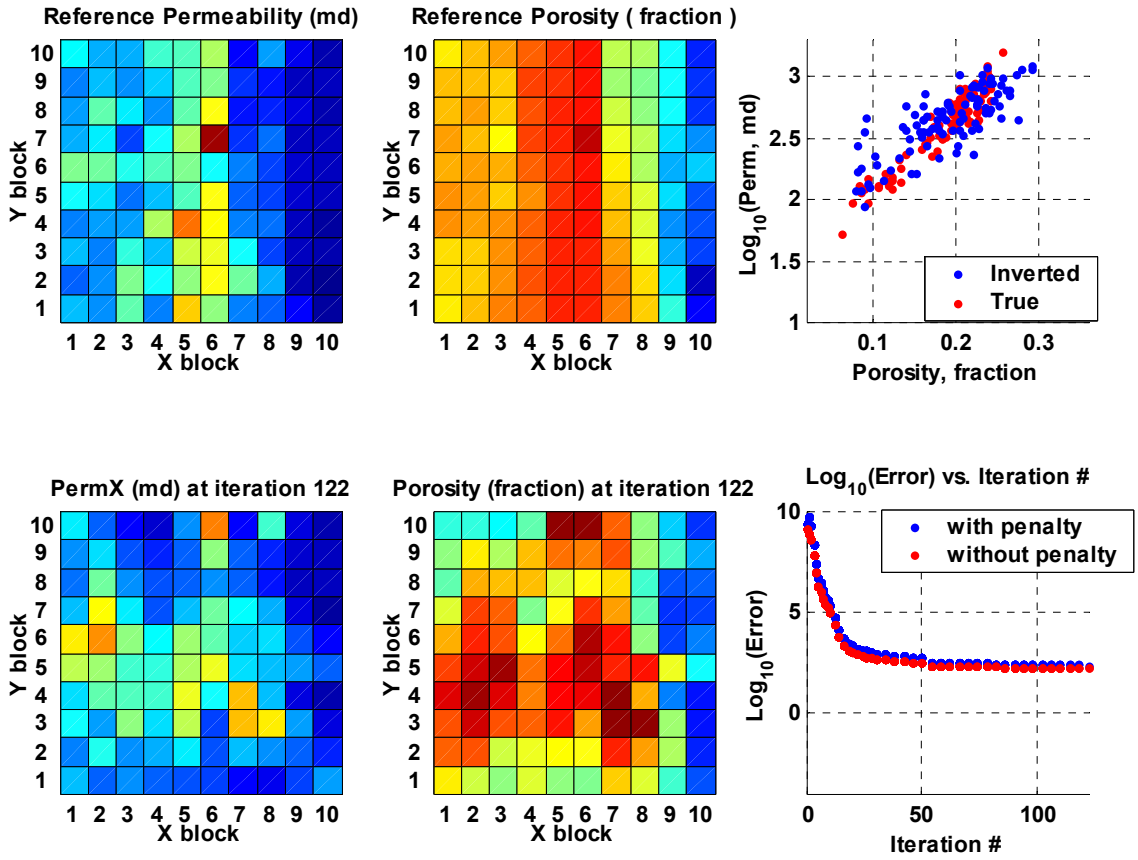

Figure 3.4: Inversion of bottom hole pressure, water cut, and change in water saturation to estimate permeability and porosity. In the top row, from left to right: Reference fields and scatter plot of $\log_{10}$(permeability) versus porosity. The red dots represent pairs of porosity and permeability from the reference fields. The blue dots, the analogous pairs from inversion results after 122 iterations. The resulting fields are in the bottom row along with a plot of error vs. iteration number.

The proof that the algorithm indeed reached a minimum depends on whether the data have been reproduced, and is given in Figure 3.5. The estimated porosity and permeability fields result in values of P_{wf}, *wcut*, and ΔSw that are a nearly perfect match to the synthetic data. Since inverted results are significantly different from the reference solution, this indicates that the inversion has converged to a local minimum.

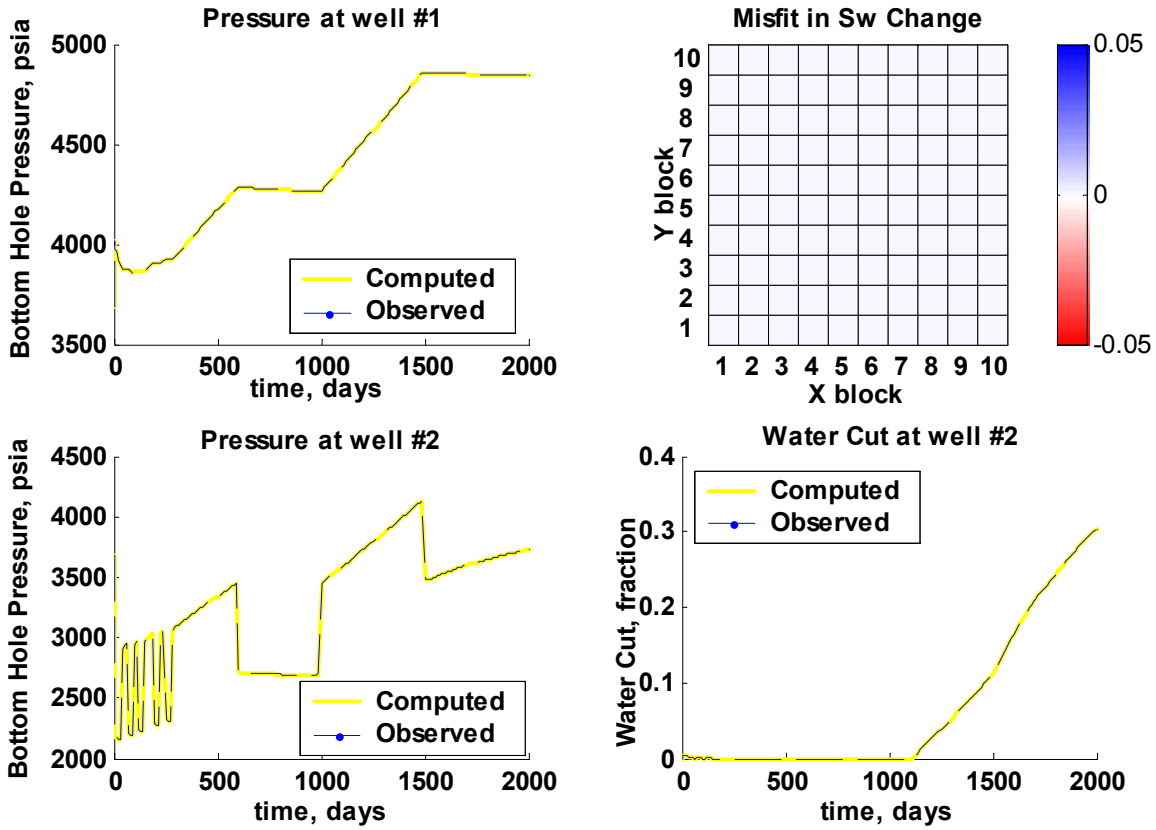

Figure 3.5: Match of observations for the inversion of bottom hole pressure, water cut, and change in water saturation to estimate permeability and porosity. Well #1 is the injection well.

3.4 Inversion of Production Data and Acoustic Impedance

In this example we invert for porosity and permeability from bottom-hole pressure, water cut and acoustic impedance. We postulate that P-wave acoustic impedance is a more reliable seismic attribute than water saturation change. As noted before, impedance is a physical property of the porous medium; it can be inverted from seismic amplitude and well logs; and it generally has a strong dependence on porosity, because impedance is the result of multiplying two porosity-dependent attributes: velocity and bulk-density. The objective function we used for simultaneously inverting production data and acoustic impedance is given by:

$$E = \sum_{i=1}^{t_{Pwf}} \sum_{j=1}^{n_{wells}} W_{Pwf} \left(Pwf_{obs}^{t_i, well_j} - Pwf_{calc}^{t_i, well_j} \right)^2 + \sum_{i=1}^{t_{wcut}} \sum_{j=1}^{n_{wells}} W_{wcut} \left(wcut_{obs}^{t_i, well_j} - wcut_{calc}^{t_i, well_j} \right)^2 + \sum_{i=1}^{t_{Ip}} \sum_{j=1}^{n_{blocks}} W_{seis} \left(Ip_{obs}^{t_i, block_j} - Ip_{calc}^{t_i, block_j} \right)^2 \quad . \quad (3.4)$$

The simplest seismic model one can take is that of a stiff reservoir rock with relatively homogeneous mineral composition, so that fluid changes have a negligible effect on impedance, and the relationship between seismic impedance and porosity becomes approximately linear regardless of saturation changes. We assume that available impedance information has been derived from a single 3D seismic survey, so the outer sum in the impedance term of equation 3.4 is not required. We use the same approach to constrain the feasible region as in the previous case.

Starting from the same initial models of porosity and permeability (Figure 3.2), the algorithm delivers the results we show in Figure 3.6, in the same template we used for the base case. In this case the match of porosity is nearly perfect. Since impedance is not directly influenced by permeability —and consequently there is less permeability information than in the base case— it is not surprising that permeability predictions are not as good as those of porosity. In general, the estimates of permeability are quite reasonable in the vicinity of wells, because permeability values in those areas are the ones that most influence production data. Permeability results still show quite a bit of influence from the initial guess of permeability. The porosity-permeability scatter plot shows that, as in the base case, inversion results deviate from the reference trend and have, in general, larger variance for a given porosity, with more outliers in this case.

The plot of error vs. iteration number shows that the algorithm reached a minimum after 43 iterations. As in the previous case, penalty terms become negligible at the minimum. Figure 3.7 shows that in this case also, the synthetic data are properly fitted by the bottom-hole pressures, water-cut, and impedance computed from the inverted porosity and permeability. Since the permeability field is far from the reference solution, the minimum reached is a local minimum.

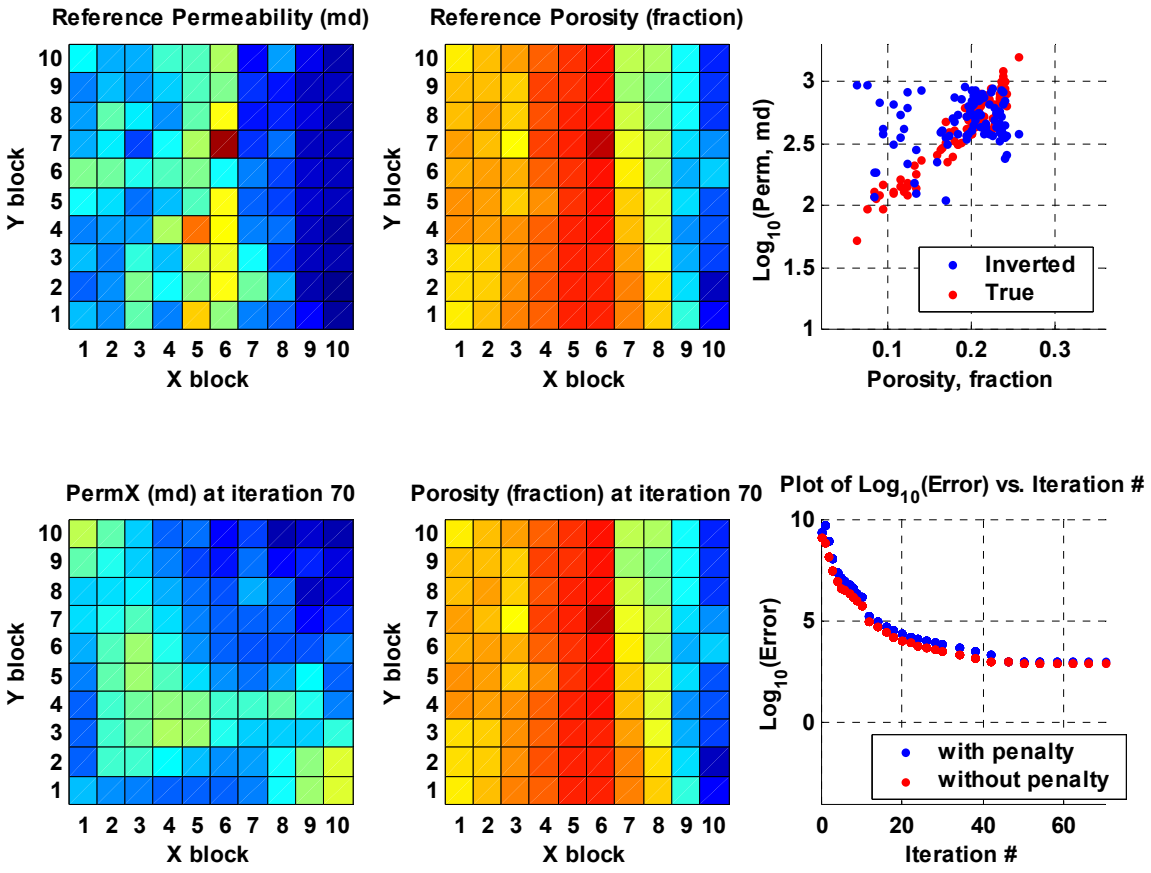

Figure 3.6: Inversion of bottom hole pressure, water cut, and acoustic impedance to estimate permeability and porosity. In the top row, from left to right: Reference fields and scatter plot of $\log_{10}$(permeability) versus porosity. The red dots represent pairs of porosity and permeability from the reference fields. The blue dots are the analogous pairs from inversion results after 70 iterations. The resulting fields are in the bottom row along with a plot of error vs. iteration number.

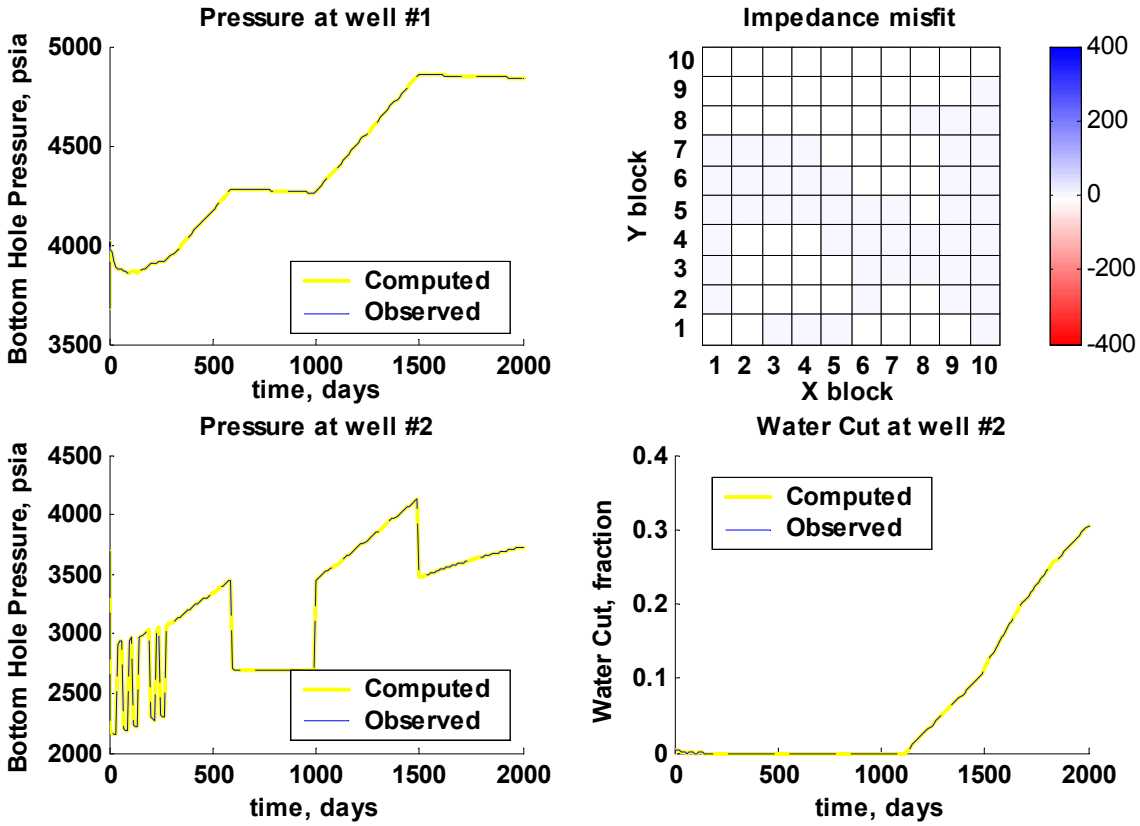

Figure 3.7: Match of observations for the inversion of bottom hole pressure, water cut, and acoustic impedance to estimate permeability and porosity. Well #1 is the injection well.

3.5 Inversion of Production Data and Acoustic Impedance with Porosity-dependent Permeability Bounds

In the previous examples I showed that, even though the inverted porosity and permeability fields resulted in excellent matches to the 'observed' data:

1. Inversion results separate from the trend of the reference solution
2. Permeability estimates for a given porosity are, in general, spread over a larger area than those of the reference solution.

The approach we have used so far to limit the feasible region consists of using maximum and minimum limits that effectively prevent the porosity and permeability estimates from going out of bounds. However, such approach fails to provide a link between porosity and permeability, and implies that any point within the limits has essentially the same

probability. As a consequence, a significant number of points in the set of inversion estimates ended up far from the trend of the reference solution.

Clearly, one can further limit the feasible region in a more effective way. Core observations can provide useful insight into better limits. Many rocks —e.g., those shown in Figure 2.3— exhibit porosity-permeability trends that can be limited by a pair of porosity-dependent, not necessarily linear, permeability bounds. The reference data set is based on core measurements from clean, well-consolidated sandstones, and shows a trend that can be limited by the following relationships:

$$Log_{10}(K_l) = 6.0\phi + 1.15 \text{ , and} \tag{3.5}$$

$$Log_{10}(K_u) = 6.0\phi + 1.85 . \tag{3.6}$$

with K_l representing the lower bound for the trend, and K_u the upper bound. We designed a penalty surface that grows away from the bounds, but is zero between them. I provide details about the implementation of this penalty term in section 2.7.1 of this dissertation. Figure 3.8 shows a plan view and a three-dimensional representation of the penalty surface, along with the reference data, and the bounds given by equations 3.5 and 3.6.

We added the aforementioned penalty term to the objective function and performed a new inversion of bottom-hole pressure, water cut and acoustic impedance for porosity and permeability. The results of this inversion are shown in Figure 3.9. While the results for porosity are similar to those of the previous case, there is a significant improvement in the permeability estimates. The error surface prevents the algorithm from converging into unreasonable values, but leaves a significant number of points aligned along the porosity-dependent bounds. Figure 3.10 shows the mean and variance of permeability estimates for 10 bins of porosity, along with those for the reference solution. The variance of permeability estimates is significantly smaller than in the former examples, and close to that of the reference solution; but the mean follows a different trend, indicating permeability is over-predicted at some porosities, and under-predicted at others.

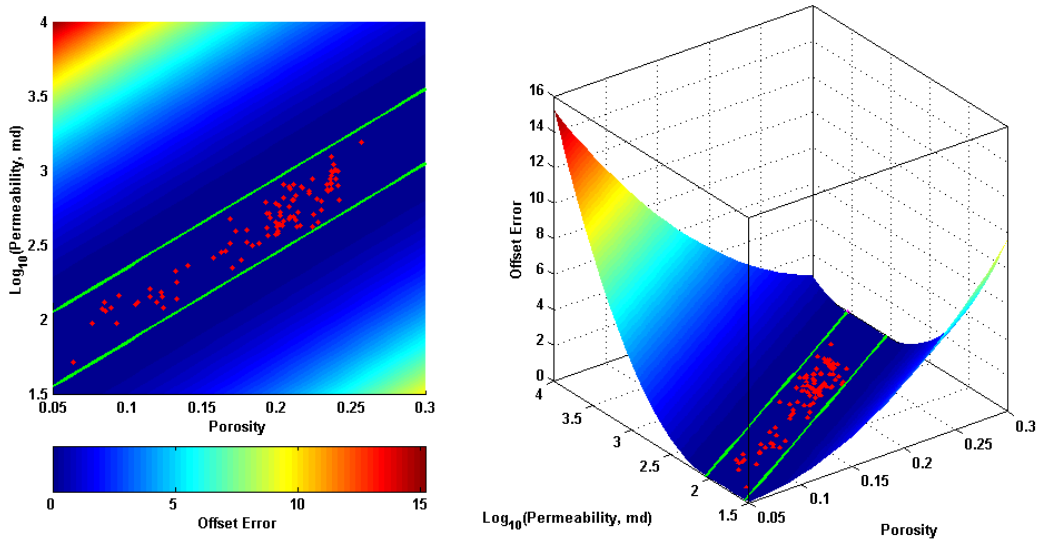

Figure 3.8: Two-dimensional and three-dimensional representations of an error surface that penalizes the offset from a set of bounds (green lines), designed from *a-priori* porosity and permeability data, along the data (red dots).

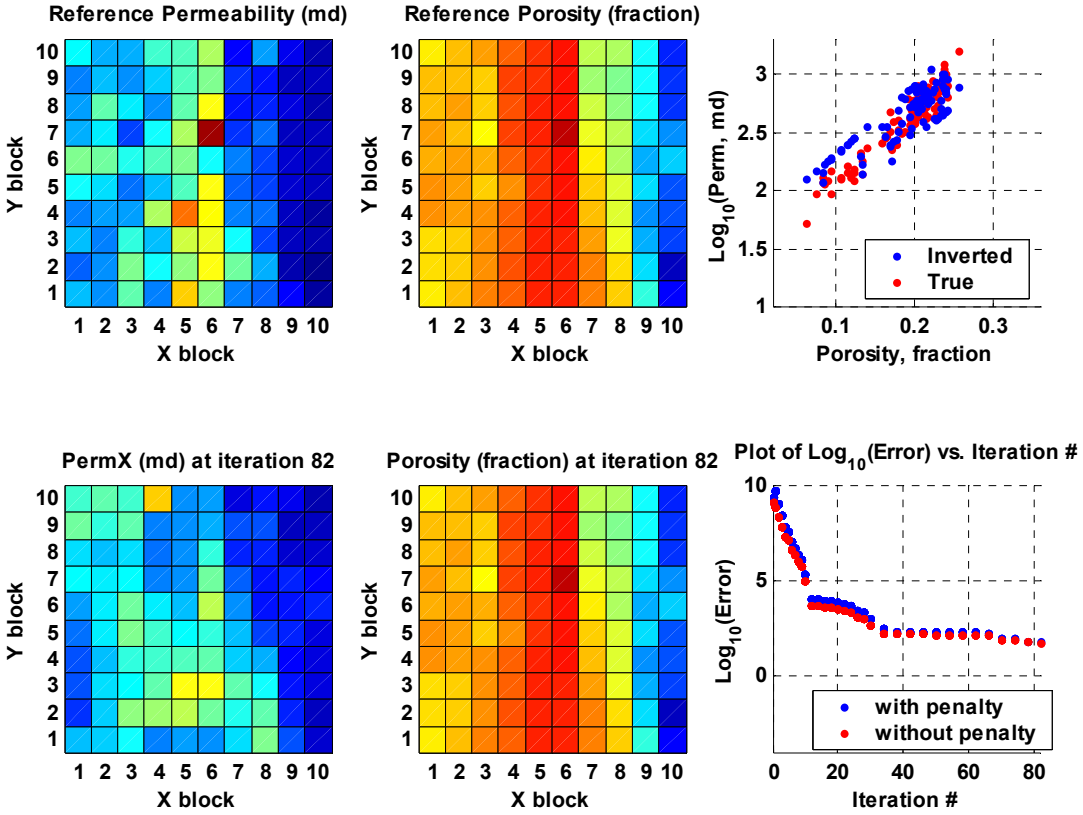

Figure 3.9: Inversion of bottom-hole pressure, water-cut, and acoustic impedance to estimate permeability and porosity, using porosity-dependent permeability bounds. In the top row, from left to right: Reference fields and scatter plot of $\log_{10}$(permeability) versus porosity. The red dots represent pairs of porosity and permeability from the reference fields. The blue dots are the analogous pairs from inversion results after 82 iterations. The resulting fields are in the bottom row along with a plot of error vs. iteration number.

Bivariate histograms provide an integrated view of the distribution of parameters within the region under examination. In Figure 3.11 we show bivariate histograms of porosity and permeability for both the inversion results and the reference dataset. The bottom plots are the corresponding three-dimensional representations of the bivariate histograms, which we aligned along the approximate direction of the porosity-permeability trend. The histograms show that the reference solution and the inversion results are distributed in considerably different ways. In some cases, the points that lie to the right and left of the trend reach frequencies as high as the mode of the population.

It is important to recall that our initial guess was purposely chosen to be out of the porosity-dependent bounds. This explains why the inversion results have a large number of points lying right on the limits of the feasible region. If we use a better initial model, the error surface guarantees that the solution is not going off-bounds, and the inversion is more likely to reach the global minimum.

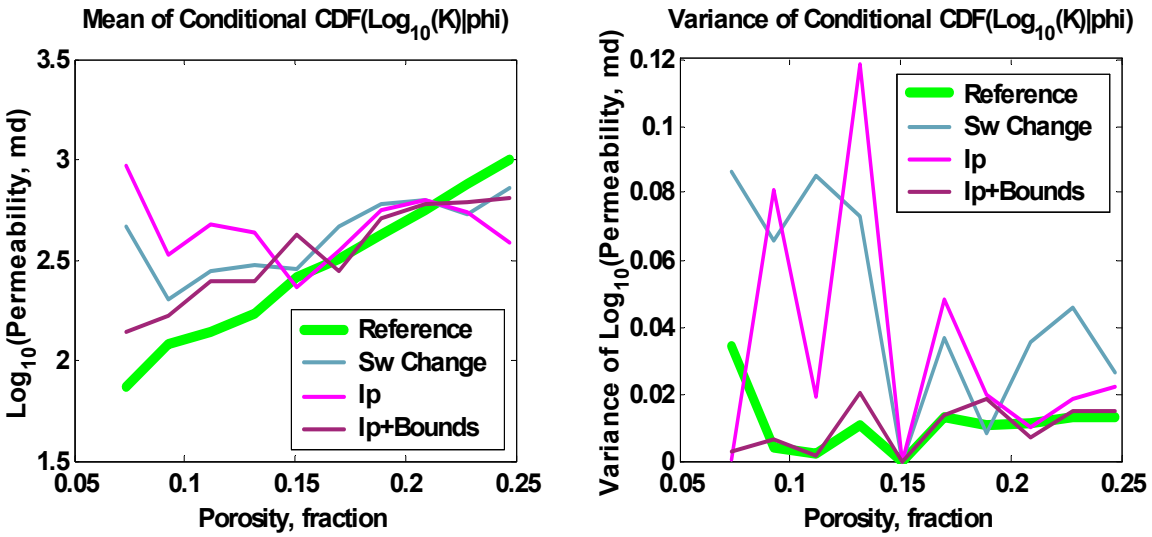

Figure 3.10: Conditional mean and variance of the logarithm of permeability estimates for 10 porosity bins. The data represent the reference solution and the three cases of inversion presented so far.

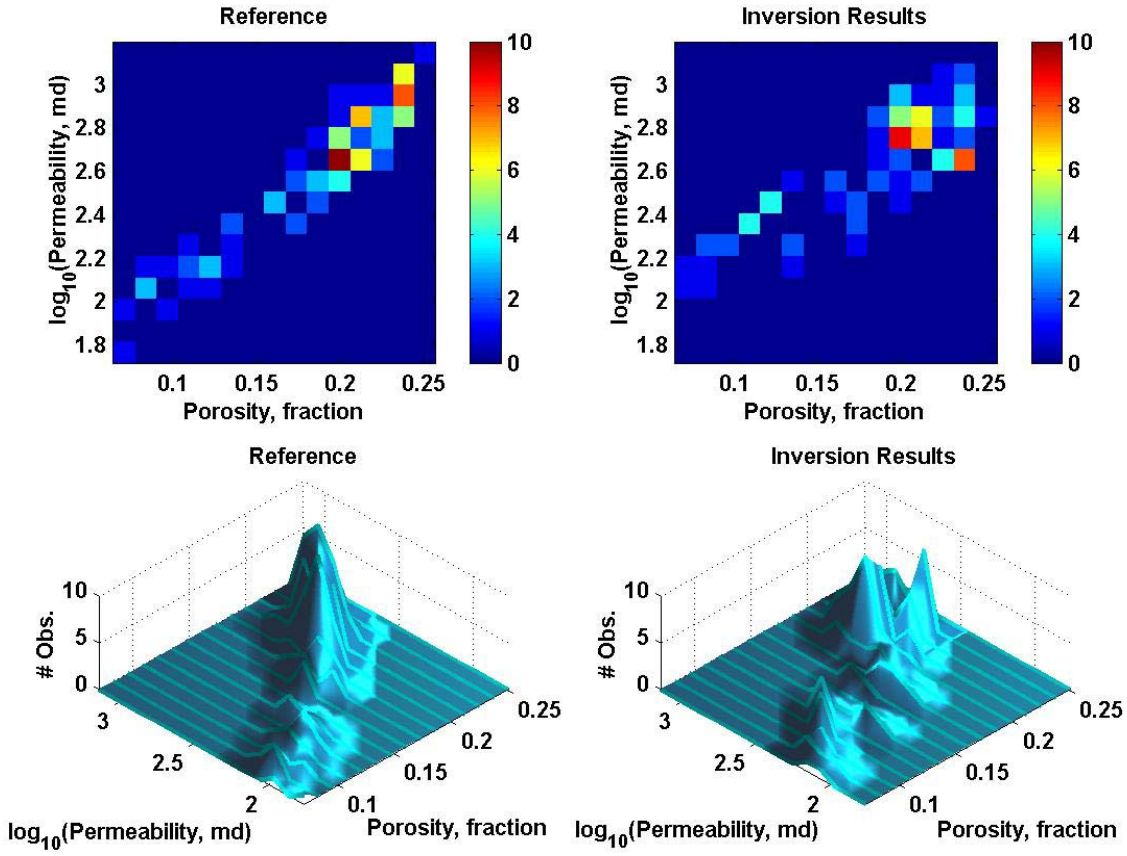

Figure 3.11: Bivariate histograms for the reference data set, and the results of inverting bottom hole pressure, water cut, and acoustic impedance to estimate permeability and porosity, using porosity-dependent bounds for permeability.

3.6 Inversion of Production Data and Acoustic Impedance with *a-priori* information

Core data can provide useful information about the conditional distribution of permeability for a given porosity. If core data are available, we can generate an *a-priori* bivariate histogram of porosity and permeability, from which we can obtain —after smoothing to account for upscaling effects— target conditional cumulative distribution functions (CCDF) for each porosity bin, of the form:

$$CCDF^{m}\left(k; K_i \mid \phi_i\right) = Prob\left\{K_i \le k \;\middle|\; \phi_i \in \left[\phi_m, \phi_{m+1}\right)\right\}, \tag{3.7}$$

where *m* represents a porosity bin with range $[\phi_m, \phi_{m+1})$. Those CCDFs can be integrated as *a-priori* information into the parameter estimation problem, using the approach I describe in section 2.7.2 of this thesis. In such case, the objective function takes the following form:

$$E = \sum_{i=1}^{t_{Pwf}} \sum_{j=1}^{n_{wells}} W_{Pwf} \left(Pwf_{obs}^{t_i, well_j} - Pwf_{calc}^{t_i, well_j} \right)^2 + \sum_{i=1}^{t_{wcut}} \sum_{j=1}^{n_{wells}} W_{wcut} \left(wcut_{obs}^{t_i, well_j} - wcut_{calc}^{t_i, well_j} \right)^2 + \sum_{i=1}^{t_{Ip}} \sum_{j=1}^{n_{blocks}} W_{seis} \left(Ip_{obs}^{t_i, block_j} - Ip_{calc}^{t_i, block_j} \right)^2 + \sum_{i=1}^{n_{bins}} \sum_{j=1}^{n_{samples_i}} W_{CCDF} \left(K_{a-priori\ CCDF}^{bin_i, sample_j} - K_{inversion\ CCDF}^{bin_i, sample_j} \right)^2 \quad . \quad (3.8)$$

We assume in this example that we know the target CCDFs of the reference solution. Figure 3.12 shows the porosity histogram, and the CCDFs for the reference porosity and permeability fields. We attempt a CCDF match only for those bins with enough available data points, which excludes bins #1 and #5. An alternative to fill those gaps would be to define a parametric CCDF for those bins.

The results of inverting bottom-hole pressure, water cut and acoustic impedance for porosity and permeability, with equation 3.8 as the objective function, are shown in Figure 3.13. Notice the improvements in the estimated permeability field, and the closer match between the trends of the reference solution and inverted results in the porosity-permeability scatter plot. Figure 3.14 shows the bivariate histograms for the reference fields and the inversion results. After integrating the CCDF term, the trend in the porosity vs. log-of-permeability bivariate histograms is retrieved much more closely matched. Incorporating *a-priori* permeability information in the parameter estimation problem results in the proper distribution of porosity and permeability estimates within the feasible region.

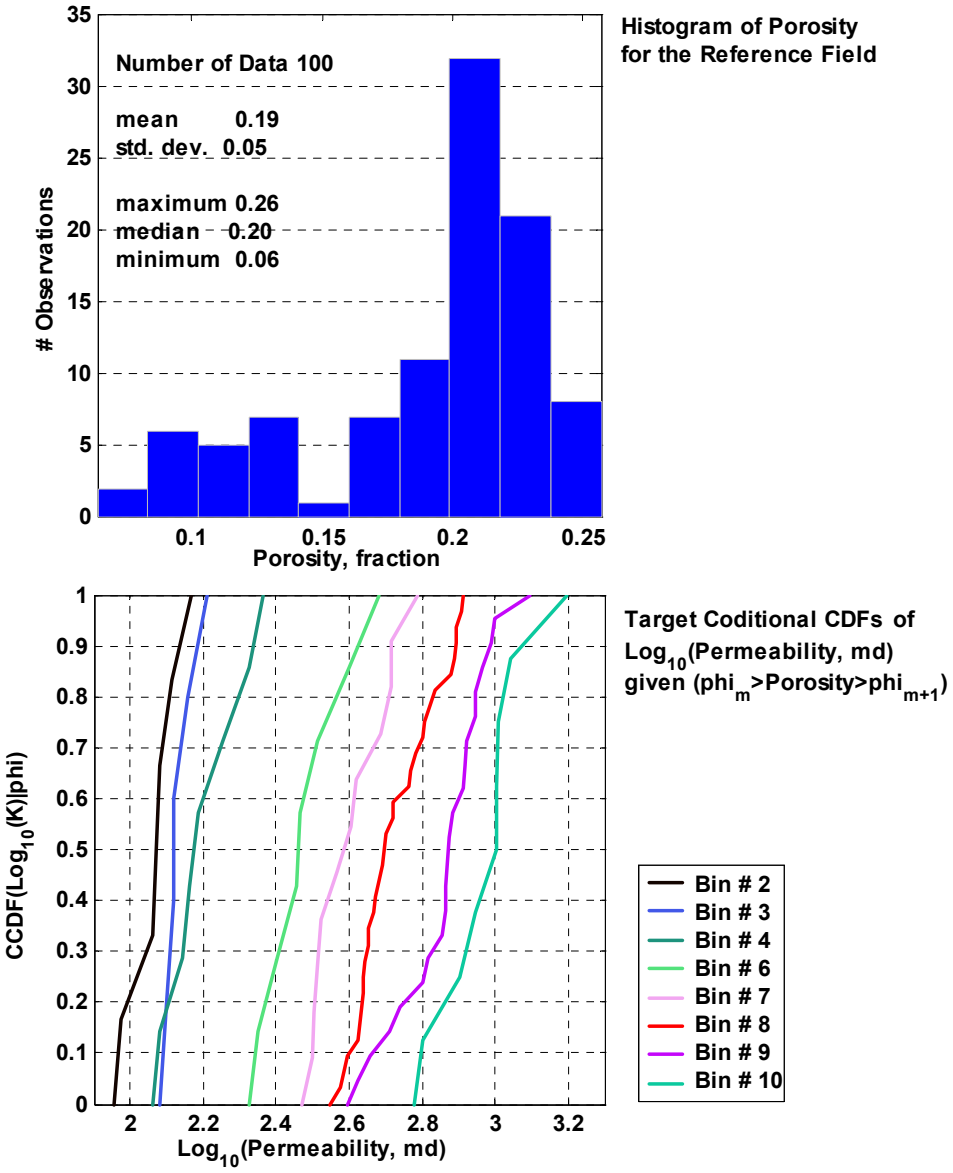

Figure 3.12: Porosity histogram (top), and plot of conditional cumulative distribution functions of log-of-permeability given $\phi_m > \phi \geq \phi_{m+1}$ (bottom) for the reference data set.

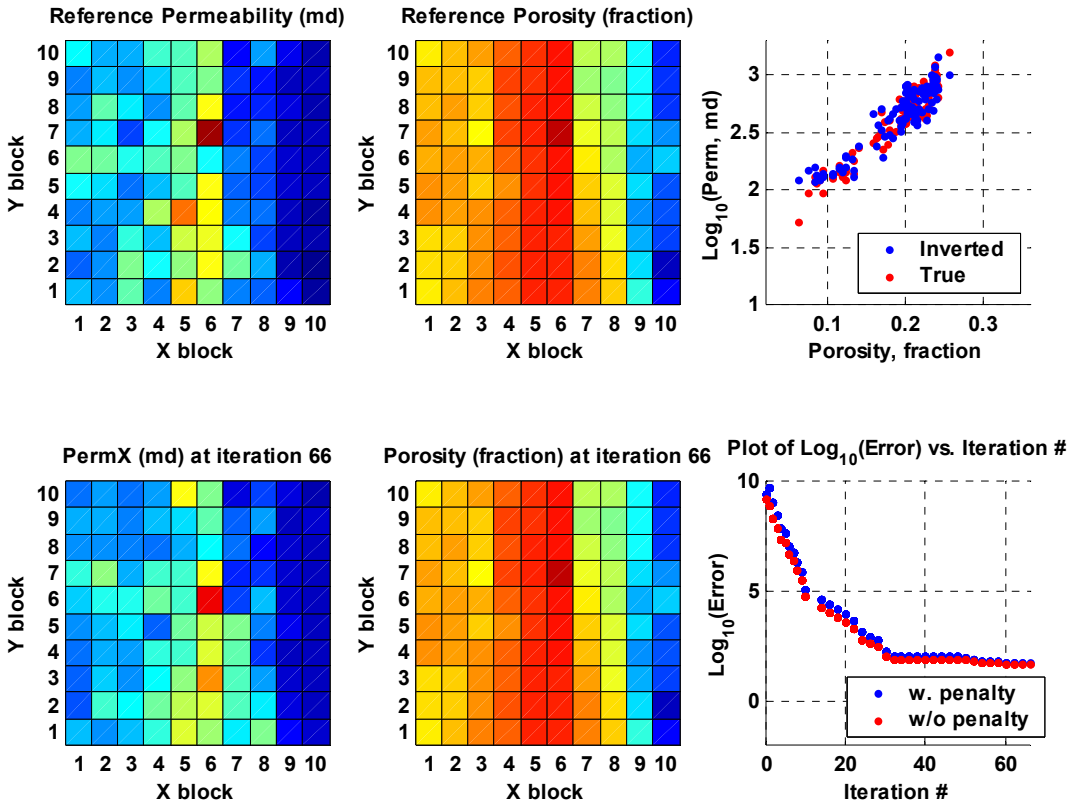

Figure 3.13: Inversion of bottom hole pressure, water cut, acoustic impedance and target CCDFs to estimate permeability and porosity. In the top row, from left to right: Reference fields and scatter plot of $\log_{10}$(permeability) versus porosity. The red dots represent pairs of porosity and permeability from the reference fields. The blue dots are the analogous pairs from inversion results after 82 iterations. The resulting fields are in the bottom row along with a plot of error vs. iteration number.

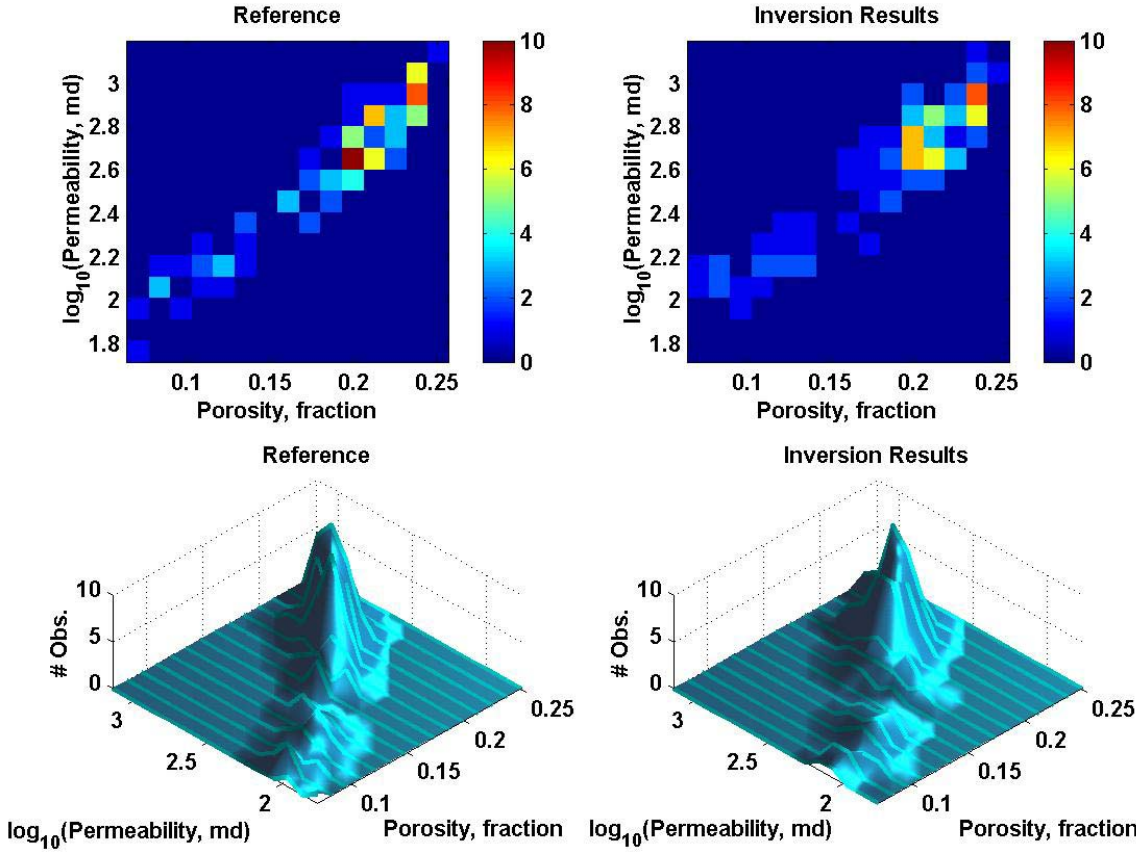

Figure 3.14: Bivariate histograms for the reference data set, and the results of inverting bottom hole pressure, water cut, acoustic impedance and target CCDFs to estimate permeability and porosity, using porosity-dependent bounds for permeability.

3.7 Inversion of Production Data and Acoustic Impedance with a fixed Porosity-Permeability relationship

Our next example involves a case of inversion for porosity only, from bottom-hole pressure, water cut and acoustic impedance, using a fixed porosity-permeability relationship. Since this relationship is unique, there is no need to use the porosity-dependent bounds or the CCDF matching approach described before. We present the results in Figure 3.15. This yields a result of permeability that is correlated with porosity, which is an acceptable solution in a scenario of small dispersion in the porosity-permeability trend. Convergence is significantly faster than in the previous cases, because in this one the problem has half the number of parameters; and all observed

variables are providing information about a single type of parameter, i.e., the sensitivity of a matching variable to permeability is translated into sensitivity to porosity via the unique relationship between the two. However, if the real trend is not well-conditioned and the dispersion around the linear trend is larger —as is generally the case— an average result obtained in this way will not be appropriate. Therefore, this formulation should be used with care.

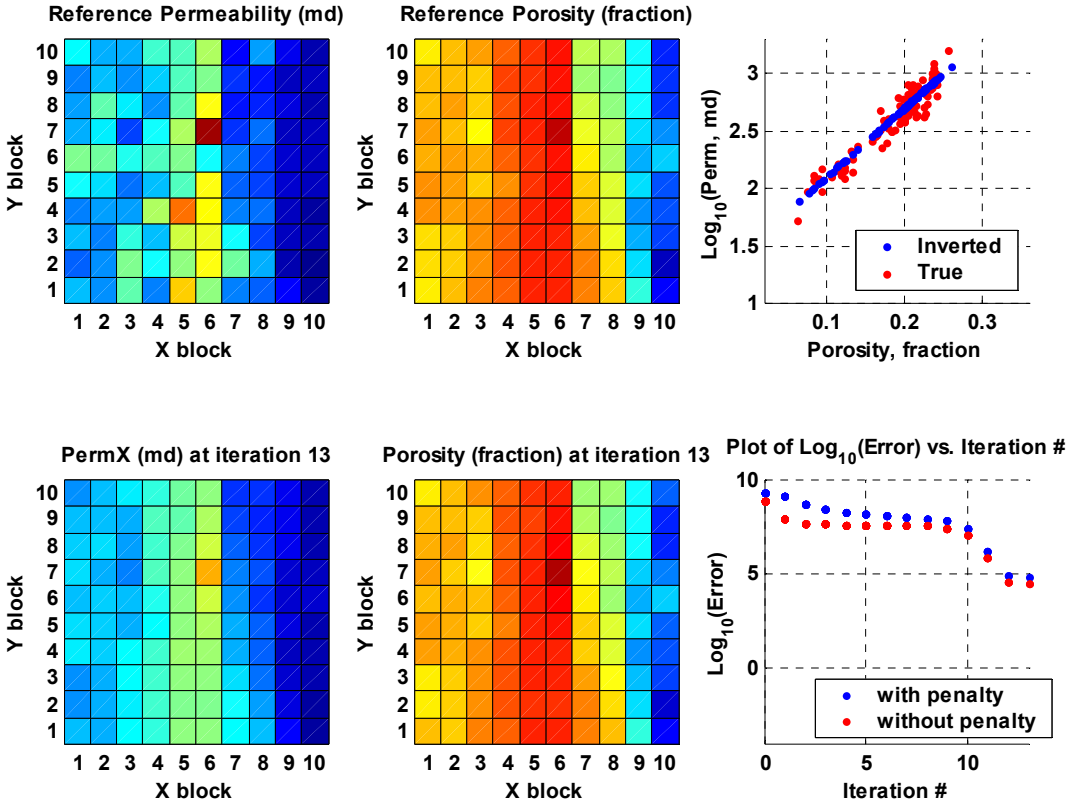

Figure 3.15: Inversion of bottom hole pressure, water cut, and acoustic impedance to estimate porosity, using a linear relationship between porosity and log of permeability. In the top row, from left to right: Reference fields and scatter plot of $\log_{10}$(permeability) versus porosity. The red dots represent pairs of porosity and permeability from the reference fields. The blue dots are the analogous pairs from inversion results after 13 iterations. The resulting fields are in the bottom row along with a plot of error vs. iteration number.

Clearly, because of its extensive areal coverage acoustic impedance is the variable that has the largest information content under the assumptions we made. This is demonstrated by the accurate estimation we made of the porosity field. Since each block's acoustic impedance depends only on the porosity of the block, the impedance

information 'whitens' the Hessian matrix, improving its conditioning number and making it easier to invert.

Excessive whitening may not be beneficial for convergence, though, as we illustrate in Figure 3.16. In this case we used the same combination of variables as in the example shown in Figure 3.15, but this time we gave a weight to impedance that is one order of magnitude larger than in the previous case. Notice that, although we obtained essentially the same results, the inversion takes 19 iterations to reach a minimum, nearly 50% more than in the previous case. For a large reservoir model, this increase in computational time may be unaffordable. This illustrates the importance of assigning proper weights to the variables being inverted.

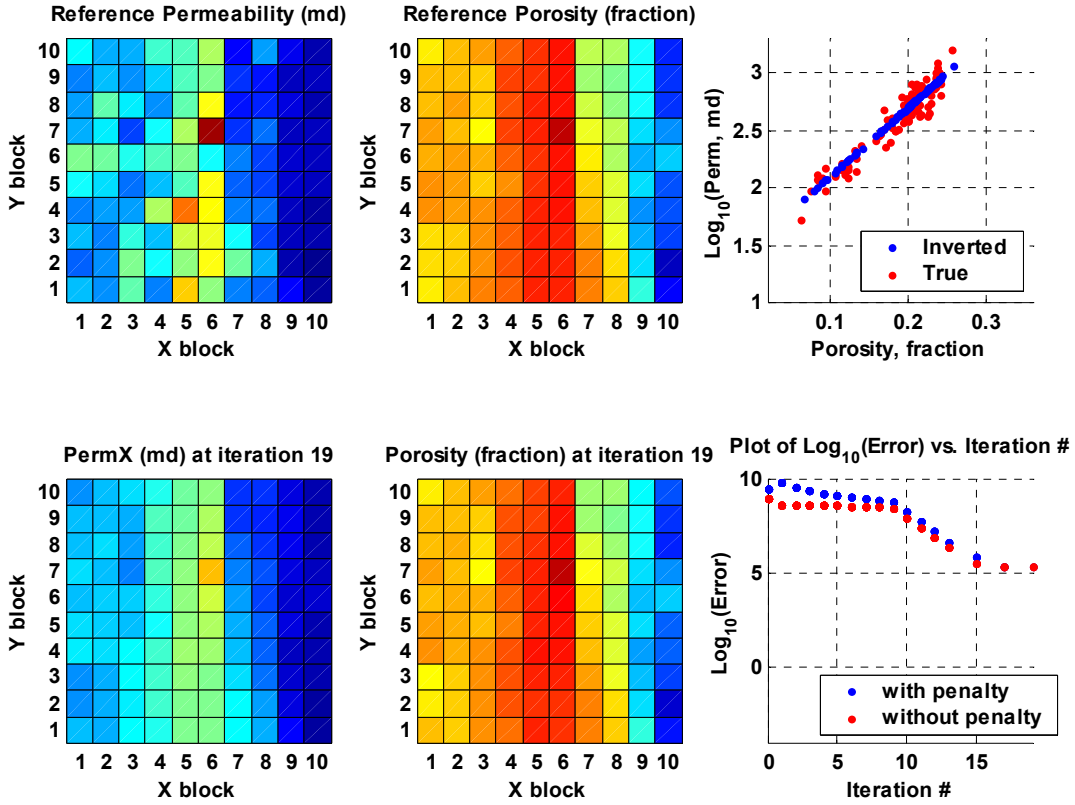

Figure 3.16: Inversion of bottom hole pressure, water cut, and acoustic impedance to estimate porosity, using a linear relationship between porosity and log of permeability. The weight given to impedance data in this case is 10 times larger than in the previous case. In the top row, from left to right: Reference fields and scatter plot of $\log_{10}$(permeability) versus porosity. The red dots represent pairs of porosity and permeability from the reference fields. The blue dots are the analogous pairs from inversion results after 19 iterations. The resulting fields are in the bottom row along with a plot of error vs. iteration number.

3.8 Conclusions

We demonstrated that it is feasible to simultaneously invert core, seismic and production data to estimate petrophysical properties.

Our methodology takes advantage of different sources of information, which helps to constrain the solution in a very effective way, avoiding unfeasible local minima.

Our examples demonstrate that seismic-derived impedance can play an important role in the estimation of petrophysical properties because it provides valuable information about the porosity field. Impedance can be independently estimated from a single 3D survey, which makes it a convenient and adequate attribute for parameter estimation purposes.

The algorithm we presented can be easily extended to include information from time-lapse seismic surveys, to model cases in which the elastic behavior of reservoir rocks is sensitive to changes in saturation, pressure, and/or temperature.

The match of conditional CDFs in our inversion scheme does not require that cumulative distribution functions follow any parametric form. This can be very useful when matching multi-modal populations, e.g., when multiple facies or rocks of different quality coexist in the same reservoir.

3.9 References

Landa, J. L., 1997, *Reservoir Parameter Estimation Constrained to Pressure Transients, Performance History and Distributed Saturation Data*, Ph.D. dissertation, Stanford University.

Lu, P., 2001, *Reservoir Parameter Estimation Using Wavelet Analysis*, Ph.D. dissertation, Stanford University.

Phan, V, 1998, *Inferring Depth-Dependent Reservoir Properties from Integrated Analysis Using Dynamic Data*, M.S. dissertation, Stanford University.

Phan, V., 2002, *Modeling Techniques for Generating Fluvial Reservoir Descriptions Conditioned to Static and Dynamic Data*, Ph.D. dissertation, Stanford University.

Chapter 4

Geological Setting and Stress Field in the Apiay-Guatiquía Area, Llanos Basin (Colombia)

The geological setting in which a certain data set is acquired provides important constraints for most geophysical and engineering analyses. For instance, paleocurrent information and stratigraphic correlations can help infer the direction of maximum continuity, and the range of spatial correlation, respectively, which are crucial parameters in the practice of geostatistics; provenance analyses and petrographic data give an idea of what minerals can be expected in the framework of reservoir rocks, which is useful information for estimating the elastic properties of rocks; knowledge about the magnitude and orientation of the components of the stress tensor in hydrocarbon reservoirs is important in the study of problems like borehole stability, sand production, hydraulic fracturing, hydrocarbon migration, and well design (e.g., *Addis et al.* [1996]; *Last et al.* [1996, 1997]; *Zoback and Peska* [1995]). Moreover, knowing the stress field is critical to computing the level of effective stress that a reservoir is subject to. Since the elastic properties of rocks depend on effective stress (e.g., *Han* [1986]), this is an important parameter to analyze when conducting a rock physics study.

In this chapter I introduce the set of data from the K2 Unit reservoir of the Apiay-Guatiquía oil field in Colombia. First I discuss the geological setting of the Apiay-Guatiquía field, with an emphasis on the regional tectonics and sedimentology considerations, which impose restrictions on the studies of stress distribution and rock physics that we performed on the K2 Unit reservoir. Next, I illustrate how we constrained the magnitude and orientation of principal stresses in the study area, by using the faulting theory proposed by *Anderson* [1937], and the model by *Peska and Zoback* [1995] for computing the distribution of stresses around an arbitrarily inclined borehole. We support our analysis with data from resistivity images, density logs, and leak-off tests.

The Cretaceous K2 Unit, a massive, laterally continuous body of medium to coarse grain sized, locally conglomeratic, white sandstones with a few streaks of laminated, gray shale, deposited in an environment of stacked, braided stream channels.

We found that the direction of maximum horizontal compression is N85E. The data suggest that the most likely faulting environment for the area is a normal faulting regime. These characteristics contrast with the highly compressive, strike-slip faulting regime and the SE-NW azimuth of the maximum horizontal stress observed in the Eastern Cordillera foothills, where most of the formations in the Llanos basin are sub-aereally exposed.

4.1 The Llanos Basin: Evolution and Stratigraphy

The Colombian Andes are made of three Cordilleras (Western, Central and Eastern) formed by alternating compressive and extensive regimes. Figure 4.1 depicts, from west to east, six tectonic regions that can be identified according to their stress regimes: a forearc region along the Pacific Ocean between the trench and the flanks of the volcanoes; a volcanic region whose activity is generated by frictional heating along the subduction zone between the descending lithosphere and the overlying continent; the altiplano region characterized by an extensional strain field; the cordillera and the foothill regions, which have a compressive stress regime that causes a shortening that is accommodated in the foothills by large thrust and strike-slip faults. The easternmost region comprises the Llanos foreland basin, and is tectonically passive and largely undeformed because of the stress release of the thrust faults in the foothills [*Charlez et al.*, 1998]. Structural activity has seemed nearly non-existent far from the mountain front in the Llanos Basin, which has been the major deterrent to oil exploration and exploratory drilling [*McCollough*, 1987].

The Llanos Basin of Colombia belongs to the long chain of foreland basins that lie east of the Andes from Argentina to Venezuela. The basin covers an area of 196,000 km^2 of savanna and is part of the catchment area of the Orinoco River, extending into the so-called Barinas Basin in Venezuela (figure 4.2). The Apiay-Guatiquía Field is located in the southwestern part of the Llanos Basin, close to the city Villavicencio, about 50 km East of the Eastern Cordillera foothills (figure 4.3). The discovery of this field by

Ecopetrol in 1981 led to the subsequent finding of other oil fields in the Apiay-Ariari sub-basin, an area that has 270 MMBO of estimated recoverable reserves.

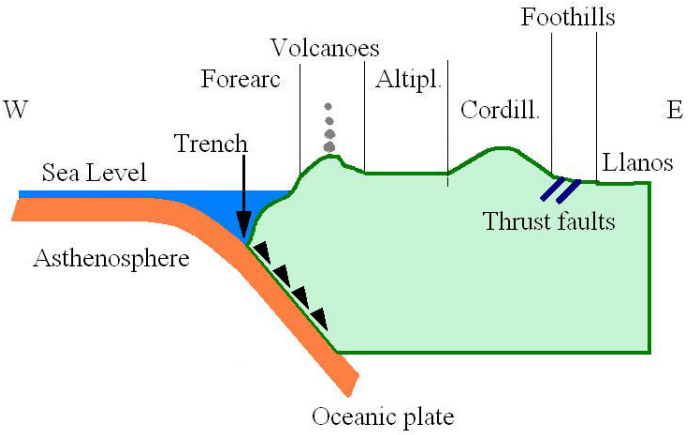

Figure 4.1: Stress regimes across the Andean Cordillera, adapted from Wdowinski and O'Connell, 1991 (adapted from *Charlez, et al.* [1998]).

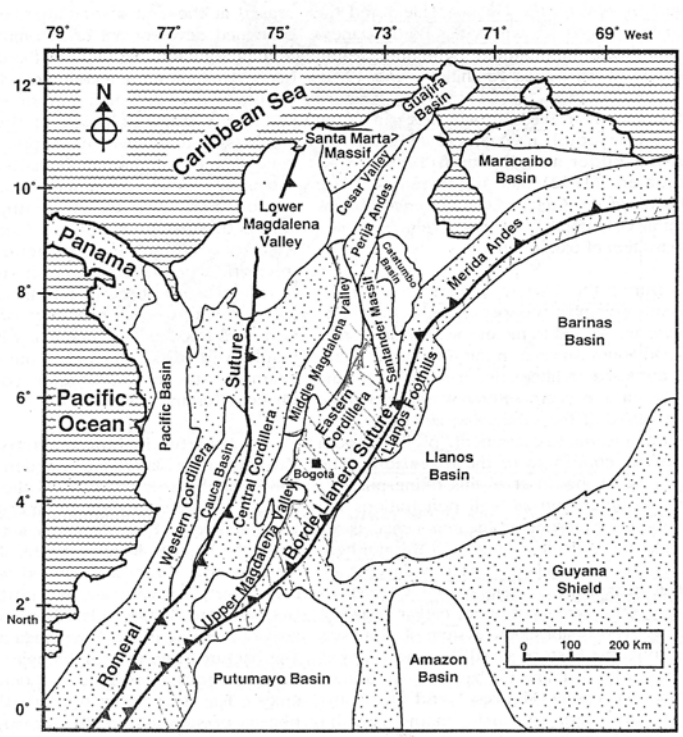

Figure 4.2: A map of the major tectonic provinces of Colombia. Present day basinal areas are white (adapted from *Cooper et al.* [1995]). The Llanos Basin lies to the east of the Eastern Cordillera.

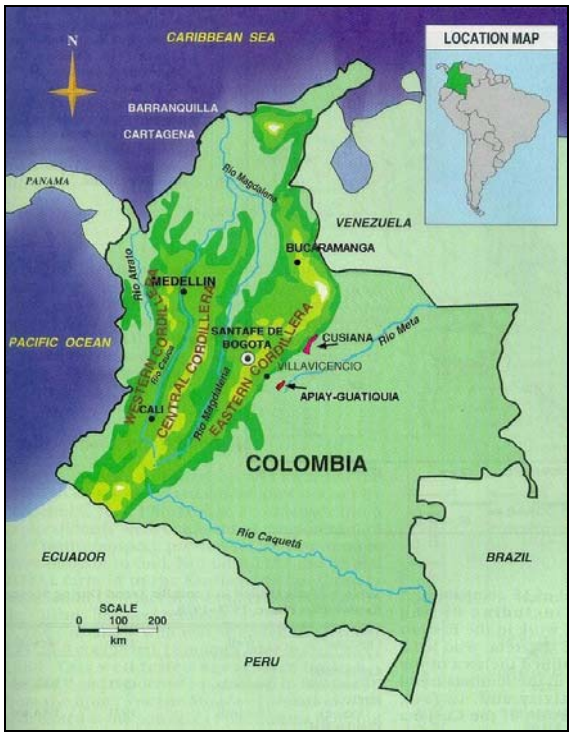

Figure 4.3: A map of Colombia with the location of the Apiay-Guatiquía oil field. The location of the giant Cusiana field is indicated for reference.

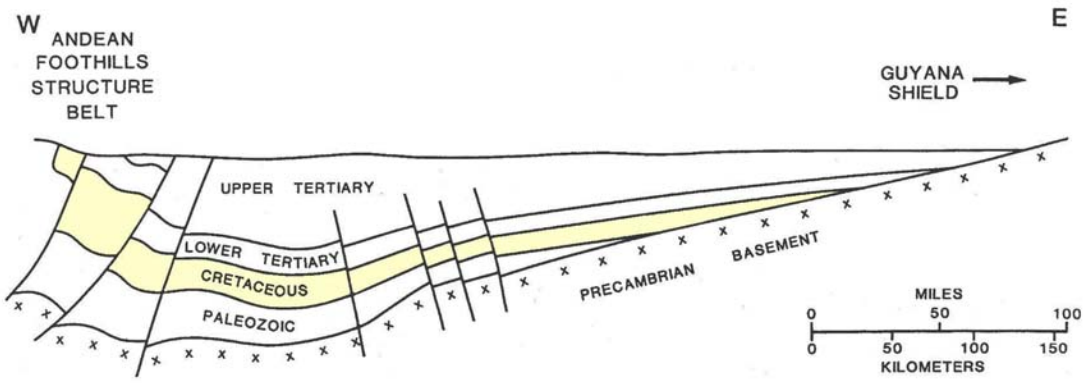

Figure 4.4: A schematic cross-section of the Llanos Basin. The K2 Unit belongs to the Cretaceous section (adapted from *McCollough* [1987]). Fault patterns along the section change from strike-slip/reverse at the Andes foothills to extensional in the foreland region.

Like many other basins in this chain, the Llanos Basin is bounded on the west by a fold-thrust belt at the mountain front, has a basin deep immediately to the east and gradually pinches out onto the granitic shield at the eastern margin [*McCollough*, 1987; *Cooper et al.*, 1995; *Villegas et al.*, 1994]. Figure 4.4 shows a schematic cross section of the basin. The Llanos Basin developed over the ancient Guyana Shield after an extensive

failed rift — the Arauca Graben — formed in the northern part of the basin during the Paleozoic era. The economic basement in the study area is composed of Paleozoic sedimentary rocks (mainly gray to black fossiliferous shales interlayered with siltstones and sandstones) that overlay the granitic Guyana Shield.

During the Cretaceous the Llanos Basin, the Eastern Cordillera, and the Magdalena Valley Basin shared the same history, as part of a former back-arc basin previously created by the accretion of the Western Cordillera. At that time, the basin deep was positioned at the current location of the Eastern Cordillera, and both of the major depocenters, the Cocuy and Tablazo-Magdalena Basins, were outside the present Llanos Basin area. The block diagram in figure 4.5 and the maps in figures 4.6 and 4.7, illustrate the depositional environment that prevailed through most of the Cretaceous era. Consequently, most sediments of Lower Cretaceous age were deposited west of the basin. Early Cretaceous deposition was entirely marine in the Llanos Basin, except for some shoreline facies on the Guyana Shield margin.

The Guadalupe Group, which extends to the limit of the Cretaceous succession, was deposited as a result of a fall in relative sea level in the Coniacian-Early Santonian, which caused a northward and westward shift in deposition and finished the anoxic conditions that prevailed in the area during the Early Cretaceous. This group reaches up to 200 m of thickness in some areas, and comprises three units (lower, middle and upper) that are variously named at different locations according to local variations in texture and composition. Guadalupe Group sediments represent two major cycles of westward progradation, aggradation, and retrogradation, and range from shallow marine at the base to deltaic and fluvial at the top. The Middle Guadalupe unit is mainly composed of mudstone and siltstone, and the other two are predominantly sandstone and siltstone. The Lower Guadalupe unit is a lower transgressive systems-tract of shallow marine sands terminating in a maximum flooding surface, while the Middle Guadalupe unit, also known as Guadalupe Shale, represents deposition in an upper high-stand systems-tract. The Campanian-Santonian Upper Guadalupe sandstone has a relatively uniform thickness (400 ft in average) over the Llanos Basin and the Llanos Foothills in the Eastern Cordillera, resulting from deposition across the shallow-marine shelf that extended over much of Llanos during the Late Cretaceous.

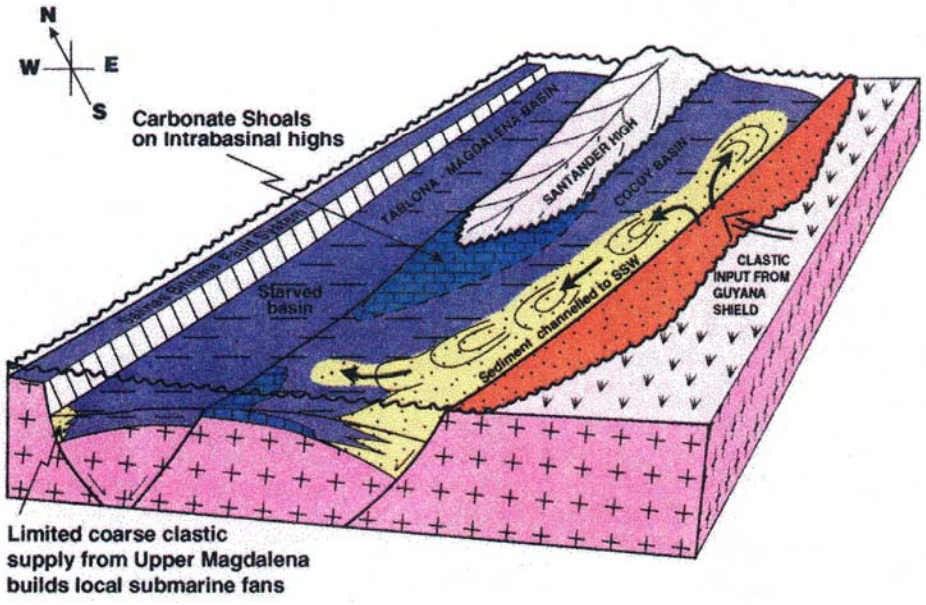

Figure 4.5: Block diagram that illustrates the location of the former Cocuy and Tablazo-Magdalena basins, which were the major depocenters during the Lower Cretaceous. (adapted from *Cooper et al.* [1995]). Very limited deposition occurred in Llanos during this period. The Guyana shield was main source of sediment supply to the Llanos Basin during the Cretaceous.

The Late Cretaceous sequence in the study area unconformably overlays the economic basement and is divided into two units for operational purposes: the Coniacian K2 unit, and the Santonian to Early Eocene K1 unit. Although both host important oil and gas reserves, the K2 unit, located about 3 km deep in the Apiay-Guatiquía field, is the main reservoir in the Apiay-Ariari area, and the focus of our reservoir characterization effort. The massive sandstone K2 interval consists of medium- to coarse-grained, locally conglomeratic, white sandstones deposited in an environment of stacked, braided stream channels. The K1 unit is composed of six genetic units deposited during the maximum transgression of the Cretaceous era in transitional marine environments in the lower section (river-dominated deltas with distributary channel facies and inter-distributary bays), and braided stream channels in the uppermost unit.

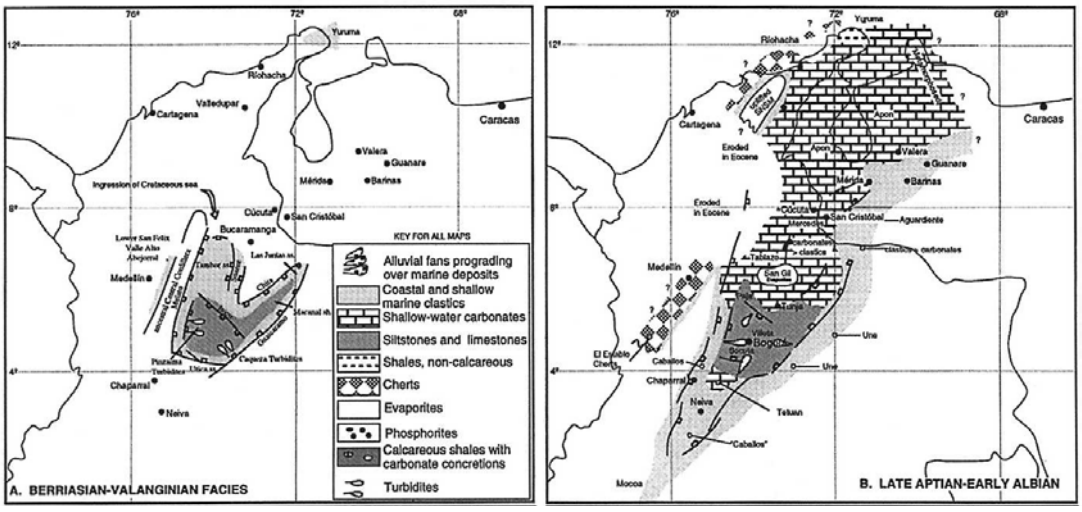

Figure 4.6: Gross depositional environment maps of Colombia that summarize the Early Cretaceous synrift and back-arc basin development (adapted from *Villamil* [1998]).

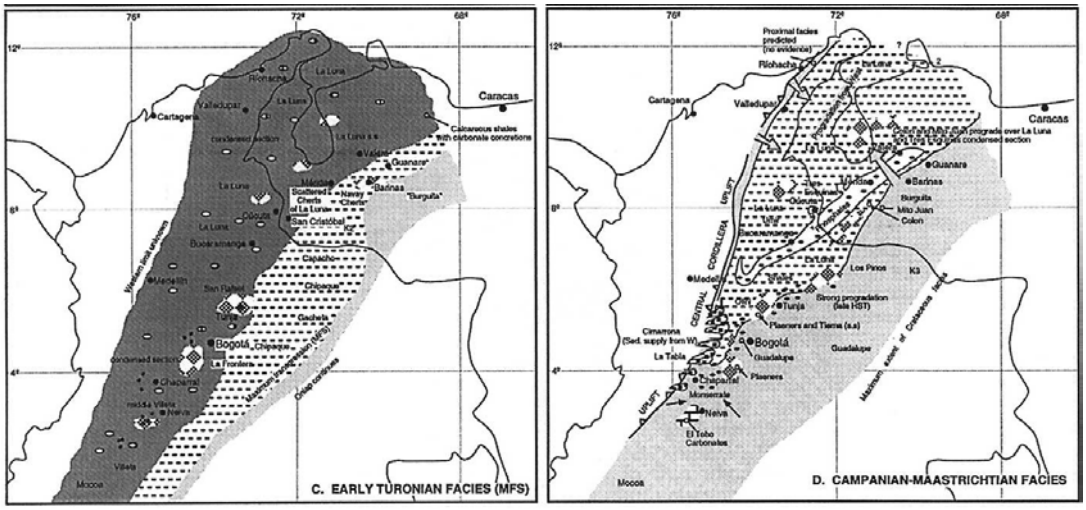

Figure 4.7: Gross depositional environment maps of Colombia that summarize the back-arc basin development during the Late Cretaceous (adapted from *Villamil* [1998]).

Figure 4.8 shows a west-east stratigraphic section from wells in the study area that uses the top of the K2 reservoir as datum depth. The low amplitudes of the gamma-ray logs, represented by the green curves, and the continuity along the section, reflect the massive character of the K2 unit sandstones, in contrast to the less developed sand bodies of the overlaying K1 unit. The sequence is thicker to the east, as a result of the additional accommodation space created by flexure and thermal subsidence on the east side of the basin. The sandstone-to-sandstone contact between the K1 and K2 units in some parts of

the Apiay-Ariari sub-basin sometimes produces a weak reflection, particularly in the nearby Suria filed.

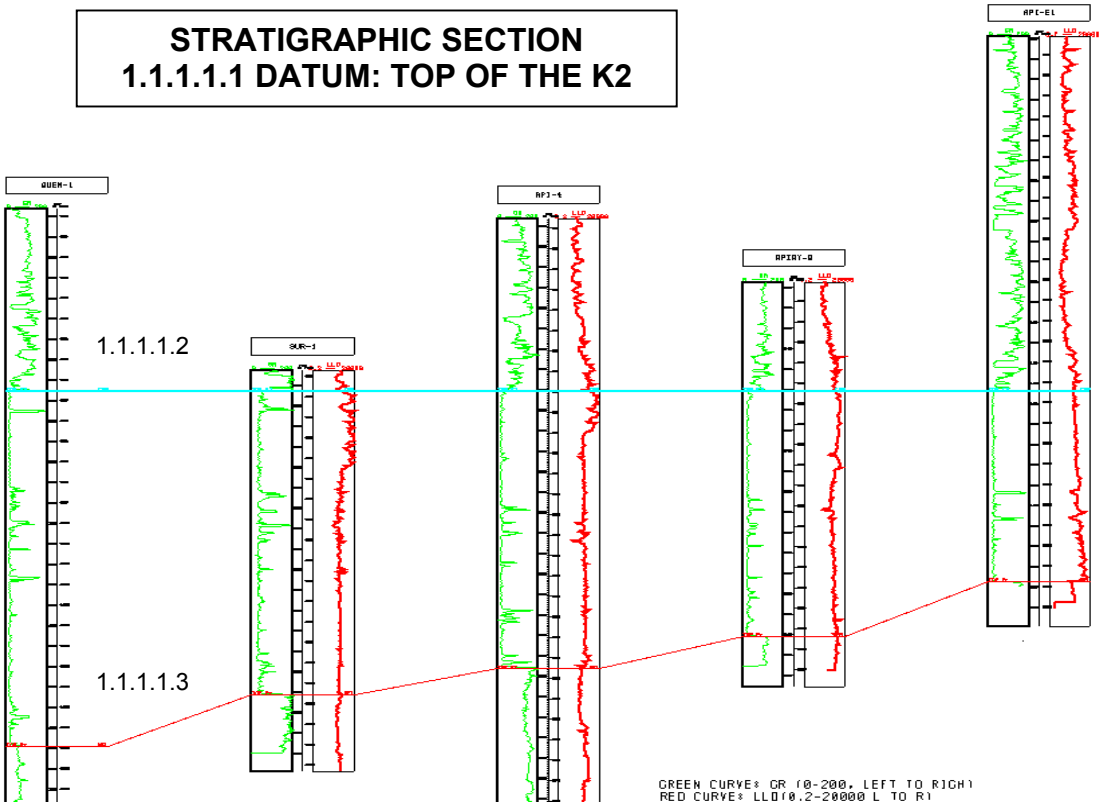

Figure 4.8: A stratigraphic section with the K2 top as datum depth. The green curves are gamma-ray logs (0 – 120 API, left to right); the red curves, resistivity logs (0.2 – 2000 Ohm-m, left to right). All wells belong to the Apiay-Ariari region.

Cretaceous sandstones in the study area have cratonic provenance, according to the concepts and models proposed by *Dickinson* [1985]. We show in figure 4.9 a triangular plot of the fractions of quartz, feldspar, and lithics, obtained from a petrographic study of samples from the study area. Sediments in the K1 and K2 Units, transported westwards from their original source in the Guyana Shield, were efficiently sorted by marine processes, which resulted in the depositon of highly mature quartz arenite sandstones [*O'Leary et al.*, 1997]. This is illustrated by the high fractions of quartz that the samples in figure 4.9 have.

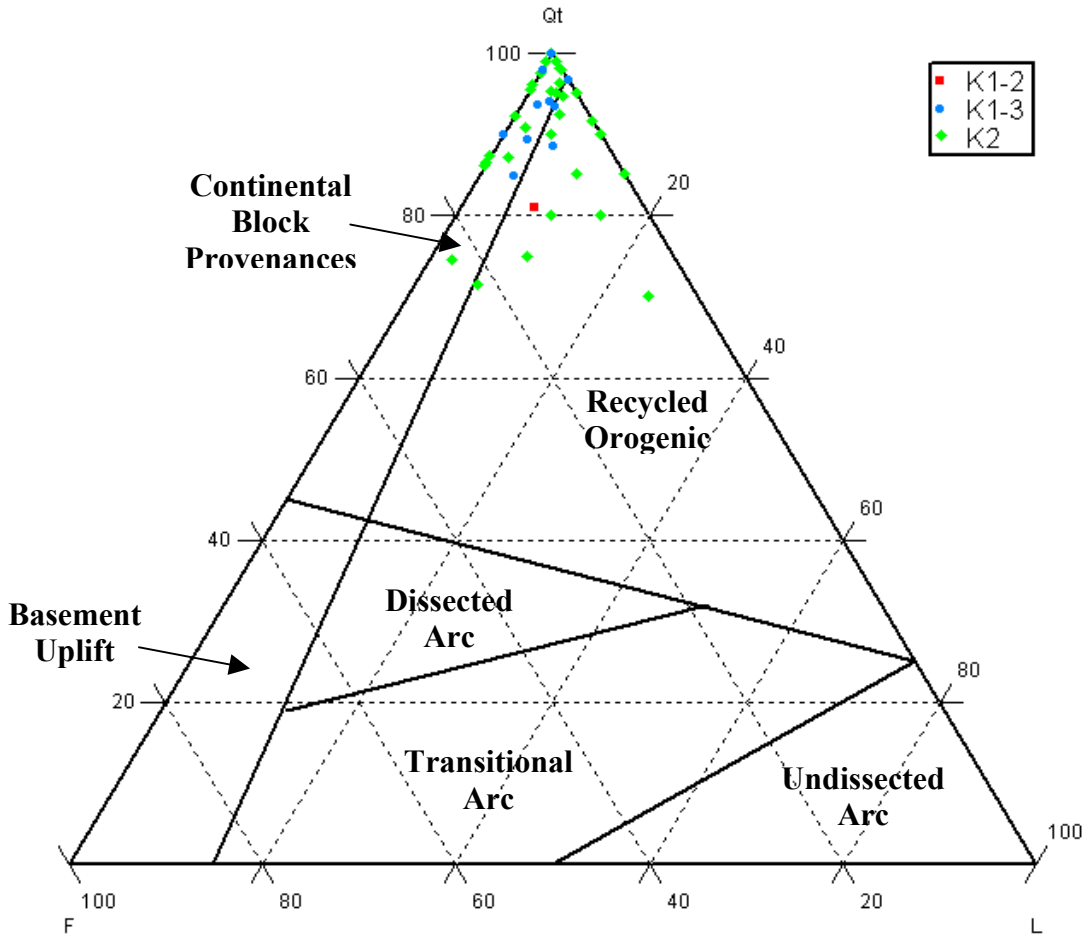

Figure 4.9: A typical QFL diagram for sandstone provenance in the Llanos Basin prior to the accretion of the Eastern Cordillera. The data are from petrographic measurements in core samples from the Apiay Field. K1 and K2 are operational units of Late Cretaceous age. The diagram reflects the continental provenance of sandstones in the sequence, whose source of sediments is the Guyana Shield.

In addition to the Cretaceous K1 unit, the reservoir overburden in the study area comprises the Mirador, Carbonera, Leon, and Guayabo-Necesidad formations. The Paleocene age Barco and Los Cuervos formations marked the beginning of a second pulse of deposition in Llanos, but they were deposited in the northwestern part of the basin, and neither of them is present in the Apiay-Guatiquía area. The Late Eocene Mirador Formation, which uncomformably overlays the Cretaceous sequence in the area, is composed of fine- to coarse-grained, sometimes conglomeratic sandstones intercalated with shales and siltstones, deposited in an environment of braided streams. The Carbonera Formation is a sequence of shales and siltstones, with a few sandstones and some coal layers at the top. It was deposited from the Oligocene to the Early Miocene

periods, during four major cycles of marine influence on coastal plain sediments. Then, from the late Miocene to the Holocene, the Eastern Cordillera uplift bisected the former basin, and the largest portion, on the eastern side, became the Llanos Basin. The Leon Formation, which concordantly overlays the sequence, comprises shallow marine, green and gray claystones. It contains the record of both the uplift and deformation of the Eastern Cordillera, and the marine transgression that was taking place at the time. Continental clastics whose main source is the Eastern Cordillera dominated all subsequent deposition in the Llanos Basin and formed the Guayabo-Necesidad molasses.

4.2 A Description of the Apiay-Guatiquía K2 Unit Reservoir Data Set

The Apiay-Guatiquía structure is an asymmetric anticline, faulted on its southwest flank, with a small depression between the areas of Apiay and Guatiquía. The anticline is 6 km long and 1.6 km wide, and its main axis is N30E (figures 4.10 and 4.11). The structure is limited to the east by the high angle, strike-slip/reverse Apiay fault, which has sealing character and separates the field from associated structures on the other side of the fault, known as Gaván and Apiay Este. The Apiay fault cuts only the sequence from Lower Tertiary to basement and its offset decreases to the NE from a maximum of 300 ft close to the Apiay-E1 well. On the east side of the fault there are normal faults of shorter length.

The K2 Unit reservoir of the Apiay-Guatiquía oil field is essentially a two-phase, oil-water system. A very active regional aquifer produces a strong water drive that keeps the system at nearly constant pore pressure. The pore pressure gradient is hydrostatic. The release of solution gas in the pore space is further prevented by the fact that bubble point pressure –about 500 psia– is much lower than reservoir pressure. The oil produced from the K2 unit in this field has a density of 25 °API and very low gas-oil ratio (30-50 scf/STB). A total of 22 wells had been drilled into the K2 unit reservoir at the time we started our study, including two wells located in the associated structures known as Gaván and Apiay-Este, located to the east of the Apiay-Guatiquía field.

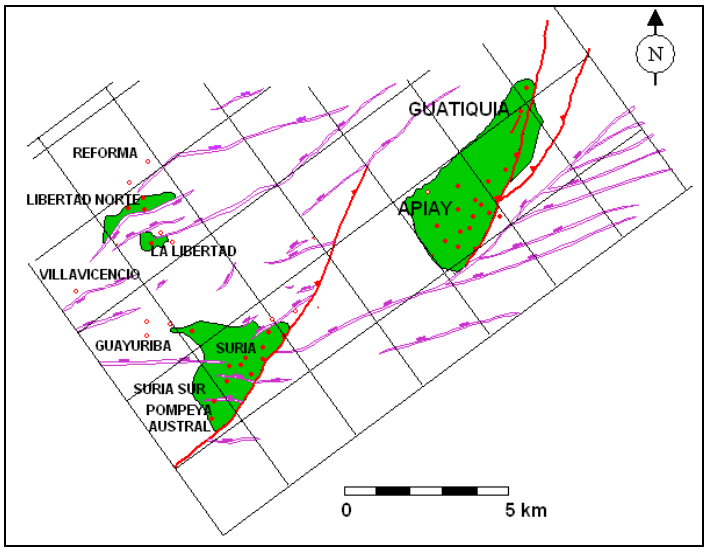

Figure 4.10: A map of oil production areas in the Apiay-Ariari region. The mesh corresponds to the coverage of the Apiay-Ariari 3D seismic program. Red lines represent reverse faults; magenta lines, normal faults.

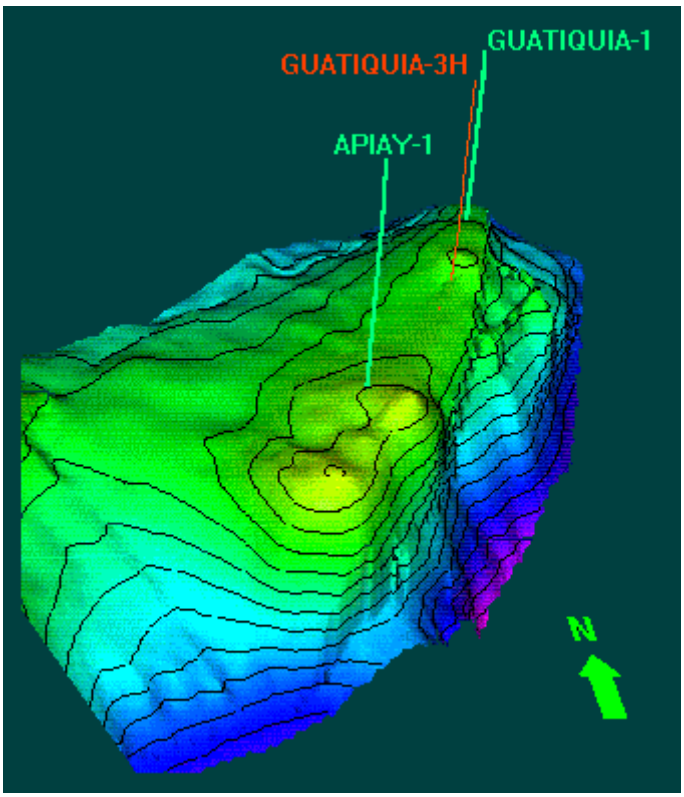

Figure 4.11: A three-dimensional structural representation of the Apiay-Guatiquía field, at the top of the K2 Unit reservoir.

Ecopetrol granted us access to a very complete set of data relevant to the K2 reservoir, including production data from all wells producing from the K2 unit, in terms of flow rates, water cut, and well flowing pressure, as well as PVT studies of reservoir fluids. We also had access to pressure transient tests from several wells in the field. The set of geophysical measurements acquired in these wells consists of logs of gamma-ray, spontaneous potential, neutron porosity, bulk density, compressional wave slowness, caliper, and shallow, intermediate, and deep resistivities for almost all wells. Shear-wave velocity has not been measured in any of the wells drilled through the K2 unit. The set also includes wellbore images generated from data acquired with a resistivity-while-drilling tool that was run on a deviated well, as well as gamma-ray, deviation and azimuth data for that same well. Formation tops interpreted by Ecopetrol geologists were also available.

Five of the wells in the Apiay-Guatiquía field have cored intervals in the K2 unit. We had access to the results of petrographic analyses, and to core measurements of bulk density, porosity and permeability. We inspected the available cores of wells Apiay-3 and Apiay-10 and selected 13 core samples, representative of the different lithotypes found in the K2 reservoir, according to the facies classification made by Ecopetrol geologists and petrophysicists.

Very few measurements of minimum horizontal stress have been made in the study area. We received the interpretation results of 3 leak-off tests and 1 formation integrity test, but could not get the raw data for them, so their quality could not be directly assessed.

The seismic information used in this project consists of a volume of 3D stacked data, two check-shots, one vertical seismic profile (VSP), and a set of time horizons interpreted from the seismic volume. Seismic data files received from Ecopetrol did not have inline and cross-line numbers stored in trace headers, which are required to correctly allocate the seismic traces and to find the position of wells in the coordinate system of the seismic survey. We retrieved inline numbers from the ASCII section of line headers, and used a sequential trace number as a proxy for cross-line numbers, observing the proper alignment of initial traces in each line.

4.3 Determination of the Stress Field in the Study Area

Understanding the stress field in Apiay-Guatiquía is very important for our rock physics study, because elastic properties vary with effective pressure, which linearly depends on the magnitude of stress in the subsurface. Knowledge about the magnitude and direction of principal stresses is also useful for optimizing drilling programs, since it can allow the appropriate selection of wellbore azimuth and mud weights to prevent the wellbore instability. It also reduces the occurrence of stress-induced wellbore enlargements, enhancing the quality of well log data. Improving the quality of logs reduces the uncertainty of reservoir characterization analyses.

Very few authors have studied the stress field on the Llanos basin, as can be seen in figure 4.12. *Castillo and Mujica* [1990] determined the direction of maximum compression from breakouts in three vertical wells of the basin. His results in one of the three wells (Guayuriba-2) were not consistent and should not be taken into account. *Last et al.* [1997] analyzed the orientation and magnitude of the stress components using breakout observations from vertical wells. In this section we explain our approach to determine the direction and magnitude of principal stresses in the study area from wellbore image data, density logs, and leak-off and formation integrity tests, and compare our results to those reported by previous studies of stress distribution in the Llanos Basin.

The field is located in a normal faulting environment and the maximum horizontal stress is approximately east-west.

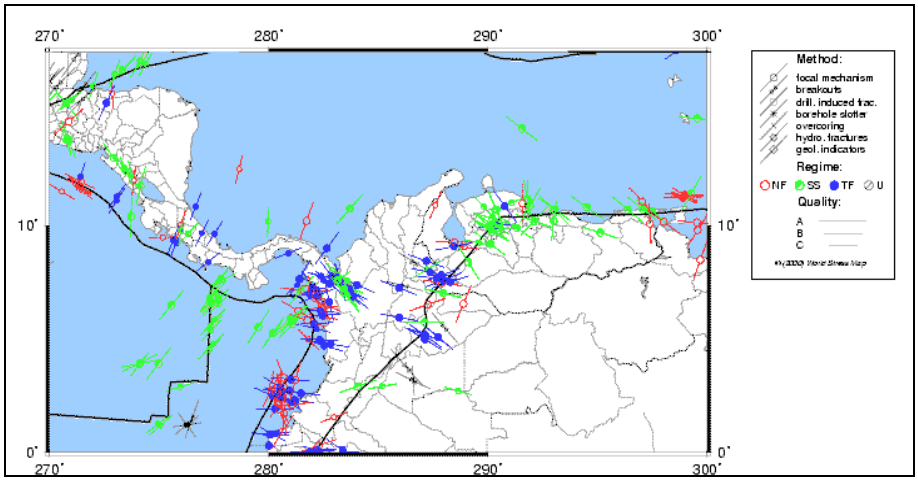

Figure 4.12: A map of stress orientations and failure regimes in the northwestern part of South America (adapted from the world stress map [*Mueller et al.*, 2000]).

4.3.1 Stress Field and Compressive Failure in Boreholes

Defining the faulting regime in an area amounts to determining the magnitude of stresses along the principal horizontal directions, with respect to the magnitude of vertical stress. Table 4.1 summarizes the relationships between principal stresses for normal, strike-slip and reverse faulting regimes [*Anderson*, 1937].

Table 4.1: Distribution of principal stresses for the different faulting regimes, according to *Anderson*'s [1937] faulting theory. S_1 is the maximum stress, S_2 the intermediate, and S_3 the minimum. S_V represents the vertical stress, $S_{H\max}$ the maximum horizontal stress, and S_{hmin} the minimum horizontal stress.

Faulting Regime	Normal	Strike-slip	Reverse
S_1	S_V	$S_{H\max}$	$S_{H\max}$
S_2	$S_{H\max}$	S_V	$S_{h\min}$
S_3	$S_{h\min}$	$S_{h\min}$	S_V

In many instances around the world it is reasonable to assume that one of the principal stresses is vertical. In such a case, the magnitude of the vertical principal stress S_V corresponds to the overburden, and can be computed from integration of bulk density from the surface to the depth of interest, as follows:

$$S_V = \int_0^z \rho(z) g dz \,. \tag{4.1}$$

If the vertical principal stress, pore pressure, and coefficient of frictional sliding μ are known, the magnitudes of principal horizontal stresses can be constrained by following the methodology proposed by *Moos and Zoback* [1990, 1993] to find the feasible range of $S_{H\max}$ and $S_{h\min}$ that are consistent with an assumption of frictional equilibrium in the crust. This assumption implies that the ratio of maximum and minimum effective principal stresses is given by the following expression [*Jaeger and Cook*, 1979]:

$$\frac{S_1 - P_p}{S_3 - P_p} = \left(\sqrt{\mu^2 + 1} + \mu\right)^2 . \tag{4.2}$$

For example, figure 4.13 shows the feasible range of $S_{H\max}$ and $S_{h\min}$ for a case with hydrostatic pore pressure gradient, and coefficient of sliding friction $\mu = 0.8$.

The cavity produced when a well is drilled generates a distribution of stresses around the borehole that was first described by *Kirsch*, [1898], which is described as follows for a vertical well drilled in a scenario where one of the principal stresses is also vertical:

$$\sigma_{\theta\theta} = S_{H\max} + S_{H\min} - 2\left(S_{H\max} - S_{H\min}\right)\cos 2\theta - 2P_p - \Delta P , \tag{4.3}$$

where ΔP is the pressure differential between the wellbore fluid pressure and the formation pore pressure P_p, and θ is the angle with respect to the azimuth of $S_{H\max}$. In such a scenario, the points of minimum compressive stress concentration align with $S_{H\max}$, and the maximum compressive stresses are perpendicular to the azimuth of $S_{H\max}$. Compressive failure (e.g. breakouts) occurs when the maximum stress exceeds the rock strength C. At the points of maximum and minimum compression this leads to:

$$S_{H\max} > \frac{1}{3}\left(S_{H\min} + C + 2P_p + \Delta P\right), \text{ and} \tag{4.4}$$

$$S_{H\min} > \frac{1}{3}\left(S_{H\max} + C + 2P_p + \Delta P\right), \tag{4.5}$$

respectively. The lines described by the limit case, i.e., when the left-hand and right-hand sides of equations 4.4 and 4.5 are equal (shown in red in figure 4.13) can be used to further constrain the range of $S_{H\max}$ and $S_{h\min}$, provided that rock strength is known and there is evidence of compressive failure along the borehole. The presence of breakouts would imply that $S_{H\max}$ is above the line defined by the limit case of equation 4.4. On the other hand, if the whole wellbore has failed under compression (washouts), one can conclude that $S_{h\min}$ should be to the right of the line that represents the limit case of equation 4.5.

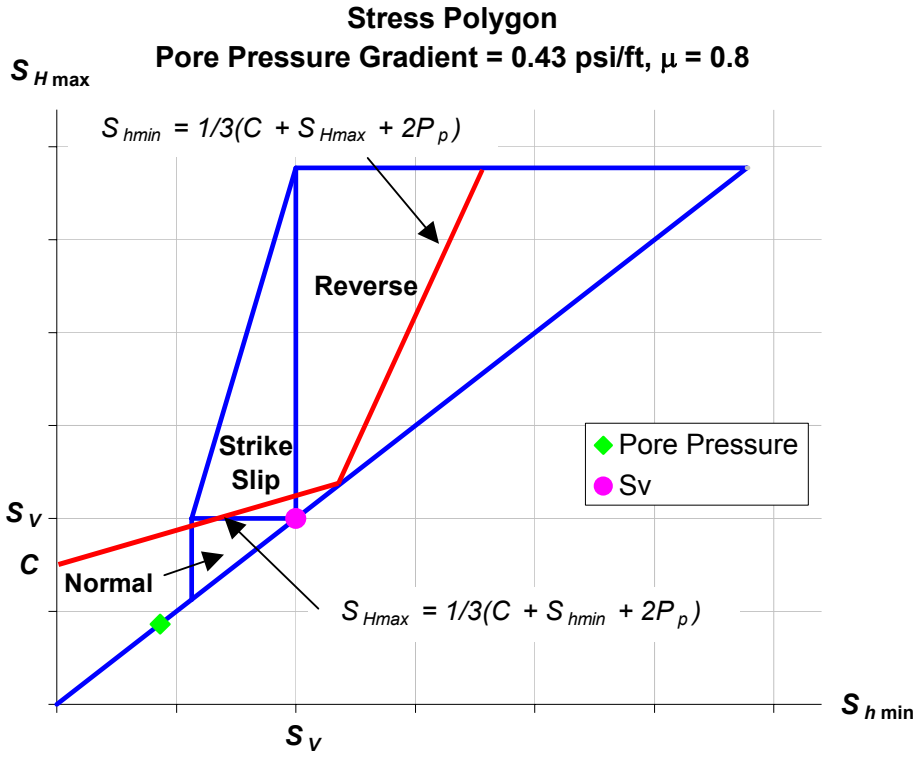

Figure 4.13: A plot of the feasible range of $S_{H\max}$ and $S_{h\min}$ for normal, strike-slip and reverse faulting regimes, subject to the assumption of frictional equilibrium in the crust. The red lines are breakout lines for vertical wells. The plot corresponds to a scenario of hydrostatic pore pressure gradient, coefficient of sliding friction $\mu = 0.8$, and $\Delta P = 0$.

Kirsch's equations [1898] are of limited applicability because they were developed for vertical wells. *Peska and Zoback* [1995] presented a method to compute stresses around the borehole for arbitrarily oriented wells and stress fields, based on the assumption that rocks are homogeneous and isotropic, and have linear elastic behavior up to the point of failure. Under such conditions the principal stresses $\sigma_{t\max}$, $\sigma_{t\min}$, and σ_{rr} at the wall of an inclined borehole (figure 4.14), are given by:

$$\sigma_{t\max} = \frac{1}{2}\left[\sigma_{zz} + \sigma_{\theta\theta} + \sqrt{\left(\sigma_{zz} + \sigma_{\theta\theta}\right)^2 + 4\sigma_{\theta z}^2}\right] \tag{4.6}$$

$$\sigma_{t\min} = \frac{1}{2}\left[\sigma_{zz} + \sigma_{\theta\theta} - \sqrt{\left(\sigma_{zz} + \sigma_{\theta\theta}\right)^2 + 4\sigma_{\theta z}^2}\right] \tag{4.7}$$

$$\sigma_{rr} = \Delta P\,. \tag{4.8}$$

where ΔP is the pressure differential between the wellbore fluid pressure and the formation pore pressure, r is the radial direction from the center of the borehole, z is parallel to the borehole axis, and θ is the angle around the wellbore wall, measured from the lowermost side of the hole.

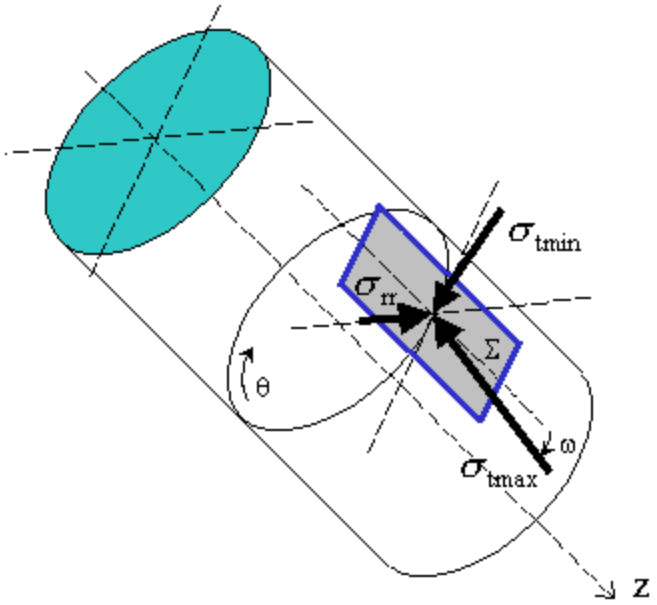

Figure 4.14: Principal stresses at the wall of an inclined borehole for a point oriented at angle θ measured from the lowermost side of the hole. σ_{rr} is the radial stress, and always acts perpendicular to the wellbore wall. The minimum and maximum tangential stresses σ_{tmin} and σ_{tmax} act in the plane Σ, which is tangential to the borehole (adapted from *Peska and Zoback* 1995).

σ_{zz}, $\sigma_{\theta\theta}$, and $\sigma_{\theta z}$ are the effective stresses in cylindrical coordinates, given by:

$$\sigma_{zz} = \sigma_{33} - 2v(\sigma_{11} - \sigma_{22})\cos 2\theta + 4v\sigma_{12}\sin 2\theta \tag{4.9}$$

$$\sigma_{\theta\theta} = \sigma_{11} + \sigma_{22} - 2v(\sigma_{11} - \sigma_{22})\cos 2\theta + 4v\sigma_{12}\sin 2\theta - \Delta P \tag{4.10}$$

$$\sigma_{\theta z} = 2\sigma_{23}\cos\theta - \sigma_{13}\sin\theta\,. \tag{4.11}$$

In equations 4.9 to 4.11 v is Poisson's ratio and the effective stresses are given by:

$$\sigma_{ij} = S_{ij} - \delta_{ij} p_p\,, \tag{4.12}$$

where δ_{ij} is the Kronecker delta, p_p is pore pressure, and σ_{ij} is a component of the total stress tensor defined in a local borehole coordinate system. This tensor can be obtained from the far-field stress state through a series of coordinate transformations, described in detail in *Peska and Zoback* [1995]. Equations 4.9 to 4.12 describe how the borehole stress state defined by equations 4.1 to 4.3 depends on the tectonic stress S_1, S_2, and S_3.

To determine whether breakouts will form at the wellbore wall it is necessary to assume a failure criterion. For a scenario defined by a certain stress field, well trajectory, and rock strength, it is possible to compute the stress concentration at a certain angle around the wellbore and compare them to a the assumed failure law to determine whether or not the rock is still behaving elastically. In this analysis we used the Mohr-Coulomb failure law, which can be written as follows [*Jaeger and Cook*, 1979; *Peska and Zoback*, 1995]:

$$\sigma_1 = \sigma_3\left(\sqrt{\mu_i^{\,2}+1}+\mu_i\right)^2 + C_0, \tag{4.10}$$

where the strength of the rock is determined by its coefficient of internal friction μ_i, and its uniaxial compressive strength C_0. Figure 4.15 is an example of failure determination for two angles around a wellbore deviated 25° from the vertical, drilled at an azimuth of 195°, through a rock with μ_i = 1 and C_0 = 5000 psi, in a strike-slip faulting area, with $S_{H\max} : S_V : S_{h\min}$ = 11000 : 10700 : 6670 psi. In this example, the hypothetical wellbore fails under compression at an angle of 180° measured from the bottom of the well, but remains intact at 105°. Breakout width can be determined by finding all angles at which the stresses do not meet the failure criterion. Notice that the calculations of stress concentration around the wellbore are completely independent of both the rock strength parameters and the failure criterion chosen to perform the analysis; they can be combined with any other failure criteria. We used the software GMI-SFIB to generate some of the results in this stress study.

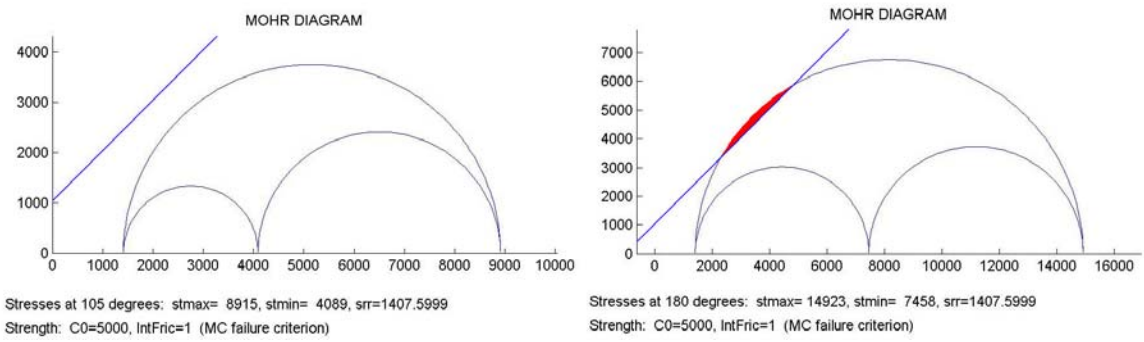

Figure 4.15: Two examples of compresive failure determination for a wellbore with deviated = 25°, and azimuth = 195°, drilled through a rock with $\mu_i = 1$ and $C_0 = 5000$ psi, in an strike-slip faulting area, with $S_{H\max} : S_V : S_{h\min} = 11000 : 10700 : 6670$ psi.

4.3.2 Sources of Data for Stress Analysis

Determining the stress field in an area requires the integration of data from multiple sources. In our stress analysis we used data from wellbore images, interpreted leak-off and formation integrity tests, well logs, and transient pressure tests. Wellbore images obtained from inclined boreholes are of great value for stress determination, because the aperture and orientation of failure patterns on the wellbore wall, such as breakouts and tensile cracks, depend on both the stress state and well orientation [*Mastin*, 1988; *Peska and Zoback*, 1995]. Therefore, the study of such failure patterns is useful to constrain the magnitudes, and to determine the orientation of horizontal stresses. Leak-off and formation integrity tests are also very valuable, because they are *in-situ* measurements of fracture initiation pressure, and provide constraints on the magnitude of the least principal stress. Well logs contain information about lithology, which can be interpreted in terms of rock strength. Furthermore, the vertical principal stress can be obtained from integration of the density log. Finally, transient pressure tests are useful to determine the average pore pressure in the drainage area of a well, which is required to compute effective stresses.

In 1997 Ecopetrol drilled the Guatiquía-3H well, which was the first horizontal well in the basin. Prior to drilling the horizontal section of the well, the operator drilled a deviated pilot hole from the same surface location to reduce the uncertainty in formation tops, and to test the bottom-hole assemblies that would be used in the horizontal section. A measure-while-drilling (MWD) tool provided the data required to control geosteering

operations, namely wellbore deviation and azimuth, while a resistivity-while-drilling tool supplied data for stratigraphic control. The good quality of resistivity data acquired in the pilot hole allowed the generation of images of the wellbore wall. These images show the real size and orientation of breakouts — represented as areas of anomalously low resistivity values in figure 4.16.

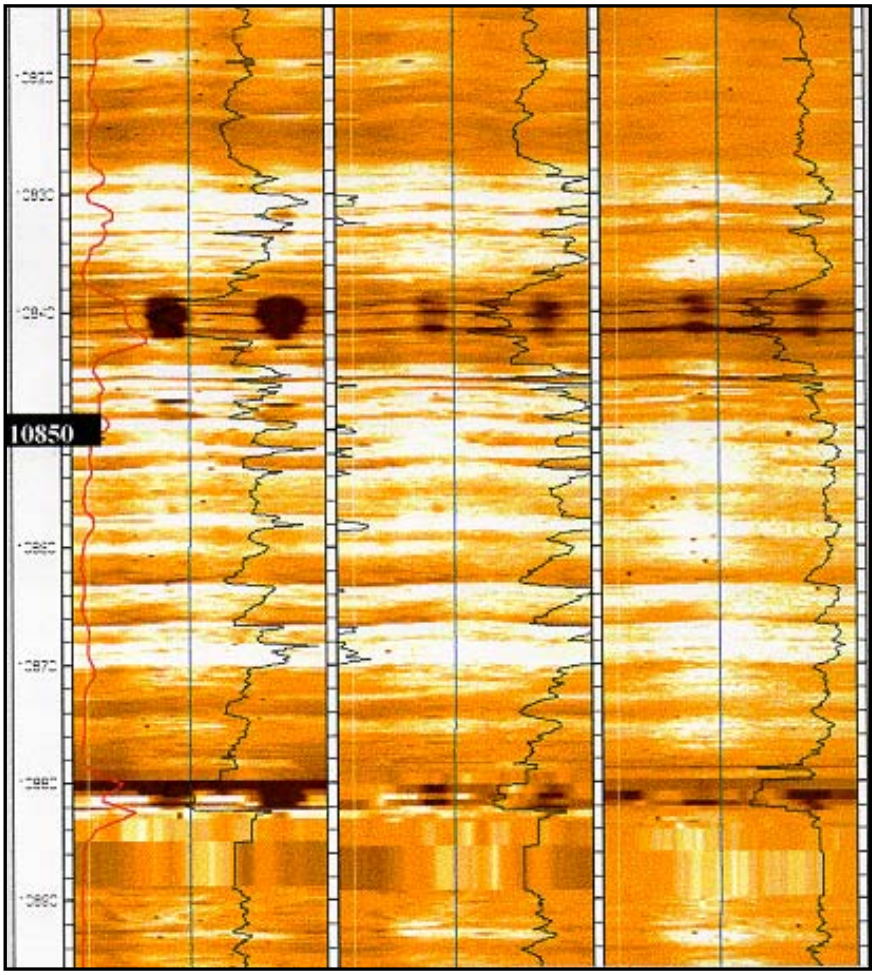

Figure 4.16: Resistivity images from the RAB tool run in the Guatiquía-3H pilot hole. Left: shallow button electrode. Center: middle button electrode. Right: deep button electrode. The black curves indicate the average resistivity for each electrode, plotted in a 2 to 2000 ohm-m scale. The red curve is the gamma-ray tool response. The top of the well corresponds to the left edge of each image, and the blue line represents the North direction. The depth axis corresponds to measured depth.

As described in section 4.2, the K2 unit is a very homogeneous sequence of well-consolidated sandstones with a few thin streaks of shale and/or silt. Thin section analyses suggest that the well-compacted and quartz-cemented sandstones of the K2 unit

are very strong, which has indeed been observed in drilling operations. Hence the intervals that are most likely to fail are the thin shale/silt layers, which can be identified in the sequence by the higher gamma-ray readings they produce. Caliper logs from other wells in the area also indicate that such streaks are weaker than the sandstones and tend to fail during drilling operations. Even though the low frequency of shale/silt streaks reduces the occurrence of breakouts, we can confidently read the dark areas in the resistivity images shown in figure 4.16 as the result of compressive failure in the wellbore wall, because their position correlates well with high values of gamma-ray, they are 180 degrees apart from each other, and their size and position is the same in the two intervals where they occur in the image.

4.3.3 Orientation and Magnitude of Principal Stresses in Apiay-Guatiquía

We determined the vertical principal stress S_V by integrating the values of bulk density from the density log of well Guatiquía-2, which is the nearest well to the pilot hole location. The measured interval for this log ranges from 50 to 10938 feet, covering virtually the entire stratigraphic sequence. The vertical stress gradient is approximately 1 psi/ft.

Table 4.2 summarizes the results of leak-off and formation integrity test. Since we did not have access to the raw leak-off test data, it is not certain whether the reported mud densities represent fracture initiation pressures, or instantaneous shut-in pressures. The latter are a better estimate of least stress. From the data we estimated a least stress gradient of 0.8 psi/ft, and assumed for the purpose of this study that this represents the upper limit of S_3.

Table 4.2: A summary of available leak-off (LOT) and formation integrity (FIT) tests.

Well	Unit	Depth	Mud Weight	Pressure Gradient	Type of Test
Guatiquía-1	E3 Shale	9520 ft	15.5 ppg	0.806 psi/ft	FIT
Guatiquía-2	T1 Sand	9663 ft	13.5 ppg	0.702 psi/ft	LOT
Apiay-3	Guayabo Shale	1460 ft	15.5 ppg	0.806 psi/ft	LOT
Apiay-11	E3 Shale	9320 ft	15.0 ppg	0.780 psi/ft	LOT

We obtained pore pressure around the pilot hole from the interpretation of transient pressure tests carried out during the completion of the Guatiquía-3H well. Figure 4.17 shows a semi-log plot for one of the build-up tests conducted in this well. The data reveal the presence of a strong aquifer that maintains reservoir pressure at a roughly constant level. The pore pressure is 3892 psi at 9000 feet, which yields a nearly hydrostatic gradient (0.432 psi/ft). This result is consistent with interpreted pore pressures from other well tests in the area.

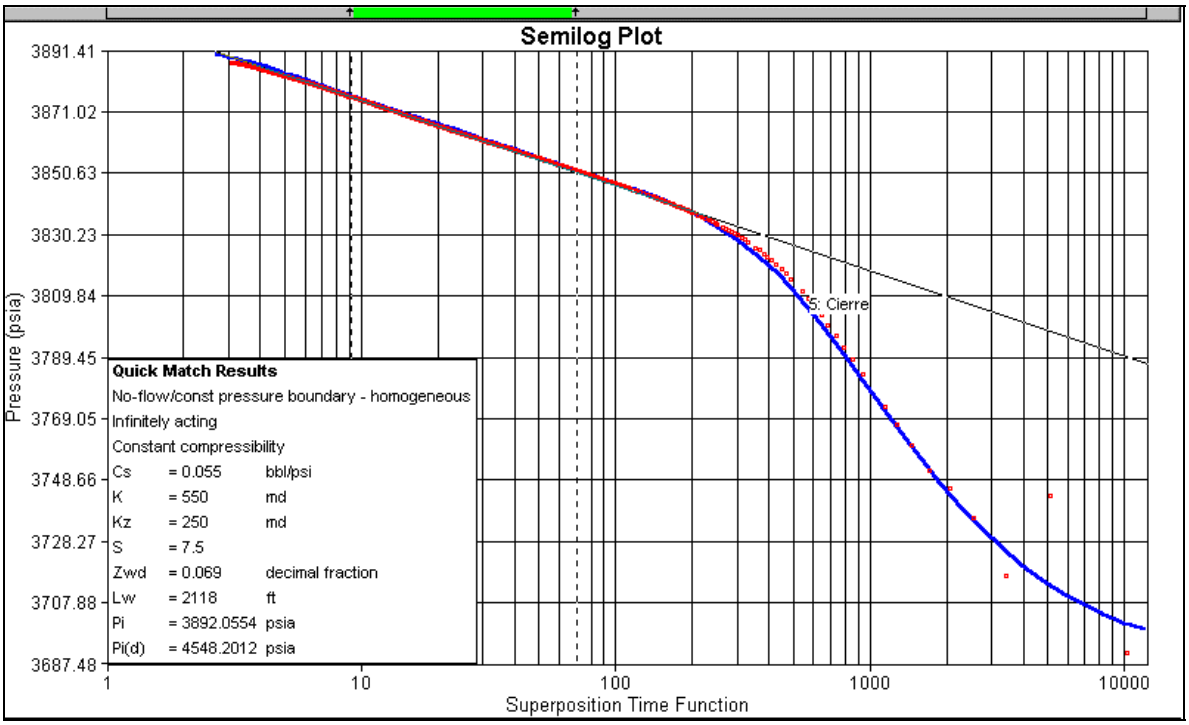

Figure 4.17: A semilog plot of pressure vs. superposition time for a build-up test conducted in the Guatiquía-3H well. Red dots are measured data, while the blue line represents the behavior predicted by the analytical model described by the parameters in the box. The green bar indicates the limits of the hemiradial flow period.

As pointed out before, the direction of maximum compression is perpendicular to the preferential azimuth of breakouts, which can be estimated from four-arm caliper data.

Figure 4.18 presents rosette diagrams that summarize breakout orientation in two vertical wells of the Apiay-Guatiquía field, including the closest well (Guatiquía-1) to the pilot hole [*Last et al*., 1997]. Breakouts in this well indicate that the azimuth of $S_{H\max}$ is 83º ± 10. The orientation (150º ± 10º) and aperture (55º ± 10º) of breakouts in the pilot hole also suggest that the direction of maximum compression is roughly east-west. Figure 4.19 is a plot of $S_{H\max}$ vs. azimuth of $S_{H\max}$ predicted by the *Peska and Zoback* [1995] model for the trajectory of the pilot hole, and subject to the breakout data from that hole.

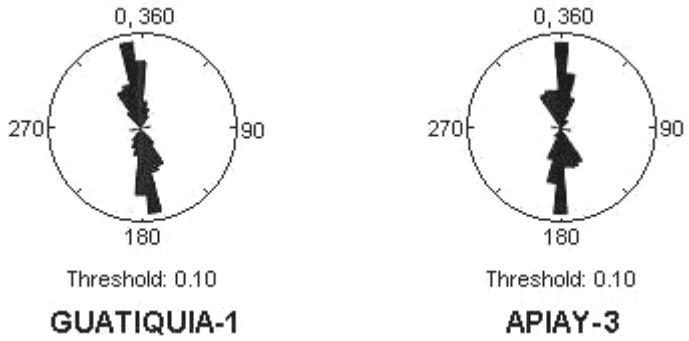

Figure 4.18: A summary of breakout orientation data from the analysis of four-arm caliper logs in two wells of the Apiay-Guatiquía field (adapted from *Last et al.*, 1997). $S_{H\max}$ is inferred to be perpendicular to the dominant breakout orientation.

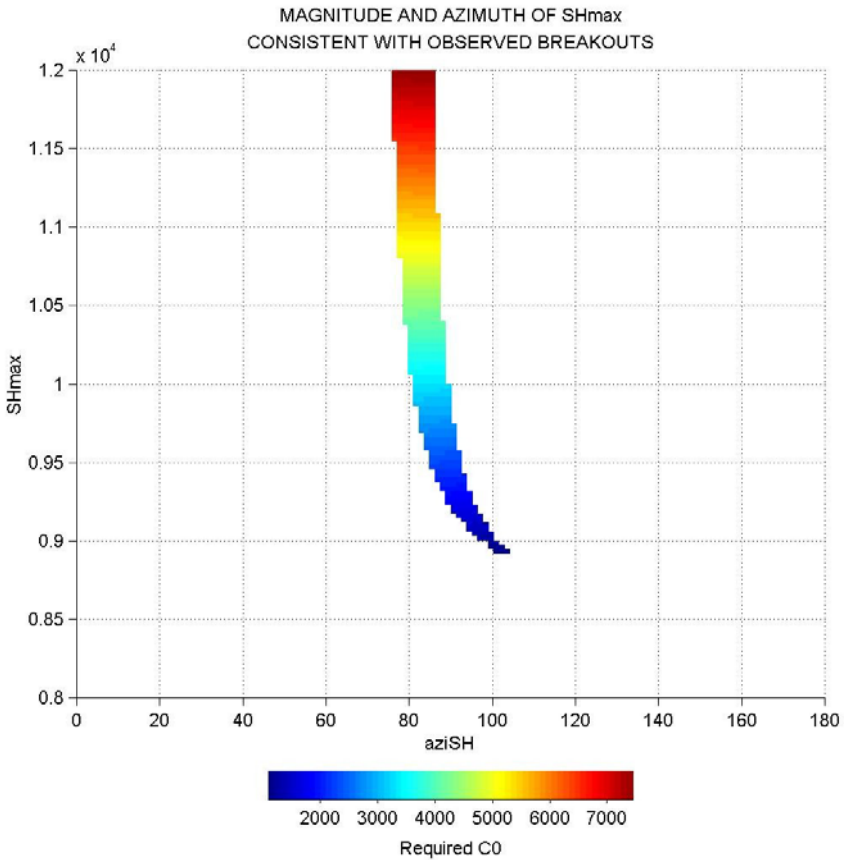

Figure 4.19: A plot of feasible combinations of orientation and magnitude of $S_{H\max}$, for $S_{h\min}$ = 6600 psi, consistent with the position and aperture of the breakouts and the trajectory of the pilot hole.

Figure 4.20 shows the variation of vertical stress, least stress, and pore pressure with depth, as well as the available measurements of minimum stress. The minimum stress gradient we estimated from data in table 4.1 (0.802 psi/ft) indicates that S_V is higher than S_3. Thus, the least stress direction is horizontal, $S_3 = S_{h\min}$, and only strike slip or normal faulting regimes can hold for the Apiay-Guatiquía area, according to the criteria given by Anderson's faulting theory.

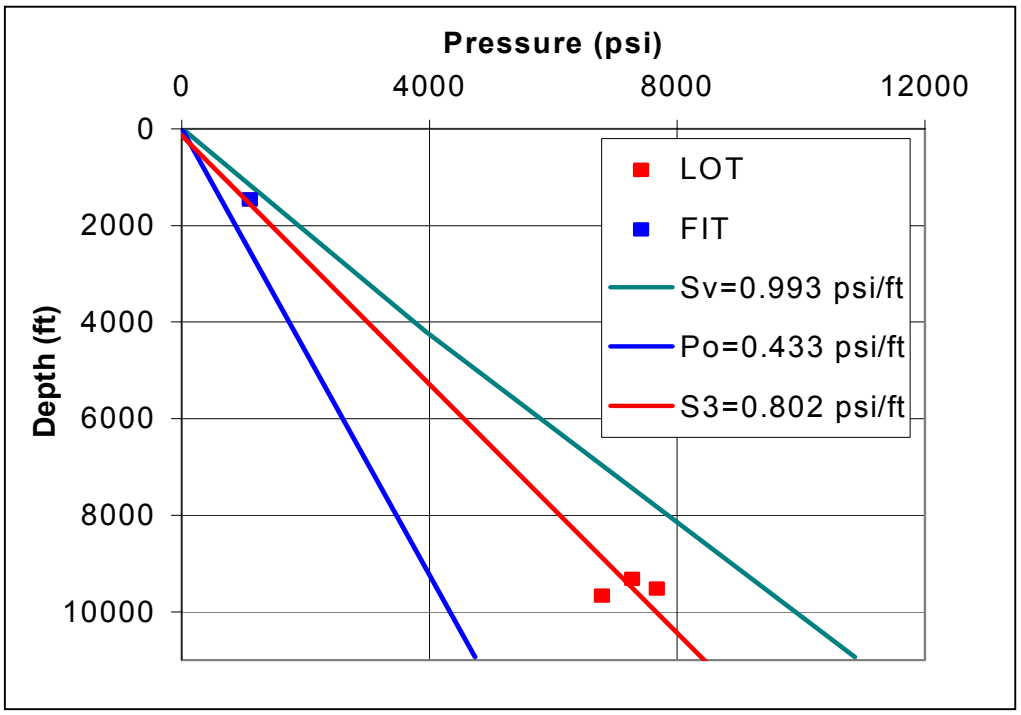

Figure 4.20: A plot of vertical stress S_V (green), least stress S_3 (red); and pore pressure P_o (blue) versus depth. Squares correspond to measurements of least stress, which we used to estimate the least-stress gradient curve. We computed S_V by integrating the density log from a nearby well, and calculated the pore pressure curve from the pore pressure gradient obtained from well tests.

Actual values of uniaxial compressive strength, Poisson's ratio and coefficient of sliding friction for rocks in the K2 unit are uncertain, because of the lack of measurements of mechanical properties. In such a scenario, one should take a sensitivity approach to address the problem of determining the magnitude of $S_{H\max}$ and $S_{h\min}$; that is, all possible stress states need be analyzed to study whether or not they make physical sense and explain all observations. Our approach in this study comprises the use of physical models to reproduce the wellbore failure patterns (i.e., orientation and aperture of breakouts) found in the resistivity image, taking into account the constraints imposed

by stress observations in the area (derived from leak-off tests and density logs). We also took into consideration the limits imposed by frictional equilibrium in the crust. According to *Byerlee* [1978], the coefficient of frictional sliding μ should be in the range $0.6 < \mu < 1.0$.

The possible range of principal horizontal stresses can be determined from the stress polygons shown in figure 4.21. The plots are analogous to that shown in figure 4.13, and are constructed from the vertical stress expected at the depth at which breakouts are observed in the resistivity image (~10700 ft.), for a coefficient of sliding friction of 0.6. We omitted the part of the polygon corresponding to the reverse faulting regime, which is not feasible for the area. The vertical line represents the upper bound of least stress, corresponding to the stress gradient of 0.8 psi/ft we estimated from leak-off test data. This further reduces the acceptable ranges of $S_{h\min}$ and $S_{H\max}$ to those given by the polygon ABCD.

Contours in the figure 4.21 represent pairs of $S_{h\min}$ and $S_{H\max}$ in the range of uniaxial compressive strength C_0 expected for the rocks in the K2 reservoir of the Apiay-Guatiquía field, computed for the deviation (25°) and azimuth (195°) of the pilot hole. Contours of C_0 are curved in this case —instead of straight lines, as in figure 4.13— because they correspond to a deviated well. The left plot shows contours of compressive strength C_0 required to prevent the initiation of breakouts; the right plot, contours of C_0 required to prevent breakout widths larger than 55° (the aperture estimated from the resistivity image). The steep contour that runs close to the upper limit of the strike slip regime corresponds to the line for initiation of tensile fractures, for a rock with tensile strength T_0 of 0 psi.

A convenient scheme for testing whether a faulting regime holds for the area is to assume reasonable values for the coefficient of sliding friction and Poisson's ratio of the rocks in the study interval, and use the *Peska and Zoback* [1995] model to predict the location and aperture of breakouts at the deviation and azimuth of a well, under the stress conditions that are typical of such faulting regime.

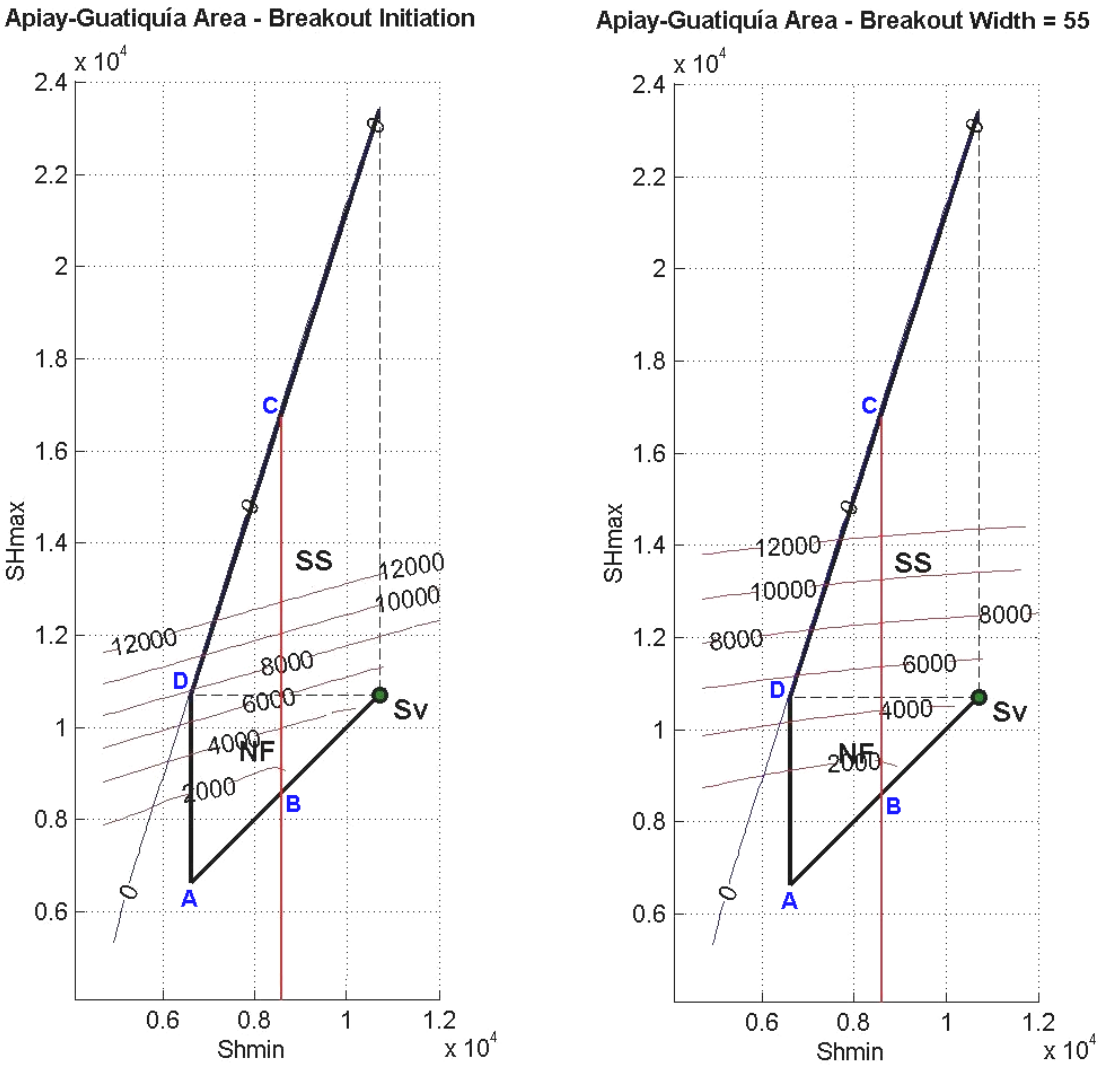

Figure 4.21: Stress state constrained by frictional strength (polygon, $\mu = 0.6$, $S_V = 10700$ psi) and by occurrence of borehole failure (contours). Contours on the left plot represent the compressive strength C_0 required to prevent the initiation of breakouts; the ones on the right, contours of C_0 required to prevent the breakouts from growing larger than 55°.

Consider a case in which the stress state is strike-slip —as has been observed in the Eastern Cordillera foothills— with $S_{h\min}$ = 7500 psi, and $S_{H\max}$ = 13600 psi. This results in a coefficient of sliding friction μ of 0.6. The circular plot on the left of figure 4.22 shows the calculated uniaxial compressive strength C_0 required to prevent the formation of breakouts in hypothetical wellbores drilled at different deviations and azimuths. The plot on the right shows the values of C_0 required to prevent the breakout aperture from growing larger than 55°.

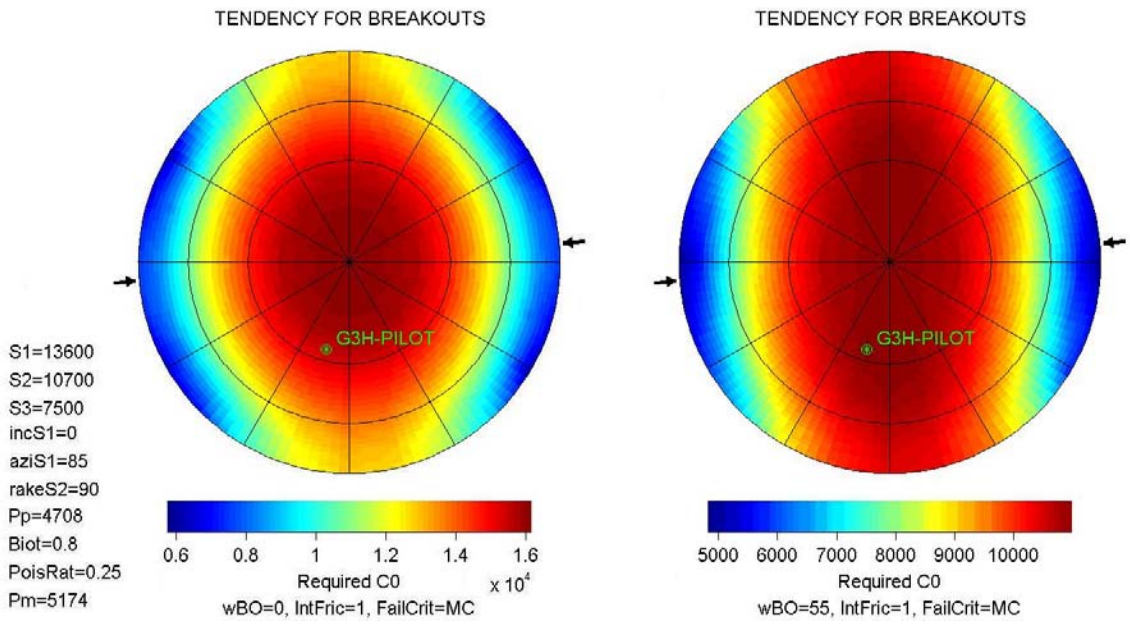

Figure 4.22: Modeling results for a strike-slip faulting regime with $S_{H\max} : S_V : S_{h\min}$ = 13600 : 10700 : 7500 psi. The left plot shows the compressive strength C_0 required to prevent the initiation of breakouts; the right plot, C_0 required to prevent the breakouts from growing larger than 55°.

The compressive strength required for breakouts to have the aperture observed in the pilot hole —whose location is indicated in the plots— seems unrealistically high for the rocks that failed under compression in the pilot hole. Recall that the breakouts shown in figure 4.16 coincide with high gamma ray readings, which indicates those are shale intervals. Core observations indicate that shales in the K2 Unit of the Apiay-Guatiquía field are strongly laminated, which makes them much weaker than sandstones, because the laminations introduce preexisting planes of weakness along which the rock would fail more easily. Notice also that the compressive strength required for preventing the formation of breakouts in vertical wells (~16000 psi) suggests that even sandstone intervals would be prone to compressive failure. The extensive drilling experience in the Apiay-Guatiquía area indicates the opposite, with most vertical wells being *in gauge*. These suggests that (1) $S_{h\min}$ is much smaller than the upper bound we assumed, implying that leak-off test data represent fracture initiation pressure, rather than instantaneous shut-in pressure; and (2) the faulting regime may not be strike-slip. Figure 4.23 shows the same plot configuration for $S_{H\max} : S_V : S_{h\min}$ = 11000 : 10700 : 6674 psi. This combination of stresses, in which $S_{H\max}$ is only slightly larger than S_V, and $S_{h\min}$ corresponds to a least-stress gradient of 0.62 psi/ft, produces a more stable scenario for

the angle and deviation of the pilot hole, although the compressive strength required to prevent breakouts in vertical wells still seems a little high for the area.

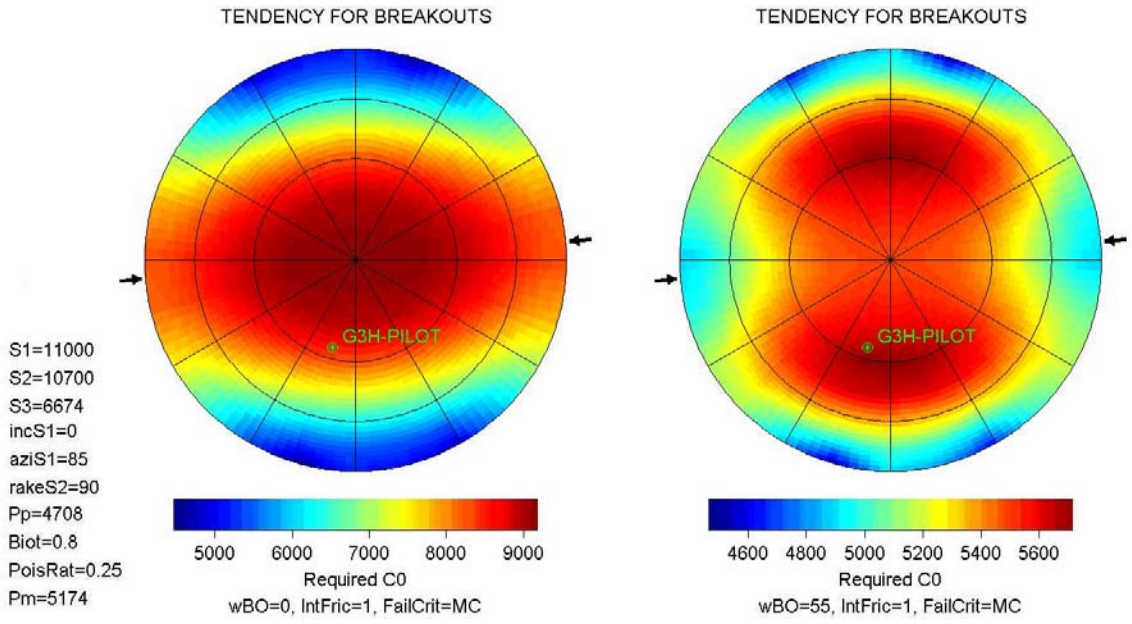

Figure 4.23: Modeling results for a strike-slip faulting regime with $S_{H\max} : S_V : S_{h\min}$ = 11000 : 10700 : 6674 psi. The left plot shows the compressive strength C_0 required to prevent the initiation of breakouts; the right plot, C_0 required to prevent the breakouts from growing larger than 55°.

Normal faulting scenarios result in smaller values of compressive strength required to prevent the initiation of breakouts. The example in figure 4.24 shows a stress state in which $S_{H\max} : S_V : S_{h\min}$ are 10700 : 8650 : 6600 psi. Wells along nearly all azimuths and deviations are more stable than in the strike-slip scenario. A scenario in which $S_{H\max}$ is closer to S_V seems more reasonable, given that the field is located in an area of transition from the strike-slip regime observed in the foothills, and the extensional regime observed on the eastern part of the basin, where most oil traps are bounded by normal faults. Such scenario is shown in figure 4.25. In this case, we show on the left plot the expected orientation of breakouts for wells at 15º increments of azimuth and deviation. Figure 4.26 shows the predicted position of breakouts in the borehole and in an image log for a hypothetical well with azimuth and deviation similar to those of the pilot hole. The result is in close agreement with the location of breakouts in figure 4.16.

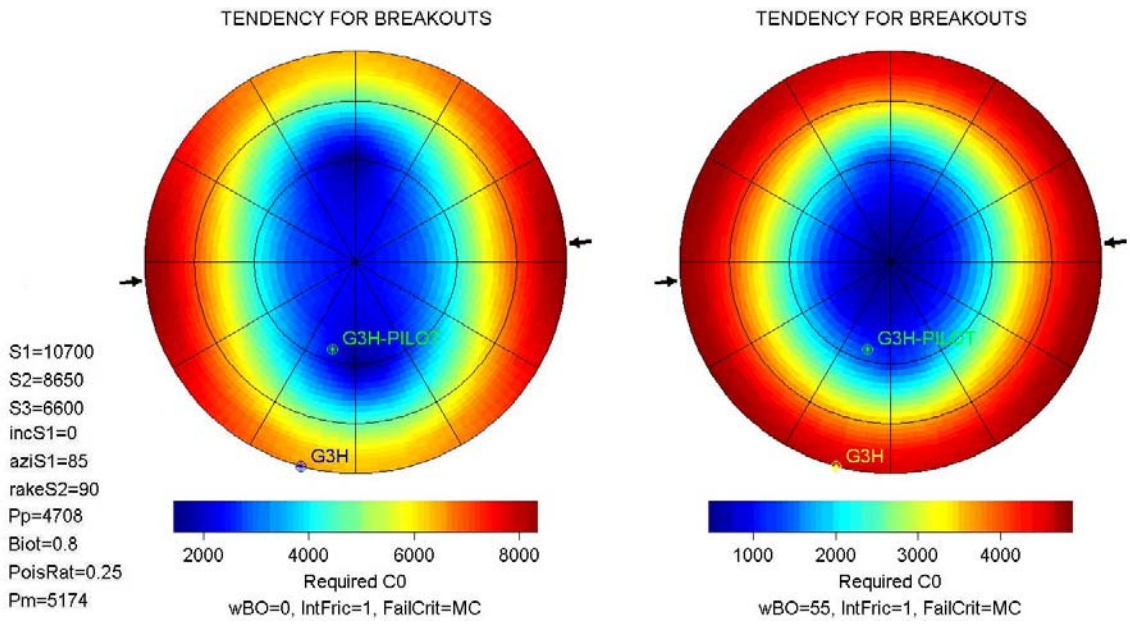

Figure 4.24: Modeling results for a normal faulting regime with $S_{H\max}$: S_V : $S_{h\min}$ = 10700 : 8650 : 6600 psi. The left plot shows the compressive strength C_0 required to prevent the initiation of breakouts; the right plot, C_0 required to prevent the breakouts from growing larger than 55°.

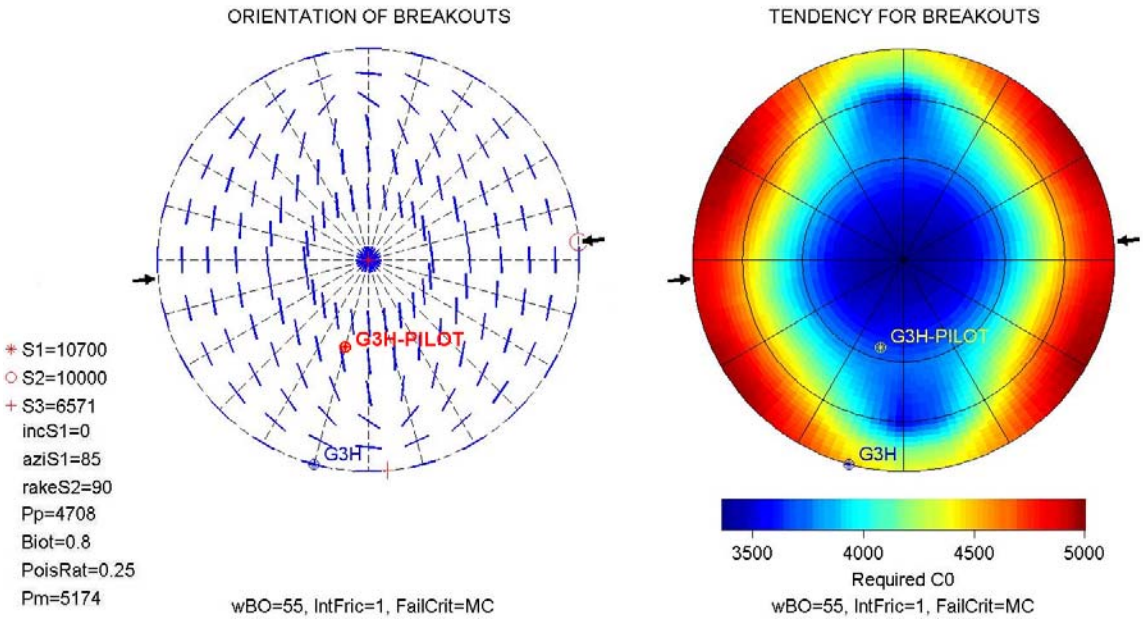

Figure 4.25: Modeling results for a normal faulting regime with $S_{H\max}$: S_V : $S_{h\min}$ = 10700 : 10000 : 6571 psi. The left plot shows the the expected breakout orientation; the right plot, C_0 required to prevent the breakouts from growing larger than 55°. The two bottom plots show the predicted position of breakouts in a wellbore image.

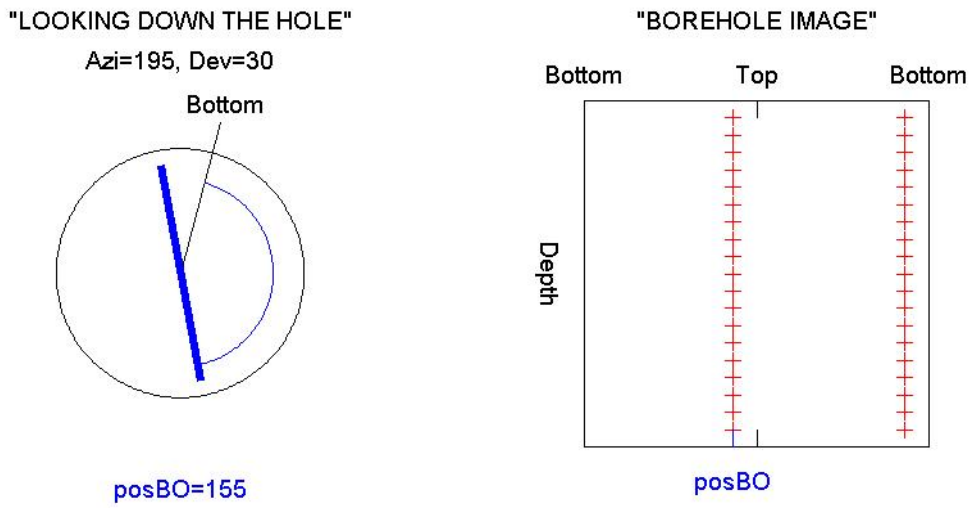

Figure 4.26: Predicted position of breakouts "looking down the hole" (left) and in a wellbore image (right), for a normal faulting regime with $S_{H\max} : S_V : S_{h\min}$ = 10700 : 10000 : 6571 psi.

The most stable trajectory for inclined wells can be estimated from the stereographic plots of compressive strength. For the case of Apiay-Guatiquía, wells drilled along the north-south direction are more stable than those drilled in the east-west direction.

As pointed out before, the data suggest that leak-off tests represent fracture initiation pressures, rather than least stress measurements. We estimate that the actual value of $S_{h\min}$ is in the range between 6200 and 6700 psi, which corresponds to least stress gradients between 0.58 and 0.62 psi/ft. Values of $S_{H\max}$ in a range from 8500 to 11000 psi produced defensible results, but it is likely that the gradient of maximum horizontal stress is close to that of vertical stress, which is 1 psi/ft.

The results of our stress field analysis are in close agreement with those of the study by *Last et al*. [1997] for the Apiay-Guatiquía area, which was based on four-arm caliper data from vertical wells. Horizontal stress magnitudes from this work are slightly lower than those found by *Last et al.* [1997]. *Last et al.* [1997] assumed a least-stress gradient (0.65), which implies a coefficient of sliding friction that is out of the range given by *Byerlee* [1978] for the Earth's crust. *Castillo and Mujica* [1990] determined the azimuth of breakouts in the well Guayuriba-2 —located relatively close to the Apiay-Guatiquía area— but did not get a consistent orientation through the interval where they found

breakous. The other two wells analyze by *Castillo and Mujica* [1990] are far from the study area, but they also show a roughly east-west direction of maximum compression.

4.4 Conclusions

The K2 Unit reservoir of the Apiay-Guatiquía oil field is essentially a two-phase, oil-water system that benefits from a very active regional aquifer that keeps reservoir pore at a nearly hydrostatic level.

The K2 Unit is a massive body of highly mature, medium to coarse, locally conglomeratic, white sandstones of cratonic provenance, deposited in an environment of stacked, braided stream channels, intercalated by a few streaks of gray, laminated shale that are prone to compressive failure.

The azimuth of breakouts suggests the direction of maximum horizontal compression is roughly east-west. Normal faulting is the most plausible faulting regime for the Apiay-Guatiquía area, although a strike-slip regime cannot be completely discarded in the absence of compressive strength data. The normal faulting regime at this location, and in the Llanos Basin in general, results from the release of compressive stresses produced by the Borde Llanero Suture, i.e., the system of strike slip/thrust faults that separates the Llanos basin from the Eastern cordillera.

We effectively constrained the range of principal horizontal stress gradients to [0.58 – 0.62] psi/ft for $S_{h\min}$, and [0.79 – 1.03] psi/ft for $S_{H\max}$. Measuring mechanical properties in cores from Apiay-Guatiquía, performing leak off tests, and acquiring image data in wells to be drilled would greatly help to precisely determine the magnitude of minimum and maximum horizontal stresses. We believe the most likely distribution of stresses is given by $S_V : S_{H\max} : S_{h\min} = 1.0 : 0.94 : 0.61$ psi/ft, which results in a mean stress gradient of 0.85 psi/ft.

Reported leak-off test data represent fracture initiation pressures, and can only be used qualitatively.

Measuring mechanical properties in cores from the K2 Unit of Apiay-Guatiquía, performing additional leak-off tests, and acquiring image data in wells to be drilled would greatly help to determine the precise magnitude of minimum and maximum horizontal stresses.

4.5 References

Anderson, E. M., 1937, The dynamics of sheet intrusion: *Proc. R. Soc. Edinburgh*, **58**, 242-251.

Addis, M. A., N. C. Last, and N. A. Yassir, 1996, Estimation of horizontal stresses at depth in faulted regions and their relationship to pore pressure variations: Paper SPE 28140.

Byerlee, J. D., 1978, Friction of rock: *Pure Applied Geophysics*, **116**, 615-626.

Castillo, J. E., and J. Mojica, 1990, Determinación de la orientación de esfuerzos actuales a partir de deformaciones tectónicas ("breakouts") en algunos pozos petroleros de los Llanos Orientales y del Valle Medio del Magdalena, Colombia: *Geología Colombiana*, No. 17, 123-132.

Charlez, P.A., E. Bathellier, C. Tan and O. Francois, 1998, Understanding the present in-situ state of stress in the Cusiana field – Colombia: Paper SPE/ISRM 47208.

Cooper, M. A., F. T. Addison, R. Alvarez, M. Coral, R. H. Graham, A. B. Hayward, S. Howe, J. Martinez, J. Naar, R. Penas, A. J. Pulham, and A. Taborda, 1995, Basin development and tectonic history of the Llanos Basin, Eastern Cordillera and Middle Magdalena Valley, Colombia: *American Association of Petroleum Geologists Bulletin*, **79**, 1421-1443.

Dickinson, W. R., 1985, Interpreting provenance relations from detrital modes of sandstones, in *Provenance of Arenites*, Zuffa, G. C. Ed., Reidel, 333-361.

Han, D.-H., 1986, *Effects of Porosity and Clay Content on Acoustic Properties of Sandstones and Unconsolidated Sediments*, Ph.D. dissertation, Stanford University.

Jaeger, J. C., and N. G. W. Cook, 1979, *Fundamentals of Rock Mechanics*, 3rd. ed., 593 pp., Chapman and Hall, New York.

Kirsch, G., 1898, Die Theorie der Elasticitaet und die Bedurnifsse der Festigkeitslehre: *VDI Z.*, **42**, 707.

Last, N. C., and M. R. McLean, 1996, Assessing the impact of trajectory on wells drilled in an overthrust region: Paper SPE 30465.

Last, N. C., J. D. Lopez, and M. E. Markley, 1997, Case history: Integration of rock mechanics, structural interpretation and drilling performance to achieve optimum

horizontal well planning in the Llanos Basin, Colombia, South America: Paper SPE 38601, *Transactions of the 1997 SPE Annual Technical Conference*, 359-374.

Mastin, L., 1988, Effect of borehole deviation on breakout orientations, *Journal of Geophysical Research*, **93**, 9187-9195.

McCollough, C.N., 1987, Geology of the super giant Caño Limon field in the Llanos Basin, Colombia: *Transactions of the Fourth Circum-Pacific Energy and Mineral Resources Conference*, 299-316.

Moos, D., and M. D. Zoback, 1990, Utilization of observations of wellbore failure to constrain the orientation and magnitude of crustal stresses: Application to continental, Deep Sea Drilling Project, and Ocean Drilling Project boreholes: *Journal of Geophysical Research*, **95**, 9305-9325.

Moos, D., and M. D. Zoback, 1993, State of stress in the Long Valley Caldera: *Geology Research*, **21**, 837-840.

Mueller, B., Reinecker, J., Heidbach, O. and Fuchs, K., 2000: The 2000 release of the World Stress Map (available online at www.world-stress-map.org).

O'Leary, J., E. Warren, G. Geehan, R. Herbert, and R. Graham, 1997, Evaluation of reservoir quality in the Llanos foothills, Colombia: *VI Simposio Bolivariano de Cuencas Subandinas*, 163-166.

Peska, P., and M. D. Zoback, 1995, Compressive and tensile failure of inclined well bores and determination of in situ stress and rock strength: *Journal of Geophysical Research*, **100**, No. B7, 12791-12811.

Villamil, T., 1998, A new sequence stratigraphic model for basinal Cretaceous facies of Colombia, in *Paleogeographic Evolution and Non-Glacial Eustasy, Northern South America*, Pindell J. L. and C. Drake Eds. SEPM Special Publication No. 58, 161-216.

Villegas, M. E., S. Bachu, J. C. Ramon, and J. R. Underschultz,1994, Flow of formation waters in the Cretaceous-Miocene succession of the Llanos Basin, Colombia: *American Association of Petroleum Geologists Bulletin*, **78**, 1843-1862.

Zoback, M. D., and P. Peska, 1995, In-situ stress and rock strength in the GBRN/DOE Pathfinder Well, South Eugene Island, Gulf of Mexico: Paper 29233.

This page intentionally left blank

Chapter 5

Rock Physics Study of the K2 Unit of the Apiay-Guatiquía Oil Field

Rock physics provides the link between seismic measurements and petrophysical properties, which control the storage and fluid-flow capacity of a subsurface reservoir, and consequently, have a great impact on the economics of a project in the petroleum industry. To take advantage of such an important link it is necessary to establish relationships that link seismic derived attributes, like P- and S-wave impedance and velocity, and rock properties, such as porosity and permeability. In any survey, results will be influenced by both system properties, such as lithology, pore pressure, reservoir heterogeneities, types and properties of pore fluids, and saturation of the different fluid phases; and by intrinsic properties of the seismic survey, like frequency, sampling rate, data quality, and available offsets.

In this chapter I address how porosity, lithology, clay content, saturation changes, pore pressure, and temperature influence the seismic response of K2 Unit reservoir rocks, under the stress conditions observed in the Apiay-Guatiquía area, which I discussed in Chapter 4 of this thesis. In our analysis we integrate laboratory measurements, well logs and rock and fluid PVT data from the K2 Unit reservoir. We explore the relationships between petrophysical properties and seismic parameters, using core and well log observations, and compare them to those derived from other datasets. We find that porosity has the largest influence on the elastic properties of this sandstone reservoir.

5.1 Available Well Logs and Core Measurements

We received a complete suite of well logs for 19 vertical wells in the Apiay-Guatiquía area, which includes curves of gamma-ray, spontaneous potential, bulk density, neutron porosity, P-wave slowness, caliper, and shallow, intermediate, and deep resistivities for nearly all wells. Four of these wells —the Apiay wells 3, 9, 10, and 11—

have cored sections of significant length. Figures 5.1 to 5.4 summarize the log data for these wells, along with previous core measurements of porosity and grain density. Table 5.1 summarizes the keywords used in those plots.

Table 5.1: A description of well log keywords.

Track	Keyword	Description
Porosity	PHID	Density porosity, computed from the bulk density log.
Porosity	PHIN	Neutron porosity log data.
Porosity	Core	Porosity, measured in core samples.
Density	RHOB	Bulk density log data.
Density	Grain	Grain density, measured in core samples.
Velocity	VP	P-wave velocity, computed from the transit time log.
Resistivity	MSFL	Shallow resistivity from the micro-spherical focused log tool.
Resistivity	LLS	Intermediate resistivity from the shallow laterolog tool.
Resistivity	LLD	Deep resistivity from the deep laterolog tool.
Caliper	CALI	Borehole diameter from the caliper log tool.
Caliper	BIT	Approximate bit size.

A quick look to the well log plots yields the following important points:

1. The relatively low readings of the gamma-ray log reflect the low clay-content of sandstones in the K2 Unit.
2. The borehole condition is generally good along the K2 section, and consequently the well log data are of good quality, with the exception of some readings at the depths of shaly/silty streaks that failed under compression.
3. Grain density values from core measurements align along a very consistent value. The median of grain density measurement is 2.65 gr/cc.
4. Density and neutron porosity (PHID and PHIN, respectively) are in good agreement for most of the K2. The quality of the density and neutron logs is considered good, which suggests that log-derived porosity data are correct at all depths, except at those where rocks failed under compression.

5. There is a consistent misfit between core porosity and log porosity, though. Core measurements are appreciably smaller than the corresponding density and neutron porosity readings.
6. The downward increasing trends of bulk density and velocity reflect a decrease in porosity due to compaction.
7. Although it is deeper than Apiay-9, the well Apiay-3 has higher porosities. Apiay-9 is significantly higher in the structure than Apiay-3, which results in a longer oil column in Apiay-9.
8. The water-based drilling fluids used in the Apiay and Guatiquía wells have different salinity than the formation water. The separation between deep, medium, and shallow resistivity curves indicates some degree of mud filtrate invasion, and implies that the K2 sandstones have good permeability. The marked reduction in deep resistivity shows the contact between the oil- and water-bearing zones.

The relationship between permeability and porosity in rocks from the K2 Unit of Apiay-Guatiquía is close to that observed for the Fontainebleau sandstone. Figure 5.5 shows cross-plots of core porosity and permeability for wells number 3, 9, 10 and 11. The gray trend belongs to the Fontainebleau sandstone, and is shown for reference. Ecopetrol researchers measured porosity and permeability at different confining pressures in some samples from wells Apiay-3 and Apiay-10, to determine the reduction in those petrophysical properties upon loading. Figure 5.6 shows the pressure-dependent porosity and permeability data.

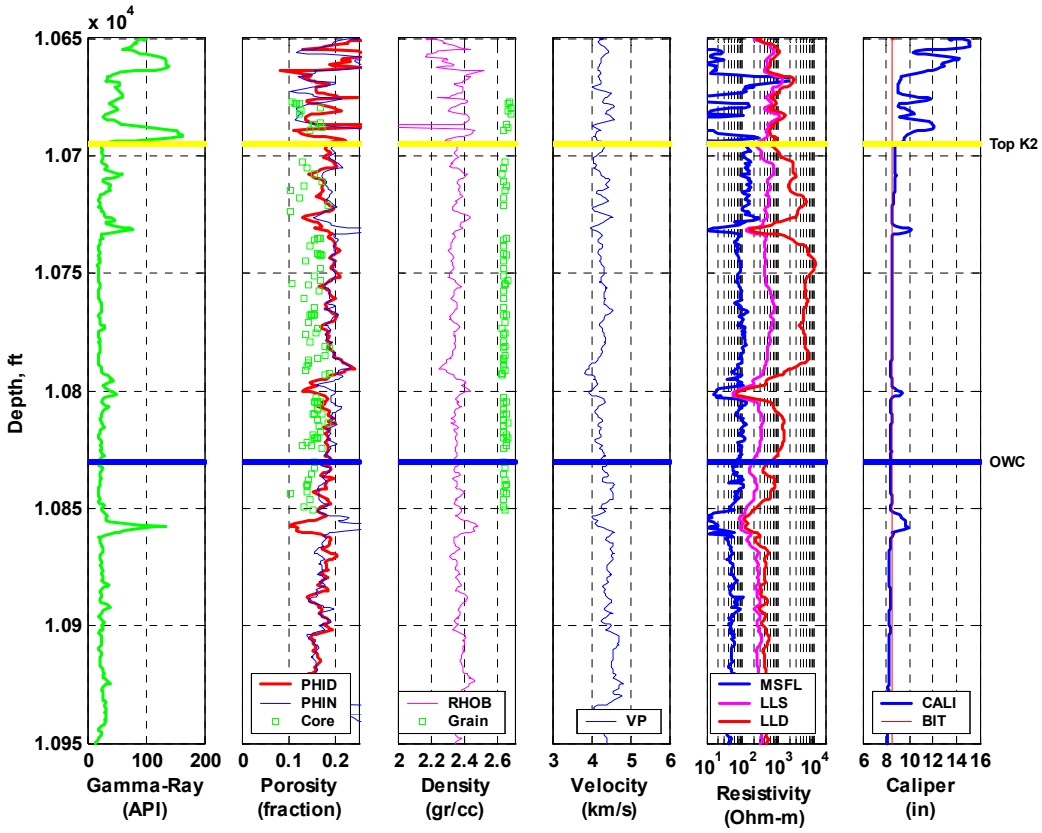

Figure 5.1: A set of plots of log data for well Apiay-3, along with core measurements of porosity and grain density. The horizontal lines represent well markers for the top of the K2 Unit (Top K2), and the oil-water contact (OWC).

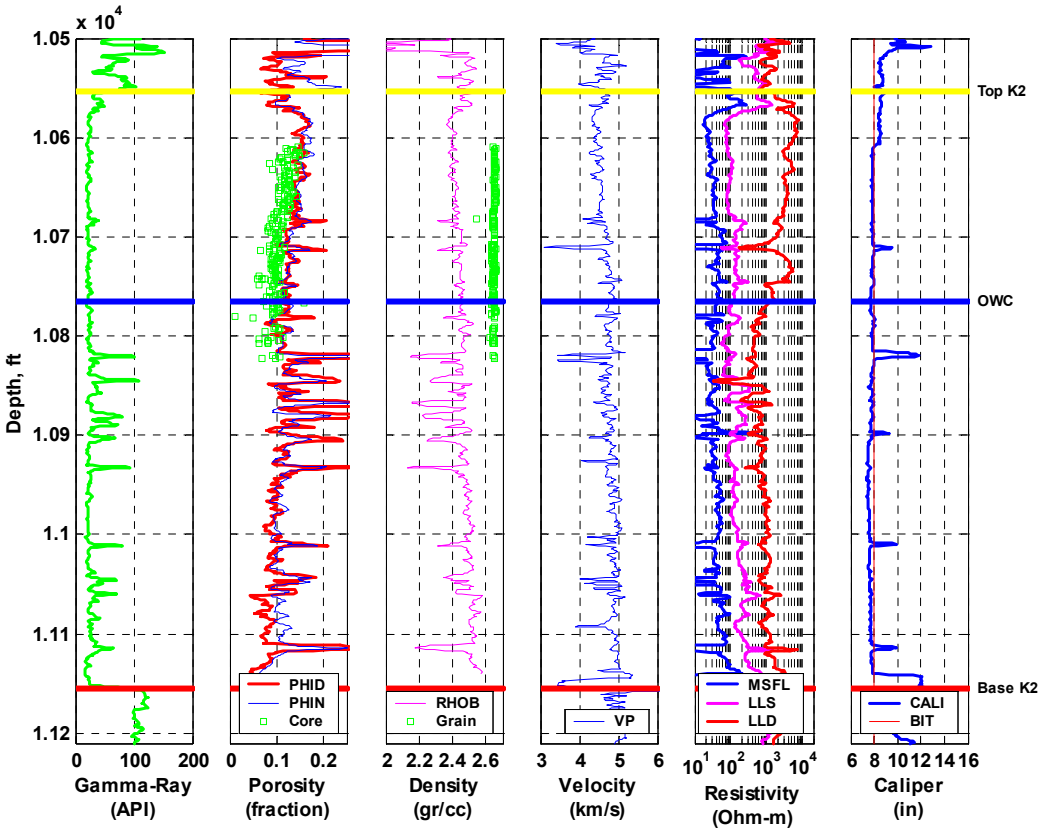

Figure 5.2: A set of plots of log data for well Apiay-9, along with core measurements of porosity and grain density. The horizontal lines represent well markers for the top of the K2 Unit (Top K2), the oil-water contact (OWC), and the top of Paleozoic-age sediments (Base K2).

.

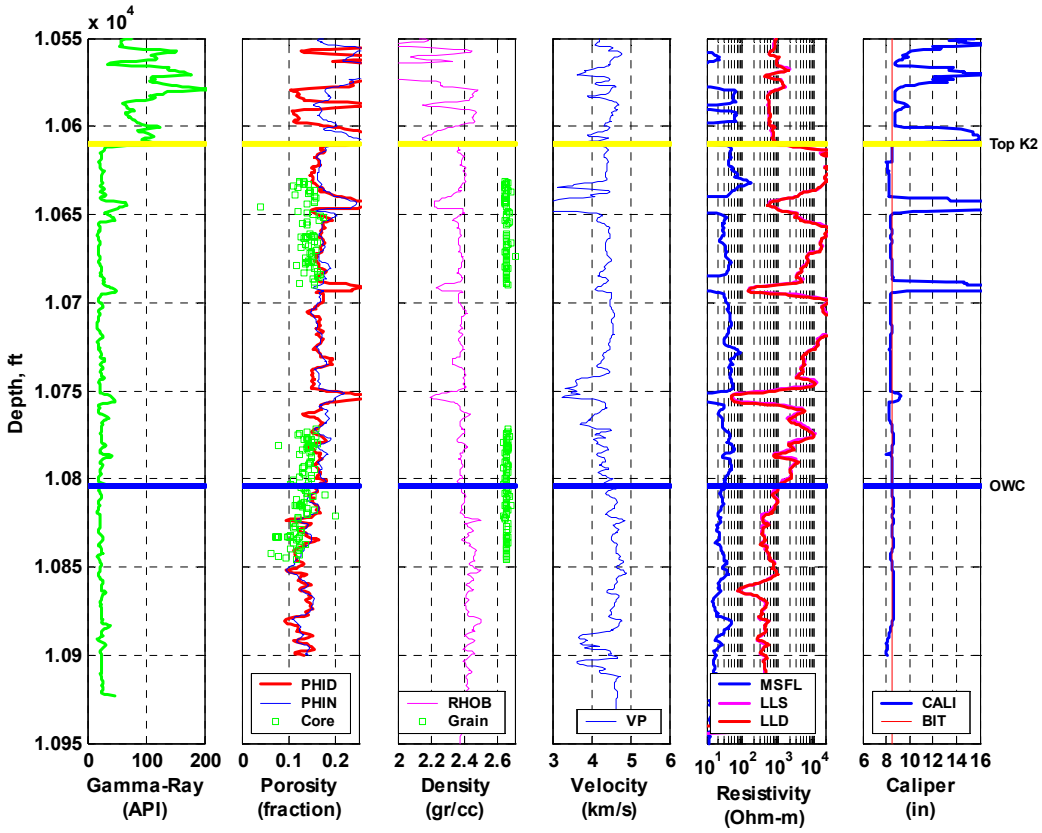

Figure 5.3: A set of plots of log data for well Apiay-10, along with core measurements of porosity and grain density. The horizontal lines represent well markers for the top of the K2 Unit (Top K2), and the oil-water contact (OWC).

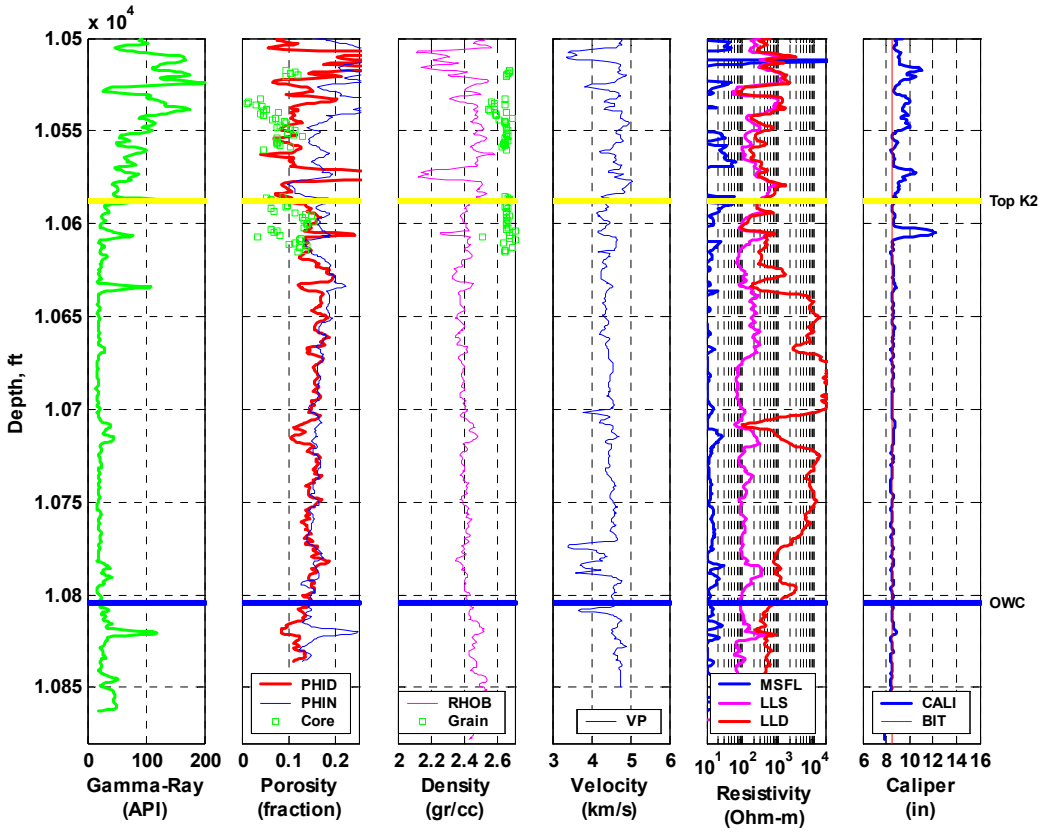

Figure 5.4: A set of plots of log data for well Apiay-11, along with core measurements of porosity and grain density. The horizontal lines represent well markers for the top of the K2 Unit (Top K2), and the oil-water contact (OWC).

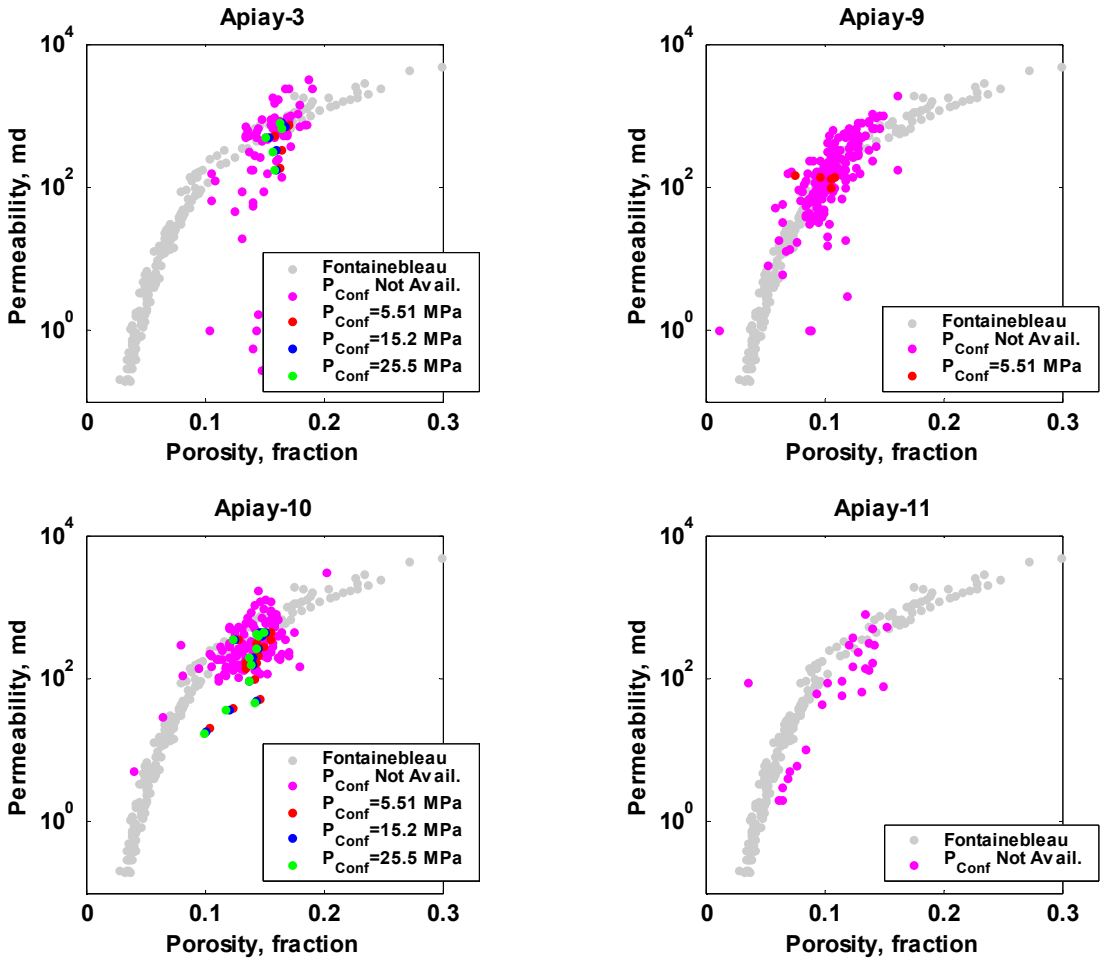

Figure 5.5: Scatter plots of permeability vs. porosity measured in core samples from wells Apiay-3, Apiay-9, Apiay-10, and Apiay-11, color-coded by confining pressure when available. Gray dots correspond to permeability and porosity measurements in Fontainebleau sandstone.

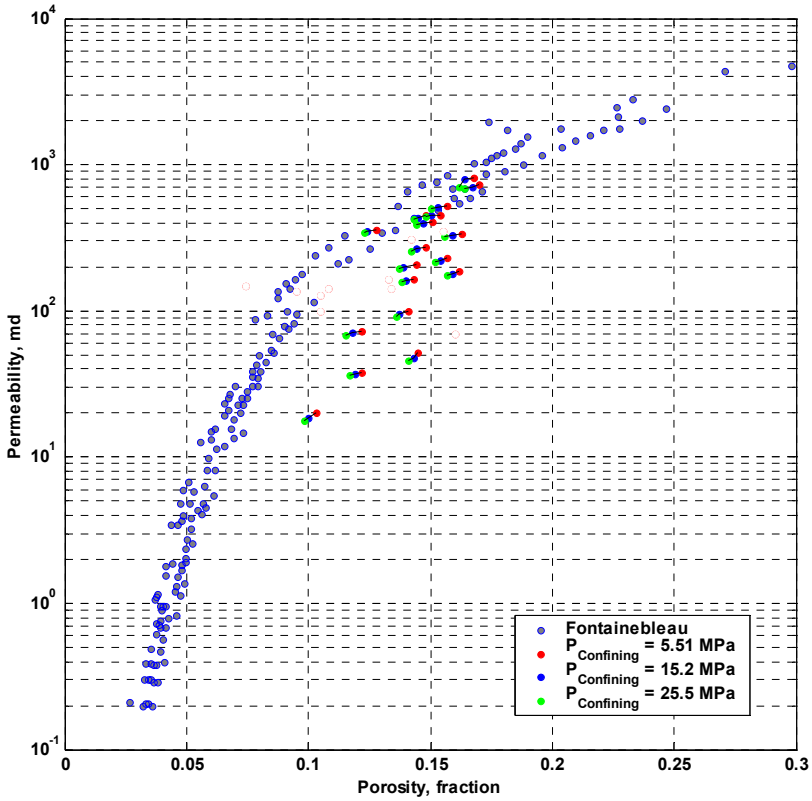

Figure 5.6: Scatter plots of pressure-dependent permeability vs. porosity measured in core samples from wells Apiay-3, and Apiay-10. Gray dots correspond to permeability and porosity measurements in Fontainebleau sandstone.

5.2 Petrography

An examination of petrographic data from thin section analyses provided by Ecopetrol indicates that the K2 Unit sandstones are mostly mature *quartzarenites* —i.e., clean sandstones (with less than 15 percent *matrix*) with no more than five percent of either feldspar or rock fragments— and *sub-litharenites* —i.e., clean sandstones with between five and 25 percent rock fragments, and a lesser amount of feldspar. Figures 5.7 to 5.9 show the location of thin section samples in wells Apiay-3, Apiay-9 and Apiay-10, along with the mineral composition of detrital grains in terms of normalized fractions of quartz, feldspar and lithics, the total percentage of cementing material (including pore-filling kaolinite), and the normalized composition of the cement fraction. Figures 5.10 shows a QFL diagram for sandstone classification and a triangular plot of the composition of the cement fraction.

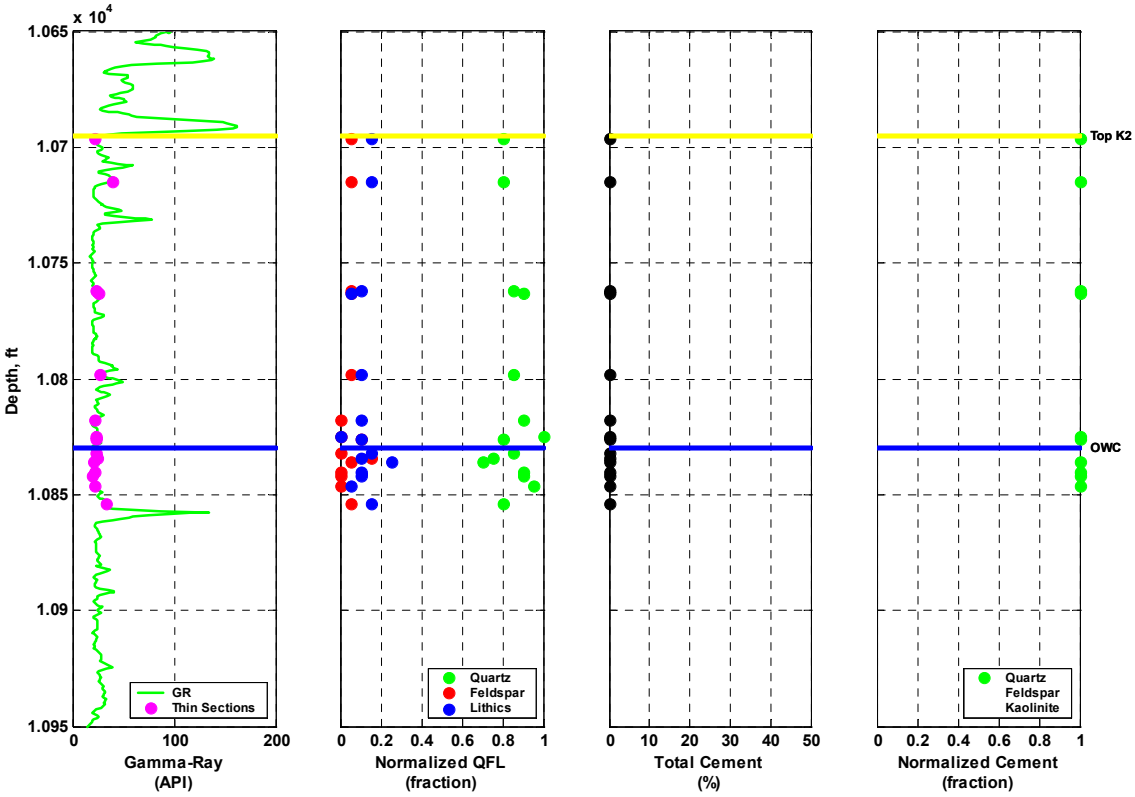

Figure 5.7: Location of thin-section samples from well Apiay-3. The second track shows the normalized composition of detrital grains. The third shows the total percentage of cement, and the fourth, the normalized composition of the cement fraction.

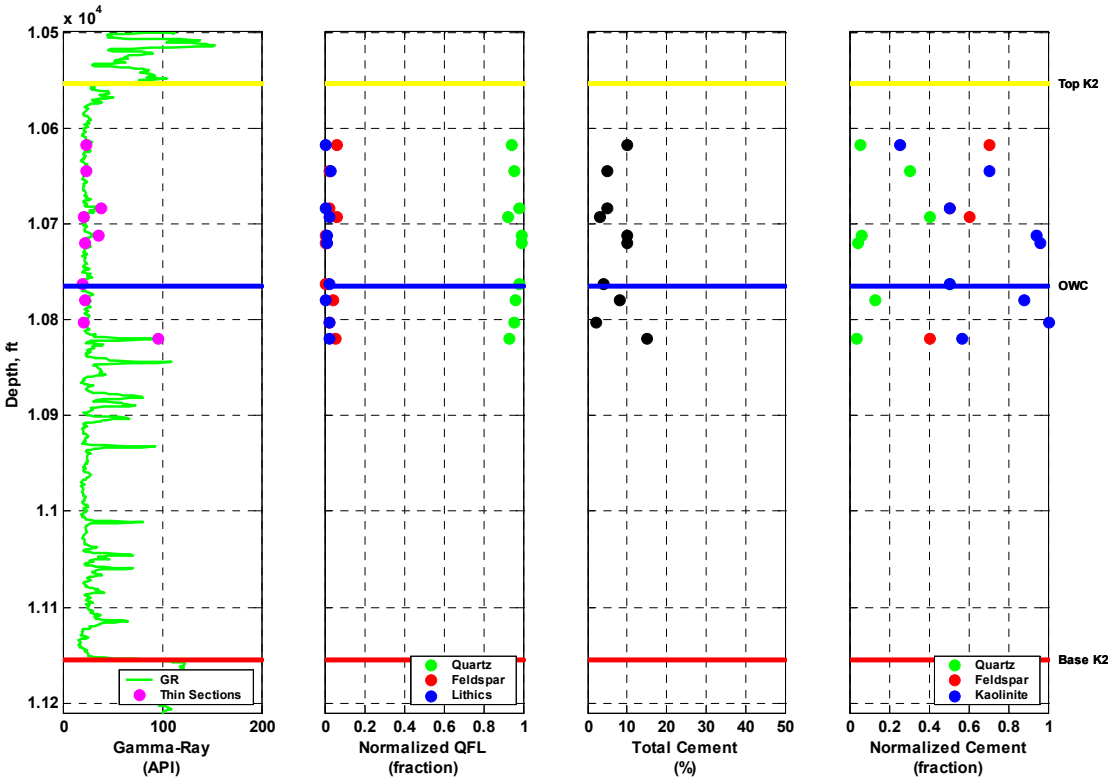

Figure 5.8: Location of thin-section samples from well Apiay-9. The second track shows the normalized composition of detrital grains. The third shows the total percentage of cement, and the fourth, the normalized composition of the cement fraction.

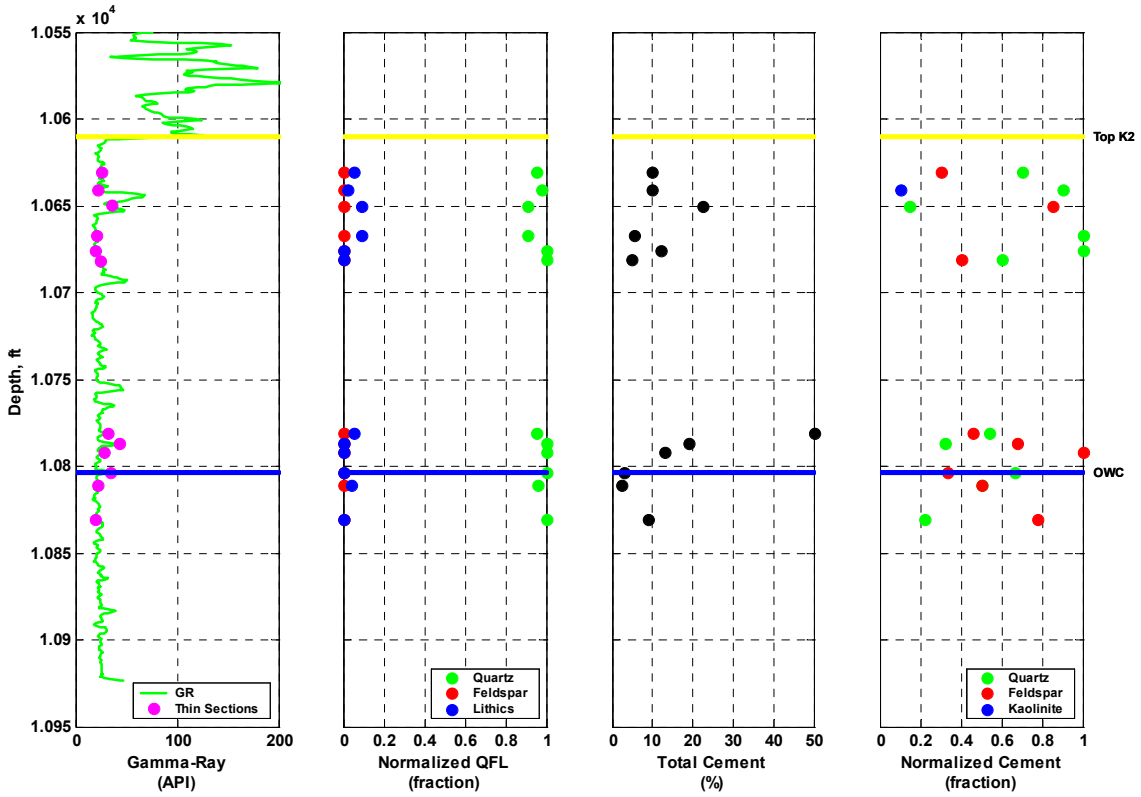

Figure 5.9: Location of thin-section samples from well Apiay-10. The second track shows the normalized composition of detrital grains. The third shows the total percentage of cement, and the fourth, the normalized composition of the cement fraction.

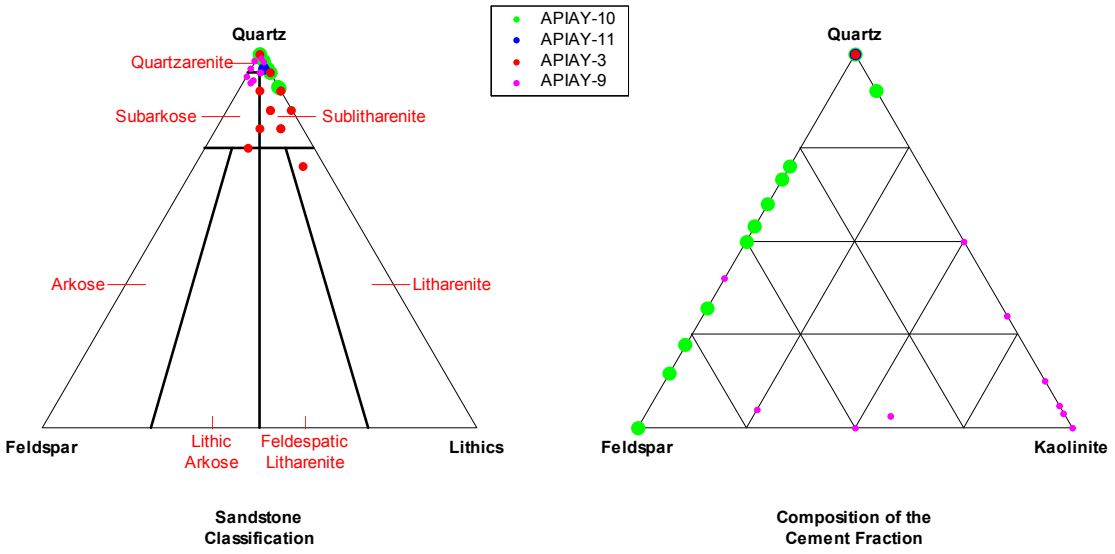

Figure 5.10: QFL diagram for sandstone classification, and composition of the cement fraction for some K2 Unit sandstone samples.

Although the K2 Unit is composed of very clean and continuous sandstone bodies, petrographic data reveals some lateral variability in terms of composition and cementation. Samples from well Apiay-3 have only traces of quartz cement, while those from Apiay-9 are cemented with quartz overgrowths, feldspar, and between 2.5 and 8.5% kaolinite, the latter most probably formed by diagenetic dissolution of feldspar grains. Samples from well Apiay-10 have a mixture of quartz and feldspar cement.

Thin sections revealed also that sandstones in the K2 are very fine to very coarse grained, sub-angular to sub-rounded sandstones, poorly sorted in some areas (Apiay-3 and Apiay-10), and well sorted in others (Apiay-9). Figure 5.11 summarizes the textural data.

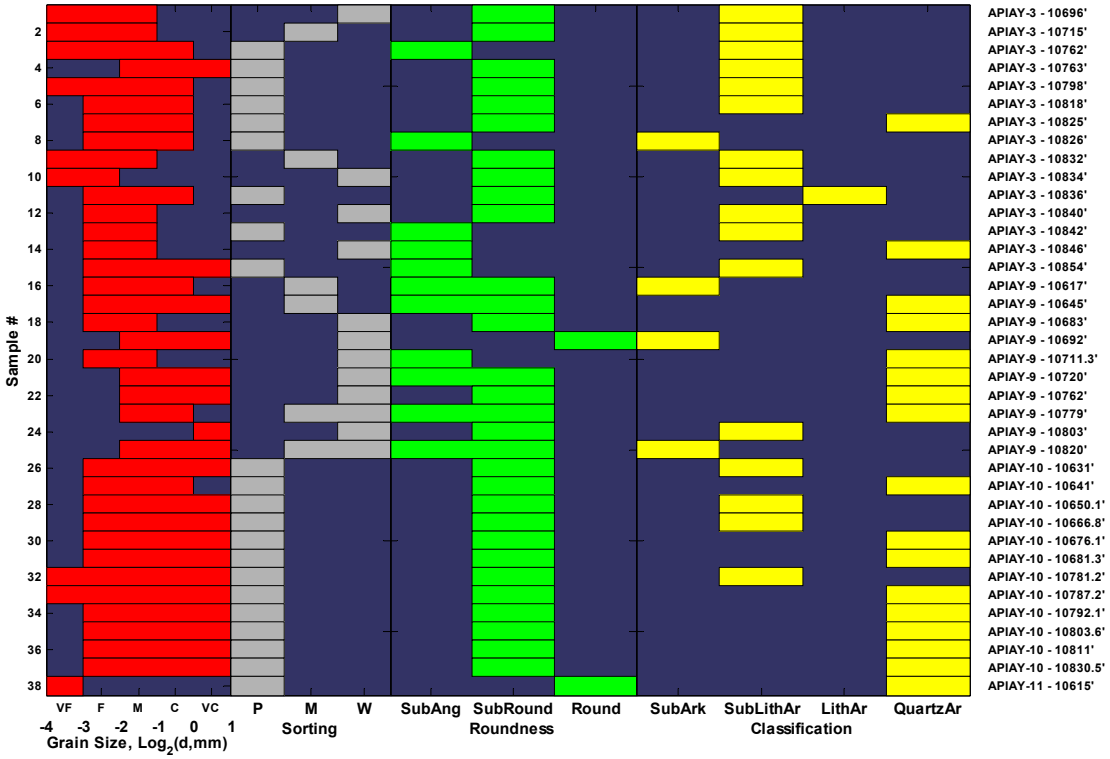

Figure 5.11: A summary of textural characteristics of K2 Unit sandstones.

5.3 K2 Unit Reservoir Lithofacies

As described in Chapter 4, the K2 Unit reservoir is a thick sequence of mostly medium- to coarse-grained, locally conglomeratic, well-cemented and well-consolidated

sandstones, with a few streaks of shale. Based on their grain size, amalgamation, internal structure, and position in the stratigraphic sequence, *Nieto and Rojas* [1998] classified the K2 Unit rocks in 13 different lithofacies. They grouped lithofacies of similar sedimentological, textural, and structural features in six lithotypes whose descriptions follow:

1. Well-sorted, fine- to medium-grained, locally conglomeratic sandstones with cross stratification (stacked channel facies).
2. Massive sandstones, with stylolites (cemented, base-of-channel facies).
3. Very fine- to fine-grained, kaolinitic sandstones with plane-parallel stratification, and evidence of microfractures (stacked channel facies).
4. Black and dark-gray shales with tiny siltstone intercalations (abandoned channel facies).
5. Well-sorted, medium-grained to conglomeratic sandstones with cross stratification, sometimes with stylolites (stacked channel facies).
6. Very fine- to fine-grained sandstones with cross stratification, and low vertical to horizontal permeability ratio (crevasse splay facies).

In terms of rock quality, lithotype 1 represents the rocks of best petrophysical properties, and has the highest volumetric proportion. Rocks of lithotype 5 are of good quality, while lithotypes 2 and 3 are intermediate to good quality facies. Lithotypes 4 and 6 are considered non-pay rocks.

5.4 Core Samples Used in This Study

Core samples are by far the most representative piece of information about reservoir rocks. We selected 14 samples for rock physics measurements from the cored intervals of wells Apiay-3 (A-3) and Apiay-9 (A-9). Table 5.2 shows a description of the samples, which are representative of the two lithologies (sand and shale) observed in the K2 Unit reservoir, and of the six lithotypes determined by Ecopetrol geologists [*Nieto and Rojas,* 1998]. The 14 samples cover nearly the entire porosity range observed in previous core measurements and in well logs. Figure 5.12 shows the gamma-ray logs of wells Apiay-3

and Apiay-9, the distribution of lithotypes in those wells, and the depths of samples we used in this study.

Table 5.2: A description of the core samples used in this study.

Number	Well	Depth	Lithotype	Visual description
1	A-3	10683'6"	4	Dark gray SHALE sample. CRACKED – Impossible to measure velocity under confining pressure.
2	A-3	10685'9"	4	Dark gray, fine-grained SHALE with vertical bedding. Releases some residual oil upon pressurization.
3	A-3	10700'5"	5	Medium- to coarse-grained, well cemented SANDSTONE without layering. Appears to have a fracture at 70º. Residual oil.
4	A-3	10749'6"	1	Brown, coarse-grained SANDSTONE with bedding at 45º and large visual porosity. Turns black upon pressurization. Residual oil.
5	A-3	10782'3"	1	Coarse-grained SANDSTONE with bedding at 45º. Large visible pores. Turns black upon pressurization. Residual oil.
6	A-3	10784'4"	3	Coarse-grained, light gray SANDSTONE with faint bedding. Turns black upon pressurization. Residual oil.
7	A-3	10789'5"	3	Fine- to coarse-grained SANDSTONE with cross stratification at 45º. Residual oil.
8	A-3	10823'11"	2	Fine-grained, cemented SANDSTONE with faint oblique bedding. Clear, no residual oil.
9	A-3	10829'6"	2	Fine-grained, cemented SANDSTONE without obvious visual layering. Clear, no residual oil.
10	A-3	10839'11"	5	Medium- to coarse-grained, well cemented SANDSTONE without layering. Clear, no residual oil.
11	A-9	10690'	6	Fine-grained SANDSTONE with black colored, almost vertical beds. Looks very dense.
12	A-9	10695'9"	6	Medium- to coarse-grained SANDSTONE with bedding at about 45º. Vertical fracture cutting through layers. Residual oil.
13	A-9	10719'4"	5	Light gray, coarse-grained, locally conglomeratic SANDSTONE with faint layering. Turns black upon pressurization. Residual oil.
14	A-9	10808'5"	5	Coarse-grained SANDSTONE with vertical bedding and large visible pores. Vertical fracture. Clear, no residual oil.

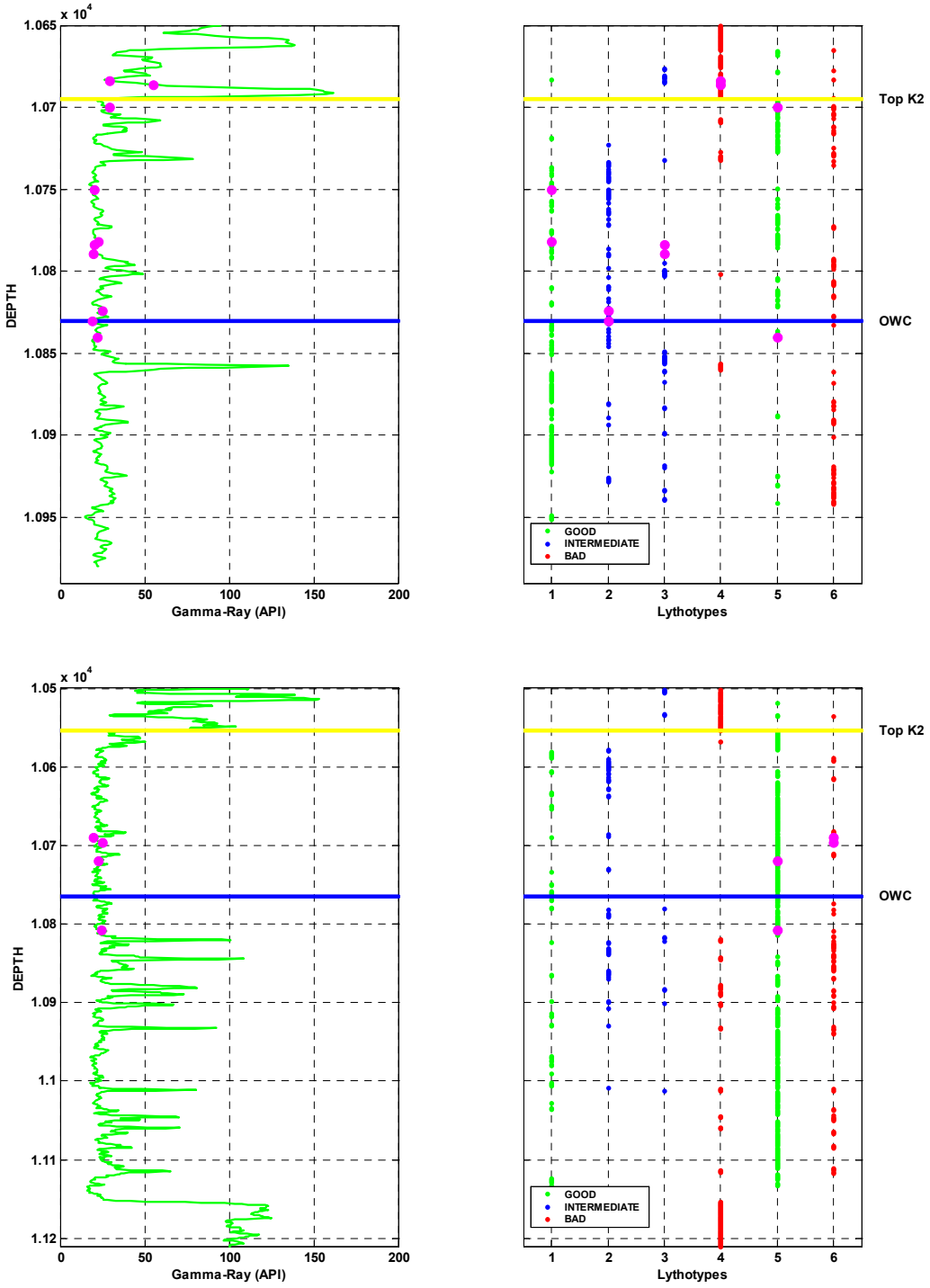

Figure 5.12: Location of core samples used in this study, along with the distribution of lithotypes for the corresponding wells. Top: Well Apiay-3. Bottom: Well Apiay-9.

Most cores from shale intervals in the K2 were fractured during recovery, making it very difficult to obtain a sample plug. Shale samples #1 and 2 were actually taken from the shale that seals the reservoir. Since the transition between the K2 and K1 sedimentary sequences is concordant, this cap shale is still representative of the K2 environment.

5.5 Core Measurements

We measured P- and S-wave velocities, bulk density, porosity and permeability on core plugs 1" long and 1" in diameter. The measurements were made under the supervision of Dr. Manika Prasad of the Stanford Rock Physics Lab. In this section I describe in proper detail the results of those measurements.

5.5.1 Porosity, Permeability, and Bulk Density Measurements

Before cleaning the 13 core samples, we determined their porosity and bulk density at room conditions, using the Boyle's law method. I summarize the results of those measurements in Table 5.3.

Table 5.3: A summary of porosity and bulk density measurements on uncleaned core samples.

Sample Number	Well	Depth	Lithotype	Porosity, fraction	Bulk Density, gr/cc	Grain Density, gr/cc
2	A-3	10685'9"	4	0.013	2.460	2.492
3	A-3	10700'5"	5	0.142	2.240	2.611
4	A-3	10749'6"	1	0.151	2.219	2.613
5	A-3	10782'3"	1	0.169	2.134	2.568
6	A-3	10784'4"	3	0.140	2.212	2.573
7	A-3	10789'5"	3	0.158	2.218	2.635
8	A-3	10823'11"	2	0.163	2.228	2.662
9	A-3	10829'6"	2	0.138	2.271	2.634
10	A-3	10839'11"	5	0.143	2.271	2.651
11	A-9	10690'	6	0.098	2.395	2.655
12	A-9	10695'9"	6	0.081	2.400	2.610
13	A-9	10719'4"	5	0.095	2.372	2.621
14	A-9	10808'5"	5	0.106	2.369	2.650

After measuring P- and S-wave velocities at high confining pressure, we sent the samples for cleaning, and re-measured porosity and bulk density, along with permeability. Table 5.4 presents the results of these measurements. Figure 5.13 is a comparison of porosity and bulk density measurements before and after cleaning. Notice that samples from the transition zone changed less than those from the oil-bearing zone. Samples from the oil-bearing zone have larger residual saturations —and therefore larger porosity changes— because oil is more viscous than water, and tends to get trapped more easily. The bottom plots show trends of bulk density versus porosity before and after cleaning. Notice that once they are cleaned the sandstone samples align along a nearly perfect linear trend.

Table 5.4: A summary of porosity, permeability, and bulk density measurements after cleaning the core samples.

Sample Number	Well	Depth	Lithotype	Porosity, fraction	Permeability, md	Bulk Density, gr/cc	Grain Density, gr/cc
2	A-3	10685'9"	4	0.023	1.62	2.437	2.494
3	A-3	10700'5"	5	0.168	447.37	2.202	2.646
4	A-3	10749'6"	1	0.184	820.82	2.162	2.648
5	A-3	10782'3"	1	0.217	1602.68	2.073	2.647
6	A-3	10784'4"	3	0.185	364.45	2.158	2.648
7	A-3	10789'5"	3	0.158	—	2.211	2.625
8	A-3	10823'11"	2	0.167	20.70	2.198	2.638
9	A-3	10829'6"	2	0.156	43.73	2.236	2.649
10	A-3	10839'11"	5	0.146	55.84	2.262	2.647
11	A-9	10690'	6	0.108	24.67	2.357	2.642
12	A-9	10695'9"	6	0.108	38.59	2.357	2.641
13	A-9	10719'4"	5	0.126	210.63	2.315	2.648
14	A-9	10808'5"	5	0.109	81.23	2.356	2.644

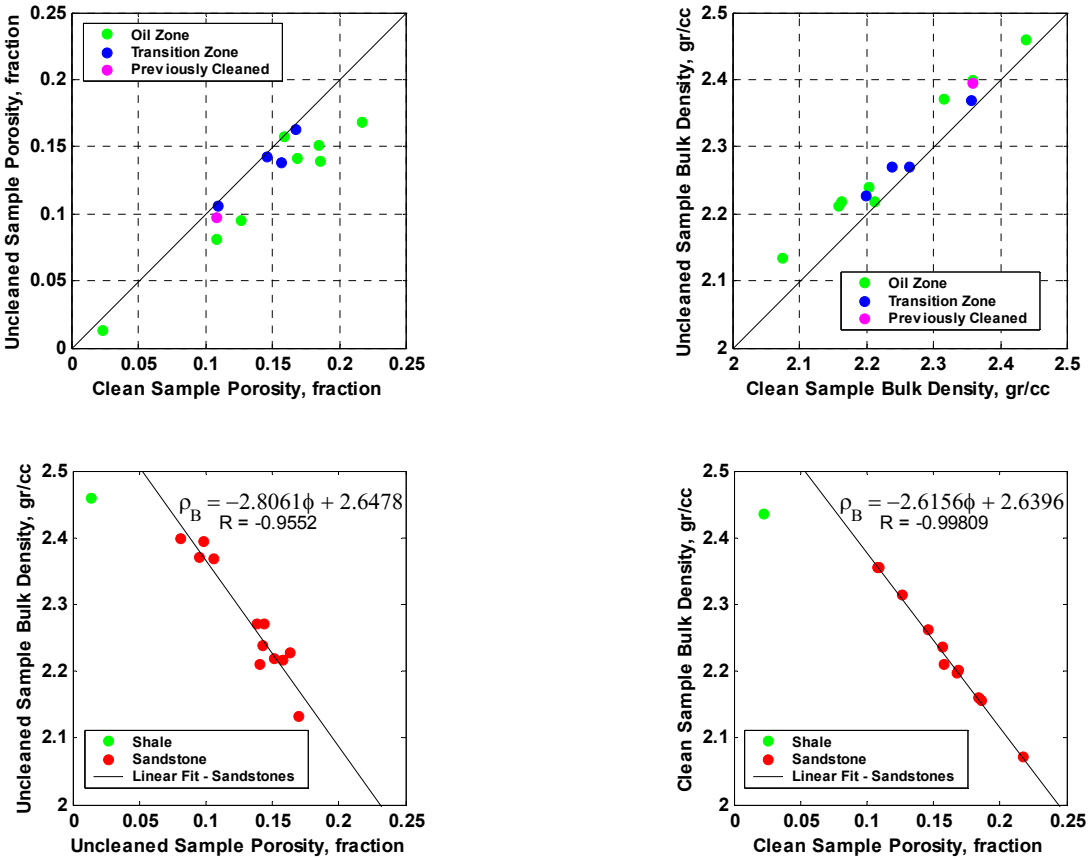

Figure 5.13: Top: Comparison of porosity (left) and bulk density (right) before and after cleaning. The black lines indicate no change in porosity or bulk density upon sample cleaning. Bottom: Plots of bulk density vs. porosity before and after cleaning. The lines represent the best linear least squares fits for the sandstone samples. The equations for the trends and their linear correlation coefficients are indicated.

The values we obtained for cleaned porosity are a better fit to those observed in well logs, indicating that the consistent porosity underestimation from previous measurements may be the result of insufficient sample cleaning. Figure 5.14 is a plot of permeability vs. log of porosity for the samples used in this study. The trend of former core measurements in samples from well Apiay-9 is shown for reference. Notice that the trend of old measurements lies to the left of cleaned samples, and is in close agreement with that of uncleaned samples. The central tracks in Figure 5.15 show the porosity logs for wells Apiay-3 and Apiay-9, along with previous core porosity measurements and the results from this study. Notice that the porosities of uncleaned samples lie close to previous measurements.

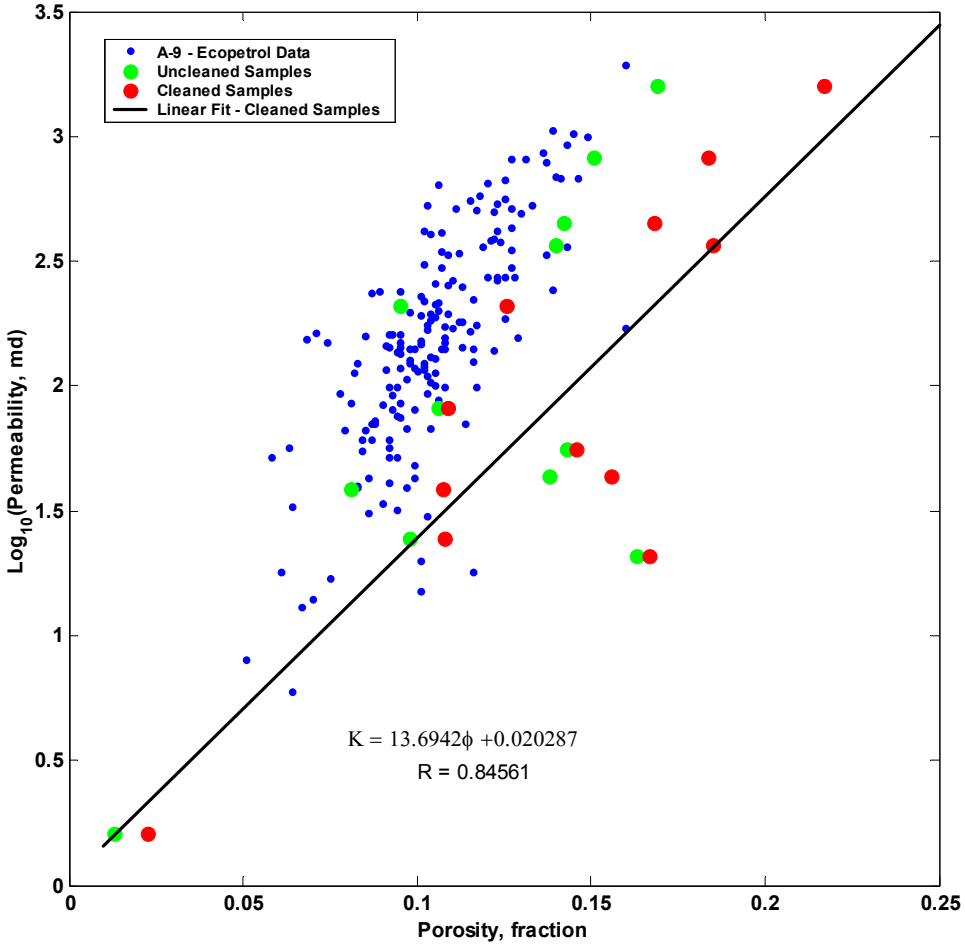

Figure 5.14: A plot of permeability vs. porosity for samples in this study, before and after cleaning. The trend of core samples from the Apiay-9 well is shown for reference.

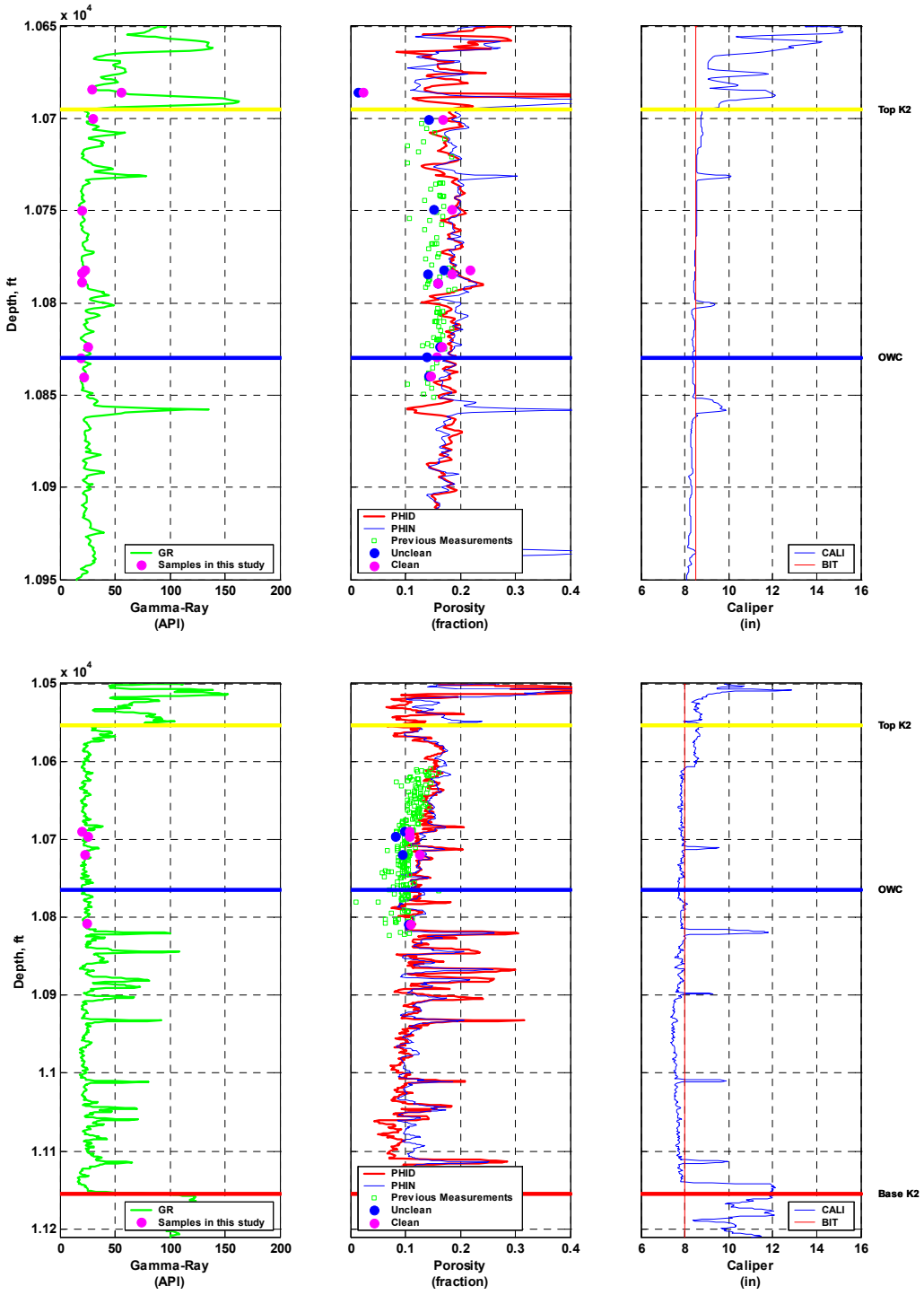

Figure 5.15: Comparison of porosity measurements before and after cleaning. Top: Well Apiay-3. Bottom: Well Apiay-9. The left track shows the gamma-ray log, with the location of samples used in this study. The center track shows neutron and density porosity logs, along with previous core porosity measurements, and the results of this study, both before and after cleaning the samples. The right track shows the caliper log, which helps determine intervals where log data may be affected by borehole enlargement.

5.5.2 Velocity Measurements

We performed hydrostatic experiments to measure P- and S-wave velocities at different confining pressures on the 13 *quasi-dry* (uncleaned) samples described above. The measurements were acquired at approximately every 5 MPa in the range from 0 to 45 MPa, under loading and unloading conditions. The purpose of measuring velocities before cleaning the samples was to prevent the destabilization and removal of pore-filling clay particles. The experiments were conducted at the Stanford Rock Physics Lab, with the experimental setup shown in Figure 5.16.

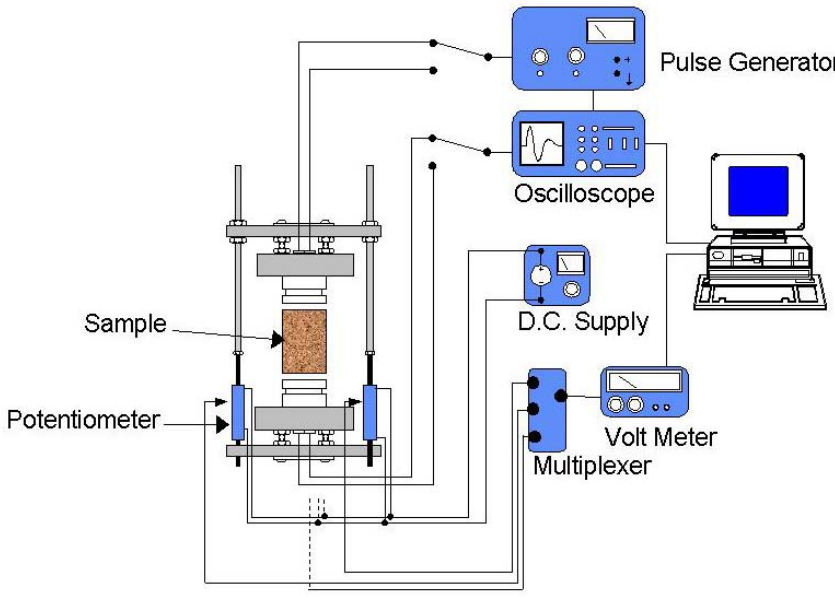

Figure 5.16: A schematic plot that depicts the application of forward and inverse problems to seismic modeling.

We compute P- and S-wave velocities from the time it takes for a pulse to travel through a sample of a certain length. The length of the sample is measured at room conditions, and the change in length under confining pressure is monitored with a pair of potentiometers. The change in porosity upon pressurization is computed from the initial volume of the sample, the volume and density of grains, and the change in length, assuming that the sample radius remains unchanged. I discuss this assumption later.

Recall the relationship between pore pressure P_p, confining pressure P_{conf}, and effective pressure P_{eff} is given by:

$$P_{eff} = P_{conf} - \alpha P_p , \tag{5.1}$$

where α is the effective pressure coefficient, which is generally close to 1, but for low porosity rocks can be significantly smaller [*Wang and Nur*, 1992]. In this work we assume α is equal to 1. Since in our hydrostatic experiments pore pressure is negligible, effective pressure becomes equal to confining pressure. Figures 5.16 to 5.19 show velocity vs. effective pressure curves for the 13 K2 Unit core samples, grouped by rock quality as inferred from their corresponding lithotype. Figure 5.21 shows P-wave velocity vs. effective pressure and porosity for all samples measured.

Velocity hysteresis is small in general, indicating that the samples did not undergo further compaction upon loading. The separation between S-wave loading and unloading paths observed in some samples is a result of the uncertainty in S-wave arrival picks, rather than an indication of compaction. The drop in P- and S-wave velocities upon loading from 25 and 35 MPa suggest that sample 9 (Apiay-3, 10829.5', shown in Figure 5.19) fractured between those two pressures.

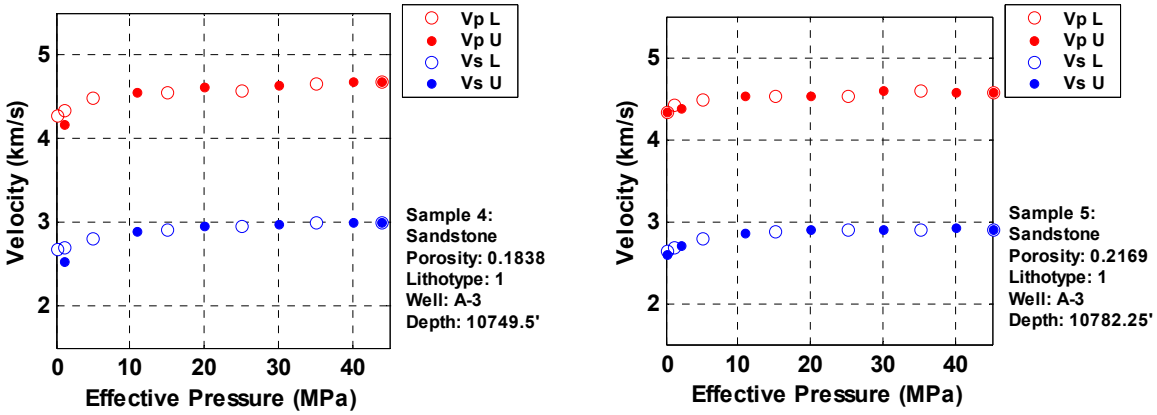

Figure 5.17: Plots of velocity vs. effective pressure data for samples of lithotype 1, the facies of best petrophysical properites. Red dots represent P-wave velocity measurements; blue dots, S-wave velocities. Open symbols correspond to loading conditions, while closed ones represent the unloading path.

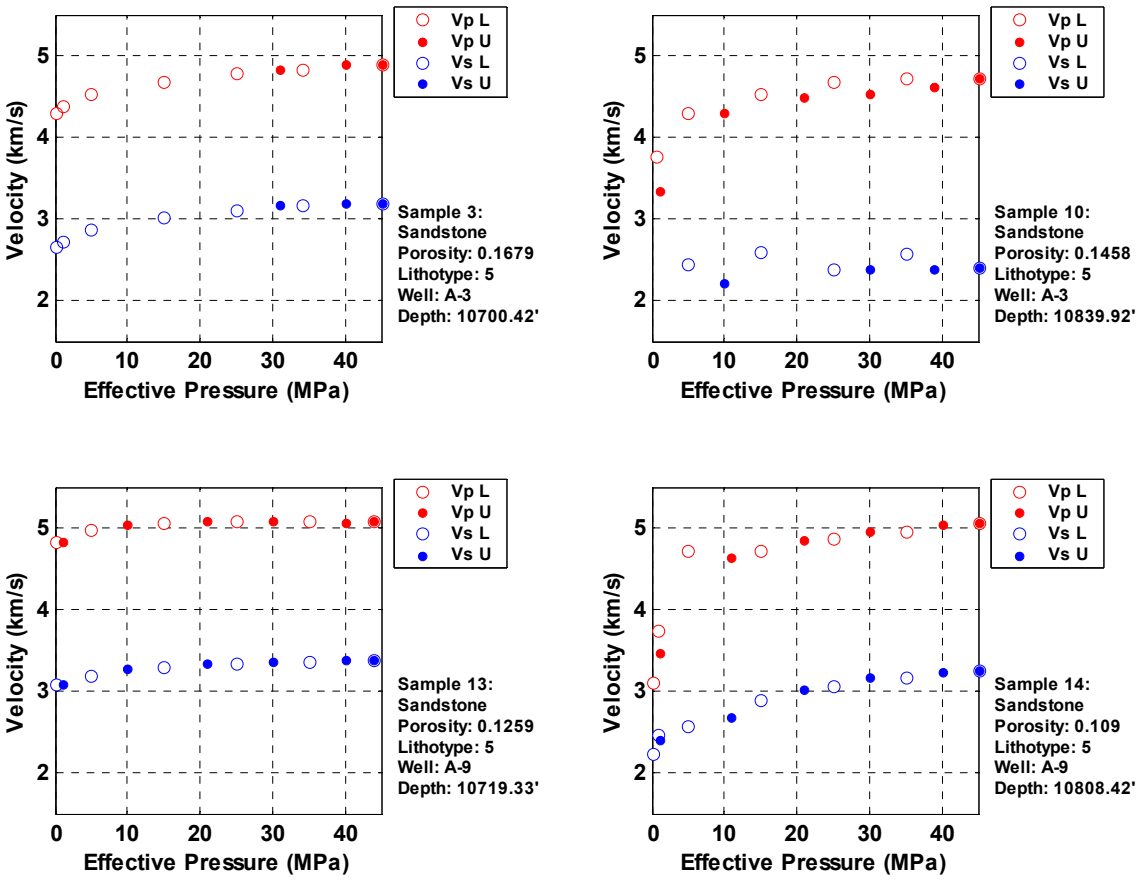

Figure 5.18: Plots of velocity vs. effective pressure data for samples of lithotype 5, which represents rocks of good quality. Red dots represent P-wave velocity measurements; blue dots, S-wave velocities. Open symbols correspond to loading conditions, while closed ones represent the unloading path.

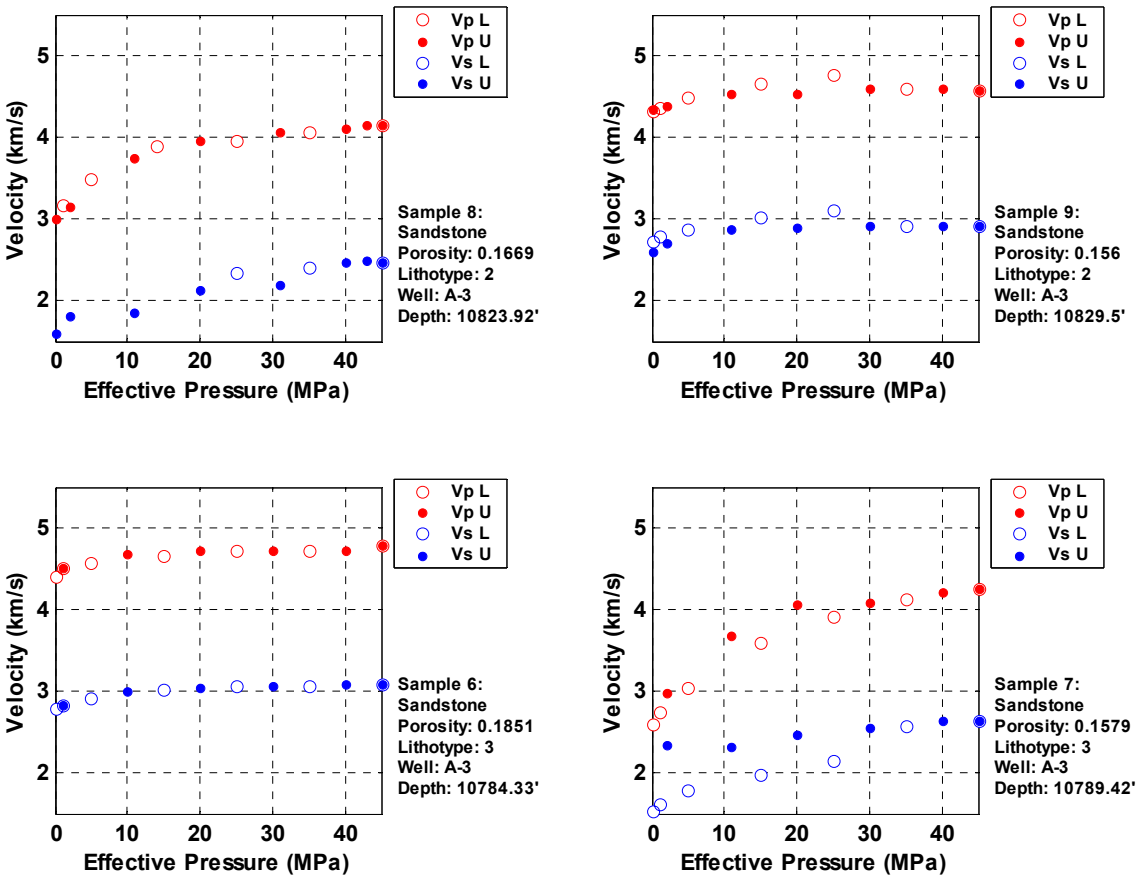

Figure 5.19: Plots of velocity vs. effective pressure data for samples of lithotypes 2 and 3, which represent facies of intermediate to good rock quality. Red dots represent P-wave velocity measurements; blue dots, S-wave velocities. Open symbols correspond to loading conditions, while closed ones represent the unloading path.

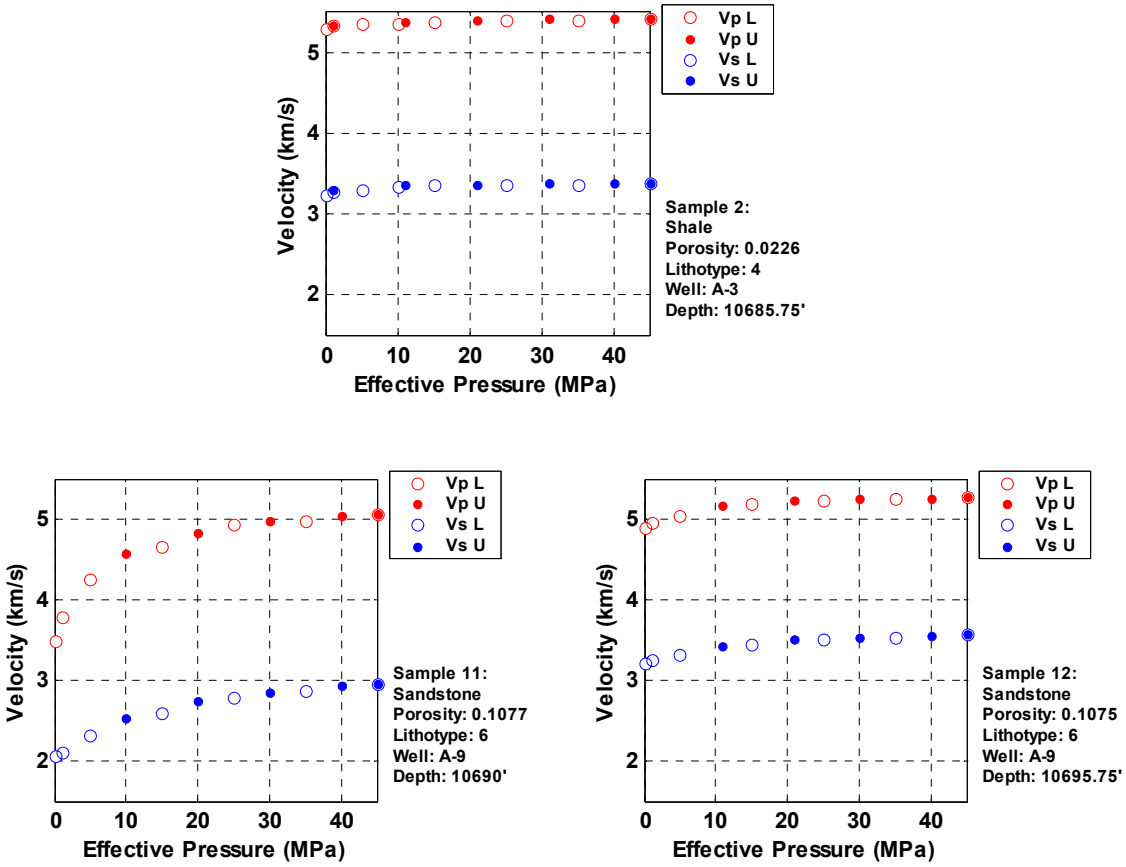

Figure 5.20: Plots of velocity vs. effective pressure data for samples of lithotypes 4 and 6, which represent facies of bad rock quality. Red dots represent P-wave velocity measurements; blue dots, S-wave velocities. Open symbols correspond to loading conditions, while closed ones represent the unloading path.

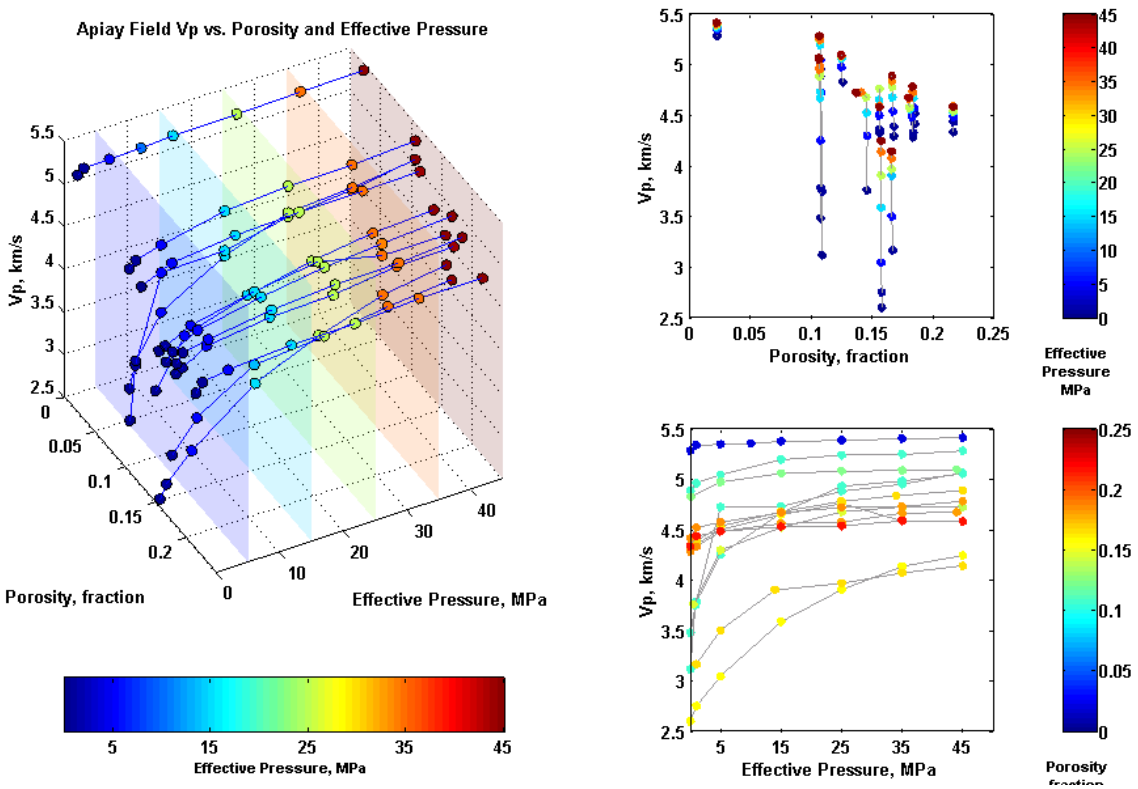

Figure 5.21: Plots of P-wave velocity data vs. porosity and effective pressure for all samples.

The non-linear behavior of velocity trends at low effective pressure reflects the closure of soft, crack-like pores, most likely formed as a result of the depressurization that cores experience when brought from the reservoir to the surface. The leftmost plot in Figure 5.20 shows that the dispersion of velocity vs. porosity trends for a given effective pressure decreases at high effective pressure, as a result of the closure of soft pores.

5.6 Effective Stress at Reservoir Conditions

One important, yet rarely addressed unknown that arises when analyzing laboratory data of velocity versus effective pressure is the range of effective pressure that is relevant to the reservoir conditions. Equation 5.1 shows that effective stress depends on pore pressure and confining stress. A reservoir system may undergo significant thermodynamic changes upon injection and withdrawal of fluids, which may induce spatial and time-dependent variations in pore pressure. To further complicate things,

subsurface reservoirs may be subject to anisotropic stress fields. The question of whether stress-induced velocity anisotropy is a first-order effect after rock consolidation remains unsolved. In one of the few efforts to address this problem, *Yin* [1992] performed velocity measurements under anisotropic stress conditions on a Berea sandstone sample. His results, summarized in terms of elastic stiffness in Figure 5.22, show a marked variation in velocity along the direction of compression, while the velocities along perpendicular directions remain nearly unaffected. In industrial applications, stress-induced velocity anisotropy is often conveniently avoided. When working with data at the laboratory and field scales, some people take the mean effective stress as the reference datum for comparison purposes, while some others assume that the vertical effective stress should be used, because most of the recorded energy in a surface seismic experiment corresponds to waves that travel almost vertically.

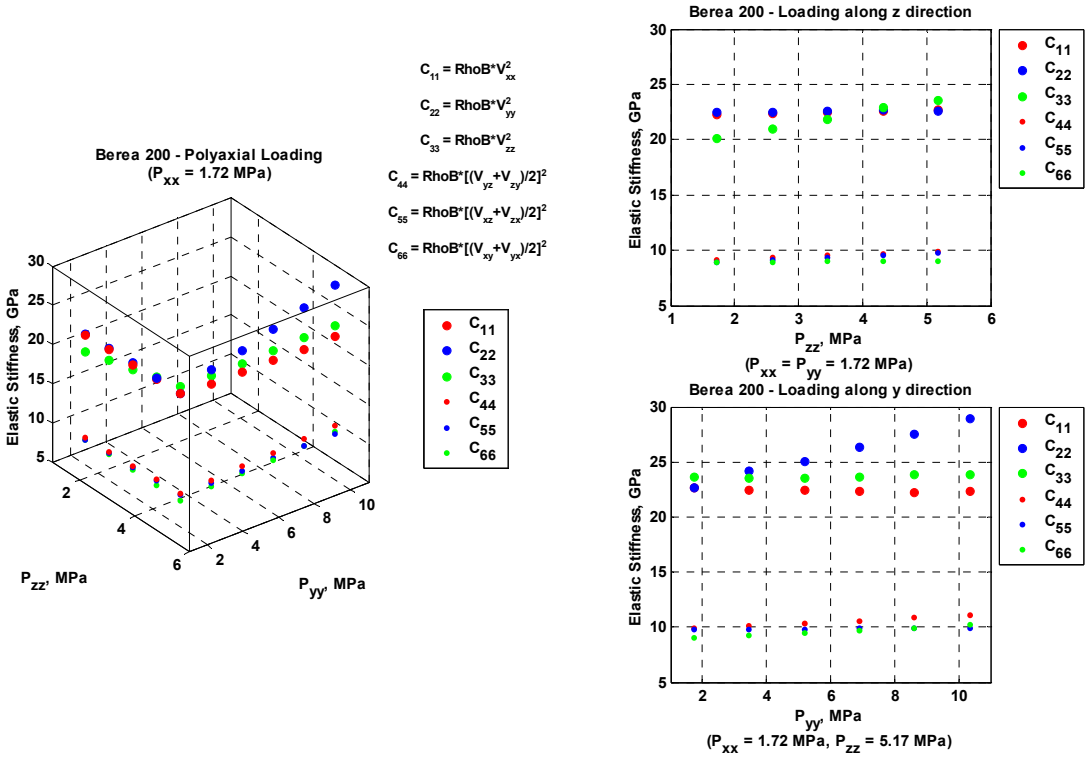

Figure 5.22: A set of plots that summarize the stress-induced velocity anisotropy measurements performed by *Yin*'s [1992] on a Berea sandstone sample.

In the case of the Apiay-Guatiquía Field, water from an active regional aquifer replaces the space left by withdrawn fluids. The aquifer provides a strong pressure support and efficiently prevents depletion, bringing the system to nearly *steady-state* conditions, and making time-lapse pressure changes a second-order effect. Therefore, the range of expected pore pressures is controlled by the distribution of pressure around producing wells.

We discussed in Chapter 4 the range of feasible stress distributions in Apiay-Guatiquía, and found that the stress field is anisotropic. Figure 5.23 shows the effective stress in the K2 Unit, as computed from Equation 5.1, for three scenarios of confining stress gradient, and assuming that pore pressure is hydrostatic —i.e., $\nabla P_p = 0.433$ psi/ft. The plot shows the stress expected at 15 well locations, at three different depths: the top of the K2, the depth of the K2 oil-water contact, and the average of these two depths, which can be thought of as the average effective stress for the oil-bearing zone. The three confining stress scenarios correspond to the vertical stress gradient in the Apiay-Guatiquía area ($S_v \sim 1$ psi/ft) and the mean stress gradient for two of the cases I presented in Chapter 4. The mean stress gradients for those cases are 0.85 and 0.81 psi/ft, and correspond to scenarios of $S_V : S_{H\max} : S_{h\min} = 1.0 : 0.94 : 0.61$, and $S_V : S_{H\max} : S_{h\min} = 1.0 : 0.81 : 0.62$, respectively.

The small variation in stress for a given curve reflects the flat character of both the K2 Unit structure —a gently dipping anticline— and the surface topography, which results from the largely passive tectonic history of the Llanos basin. If one assumes that the mean effective stress should be used for comparing velocity measurements at the laboratory and field scales, then the range of effective stress in the K2 Unit may vary between 27 and 32 MPa, depending on the stress field assumed. On the other hand, if the vertical effective stress is what is relevant for elastic property comparison purposes, the effective stress in the K2 reservoir ranges from 41 to 43 MPa. Notice that the significant difference in terms of effective stress between these two approaches may lead to uncertainty in the core-derived relationships between elastic and petrophysical properties.

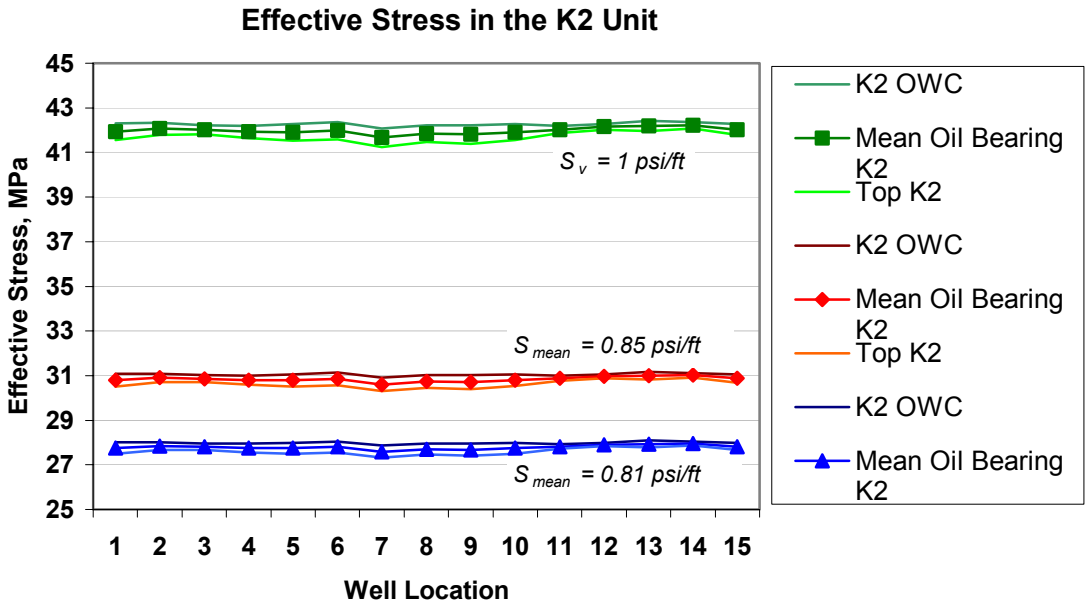

Figure 5.23: A plot of effective stresses in the K2 Unit of Apiay-Guatiquía, at 15 different well locations.

Fortunately, the change in velocity over the range of stresses expected for the K2 Unit under all assumptions—between 27 and 43 MPa— is small (see Figures 5.17 to 5.21), indicating that most soft, crack-like pores are already closed at 27 MPa. Furthermore, core observations show that K2 Unit rocks are well compacted, and in most cases also well cemented. Therefore, even though the influence that anisotropic stress conditions observed in the field may have on velocities is not well understood, the aforementioned observations indicate that there is little variation in velocity over the range of possible effective stresses in Apiay-Guatiquía. This also lets us confidently assume that for the K2 Unit reservoir the relationship between velocity and effective pressure is linear, with a nearly flat slope. We assume in this work a reference effective stress of 40 MPa for the K2 Unit reservoir, and explore the relationships among petrophysical and elastic properties at that reference effective stress.

5.7 Porosity Change with Confining Pressure

In this section I address the possible error in porosity estimates inferred from length change. The experimental setup we used for measuring velocities allows us to determine

how the length of a given sample changes with effective pressure, but not how its diameter varies. Changes in porosity upon pressurization can be estimated from the initial volume of the sample, the volume and density of grains, and the observed length changes, given an assumption about the change in radius with confining pressure. Some researchers assume that changes in radius during pressure loading and unloading experiments are negligible, which may be reasonable in some cases. However, since the volume of cylindrical samples varies with the square of their radius, the reduction in diameter that samples experience upon pressurization may lead to significant porosity underestimation if the change in radius is considerable, i.e., if the rock samples are not stiff enough. The alternative in such case is to estimate the change in diameter from observed sample length data.

The change in length ΔL of a sample subject to compression in the axial direction z is related to its initial length by:

$$\Delta L = L_0 \varepsilon_{zz} . \tag{5.2}$$

Similarly, the change in radius of a sample under radial compression is given by:

$$\Delta r = r_0 \varepsilon_{rr} . \tag{5.3}$$

For a hydrostatic experiment, the radial strain ε_{rr} and the axial strain ε_{zz} are equal. Thus, we can relate the change in radius to the change in length as follows:

$$\Delta r = r_0 \frac{\Delta L}{L_0} . \tag{5.4}$$

In the case of the Apiay-Guatiquía samples, I used previous pressure-dependent porosity data to determine the most appropriate way of computing the change in porosity with confining pressure from the observed length changes. The top plot in Figure 5.24 shows the porosity —measured by the Boyle's law method— of samples from the Apiay-

Guatiquía Field that were confined in two steps: from 5.5 to 15.2 MPa, and then from 15.2 to 25.5 MPa. The bottom left plot shows the porosity of samples in this study, computed from length change, assuming that the change in radius is negligible. The bottom right plot shows the porosity obtained by assuming that the axial and radial strains are the same, which is a valid assumption for the type of experiment performed to measure P- and S-wave velocities. All plots are shown with the independent variable in the vertical axis to ease the comparison.

The K2 Unit rocks are well compacted, so the overall reduction in porosity is not very large, as can be seen in the plots. Porosity estimates from length change underestimate the total decrease in porosity, though. The plots show that the assumption of negligible radius change can be questionable for rocks that are softer than those we used in this study. In our experiments, the change in porosity due to compression of the samples from zero to 45 MPa of effective pressure ranges from -1.0×10^{-4} to -8.9×10^{-3}. The highest change is for sample 11, whose porosity change is considered anomalous beyond 25 MPa. The mean and median of porosity changes are -1.9×10^{-3} and -1.3×10^{-3}, respectively. The median is less sensitive than the mean to outlier values, such as that of sample 11. In Boyle's law experiments, the decrease in porosity between 5.5 and 25.5 MPa of effective pressure lies in the range between -4.0×10^{-3} and -7.0×10^{-3}, respectively, with an average change of -5.6×10^{-3}. The median of porosity changes is of -5.0×10^{-3}.

The total decrease in porosity tends to level off at high effective pressures. Pressure-dependent Boyle's law porosity measurements show a smaller decrease in porosity for the second confining step (from 15.2 to 25.5 MPa) than for the first (from 5.5 to 15.2 MPa). The median of porosity changes during the first compression step is -3.5×10^{-3}, while for the second step it is -2.0×10^{-3}. This reflects the closure of soft, crack–like porosity, and is consistent with the opposite behavior of velocities over the same intervals, i.e., there is a smaller *increase* in velocity for the second compression step than for the first (see, for instance, Figure 5.21 for changes in P-wave velocity).

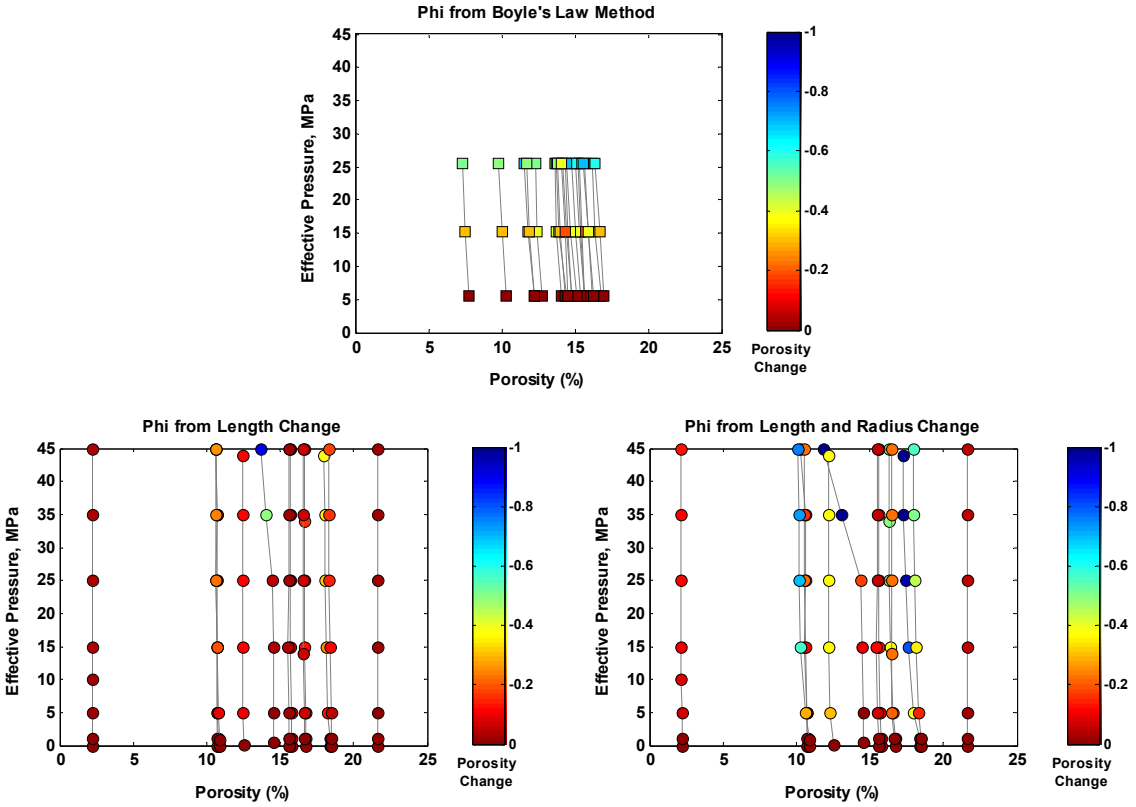

Figure 5.24: Plots of porosity reduction upon pressurization in two types of hydrostatic experiments. The left plot shows porosities computed from length change experiments designed to measure ultrasonic velocities. The right plot shows porosities computed by the Boyle's law method at three different effective pressures. The samples shown in the left and right plots are not the same, but all come from the Apiay-Guatiquía Field.

5.8 Effects of Residual Saturation on Velocity

Since we measured P- and S- wave velocities before cleaning the samples, the results do not represent truly dry conditions. Figure 5.25 shows a comparison of P-wave velocity computed from the transit time log, and the core measurements in this study. Notice that core measurements are significantly higher than well log data, which shows the effect of residual saturation. Residual saturation can affect core velocities in two ways: the first effect is that of compressible saturating fluids, which can be modeled using the *Gassmann*'s [1951] and squirt [*Mavko and Jizba*, 1982] models at the low and high frequencies, respectively; in addition to this, degraded, asphaltene-rich oil can act as interparticle cement, stiffening the rock and increasing the velocity of our samples.

To account for residual saturation I performed fluid substitution using the Gassmann's model to compute the low-frequency, dry velocities from the high-frequency measurements we made on uncleaned samples. To assess the influence of saturation scales I present in Figure 5.25 the results of fluid substitution under *patchy* and *uniform* saturation asssumptions, for the data at 35 and 45 MPa. The difference in velocity between the patchy and uniform models is negligible. Since in this case the residual saturation is small, the difference in saturation scales does not constitute a source of uncertainty. From these results I computed the velocities expected for the fully water saturated samples, which can be compared to well log data. Log-derived P-wave velocity is still considerably smaller after fluid substitution to 100% water saturation conditions, indicating that the residual oil is indeed causing a cementation effect.

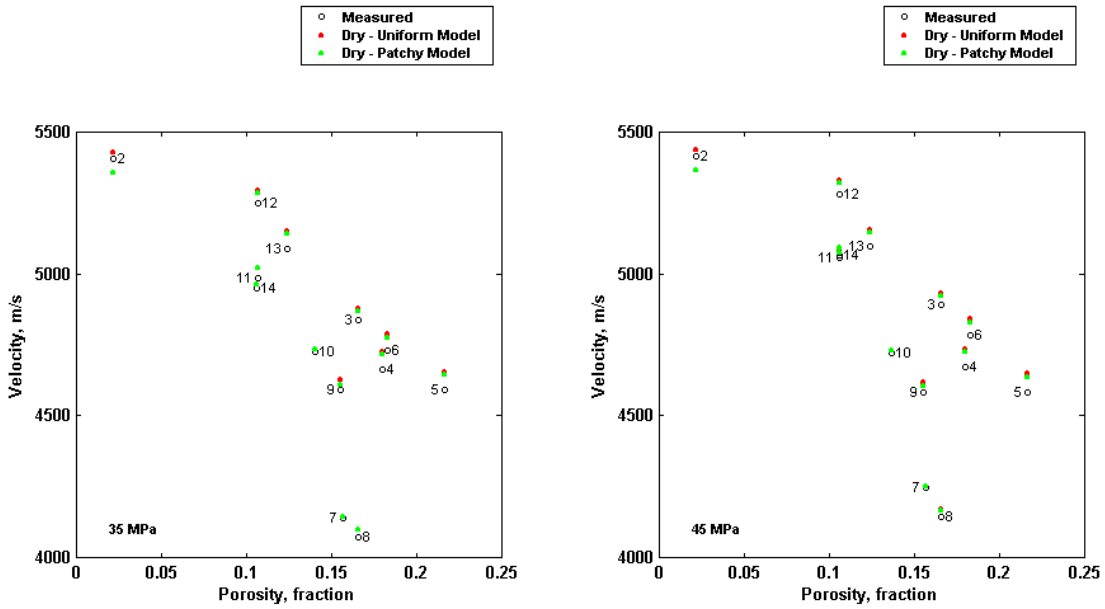

Figure 5.25: A plot of velocity vs. porosity for the samples in this study. Open circles represent the measured velocities, at residual saturation conditions. Red and green filled circles represent dry conditions obtained by Gassmann's fluid substitution, for the uniform and patchy models, respectively.

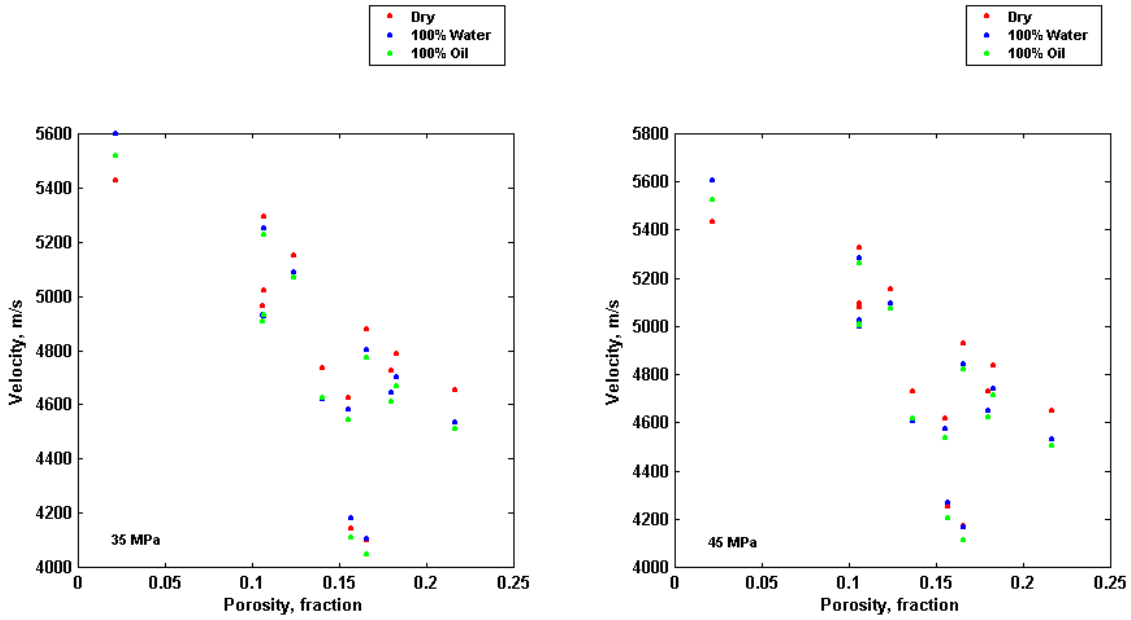

Figure 5.26: A plot of velocity vs. porosity for the samples in this study. Red dots represent dry conditions. Blue and green dots represent fully water-saturated, and fully oil-saturated conditions, respectively.

Core measurements show a clear trend between velocity and porosity, though; recall that sample 9 is likely to have fractured while it was being compressed from 25 to 35 MPa, so its velocity at the effective pressures shown in Figure 5.25 should be higher. Samples 7 and 8, which represent lithotypes 2 and 3 —cemented, base of channel, and kaolinite-rich sandstone facies, respectively— have lower velocities than the other samples. These samples are likely to have higher clay content than those from other channel facies. However, the other samples of these lithotypes do not present the same behavior. The population of samples from each lithotype is too small to derive conclusions from the results. Given the influence of stiff residual oil on velocities, well log data are the most valuable piece of information for this study. In Section 5.11 I use well log data to study the relationships between petrophysical properties and seismic variables.

5.9 Elastic Model

Studying the elastic behavior of rocks in the K2 unit is important for modeling and interpretation purposes. Knowing the relationship between bulk modulus and porosity allows the determination of pore stiffness. A bulk modulus – porosity relationship allows the inference of S-wave velocity from P-wave velocity and bulk density data, which is important for performing fluid substitution using the full Gassmann's approach and modeling AVO effects, among other applications.

Figure 5.27 shows the relationships between dry bulk modulus (normalized by mineral bulk modulus) and porosity for the 13 core samples from the K2 unit. Red dots represent bulk modulus computed from density and compressional and shear velocities measured in the lab at a differential pressure of 45 MPa. Blue dots correspond to samples with bad S-wave signal. For these two samples the shear wave was determined from a regression of S-wave and porosity found with the other sandstone samples. Blue contours in the top plot are lines of constant pore stiffness. Notice that most of the samples lie on the contour of $K_\phi/K_{mineral} = 0.2$. This implies that by making a reasonable assumption about the mineral bulk modulus and knowing the porosity, it is possible to determine the dry bulk modulus. The value of K_{dry} found in this way can be used with Gassmann's fluid substitution relationships to find the bulk modulus of a rock saturated with a fluid of known properties. If the P-wave velocity and density of the saturated rock are known, the shear wave velocity of the saturated rock can be predicted. The degree of accuracy of predicted S-wave velocities depends on the appropriateness of the assumption made for $K_\phi/K_{mineral}$, and on the value of $K_{mineral}$ itself.

Fitting the data to the modified Voigt average proposed by *Nur et al,* [1995] (bottom plot) yields an estimate of critical porosity. The critical porosity for sandstones in the K2 unit is slightly over 36%, which is consistent with values reported in the literature for other sandstones.

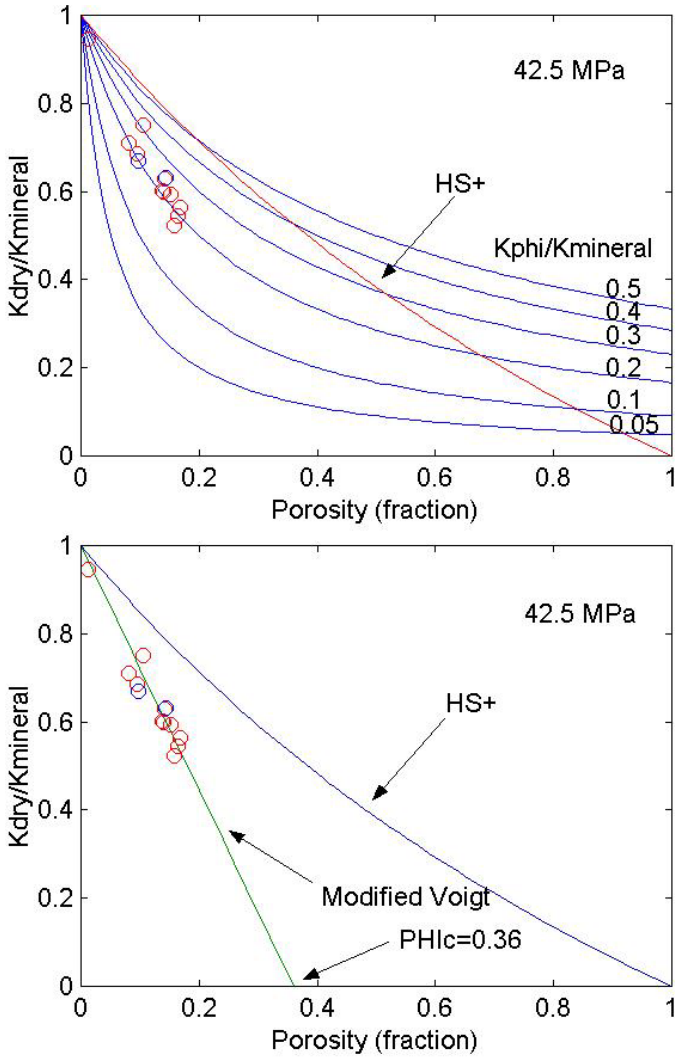

Figure 5.27: Relationships between dry bulk modulus and porosity.

5.10 Scattering Effects

Heterogeneities in elastic media produce wave-scattering effects that may in turn translate into dispersion of acoustic wave velocities [*Mukerji*, 1995]. On the other hand, the difference in frequency between lab measurements, well logs and seismic imply a difference in wavelength relative to the scale of heterogeneities. Faster velocities are expected in the short wavelength limit than in the long wavelength limit for heterogeneities of a given size. The velocity in the high-frequency limit can be predicted using ray theory, while effective medium theory gives estimates of velocity in the low-frequency limit. These limits are given by the *Backus average* —i.e., the layer thickness-

weighted average— of the elastic compliances (effective medium theory), and *Backus average* of the slowness (ray theory) of each layer in the medium.

In order to determine the importance of scale-dependent effects in the K2 Unit of Apiay-Guatiquía Field, we compared the average velocities predicted by ray theory and effective medium theory at 35 Hz, computed from density and sonic logs acquired in well Apiay-9. Figure 5.2 shows the set of logs acquired in this well. Notice the anomalous values of velocity and density at depths where the caliper log shows some deflection. Although the velocity of shales might be lower than the trend exhibited by sandstone samples —as some of the core measurements suggest— the strong reduction in velocity associated with some shale streaks is due to bad log measurements in washed out intervals. High bulk density measurements in those layers would give rise to abnormally high porosity values, which are not consistent with laboratory observations either.

We edited the logs at those depths to avoid biased results. We correct the log values in those intervals using the trends of velocity and density from shale intervals not exhibiting wellbore enlargement. Figure 5.28 shows the modified logs and the upscaled density and velocity curves. I also present the acoustic impedance computed from velocity and density logs at both scales. I estimated the wavelength from the average velocity for the entire interval, assuming the leading frequency in the seismic survey is 25 Hz. Upscaled velocities correspond to the effective medium and ray theory limits described above, computed over a window one tenth of a wavelength long. I upscaled the density curve by taking the arithmetic average of each layer's density.

The separation between the effective medium theory (red upscaled curve) and the ray theory (green upscaled curve) limits for velocity is subtle, which means that scattering effects are not very relevant between log and seismic frequencies.

The upscaled impedance curve follows quite nicely the trend observed for log-derived impedance, particularly in the upper part of the section, which exhibits less sand/shale layering than the section in the bottom. This cleaner section at the top of the K2 unit is a trend that appears in all of the Apiay-Guatiquía wells, and corresponds to the oil-bearing zone.

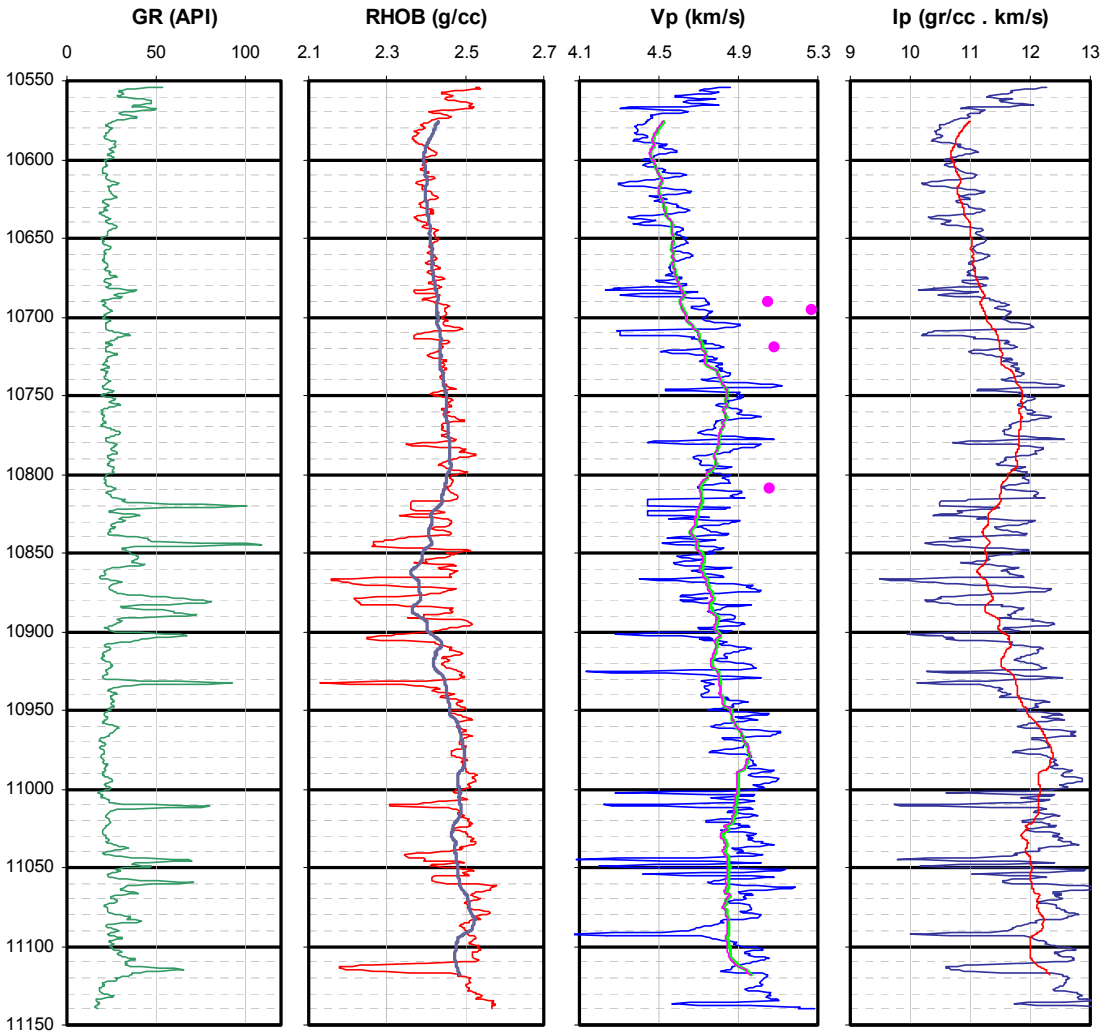

Figure 5.28: Corrected logs and upscaling predictions. The green curve in the velocity track is the short wavelength (ray theory) limit, whereas the red curve is the long wavelength (effective medium theory) limit. Pink dots represent velocity measurements in core samples taken at that depth.

5.11 Rock Physics Relationships at the Well Log Scale

Core data indicate that there is a good relationship between porosity and P-wave velocity for rocks in the K2 Unit of the Apiay-Guatiquía Field. To further explore the feasibility of inferring porosity from acoustic properties we generated cross-plots of well log porosity versus both P-wave velocity and impedance. Rock physics relationships based on well logs are very important, because log data are acquired at *in situ* conditions of stress, pore pressure, temperature, and saturation. I present in Figure 5.29 an example of the cross-plots we used in this section, generated from the logs of well Apiay-9.

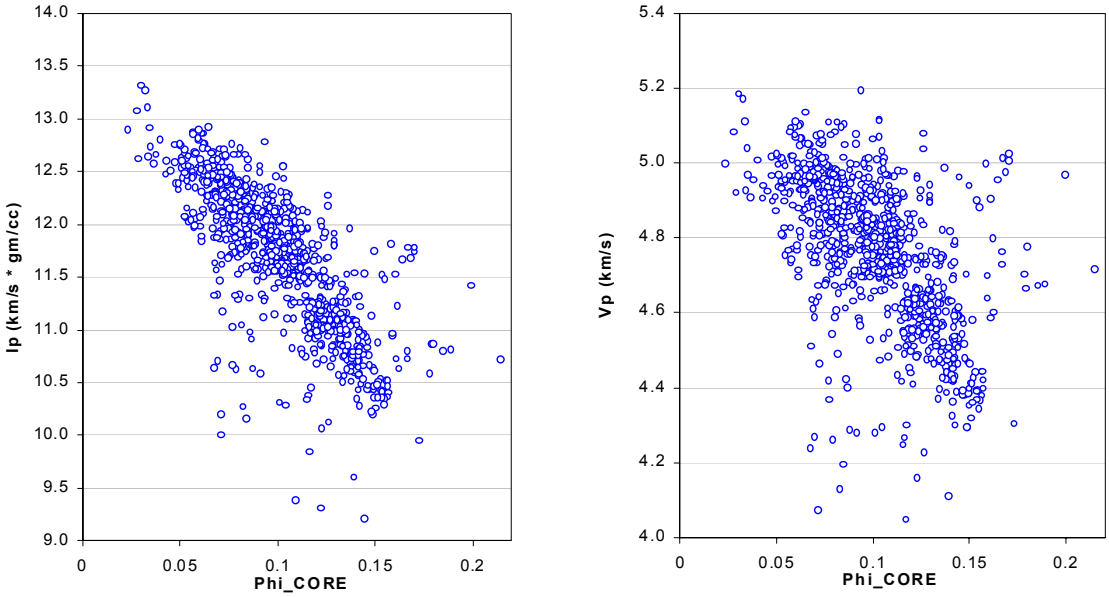

Figure 5.29: Rock physics relationships for porosity. Left: Acoustic impedance vs. porosity. Right: Compressional velocity vs. porosity. The porosity data are from density log readings adjusted by core data measurements.

From these plots, it can be concluded that there is a good correlation between acoustic impedance and porosity in the K2-Unit. The correlation between acoustic velocity and porosity is also good. This implies that the results of inverting the seismic traces for acoustic impedance would be an important source of soft data to predict porosity in Apiay-Guatiquía.

We also examined the rock physics relationships for permeability (Figure 5.30). Not surprisingly, the trend between P-wave impedance and permeability is not as good as the one for porosity. This results from the fact that storage properties of the rock have a much stronger influence on the propagation of acoustic waves than transport properties. However, there is a reasonably good trend in the plot of permeability versus porosity. Hence, the porosity field obtained from impedance inversion could potentially be used to condition permeability estimates.

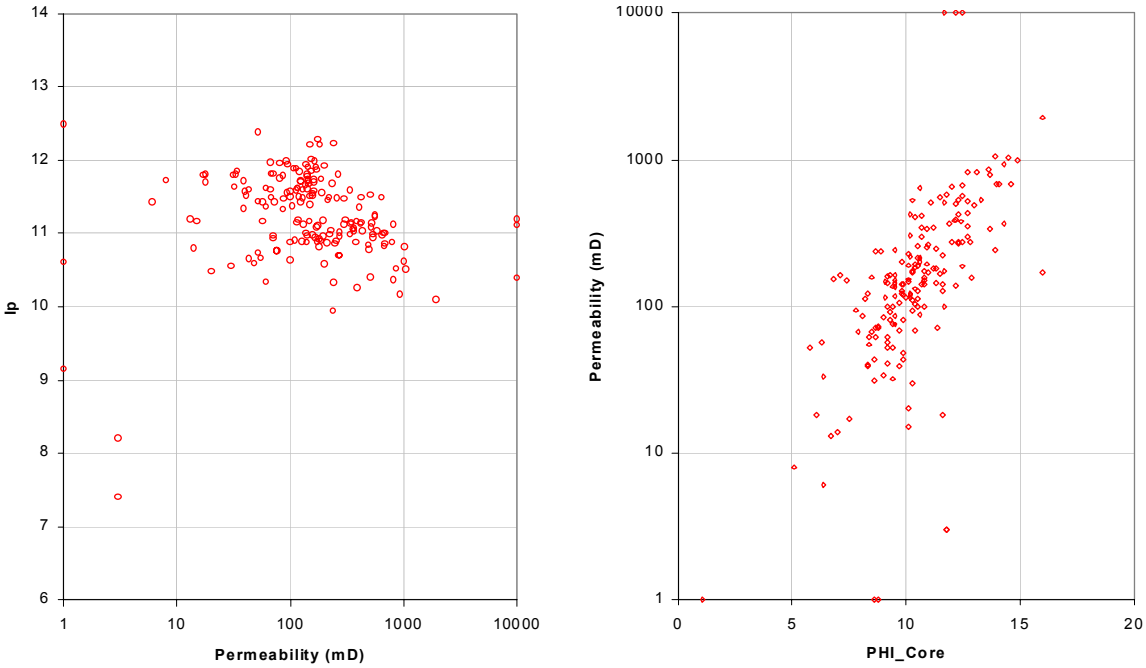

Figure 5.30: Rock physics relationships for permeability. The left plot shows the relationship between permeability measured in cores, and acoustic impedance derived from logs at the corresponding depth of the permeability samples. The right plot is a permeability vs. porosity scatter plot obtained from core measurements.

5.12 Conclusions

Cretaceous sandstones found in the K2 Unit of the Apiay-Guatiquía Field are mostly very fine to very coarse grained, sub-angular to sub-rounded, medium- to well-sorted quartzarenites and sublitharenites, and have a critical porosity of approximately 36%.

Previous core measurements consistently underestimate the porosity of sandstones in the K2 Unit. Heavy components of the oil mixture that precipitated in the pore space are the cause of abnormal porosity results, indicating the need for better cleaning procedures when treating core plugs from this system

The K2 Unit rocks form a trend of permeability vs. porosity that is similar to that of the Fontainebleau sandstone.

Velocity dispersion effects related to fluid flow and scattering processes are not expected to have a strong influence on porosity estimations from seismic, according to modeling results.

Scale-dependent effects due to scattering are not very relevant between log and seismic frequencies.

Core measurements available to date suggest that the pore stiffness of sandstones in the K2 Unit is approximately 0.21 times the mineral bulk modulus. Based on this assumption it is possible to make a reasonable prediction of shear wave velocities.

There is a good correlation between porosity and seismic properties, such as P-wave velocity and acoustic impedance.

The correlation between permeability and seismic properties is not as good as that for porosity. However, the porosity distribution estimated from impedance can be used as soft data to compute the permeability field.

5.13 References

Gassmann, F., 1951, Über die elastizität poröser medien: *Vier. der Natur*, Gesellschaft, **96**, 1–23.

Mavko, G., and D. Jizba, 1991, Estimating grain-scale fluid effects on velocity dispersion in rocks: *Geophysics*, **56**, 1940-1949.

Mukerji, T., 1995, Waves and scales in heterogeneous rocks: Ph.D. dissertation, Stanford University.

Nieto, J, and N. Rojas, 1998, Caracterización geológica y petrofísica del yacimiento K2 en los campos Apiay, Suria y Libertad. ECOPETROL, internal report.

Nur, A., G. Mavko, J. Dvorkin, and D. Galmudi, 1995, Critical porosity: A key to relating physical properties to porosity in rocks: *The Leading Edge*, **17**, 357-363.

Wang, Z, and A. Nur, 2000, *Seismic and acoustic velocities in reservoir rocks, volume 3: Recent developments*: Society of Exploration Geophysicists, Tulsa, 623 pp.

Yin, T., 1992, Acoustic velocity and attenuation of rocks: Isotropy, intrinsic anisotropy, and stress induced anisotropy: Ph.D. dissertation, Stanford University.

Chapter 6

Seismic and Production Data Inversion in the K2 Unit of the Apiay-Guatiquía Oil Field

In this chapter I describe a practical application of our approach to inverting seismic and reservoir engineering data for petrophysical properties. Through the application of this methodology we estimated the porosity and permeability in the drainage area of the Apiay-9 well, from seismic-derived P-wave impedance, water cut data, and core-based conditional cumulative distribution functions of permeability given porosity.

In the first part of the chapter I present a pilot study we conducted in an area of the field, to address the feasibility of obtaining reliable impedance estimates from the inversion of seismic amplitude. To study such feasibility I compare the outcome of impedance inversion to well log observations, and analyze the misfit between synthetic seismic generated with the convolutional model, and the real traces from a 3D survey acquired in the field. I provide an interpretation of the impedance results in terms of depositional features. The close agreement between our interpretation and previous sedimentology and stratigraphy analyses —e.g., *Nieto and Rojas*, [1998]— gives us confidence that our impedance estimates are suitable for petrophysical property estimation.

In the second part of the chapter I present the criteria we used for selecting a study area for petrophysical property estimation from our inversion method, and provide a description of the available data. Then I discuss in detail all the steps and assumptions involved in data preparation, including the conversion of impedance data from time to depth, production data filtering, and the estimation of conditional cumulative distribution functions from core observations. Next I introduce our reservoir model for the drainage area of the Apiay-9 well, and describe the assumptions involved in our exercise, with

emphasis on the strengths, limitations, and possible improvements. Finally, I present and discuss the results of our joint inversion approach.

We obtained petrophysical properties that reproduce the history of liquid rate observed in the Apiay-9 oil well, and result in a good match of impedance and water cut data.

6.1 Feasibility Of Porosity Prediction From Seismic Data

Our approach to characterizing subsurface reservoirs from seismic data requires reliable seismic-derived estimates of acoustic velocity and/or impedance, in addition to good relationships between petrophysical and acoustic properties. I demonstrated the condition exists for rocks in the K2 Unit of the Apiay-Guatiquia Field. In this section I address the quality of impedance inversion results. Since the seismic frequency is orders of magnitude lower than the sonic log frequency, it is not possible to get the vertical resolution of a sonic log. But if the trends we observe between porosity and log-derived acoustic impedance, or velocity, hold at the seismic scale, and if the quality of impedance inversion results is good, we can take advantage of the excellent spatial coverage of seismic and use our inversion technique to predict petrophysical properties from acoustic impedance and production data.

We selected a volume of data from the Apiay 3D seismic survey to perform a pilot inversion study. Figure 6.1 shows a projection of an impedance horizon slice on top of the K2 seismic horizon, delineating the study area. We used the commercial software STRATA for this study. The inversion algorithm used by this software is based on the convolutional model, which I described in Chapter 2. The algorithm inverts the seismic data to yield impedance, using a coarse, well-log based model of impedance to correct for the lack of low frequencies in the seismic data.

We conducted two tests to address the feasibility of using impedance inversion results for porosity prediction. First, we inverted some lines and generated error plots to evaluate the fit between the convolutional model predictions and the seismic data. This proves the appropriateness of using the convolutional model to reproduce the seismic traces. Then we extracted an impedance trace in the vicinity of a well from the inverted volume, and compared it to well log data. This test allows us to confirm that the trends of impedance at the seismic and well log scales are comparable.

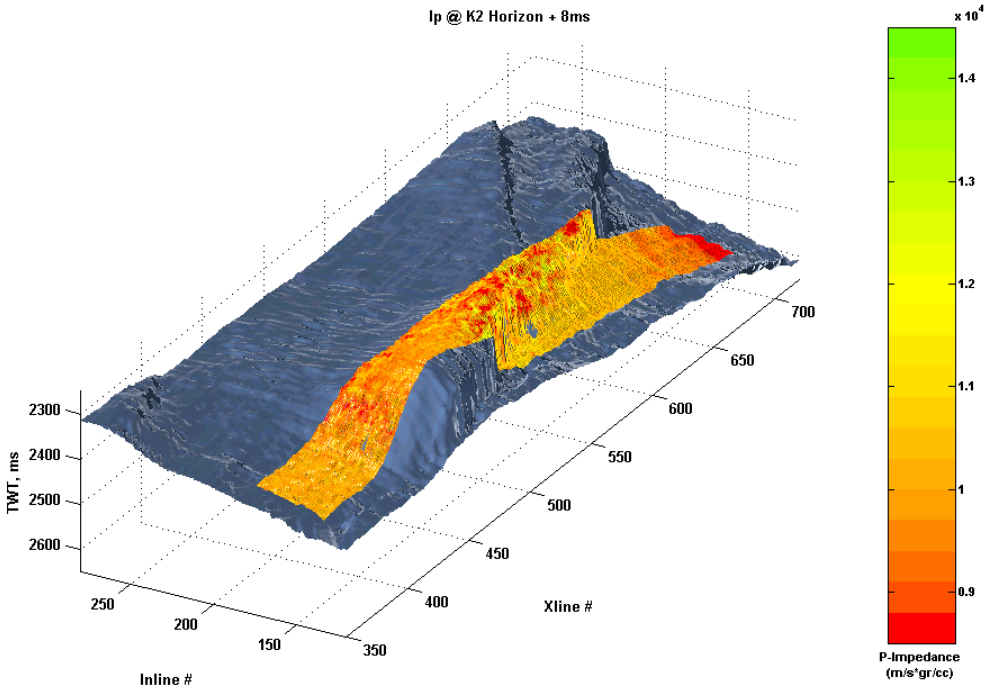

Figure 6.1: A surface plot that shows the area of study. The K2 seismic horizon is shown in gray, and a horizon slice of inverted impedance 8 ms below the K2 seismic horizon is projected on top of it.

I summarize the results of the first test in Figure 6.2. The top plot shows the seismic data for inline # 184, with seismic horizons shown as blue lines, and two well locations indicated. Our interest is in characterizing the reservoir located immediately below the K2 seismic horizon, represented by the blue line that lies between the other two. The lowermost seismic horizon corresponds to Paleozoic-age strata, considered the basement in the area. We used the wells Apiay-5 and Apiay-13, located in the vicinity of the depicted inline, to obtain the initial, low-frequency model in this area. We selected these wells because they have excellent borehole condition in the K2 Unit —i.e., good caliper— which guarantees the quality of density and velocity data acquired in them, and by extension, the quality of our low-frequency impedance model.

The intermediate box contains the misfit plot. Dark green areas represent large errors; white areas, low errors. Notice the results are very good for the top part of the K2 Unit, which is the oil-bearing section, and the focus of our reservoir characterization efforts. There are some areas of considerable misfit in the uppermost part of the plot, associated with the bad quality of the logs —and consequently, of the initial model— that results

from borehole enlargement in this section. Large errors in the bottom part derive from the lack of a reliable impedance model in this section. Since most wells were drilled to a few feet below the oil water contact, the bottom section has little control from logs. This section is of little economic interest, though, because it is water-bearing. This large, low-salinity aquifer may become appealing in a few decades, though.

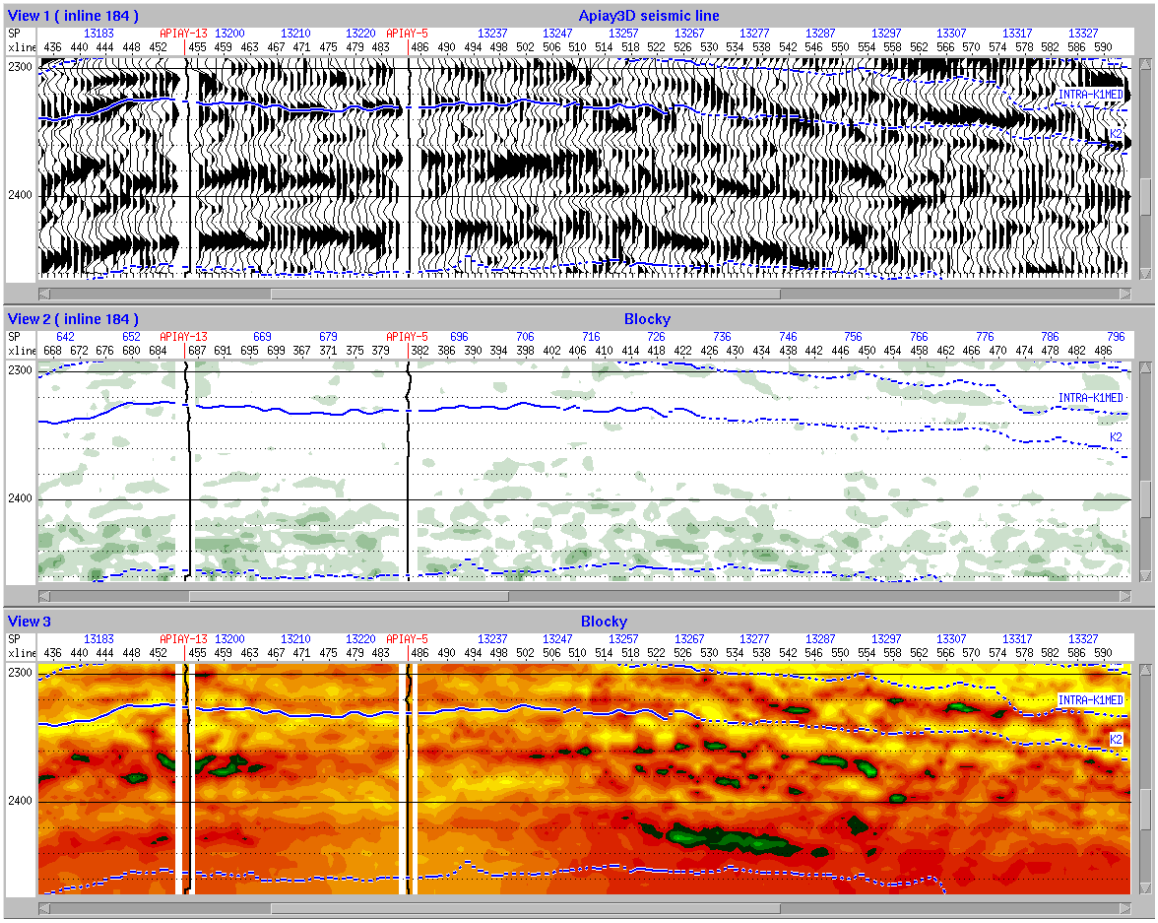

Figure 6.2: Seismic line, error plot and inversion results (impedance).

The lowermost plot is the inverted impedance section. Yellow colors are low impedance (high porosity), orange colors are intermediate impedance (fair porosity) and green colors are high impedance (low porosity). The oil water contact is located about 25 ms below the K2 top. Notice the variability of impedance in the oil-bearing zone, which reflects lateral porosity changes, and the presence of somewhat discontinuous green bodies, which are likely to be related to low-porosity and permeability rocks, such as those found in cemented channel-base and abandoned channel facies.

I present the results of the second test in Figure 6.3. The velocity and impedance logs are from the Apiay-9 well, and the respective traces are taken from the inverted volume at the location closest to the well. The match is good in both cases for almost all the logged interval. In particular, the section from 2300 to 2325 ms., which corresponds to the oil-bearing zone, shows a close agreement between the inversion results and the well logs. In the bottom part, inverted traces deviate from the log measurements, but as mentioned before, this zone is not the focus of our characterization efforts. From these two tests we conclude that porosity can be reliably inferred from seismic measurements.

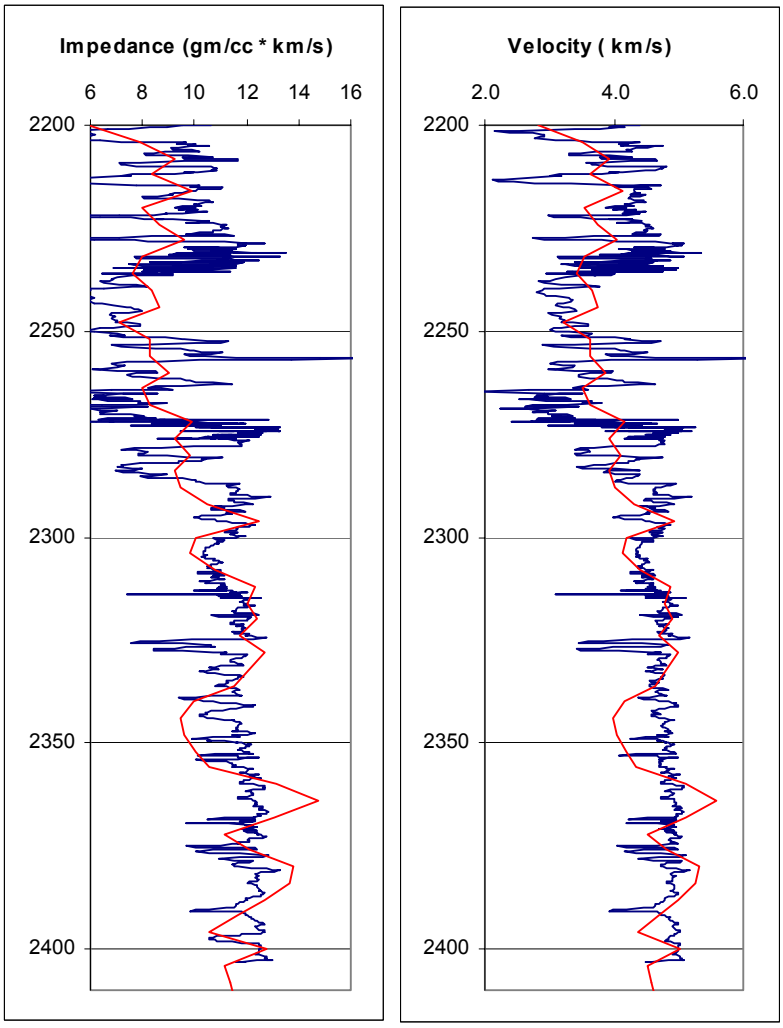

Figure 6.3: Comparison between well logs and inverted velocity and impedance traces.

We extracted seven horizon slices —i.e., parallel to a seismic horizon— from the impedance cube every 4 milliseconds from the K2 seismic horizon (Figure 6.4); these depict the lateral variability of seismic impedance in the volume. The slice at the interface is too influenced by border effects, so we will not use it for porosity prediction. All the slices are parallel to the K2 top, and cover the whole oil-bearing interval in the area shown.

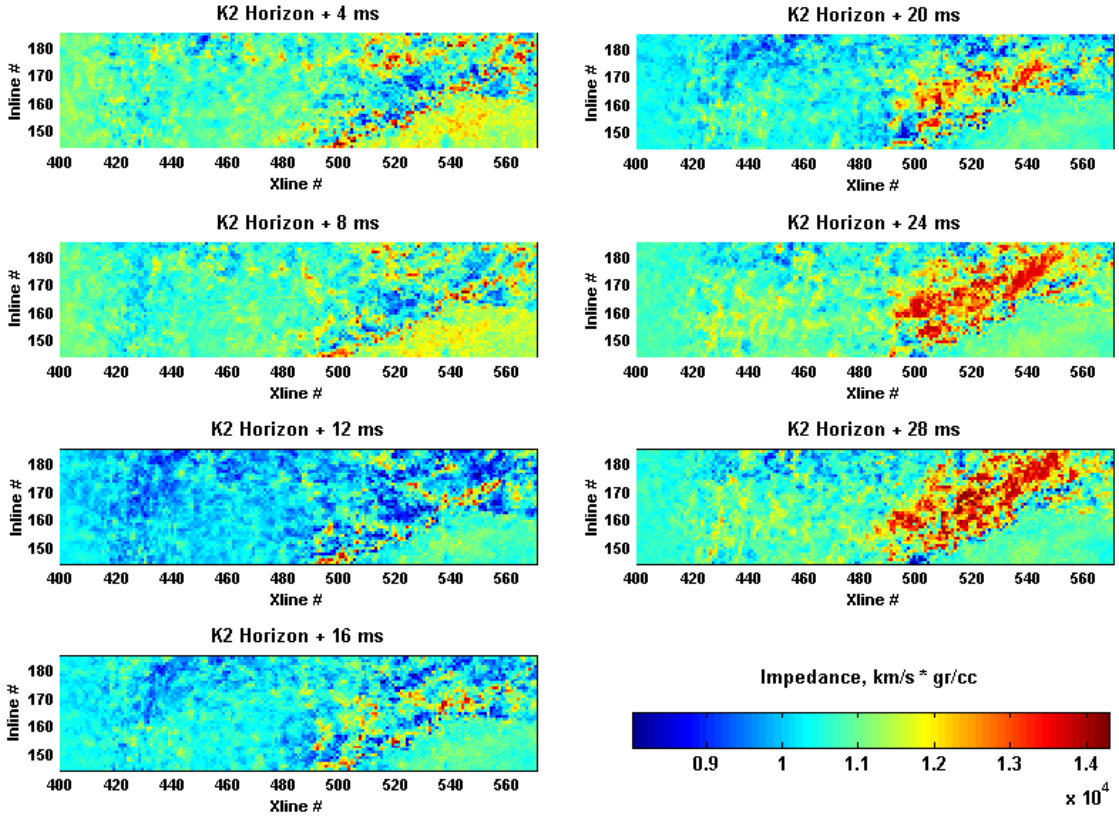

Figure 6.4: Horizon slices extracted from the inverted impedance cube.

Some stratigraphic features become evident in these horizon slices: the continuity of low impedance points can be interpreted as a fluvial channel, which is the depositional environment for the K2 Unit according to sedimentology studies. The linear feature going from xline 490, inline 145 to xline 575, inline 185 is a reverse fault that separates the structures of Apiay and Apiay-Este. The fault affects the inverted impedance values in its immediate neighborhood, where any interpretation should be conducted with care.

The plots in Figure 6.5 result from applying thresholds to the color scale, and are intended to highlight different types of facies. Black patches in the left column plots

highlight low impedance values, i.e., good porosity facies. Plots in the right column draw attention to high impedance values that can be interpreted as low porosity rocks. A channel interpretation is indicated. A closer look at the images in Figures 6.4 and 6.5 shows that the position of highlighted features shifts between time frames, which is normal in a fluvial depositional system.

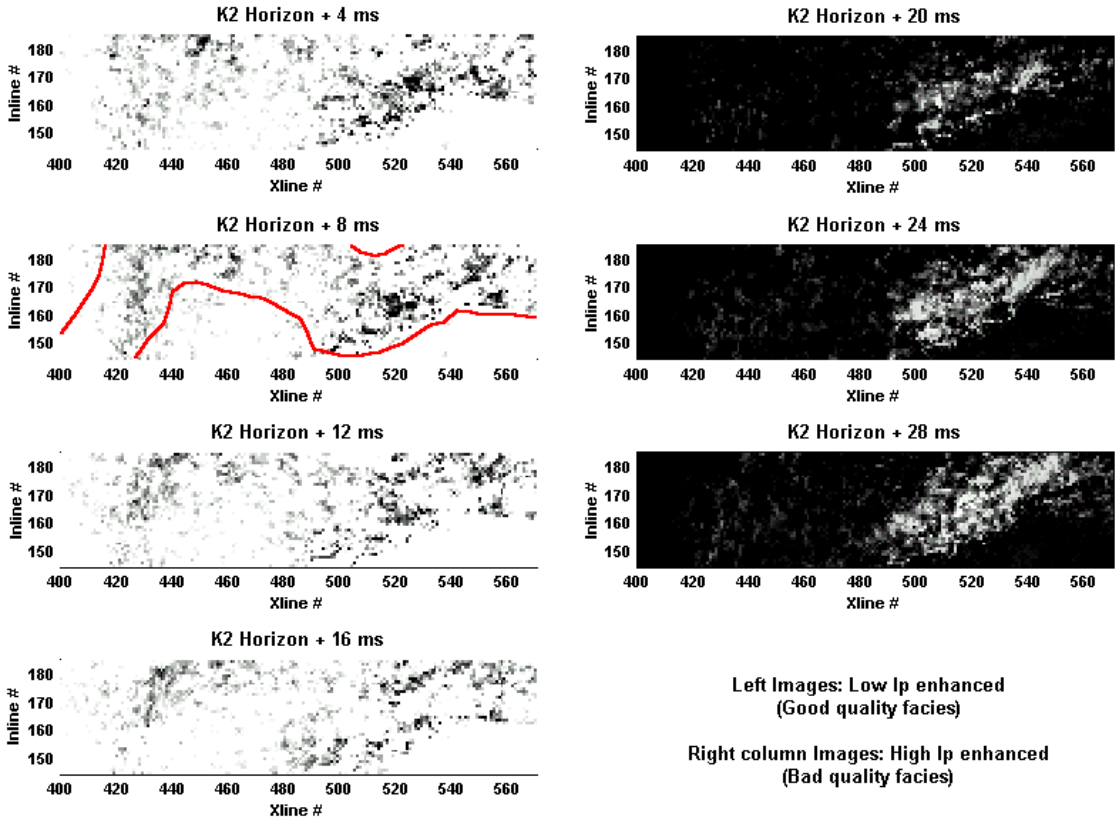

Figure 6.5: Horizon slices extracted from the inverted impedance cube, highlighting good quality (left column) and bad quality (right column) facies.

The interpretation is consistent with features observed along other planes. Figure 6.6 shows a three-dimensional representation of the inverted impedance results, together with slices along the three planes. Once more, all slices have been flattened parallel to the K2 seismic horizon. Notice the channel-like feature at crossline # 522, and the occurrence of low-impedance values at the top of the inline plot, which cuts mostly through the center of the channel. These plots let us confidently conclude that impedance data is a powerful tool for stratigraphic and petrophysical interpretation in reservoirs that belong to the K2 Unit of the Apiay-Ariari province.

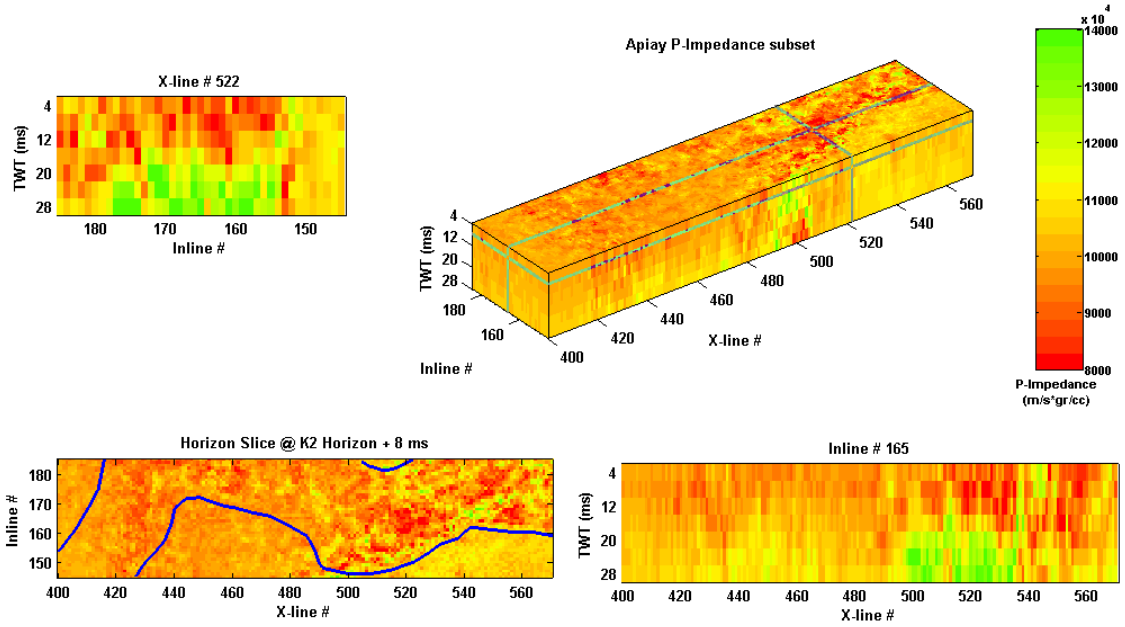

Figure 6.6: Impedance cube with slices at crossline # 522, inline # 165, and the K2 seismic horizon + 8 ms.

6.2 Selection of a Study Area for the Joint Inversion of Impedance and Production Data

Estimating petrophysical properties from inversion of seismic and reservoir engineering data is both computationally and data intensive. This is mainly because the fluid flow forward model —i.e., the reservoir simulator— is expensive to evaluate. Solving the problem requires efficient codes and excellent computer performance, on top of good quality data. On one hand, our computer code is designed for experimental purposes, and lacks the efficiency of commercial reservoir simulators. On the other hand, although we benefited in this project from reasonably fast hardware resources, our computational capabilities are modest when compared to the leading edge of computer technology.

Because of computational and data limitations, we could not estimate the petrophysical properties in the whole Apiay-Guatiquía Field. Thus, we selected a study area based on the availability of impedance, core and production observations. Availability of core data reduces the possibilities to wells Apiay-3, Apiay-9, Apiay-10, and Apiay-11. Of these wells, Apiay-3 is out of the area of the pilot impedance inversion

we performed. We also took into account structural position, to obtain a maximum number of seismic samples in the oil-bearing zone. Figure 6.7 shows a structure map of the K2 Unit top in the Apiay-Guatiquía Field. Notice that well Apiay-9 has highest structural position. The oil column in the Apiay-9 well is 211 ft. The well has a good set of core measurements and log data, which I presented in Chapter 5. Production data in the form of monthly flow rates is also available for this well. Based on these considerations we selected the area around the well Apiay-9 for our study.

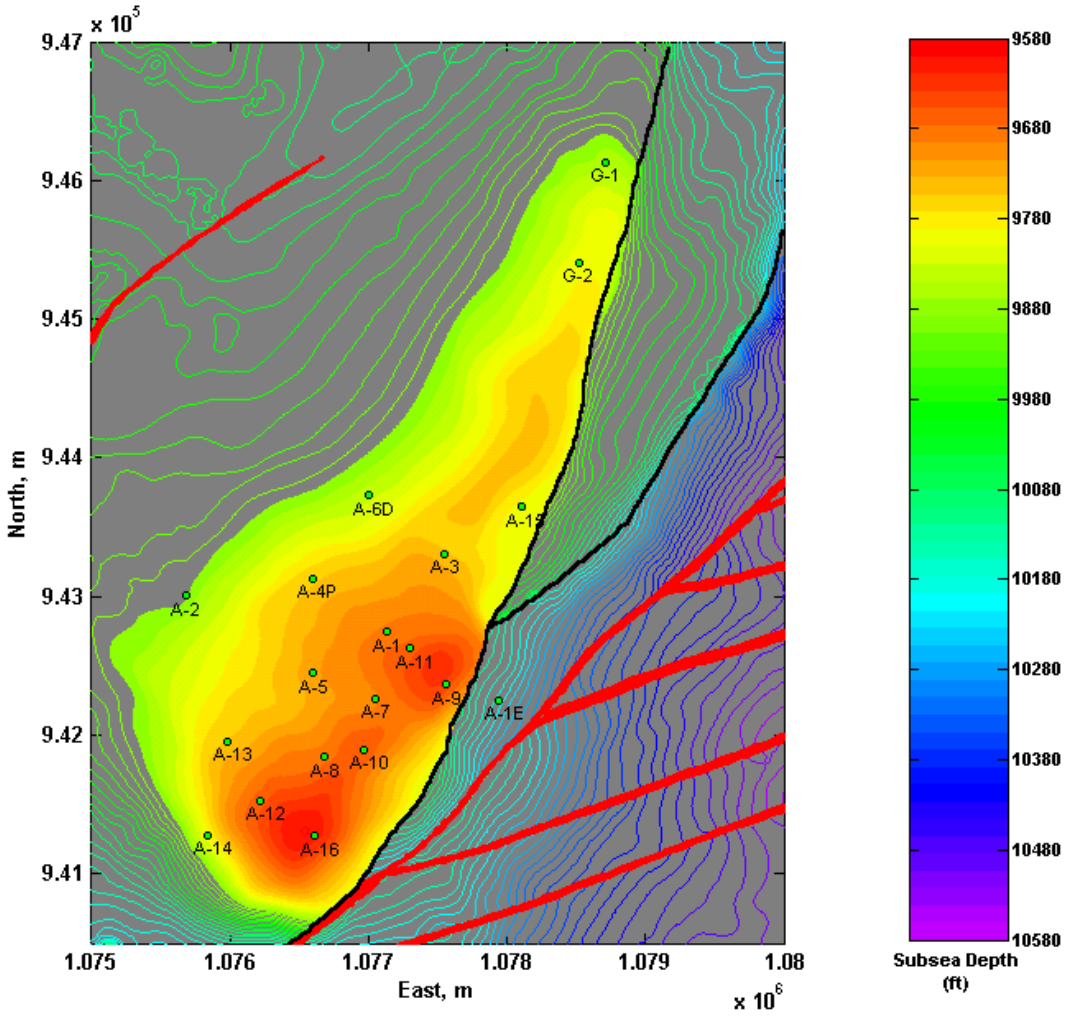

Figure 6.7: A map of the top of the K2 Unit, with the location of vertical wells annotated. The reference datum depth is the sea level. Filled contours represent the oil-bearing zone. Black lines are reverse faults; red lines, normal faults.

6.3 Data Preparation

The steps involved in data preparation include the conversion of inverted impedance data from time to depth, production data filtering, and derivation of conditional cumulative probability density functions from core observations. In this section I describe those steps.

6.3.1 Time-to-Depth Conversion of Impedance Data

We based our time-to-depth conversion of impedance data on the structure map of the K2 —which Ecopetrol geophysicists obtained from the same seismic survey we used in our impedance inversion pilot— as well as the K2 seismic horizon shown in Figure 6.8, and the logs of well Apiay-9. We followed a two-step procedure to convert impedance data from time to depth: In the first step we determined the depth of the K2 Unit top at the location of each common-depth point (CDP). In the second step we determined the depth of each time sample from the velocity logs. Details about these two steps follow.

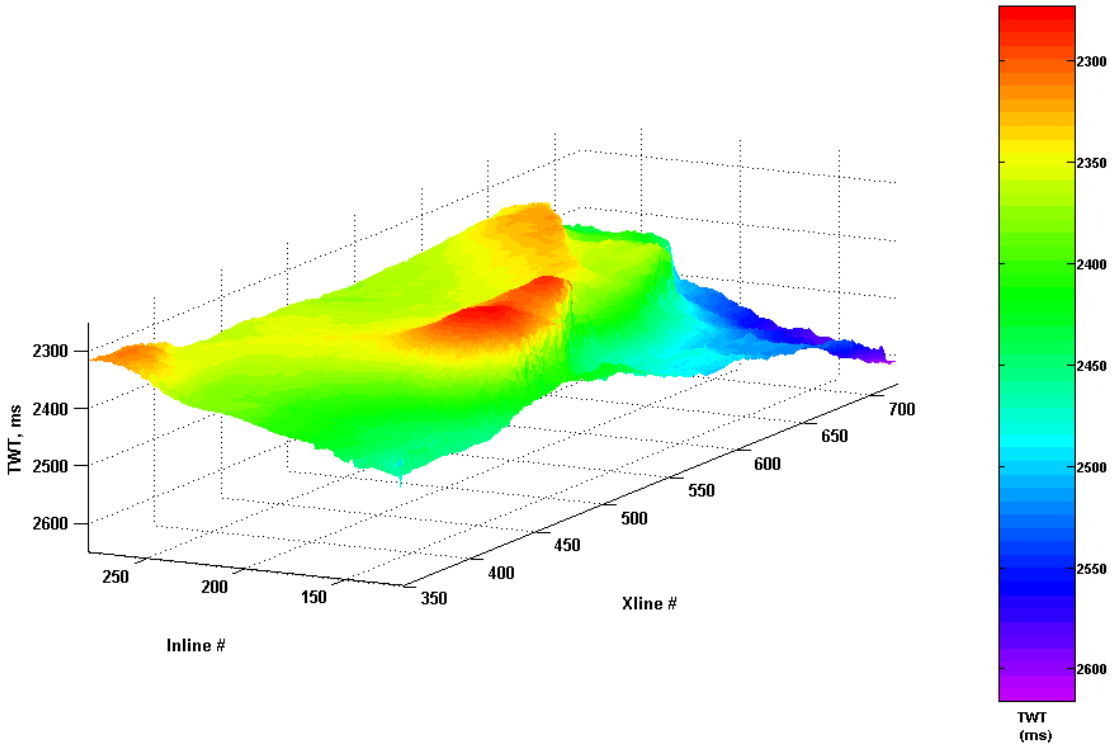

Figure 6.8: A surface plot that represents the K2 seismic horizon.

The structure map shown in Figure 6.7 is based on digitized geographic coordinates for each depth contour. We retrieved the geographic coordinates for each CDP in the 3D survey and performed a bi-dimensional interpolation of the depth contours, to determine the depths at each CDP's geographic location. As a result we obtained a depth map for the top of the K2 Unit, based on the system of coordinates of the Apiay 3D seismic survey.

The second step consists of determining the depth of each impedance sample in the cube, which is a time-to-depth conversion within the reservoir, and requires a proper velocity model. We used the logs of well Apiay-9 to construct that velocity model. First we edited the log to remove abnormal data, namely the readings at washed-out intervals. Then we accounted for scale-dependent frequency dispersion caused by heterogeneities of small thickness by computing the low-frequency, effective-medium theory limit of the velocities [*Mukerji*, 1995], which we approximated by a moving Backus average of well log velocities with a window one-tenth of a wavelength long. We estimated the wavelength from the average well log P-wave velocity in the upper part of the K2 Unit, assuming that the dominant seismic frequency is 35 Hz. We converted the upscaled, low-frequency limit log from time to depth by computing the two-way time of each sample, and from the result we estimated the velocity function that I show in Figure 6.9. Finally, we used this velocity function to compute the depth that corresponds to each time sample. Figure 6.10 shows the depth-converted impedance data in the area of well Apiay-9.

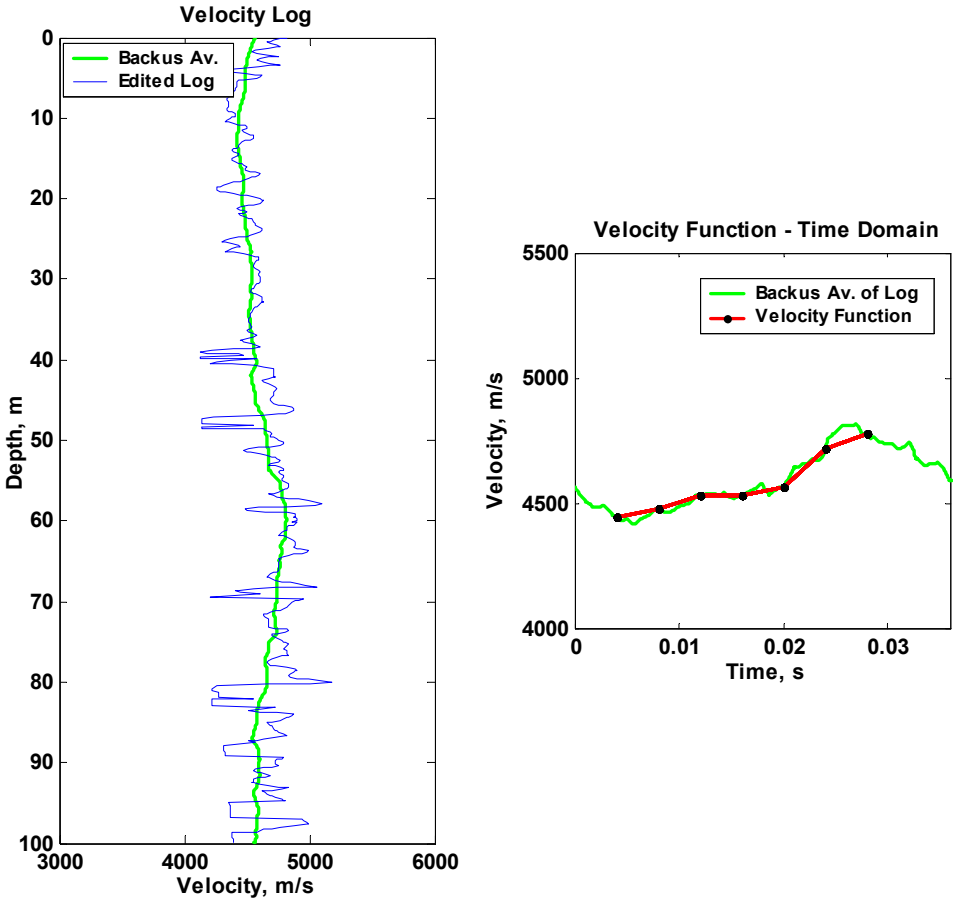

Figure 6.9: A set of plots that summarize the estimation of a velocity function for time-to-depth conversion of seismic data in the area of well Apiay-9. The left-hand plot shows in blue the velocity log after editing. The green curve corresponds to the low-frequency limit upscaled velocity log. The plot on the right shows in red the estimated velocity function in the time domain.

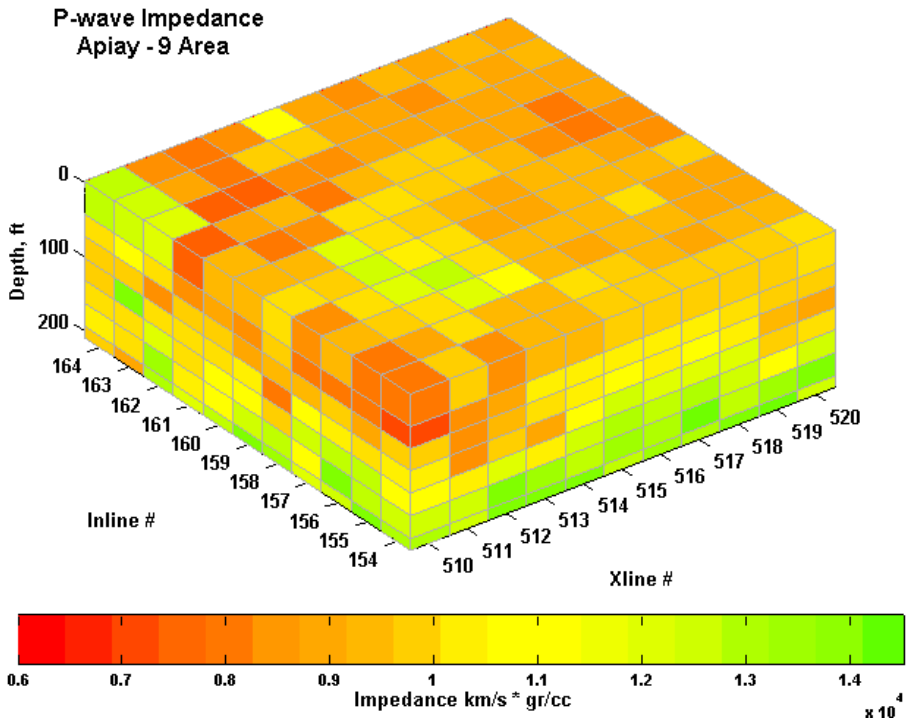

Figure 6.10: A plot of depth-converted P-wave impedance data in the area of well Apiay-9. The vertical axis corresponds to depth from the K2 Unit top.

6.3.2 Production Data Filtering

We received from Ecopetrol the production history of well Apiay-9. I summarize the data in Figure 6.11, which is a plot of flow rates, as measured in the field separation facilities. Figure 6.12 shows curves of gas-oil ratio and water cut computed from flow rates. The bubble point pressure for the oil produced from the K2 Unit of the Apiay-Guatiquía Field ranges between 200 and 500 psia, which is by far smaller than the well-flowing pressures recorded in the field. All the produced gas comes out of solution while the fluid travels from the sand face to the separation facilities. Thus, only two phases — oil and water— coexist in the reservoir.

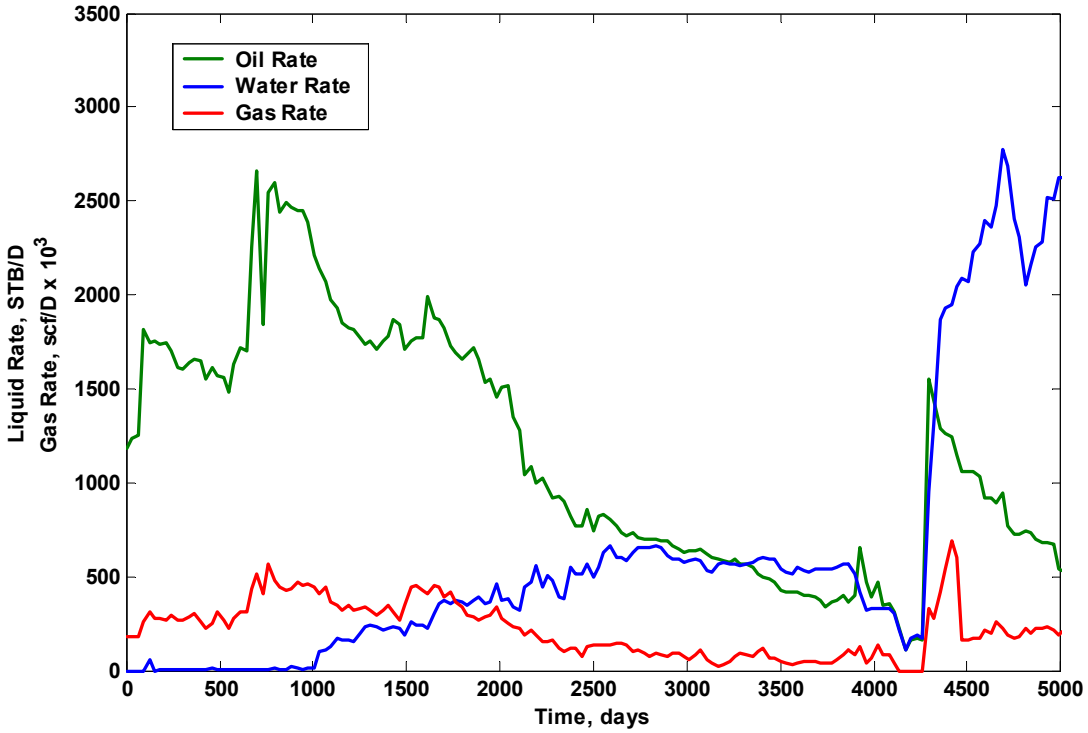

Figure 6.11: A plot of oil and water flow rates data for the Apiay-9 well.

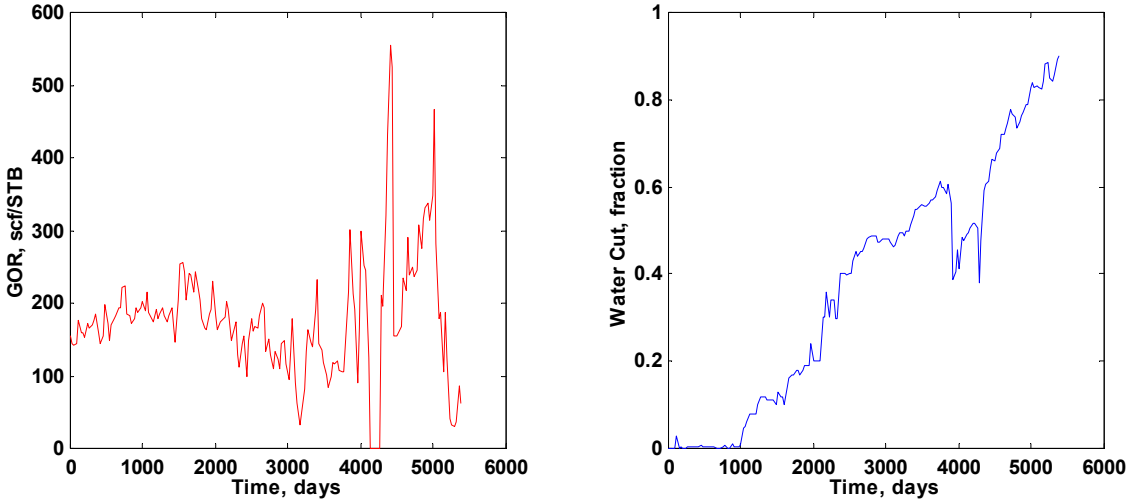

Figure 6.12: Plots of gas-oil ratio and water cut data for the Apiay-9 well.

The data shows a reduction in water cut right before 4000 days of production, followed by a sharp increase in well productivity. These two events reflect the results of either workover jobs, or changes in the production well control conditions. The second event corresponds to the installation of a submersible pump in the well. We did not have any further information about the record of workovers, and could not determine the source of the behavior observed before 4000 days. Consequently, we restricted our efforts to matching the primary production part of the history, up to 3867 days.

Even though we had access to some pressure data from the field, none of the well tests we received were conducted on the Apiay-9 well. In the absence of bottom-hole pressure information our approach to production history matching in this study is to fix the total liquid rate produced by the well, and invert the water cut observations.

The inversion approach we implemented in this work is based on least squares, as we discussed in Chapter 2. Although this is a powerful inversion technique, recall that least squares is quite sensitive to outliers. Thus, it is important to filter any data involved in a least-squares inversion to separate the trends that represent the response of a physical system from local changes that result from to temporal perturbations. The system response we are interested in is given by the low frequency trend in the water cut curve. To retrieve this trend we convolved the data with a bow-car operator of length seven. Figure 6.13 shows the resulting filtered water cut curve, overlying the original data.

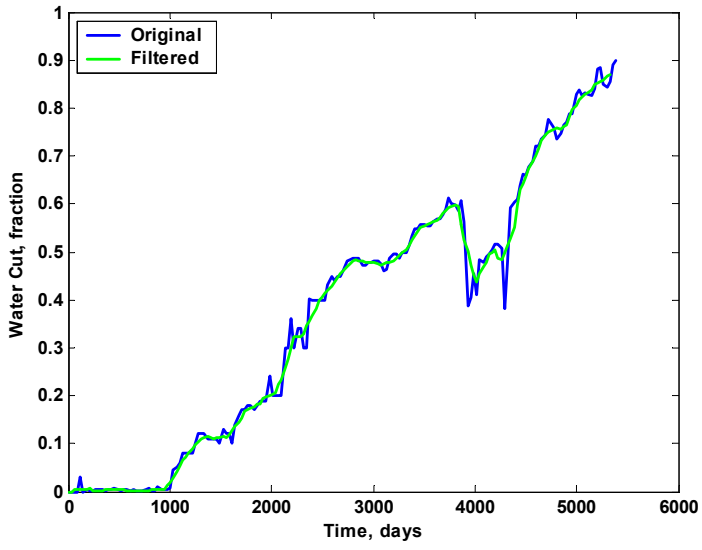

Figure 6.13: A plot of original and filtered water cut data for the Apiay-9 well.

6.3.3 Determination of Conditional CDFs of Permeability given Porosity

We showed in Chapter 3 the advantages —in terms of faster convergence and accuracy of results— of integrating many different types of relevant data into the inversion process. Core data are an important piece of information, because they are direct measurements of the properties we want to invert for, and help constrain the region of feasible results. In this work we used conditional cumulative distribution functions of permeability given porosity to inform the relationship between porosity and permeability within the feasible region. The estimation of conditional CDFs of permeability given porosity should account for the effects of *upscaling*, *undersampling* and *biased sampling*, and differences in effective pressure.

Consider the porosity and permeability data in Figure 6.14, which correspond to measurements in core samples from different areas.

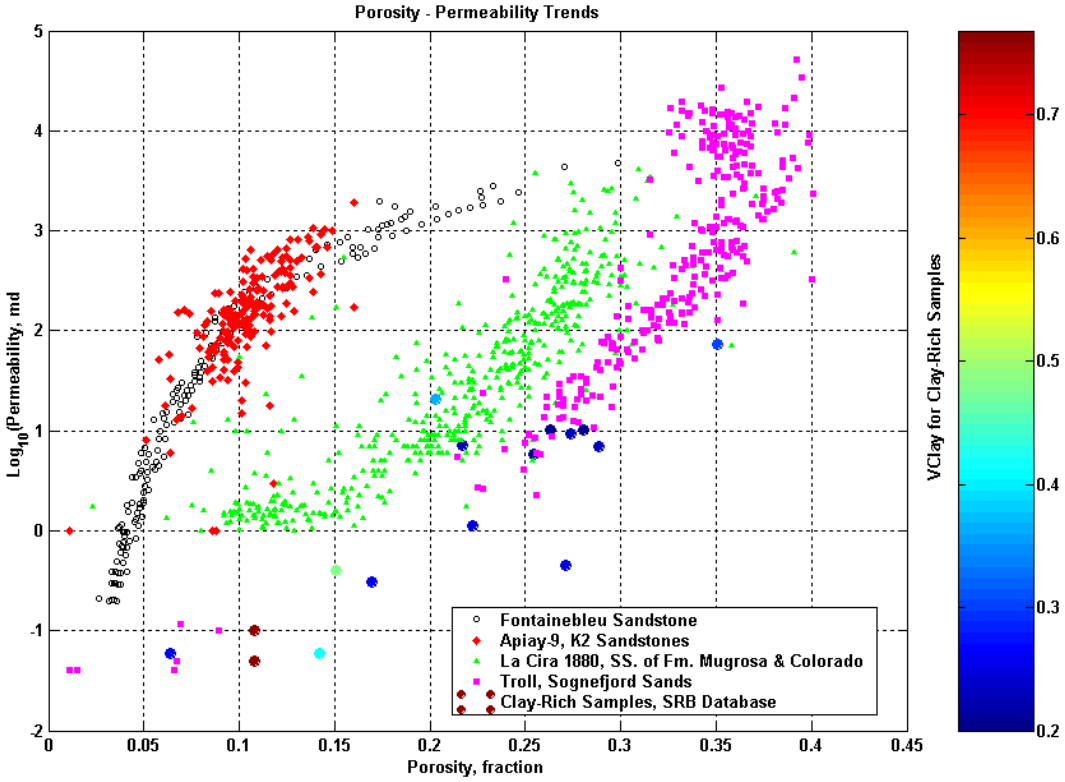

Figure 6.14: A plot of porosity and permeability from various data sets. The color bar on the right corresponds to the fraction of clay for the set of clay-rich samples, shown as large-size, colored circles.

Clearly, the data suggest that porosity and permeability estimates for the K2 Unit sandstones should follow a trend that is similar to that of Fontainebleau sandstones, and is far from the trends of subarkoses from the Formations Mugrosa and Colorado in La Cira Field, and far from the poorly consolidated, muscovite-rich Sognefjord sands from Troll Field. Although this is important information for modeling the CCDFs of permeability given porosity, the direct estimation of CCDFs from core data may yield inaccurate results for the following reasons:

1. Core plugs are orders of magnitude smaller than reservoir simulation grid blocks. The variance of conditional CDFs of permeability given porosity at scale of the simulation grid will be smaller than at the core scale. On the other hand, permeability is often an anisotropic tensor. Permeability upscaling should account for the direction of pressure gradients.
2. The total volume of available cores is limited. Thus, cores may fail to represent areas of the reservoir with either better or worse rock quality than that of the samples measured (*undersampling*).
3. Core sampling is often biased towards the best quality facies, which are the most productive and the emphasis of reservoir characterization studies. Limited core recovery in shale intervals aggravates the problem. Other facies exist in the reservoir, though, and need to be modeled.
4. Core data are often measured at effective pressures that are different —typically lower— than those observed at reservoir conditions, which may introduce significant differences that should not be overlooked.
5. Sample cleaning may leave remnants of saturating fluids —as in the case of the K2 Unit sandstones— and/or may destabilize and remove loose pore-filling clay particles.

The aforementioned reasons indicate that the proper estimation of conditional CDFs of permeability given porosity requires further investigation. In this work we based our estimation of CCDFs on core data, and made educated assumptions when applying corrections, in most cases supported by data, but sometimes driven by common sense. The corrections we made are based on the following observations and assumptions:

1. The average change in permeability between 5 and 25 MPa of confining pressure observed in samples from the Apiay-Guatiquía Field is 20 md. The

average porosity reduction over the same pressure range is 0.6 % (see Figure 5.6).

2. Figure 6.15 shows that insufficient cleaning produces an average underestimation in porosity of 3 %.
3. Based on the latter two observations we assumed a constant correction of +2 % to core porosity data.
4. We accounted for insufficient sampling by assuming that outside the range of porosity observed in core samples, the trend of permeability vs. porosity is slightly lower than that of the Fontainebleau sandstones.
5. The vertical-to-horizontal permeability ratio *Kv/Kh* in core samples ranges from 0.01 to 1, with a median ratio of 0.35, as shown in Figure 6.16. This indicates that the K2 Unit sandstones can be quite isotropic in some cases, but on average have a *Kv/Kh* ratio of about 1/3. This is only at the core scale, though. To account for the further reduction in vertical effective permeability due to upscaling we assumed a *Kv/Kh* ratio of 1/5.
6. We assumed that conditional CDFs of permeability given porosity have the shape of a truncated Gaussian cumulative distribution function.

After applying the aforementioned corrections and assumptions we obtained the conditional cumulative distribution functions that I show in Figure 6.17.

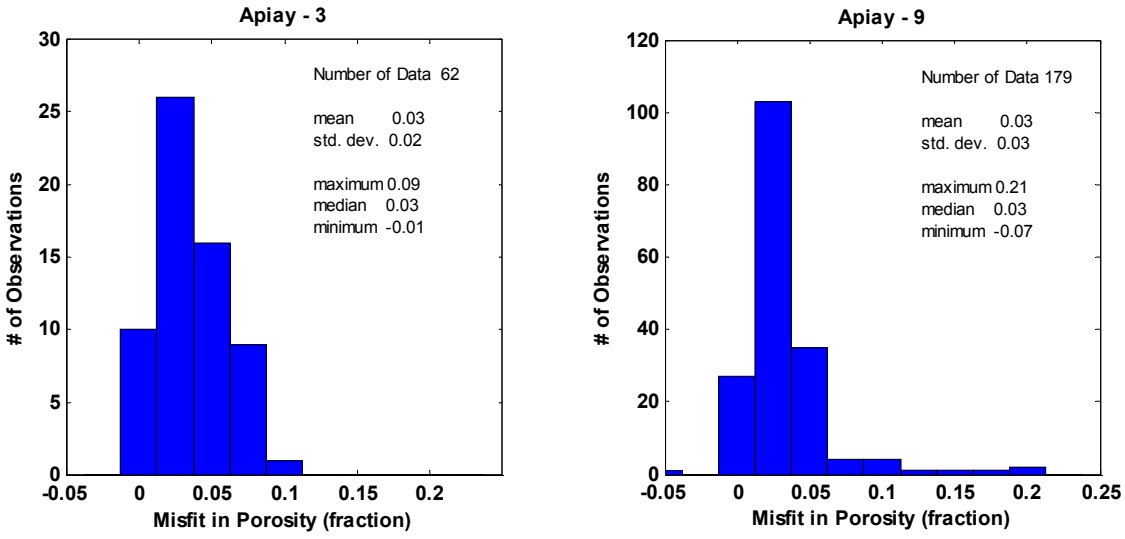

Figure 6.15: Histograms of the misfit between core porosity and log porosity (as computed from the density log) for wells Apiay-3 and Apiay-9.

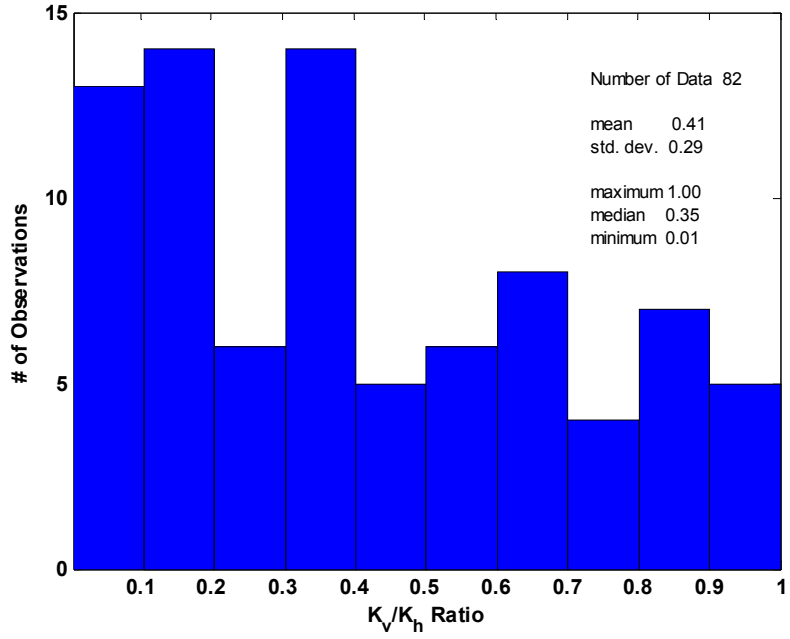

Figure 6.16: A histogram of the vertical-to-horizontal permeability ratio in samples from the Apiay-Guatiquía Field.

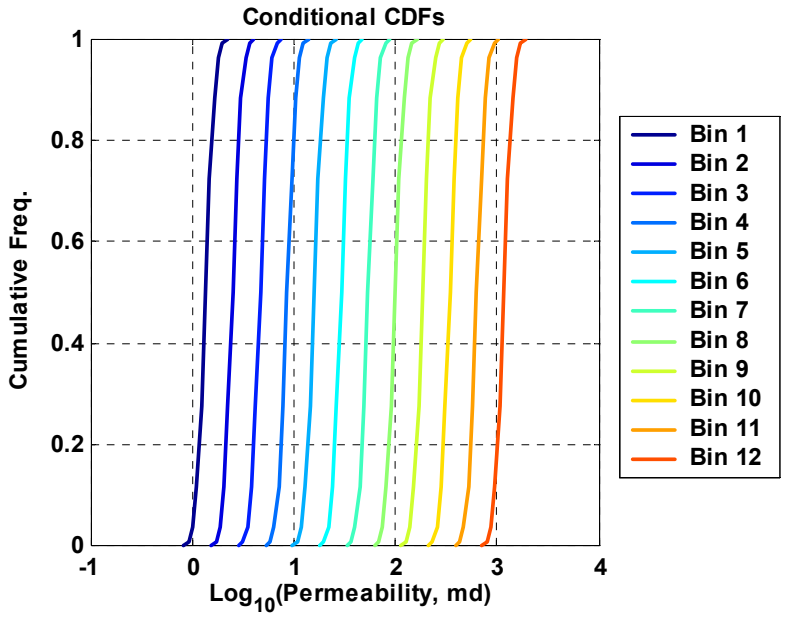

Figure 6.17: A plot of conditional cumulative distribution functions of permeability given porosity.

6.4 Reservoir Model

Our reservoir model for the drainage area of well Apiay-9 is composed by a grid of 11x11x8 blocks. We setup a model such that the seismic and fluid flow grids are the same. Consequently, grid blocks have constant length and width, but their thickness corresponds to those we obtained from the time-to-depth conversion of impedance data. The massive character of the K2 Unit let us assume that the reservoir can be modeled with grid blocks this thick. Figure 6.18 shows our reservoir model.

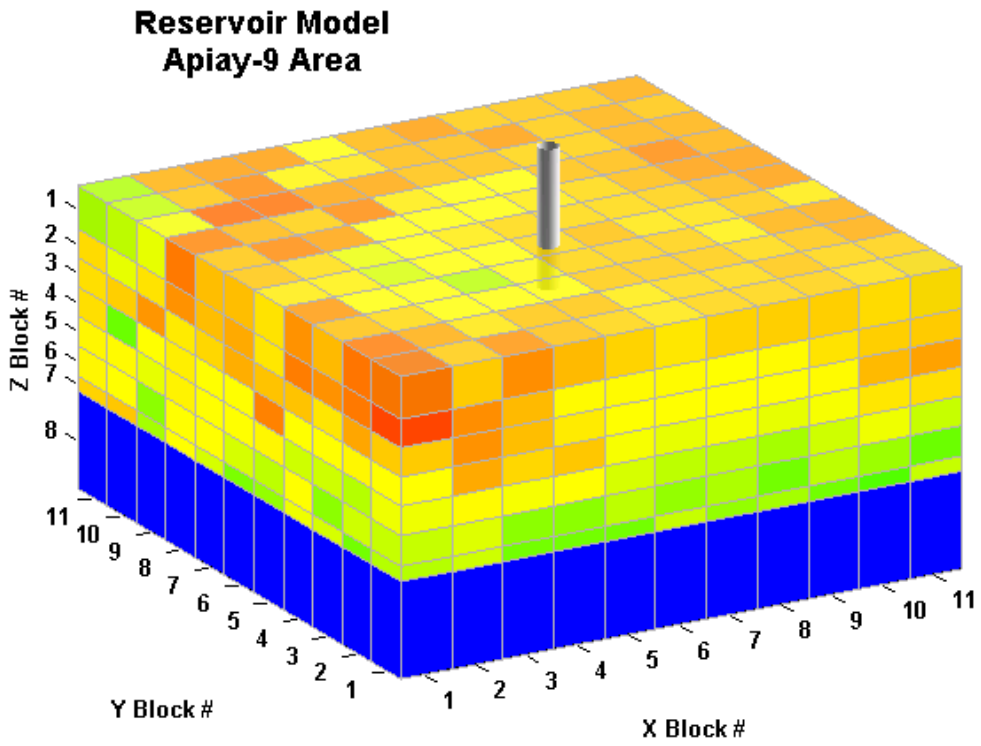

Figure 6.18: A plot of the discrete model that represents the K2 Unit reservoir in the area of well Apiay-9. The well, whose location is indicated, is connected only to the uppermost grid block. The blue layer represents the bottom constant pressure boundary, whose properties we assumed were constant.

Reservoirs in the K2 Unit of the Apiay-Ariari province benefit from the strong water-drive produced by a regional aquifer. The direction of flow of formation waters in Cretaceuos strata varies from West-East to Northwest-Southeast in the southwestern part of the Llanos Basin [*Villegas et al.* 1994], where the Apiay-Guatiquía Field is located. To model the strong pressure support from the aquifer we enforced constant pressure boundaries at the bottom and back edges of the model —i.e., the layers located at $Z = 8$,

and Y = 11. We considered other boundaries impermeable, which is reasonable considering that the drainage area of the well is bounded by a sealing reverse fault to the East, i.e., the front and right edges of the model. To account for producers located to the East and Northeast of well Apiay-9, we allow the back edge pressure boundary to be weaker than the bottom pressure boundary. We fixed the petrophysical properties of the latter, but let vary those of the former. The oil-water contact in our model lies at the interface between Z layers number 7 and 8.

The well is located at the block X = 6, Y = 5. Although the Apiay-9 well drilled the entire K2 Unit, it was completed only on the uppermost part of the section to prevent early water breakthrough, which would have seriously reduced the well's recovery factor. Thus, we assumed that the well is connected to only the uppermost block. As expected, this produces a cone of water that grows with time. Figure 6.19 shows three slices that depict the shape of the cone, as predicted by the model after 760 days of production, at an intermediate step of the inversion. At this production time the reservoir simulator predicts a water-cut of 0.75 from the petrophysical properties at this inversion iteration —clearly, a significant misfit, considering the water cut curve shown in Figure 6.13.

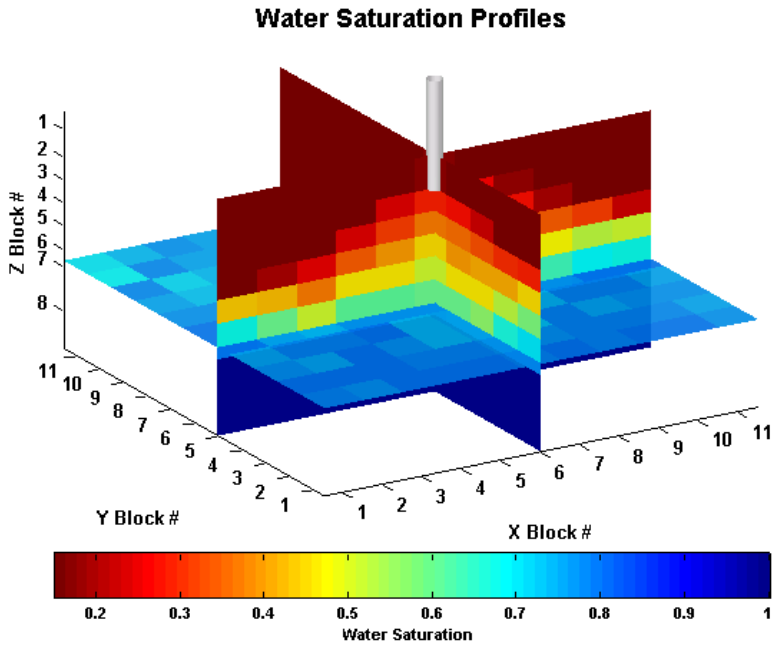

Figure 6.19: A plot of water saturation profiles in the area of well Apiay-9, as computed by the fluid flow model after 760 days of production.

6.5 Inversion Results and Discussion

The variables involved in our objective function include seismic-derived P-wave impedance, water cut data, and core-based cumulative distribution functions of permeability given porosity, i.e.,

$$E = \sum_{i=1}^{t_{Ip}} \sum_{j=1}^{n_{blocks}} W_{seis} \left(Ip_{obs}^{t_i, block_j} - Ip_{calc}^{t_i, block_j} \right)^2 + \sum_{i=1}^{t_{wcut}} \sum_{j=1}^{n_{wells}} W_{wcut} \left(wcut_{obs}^{t_i, well_j} - wcut_{calc}^{t_i, well_j} \right)^2 + \sum_{i=1}^{n_{bins}} \sum_{j=1}^{n_{samples_i}} W_{CCDF} \left(K_{a-priori\ CCDF}^{bin_i, sample_j} - K_{inversion\ CCDF}^{bin_i, sample_j} \right)^2 . \quad (6.1)$$

Because of the lack of bottom-hole pressure data, the amount of information — particularly for permeability— in this case is smaller than in the synthetic cases I presented in Chapter 3. In addition to this, there is only one well, and there are about 10 times more grid blocks in the model. This makes the problem a lot harder to solve.

We used a homogeneous distribution of properties, shown in Figure 6.20, as the initial model for our inversion. As in the cases presented in Chapter 3, updates to the permeability model are slower than those of the porosity model. After five iterations the algorithm predicts a porosity field that results in a reasonable match of the impedance data, but the misfit in water cut is still significant, and falls into a local minimum for permeability. This indicates that the problem does not tolerate an initial model that is too far from the solution. Thus, we fixed the porosity estimates, perturbed the permeability model with the results of a linear regression with porosity, and restarted the inversion. I show in Figure 6.21 the resulting fields of porosity and permeability. Figure 6.22 shows the misfit in P-wave impedance, while Figure 6.23 shows the calculated and observed water cut curves. The results indicate that, after a total of 13 iterations, the algorithm produces porosity and permeability estimates that lie within a feasible region constrained by core observations, and yield a reasonable match of both impedance and water cut.

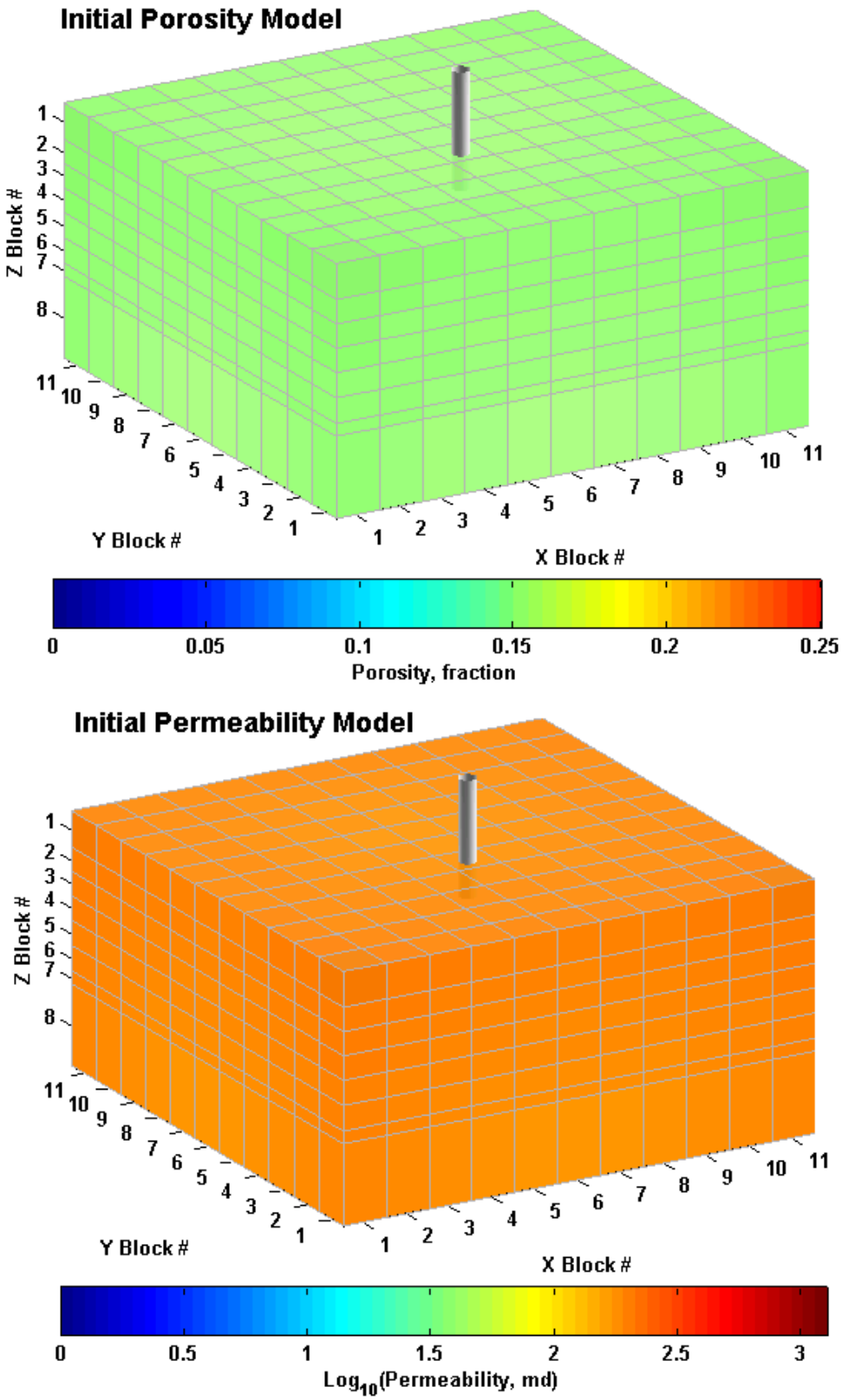

Figure 6.20: Initial models of porosity and permeability.

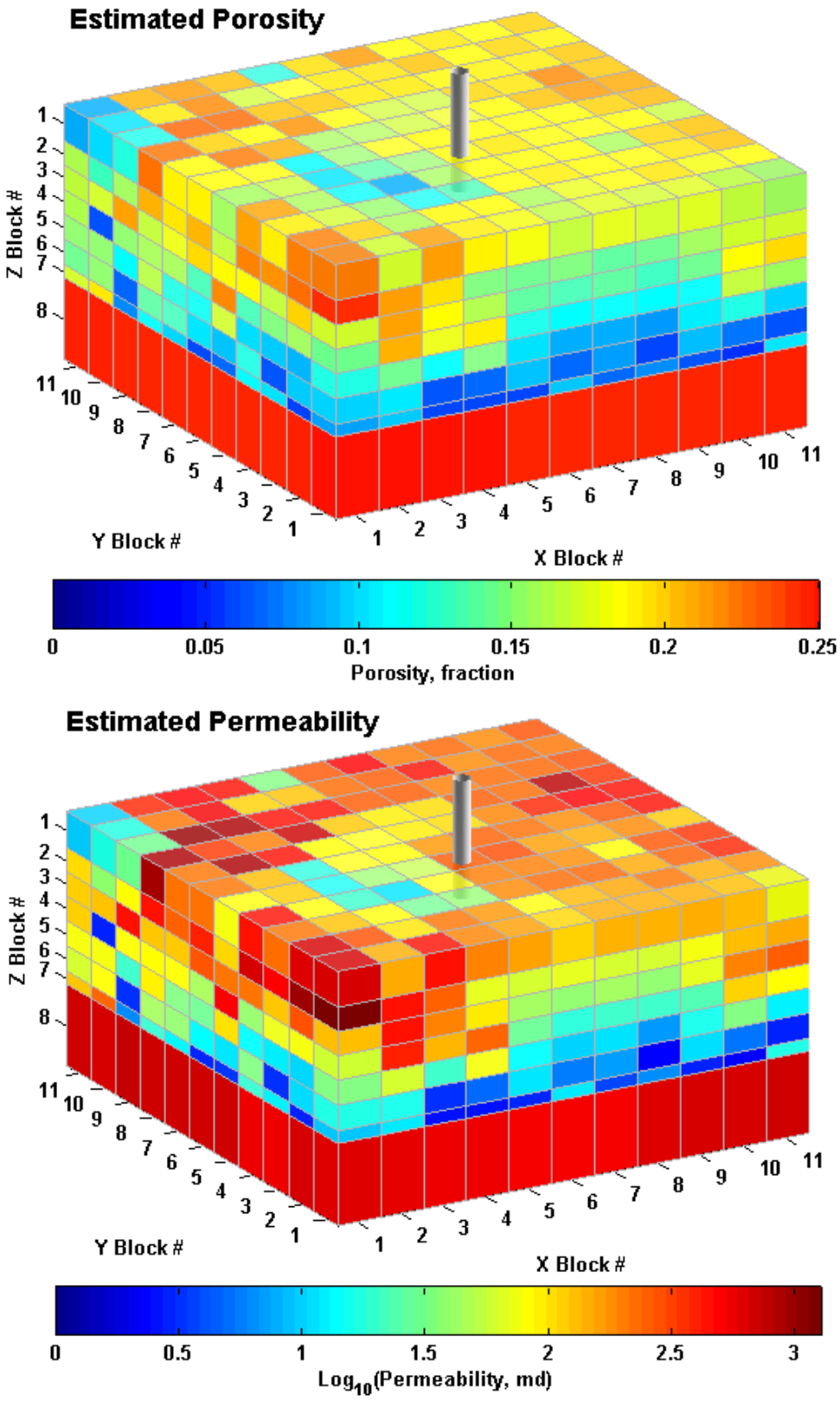

Figure 6.21: Porosity and permeability estimated from the integrated inversion of seismic and production data.

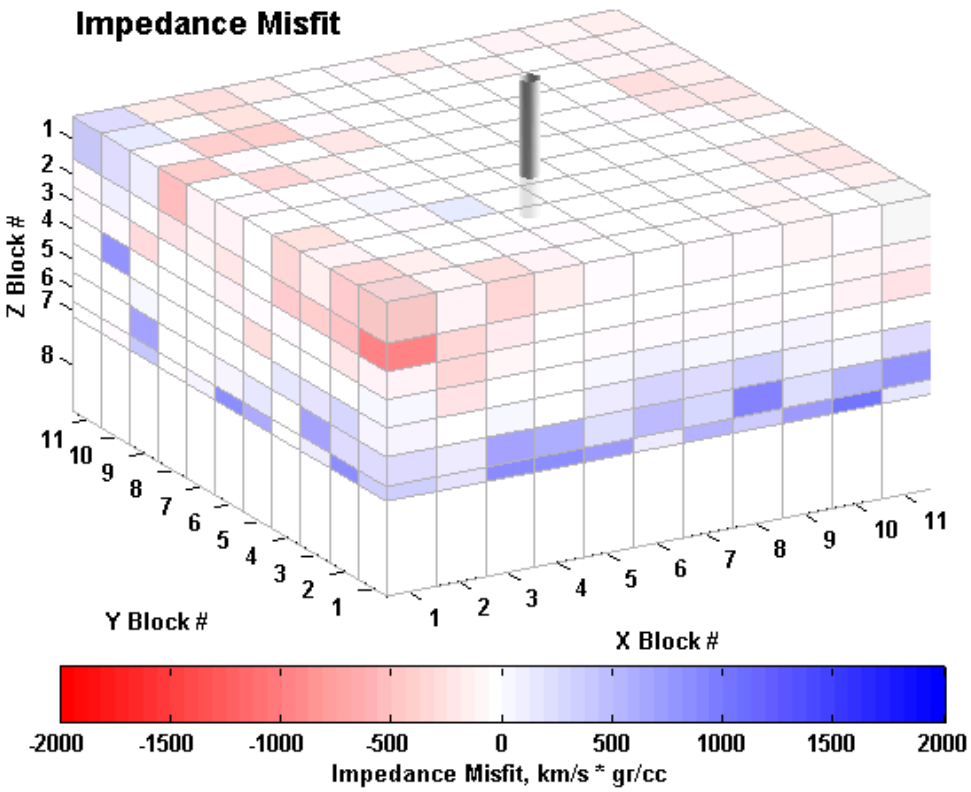

Figure 6.22: Misfit between the "observed" and calculated values of P-wave impedance. The term "observed impedance" actually refers to the results of the inversion of seismic amplitude data, as described in section 6.1.

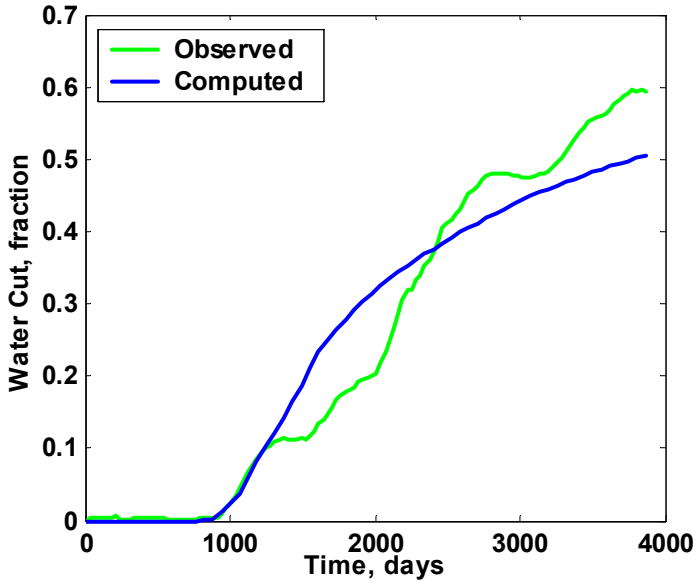

Figure 6.23: A plot of observed and calculated water cut curves.

The porosity and permeability estimates, and the match of production and seismic data we obtained, are influenced by, and subject to the validity of a number of assumptions. For instance, the reservoir simulator outcomes are significantly affected by relative permeability curves, permeability anisotropy, and boundary conditions, while the seismic match depends on the quality of impedance data, and relies on the dependence of impedance on porosity. Impedance cannot be directly measured; its estimation depends on the quality of seismic data and velocity models used at different seismic processing stages, in the inversion of amplitude data, and in the conversion of amplitude and impedance data from time to depth. All these facts stress the importance of good data and proper models, and in the case of impedance, call for careful processing, and for a major involvement of seismic interpreters in processing.

We visualize that in many instances —the case of the K2 Unit of the Apiay-Guatiquía Field included— facies classification can lead to significant improvements in reservoir property estimation. The works of *Takahashi*, [2000] and *Mukerji et al.*, [2001a, 2001b] showed the benefits of using multiple attributes in classification. The use of depositional trends such as those we identified in this work when performing classification may improve facies prediction and would ensure that the results make geologic sense. Different facies may have dissimilar trends of permeability vs. porosity, different relative permeabilities, distinct elastic properties, and so on. Therefore, the use of either facies classification results, or forward models that can reproduce other seismic attributes may represent a significant reduction in the uncertainty of parameter estimation results. Consequently, a possible improvement to our joint seismic and production data inversion approach is to include classification techniques in the estimation.

Inversion results obtained from gradient-based optimization methods are also affected by the choice of initial models. The ideal approach for reservoir characterization is to perform an analysis of the sensitivity of results to different initial models and varying parameters, such as relative permeability curves and permeability anisotropy ratios. The cost of evaluating the forward model determines whether it is practical to perform such an analysis. The state of computer technology still makes prohibitive such an analysis in most cases, but we are confident that advances in hardware and software will make this analysis feasible. An alternative to gradient-based methods in a scenario of faster

computers is the use of simulated annealing techniques to find the global minimum of petrophysical property estimates.

6.6 Conclusions

Inversion tests show that both velocity and impedance computed from seismic are in close agreement with well log trends in the oil-bearing zone of the K2 Unit in Apiay-Guatiquía. Given the good relationship between porosity and impedance in rocks from the K2 Unit of the Apiay-Guatiquía Field, this indicates that our results are suitable for the estimation of petrophysical properties.

Areal and vertical changes in seismic-derived impedance can be related to porosity trends. Horizon slices may become a powerful tool for stratigraphic and petrophysical interpretation in the oil fields of the Apiay-Ariari province.

We successfully applied our methodology to the integrated inversion of seismic-derived P-wave impedance, water cut data, and core-based cumulative distribution functions of permeability given porosity, to estimate petrophysical properties in the drainage area of well Apiay-9.

Our porosity and permeability estimates result in a good match of water cut and seismic-derived acoustic impedance, and are in good agreement with measurements of porosity and permeability in core samples from the K2 Unit of the Apiay-Guatiquía Field.

6.7 References

Mukerji, T., 1995, Waves and scales in heterogeneous rocks: Ph.D. dissertation, Stanford University.

Mukerji, T., P. Avseth, G. Mavko, I. Takahashi, and E. F. González, 2001b, Statistical rock physics: Combining rock physics, information theory, and geostatistics to reduce uncertainty in seismic reservoir characterization: *The Leading Edge*, **20**, 313-319.

Mukerji, T., A. Jørstad, P. Avseth, G. Mavko, and J. R. Granli, 2001a, Mapping lithofacies and pore-fluid probabilities in a North Sea reservoir: seismic inversions and statistical rock physics: *Geophysics*, **66**, 988-1001.

Nieto, J, and N. Rojas, 1998, *Caracterización geológica y petrofísica del yacimiento K2 en los campos Apiay, Suria y Libertad*. ECOPETROL, internal report.

Takahashi, I., 2000, Quantifying information and uncertainty of rock property estimation from seismic data: Ph.D. dissertation, Stanford University.

Villegas, M. E., S. Bachu, J. C. Ramon, and J. R. Underschultz, 1994, Flow of formation waters in the Cretaceous succession of the Llanos Basin, Colombia: *American Association of Petroleum Geologists Bulletin*, **78**, 1843-1862.